Diss ETH No. 14872

Characterization and Development of Direct Methanol Fuel Cells

A dissertation submitted to the
SWISS FEDERAL INSTITUTE OF TECHNOLOGY
ZURICH

for the degree of
Doctor of Technical Sciences

presented by

Arne Geiger

Dipl.-Ing. (TU)
born on May 28, 1973
citizen of Germany

accepted on the recommendations of
Prof. Dr. A. Wokaun, examiner
Prof. Dr. M. Morbidelli, co-examiner
Dr. G.G. Scherer, co-examiner

2002

„In der Weite des Meeres siehst Du vielleicht die zurückgelegte Meile nicht, aber sie ist gesegelt.“

Verfasser unbekannt

Acknowledgements

Financial support of the Swiss Federal Office of Energy (BfE) is gratefully acknowledged.

It gives me a great pleasure to express my gratitude to my advisor Prof. Dr. A. Wokaun for his clear-sighted suggestions throughout this work, and my supervisor Dr. G.G. Scherer for his interest, advice, and insights he gave me during the course of my PhD-studies. I have greatly benefited from our interaction during my stay at PSI.

I wish to thank Prof. Dr. M. Morbidelli from the *Chemical Engineering Laboratory* at the *Swiss Federal Institute of Technology* (ETH) for acting as co-examiner of this thesis.

I would like to thank the following persons who contributed to the content of this thesis: Dr. E. Lehmann, Dr. P. Vontobel, and G. Frey for their assistance before, during, and after the measurements at NEUTRA; P. Binkert, R. Hugi, C. Marmy, R. Panozzo, and F. von Roth for their valuable technical advice and assistance throughout the work; M. Kull for his aid to building the last three fuel cell teststands.

Special thanks go to the following persons who helped to this work during their master thesis: R. Eckl for his dedicated work on the current distribution measurements; M. Gisiger and R. Picenoni for their help in characterizing the DMFC.

During the course of my PhD-work I have benefited from discussions with and the assistance of all members of the *Electrochemistry Laboratory* and especially of my own group the *Fuel Cell Group*. Special thanks are due to B. Andreaus, U. Paulus, L. Gubler, and T. Schmidt (many thanks for untiring checking through this document) who have been a great source of encouragement and have helped me to get through the ups and downs of experimental life.

Most of all, I express my deep appreciations to Judith and my parents for tireless encouragement, support, inspiration, friendship, and love.

Summary

This piece of work is concerned with the characterization, development, and optimization of the liquid-feed direct methanol fuel cell (DMFC), which is based on the concept of the polymer electrolyte fuel cell (PEFC). The central themes throughout the thesis are the terms “methanol crossover” and “mass transport”. Thus, this work deals with the implications of the operating conditions on the DMFC efficiency; the potential of radiation-grafted membranes to reduce the methanol crossover were explored and experimental methods to study *in situ* mass-transport limitations in PEFC’s were developed.

A major part of the thesis is devoted to characterize various radiation-grafted membranes based on FEP (fluorinated ethylene propylene copolymer) films under DMFC operating conditions. The implications of different membrane properties such as thickness, degree of grafting (DG), and degree of cross-linking (DC) on the DMFC performance were investigated. An emphasis was put in this connection on the methanol permeability across the membranes. It was found that the methanol crossover and the membrane’s conductivity scaled with the DG for constant thickness and constant DC. While the influence of the DC on the methanol crossover was only small, the methanol permeability across the membrane could be significantly reduced by increasing the thickness of the membrane.

The operating conditions of the cell strongly influence the polarization characteristics and the methanol crossover across standard membranes (Nafion 117) as well as across radiation-grafted membranes. Both are predominantly controlled by the cell temperature and the anodic methanol concentration. The power performance of MEA’s based on radiation-grafted membranes was as good as those made with Nafion 117 membranes. However, lower methanol crossover could be achieved with thick radiation-grafted membranes under identical operating conditions. Finally, a long-term durability test of 600 hours was carried out at high temperature with a MEA, which was based on a radiaton-grafted membrane. A fairly stable cell performance with only slight degradation over time could be demonstrated.

The methodical aspects of characterizing PEFC's are adressed in a separate chapter. Two novel *in situ* methods were developed that give further insights in the processes involved in operating PEFC's. One method allows to visualize the gas-liquid distribution within the flow field during operation of the cell, whereas the second method gives *in situ* information about the local current distribution. Finally, the combination of both methods allowed to obtain simultaneously information about the state of the flow field and the current distribution. With the aid of these methods, the effects of the operating conditions on the two-phase and current distributions of DMFC's were investigated. The occurance of gas-liquid distributions could be shown for both sides of a DMFC, *i.e.*, in the anodic and the cathodic flow channels. Furthermore, the current distribution of a DMFC was found to be highly sensitiv to the oxygen concentration.

Zusammenfassung

Die vorliegende Arbeit beinhaltet die Charakterisierung, Entwicklung und Optimierung der flüssig gespiesenen, auf der Polymerelektrolyt Brennstoffzellentechnologie basierenden Direktmethanol-Brennstoffzelle (DMBZ). Als thematischer „rote Faden“ leiten die Schlagworte „Methanoldurchtritt“ und „Massentransport“ durch die Arbeit. Im Rahmen dieser Themenblöcke wurden die Auswirkungen der Betriebsbedingungen einer DMBZ auf ihre Effizienz hin untersucht, das Potential strahlengepfropfter Membranen den Methanoldurchtritt zu vermindern ausgelotet und neuartige *in situ* Messmethoden für die Charakterisierung von Massentransporten in Polymerelektrolyt-Brennstoffzellen entwickelt.

Ein wesentlicher Teil der Arbeit behandelt die Charakterisierung strahlengepropfter, auf FEP (Tetrafluorethylen-Hexafluorpropylen-Copolymerisat) basierenden Membranen unter DMBZ-Bedingungen. Der Einfluß verschiedener Membranparameter wie Dicke, Propf- und Vernetzungsgrad wurde hinsichtlich des Leistungsverhalten einer DMBZ untersucht. Zusätzlich wurde besondere Aufmerksamkeit der Methanolpermeabilität der Membranen gewidmet. Eine generelle Zunahme des Methanoldurchtritts sowie der Protonenleitfähigkeit der Membranen wurde mit steigendem Propfgrad bei ansonsten „konstanten“ Membranparametern (Dicke und Vernetzungsgrad) festgestellt. Hingegen zeigte die Variation des Vernetzungsgrads einer Membrane nur geringe Auswirkungen auf den Methanoldurchtritt. Eine deutliche Reduktion des Methanoldurchtritts konnte allerdings durch dickere Membranen erreicht werden.

Die Strom-Spannungs Charakteristik einer DMBZ sowie auf die Methanolpermeabilität der Membrane hängen zudem stark von den Betriebsbedingungen ab. Die Betriebstemperatur und die anodische Methanolkonzentration stellen dabei die größten Einflußgrößen dar. Das Leistungsverhalten von Membran-Elektrodenheiten basierend auf strahlengepfropften Membranen waren weitestgehend identisch zu solchen, die auf Nafion 117 Membranen basierten. Mit strahlengepfropften, dicken Membranen konnte jedoch ein deutlich niedriger Methanoldurchtritt und damit geringerer Methanolverlust bei gleichen Betriebsbedingungen erreicht werden. In einem 600 Stunden umfassenden

Langzeittest einer strahlengepfropften Membrane konnte eine nur geringer Degradation unterworfene Zellenleistung demonstriert werden.

Die methodischen Aspekte der Charakterisierung von Polymerelektrolyt-Brennstoffzellen werden in einem separaten Kapitel behandelt. Zwei neuartige *in situ* Messmethoden wurden entwickelt, die es erlauben zusätzliche Einblicke in die Prozesse der Polymerelektrolyt-Brennstoffzelle zu erlangen. Mit der einen Meßmethode ist es nun möglich die Zweiphasen Verteilung (Gas – Flüssigkeit) im Flussfeld einer im Betrieb befindlichen Brennstoffzelle zu visualisieren, mit der anderen *in situ* Meßmethode kann die örtliche Stromverteilung erfasst werden. Die Kombination dieser beiden Methoden erlaubt es nun gleichzeitig eine visuelle Information über den Zustand des Flussfeldes und über die örtliche Stromverteilung zu bekommen. Mit Hilfe dieser Anordnung wurde der Einfluß der Betriebsbedingungen auf die Gas-Flüssigkeitsverteilung im Flußfeld einer DMBZ und deren Rückkopplung auf die Stromverteilung der Zelle hin untersucht. Dabei konnte unter anderem festgestellt werden, daß eine Zweiphasenströmung sowohl im anodischen, wie auch im kathodischen Strömungsverteiler auftritt. Zudem wurde eine hohe Sensitivität der Stromverteilung hinsichtlich der lokalen Sauerstoffkonzentration festgestellt.

Table of Contents

I Why Go Fuel Cell? 1

1 The Incentives for Fuel Cell Development 2

2 Introduction to Fuel Cells 6

3 The Polymer Electrolyte Fuel Cell 10

4 Structure of the Thesis 14

5 References 16

II The Fundamentals of the DMFC 17

1 Introduction 18

2 Thermodynamics 20

3 Kinetics 22

4 DMFC Efficiency 30

5 The Electrochemical Components of the DMFC 32

6 References 34

III The Challenges of the DMFC Development 36

1 Introduction 37

2 Electrochemistry 38

3 Process Engineering 43

4 Conclusions 46

5 References 47

IV Solid Polymer Electrolytes 51

1 Introduction ... 52

2 Experimental ... 54

3 Nafion 117 ... 72

4 Radiation-Grafted Membranes ... 93

5 Comparison of FEP-Membranes with Nafion 117 ... 120

6 Conclusions ... 124

7 Outlook ... 126

8 References ... 128

V Characterizing Mass Transfer Phenomena 132

1 Introduction ... 133

2 In situ Visualization ... 135

3 Current Distribution in the DMFC ... 161

4 Combination of In situ Methods ... 182

5 Conclusions on DMFC Cell Design ... 193

6 References ... 195

VI Synopsis & Future Work 198

1 Conclusions ... 199

2 Recommendations for Future Work ... 201

3 References ... 205

Curriculum Vitae

Chapter I

Why Go Fuel Cell?

1 THE INCENTIVES FOR FUEL CELL DEVELOPMENT 2

2 INTRODUCTION TO FUEL CELLS 6

3 THE POLYMER ELECTROLYTE FUEL CELL 10

4 STRUCTURE OF THE THESIS 14

5 REFERENCES 16

1 The Incentives for Fuel Cell Development

Global background

Over the last 30 years, the world population has grown by about one billion people every 12 to 14 years. By 2012 a world population of approximately seven billion is projected, *i.e.*, in less than half a century mankind will have doubled [1]. Interlinked with it is the rapid growth of the world energy consumption as illustrated in Figure 1. In 2000, the total amount of primary energy consumed by about 6 billion people was approximately 416 EJ [2]. However, Figure 1 is somehow misleading as about two thirds of the total world primary energy is consumed by only about one third of the world population [3]. If the economies of countries at the economic take-off, such as China, meet the aspiration of similar standards of living as in the industrialized nations the world energy demand will increase even faster.

Unfortunately, the production of energy is, up to the present day, strongly linked to the emissions of greenhouse gases (GHG), which is primarily carbon dioxide (CO_2). The emissions of CO_2 from fossil fuel combustion, which accounts for the majority of the anthropogenic CO_2 emissions, increased between the years 1971 to 1999 by over 50% from approximately 14.3 Gt CO_2 in 1971 [4] to about 23.2 Gt CO_2 in 1999 [5]. Therefore, the increase of the carbon dioxide concentration in the atmosphere over the past 300 years (see Figure 1) can mainly be related to anthropogenic CO_2 emissions [3].

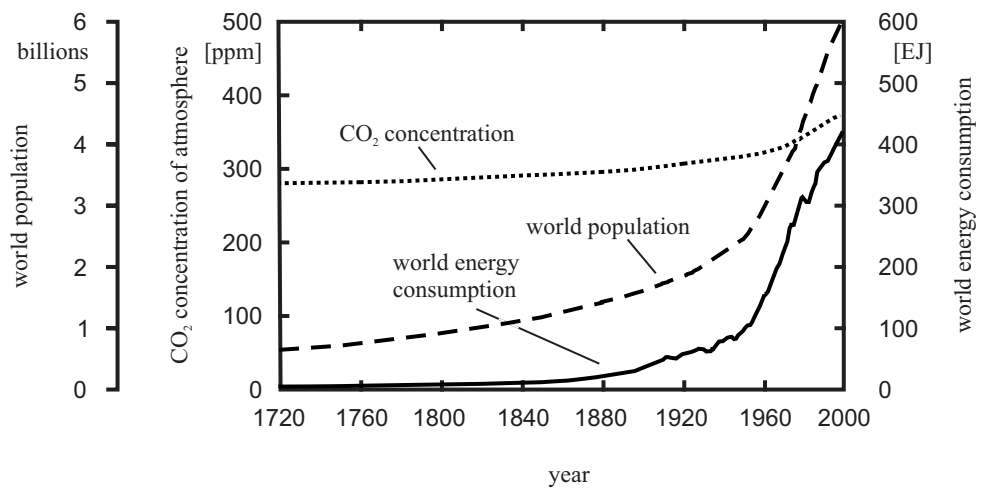

Figure 1: Global consequences of the growing world population [2].

Because of our limited resources of fossil fuels, which will be depleted in the range of a hundred or a few hundred years [3], the concerns for global warming, and, more affecting the individual person, local environmental pollution, such as ozone, have lead to turn the sustainable development into an integral aspect of energy-related issues. In 1987 the Brundtland Report [6], also known as *Our Common Future*, provided a key statement on sustainable development, defining it as "development that meets the needs of the present without compromising the ability of future generations to meet their own needs". Finally, under the Kyoto Protocol [7], the European Union (EU), besides other nations, committed to reduce its GHG emissions by 8% from 1990 levels by the years 2008 to 2012. Most of the other industrialized nations of the world made similar commitments, although the exact percentage of reduction varies from country to country.

Strategies to reduce energy & GHG emissions

In general, GHG emissions can be reduced by three different strategies, including

(i) *reducing* the energy consumption,

(ii) *rising* the efficiency of energy use, and

(iii) on the long term, *replacing* fossil fuels with renewable energy sources.

Besides the improvement of conventional technologies, *e.g.*, of heat turbines, new processes are sought which allow to convert the chemical energy of a fuel clean and highly efficiently into electricity.

For a long-term reduction of the GHG emissions, however, parts of the primary energy which are based on fossil fuels have to be replaced by renewable energy sources. However, the share in the global total primary energy supply (TPES) of the "new renewable" energy sources that include geothermal, wind, solar, etc. was only about 0.5% in 1999. In addition, the hydropower accounted for about 2.3% and the "conventional renewables", which include combustible renewables and waste, had a share of approximately 11.1% in the world TPES [5]. Therefore, the introduction of considerable amounts of "new renewables" into the energy portfolio will probably only be possible on the long-term, as illustrated in Figure 2. The predictions given by the International Energy Agency for the year 2020 [5] forecasts even a decreasing share of

renewable energy resources, which include the "conventional" plus the "new" renewables, to in total about 10% of the world TPES. This decreasing share of renewables in the world TPES is caused by the expected rapid growth of the world energy consumption.

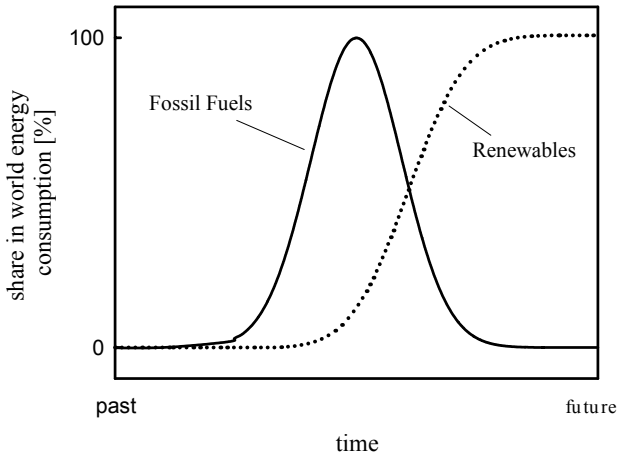

Figure 2: Replacing fossil fuels by renewables. The transfer from fossil fuels to renewable energy sources can only be on the basis of a smooth transition.

Fuel cells for transportation & stationary applications

Employing a significant amount of "new renewable" energy to the electrical grid requires storage systems to compensate for seasonal, monthly, or even daily fluctuations of the energy supply of "new renewable" energy sources, such as wind or solar energy. Moreover, energy reserves must be maintained to ensure that load can be met in case of an unexpected failure of a plant or the load changes in ways not estimated. In general, electricity can be converted into some other form in which it can be stored such as:

- Potential energy, *e.g.*, pumped hydroelectric systems.
- Kinetic energy, *e.g.*, spinning flywheels.
- Thermal Energy, *e.g.*, hot fluids.
- Chemical Energy, *e.g.*, batteries, production of hydrogen by hydrolysis.

Nevertheless, these storage systems have to be highly efficient to preserve the advantages of renewable energy sources.

The fuel cell technology may have the potential to provide highly efficient and clean energy converters for stationary [8] as well as for mobile applications [9, 10]. Therefore,

fuel cells are on the one hand a technology that has the potential to improve the efficiency of energy use. On the other hand, fuel cells provide systems that allows to supply electricity efficiently on demand because they could be operated decentralized and can follow fast load changes [11]. The latter may help to introduce a bigger share of "new renewables" in the electrical grid.

In most industrialized nations, a major source of CO_2 emissions comes from the transportation sector, which, for instance, accounted for 26% of the total CO_2 emissions in the EU-15 countries in the mid-1990s (17% in the early 1980s) [12]. Furthermore, transport is the second-fastest growing area of fuel emissions (electricity and heat is the largest-emitting sector) on a global level [4] and thus its impact on the total emissions will increase further in future.

Electric vehicles with fuel cells as electric power sources may help to abate the adverse effects of the consistently-growing demand for the service of mobility because of their inherent low emissions (at least locally) of the electrochemical conversion process and the potential for high efficiencies of fuel cell systems [13].

2 Introduction to Fuel Cells

The principle of fuel cells

Fuel cells are highly efficient, electrochemical converters that transfer the chemical energy of a fuel together with oxygen directly into electricity and heat. The appealing simplicity of the fuel cell, which excludes any further conversion steps of energy, is illustrated in Figure 3 together with the conventional electricity production, *e.g.*, of gas turbines.

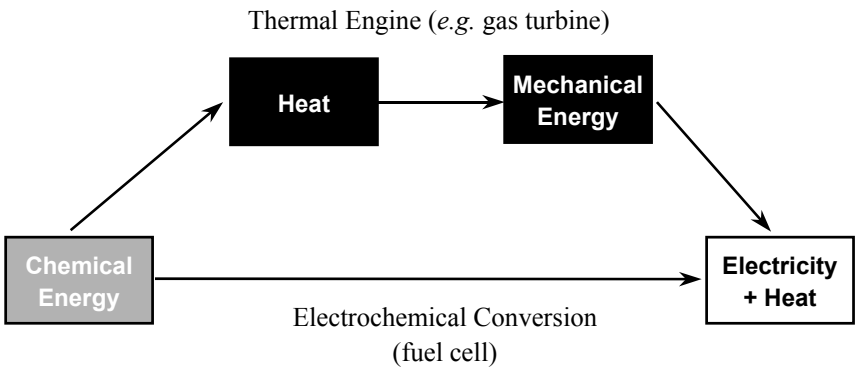

Figure 3: The principle of fuel cell technology compared to conventional energy production.

Fuel cells are similar to batteries because of the electrochemical principle. In contrast to batteries, the fuel cell does not store its fuel within the housing but can work continuously as long as fuel is supplied, much like a conventional combustion engine. Therefore, the fuel cell needs not to be recharged like a battery but the fuel tank has to be refueled from time to time, which is considerably faster than recharging a battery. One of the main advantages of fuel cells is their potential to produce high quality electricity at high electrical efficiencies and low emissions [14]. Furthermore, the efficiency of a fuel cell theoretically rises under part load conditions, which is contrary to conventional energy production [13]. In addition, fuel cells are not limited by Carnot's theorem and thus efficiencies above 70% could theoretically be achieved.

The types of fuel cells

The different types of fuel cells together with their characteristics are summarized in Table 1 and classified, most commonly, by the type of electrolyte used in the cells. In general, there are five different types of fuel cells, which include the solid oxide fuel cell (SOFC), molten carbonate fuel cell (MCFC), phosphoric acid fuel cell (PAFC), alkaline fuel cell (AFC), and polymer electrolyte fuel cell (PEFC). A brief description of each of these fuel cell types follows in the order of Table 1. Further details on the various fuel cells can be found in one of the textbooks on fuel cells, *e.g.*, in references [14-16].

Table 1: The types of fuel cells [16, 17].

Type (Electrolyte)	Operating Temperature [°C]	Fuel	Applications
Solid Oxide (SOFC)	600 - 1000	Hydrogen Carbon monoxide Reformate	Utility
Molten Carbonate (MCFC)	600 - 700	Hydrogen Reformate	Utility
Phosphoric Acid (PAFC)	120 - 250	Hydrogen Reformate	Small utility
Alkaline (AFC)	65 - 220	Hydrogen	Aerospace
Polymer Electrolyte (PEFC)	< 120	Hydrogen Reformate Methanol	Motive Small Utility Portable

SOFC: This type of fuel cell has the highest operating temperature among the various sorts of fuel cells, which ranges from 600 to 1000°C. The electrolyte consists of a solid, nonporous metal oxide, which is usually Y_2O_3-stabilized ZrO_2 and, at these operating temperatures, conducting to oxygen ions. Because of the high operating temperature, a wide range of carbonaceous fuels can be supplied to SOFC's and high-grade heat is available. Therefore, SOFC's are mainly considered for stationary applications and to be used by utilities.

MCFC: Similar to the SOFC, the MCFC operates at high temperature (600-700°C). Consequently, the electrode kinetics are fast and noble metals are not needed. The

electrolyte is usually a combination of alkali carbonates, which is immobilized in a ceramic matrix of lithium aluminate. The melting point of the electrolyte is at around 480°C and thus a highly conductive molten salt with carbonate ions as charge carriers is formed at operating temperature. High-grade heat is available, which predestines the MCFC for stationary applications and for the use by utilities, too.

PAFC: The electrolyte of the PAFC consists of concentrated phosphoric acid, which is held typically at an operating temperature of 195°C. This operating temperature allows, on the one hand, to compensate for the relatively poor ionic conduction of phosphoric acid at low temperature and, on the other hand, to tolerate impurities in the hydrogen gas.

AFC: The AFC features high specific power and energy density when used as hydrogen / oxygen fuel cell. In addition, less cost-intensive catalysts such as Ag-based catalysts could be used. However, concentrated potassium hydroxide is used as the electrolyte, which does not reject CO_2. Therefore, the choices on fuels and oxidants are limited to those that do not contain CO_2 and where CO_2 cannot be produced from. Therefore, the AFC is usually operated on H_2 / O_2, which, in principle, restricts its range of possible applications to those in the aerospace.

PEFC: The PEFC consists of a proton-conducting membrane, which requires at present sorbed water to achieve adequate conductivities. Therefore, the operating temperature is usually limited to less than 120°C. Because of the relatively low operating temperature noble metal electrocatalysts are required and the CO tolerance of the PEFC is limited to the low ppm level (< 100 ppm [18]). The direct methanol fuel cell (DMFC) directly converts methanol together with oxygen to electricity. The DMFC is usually based on the PEFC, *i.e.*, in principle the cell assembly is the same.

The short introduction into the different fuel cell types above made clear that the operating temperature has a major impact on possible applications for a specific type of fuel cell. Normally, some start-up time is needed to reach high operating temperatures. Consequently, those types of fuel cells requiring a high operating temperature are best suited to stationary applications. In contrast, fuel cells with an inherent low operating temperature, such as the PEFC, are better for rapid and frequent start-ups and

shut-downs and therefore are best suited for mobile / portable applications or for energy on-demand systems. Especially the PEFC with its high power density may meet best, among all other fuel cell types, the stringent space and weight requirements imposed on a fuel cell employed in mobile (cars) or portable (battery-replacement) applications [9, 10, 19]. In the following, a more detailed description of this type of fuel cell will be given.

3 The Polymer Electrolyte Fuel Cell

The "electrochemical heart" of the PEFC is the membrane electrode assembly (MEA) consisting of a solid polymer electrolyte (membrane), which is sandwiched between two electrodes (Figure 4). The membrane is an electronic insulator with high proton-conductivity and serves as barrier for the reactants. Usually, it is based on a fluorinated backbone with a thickness between 25 and 200 µm. At present, the proton conductivity of the perfluorosulfonated membranes is a function of its water content, and thus good hydration of the membrane must be maintained.

The electrodes are made of a porous carbon support (backing) that serves as substrate for the electrochemical active layer as illustrated in Figure 4. Furthermore, the porous backing enables the electronic connection between the flow field† and the electrochemically active layer and regulates the flow of the reactants to and the removal of the products off the electrochemically active layer.

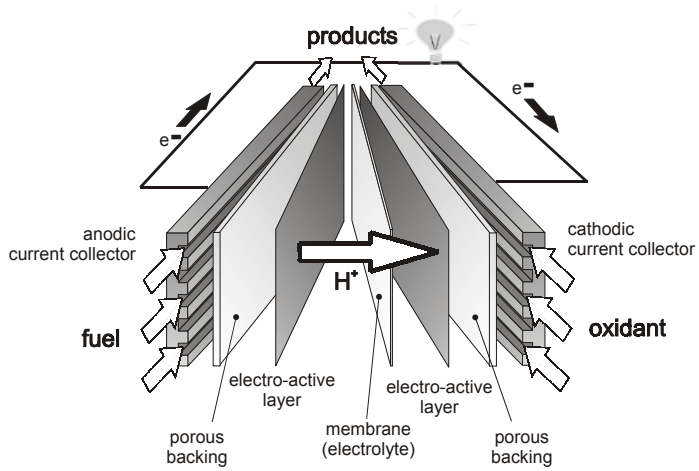

Figure 4: Schematic drawing of the PEFC. The fuel can be hydrogen, hydrogen-rich gas, or methanol, the oxidant is oxygen (in practice derived from air). The cathodic reaction product is water only; if methanol is used as fuel, carbon dioxide is produced at the anode additionally.

In operation, hydrogen ions and electrons are produced at the anode, as schematically shown in Figure 4, by the oxidation of the fuel, which is in the simplest case hydrogen.

---

† For simplicity, the flow field and the current collector are depicted as a single component in Figure 4.

$$H_2 \longrightarrow 2H^+ + 2e^- \tag{1}$$

The protons are transported through the membrane, while the electrons have to flow via the external circuitry, where they can deliver power to an external device, to the cathode. At the cathode, oxygen is reduced with the electrons and the protons to water.

$$\tfrac{1}{2}O_2 + 2H^+ + 2e^- \longrightarrow H_2O \tag{2}$$

The H_2-fuelled PEFC

Using hydrogen as fuel for portable or vehicular applications, the only emission on site will be water. In principle, hydrogen would be the ideal fuel for a fuel cell because it permits a fast and highly efficient cell reaction and, in addition, the reaction mechanisms are, compared to others, relatively well understood. However, there are three major drawbacks for hydrogen to use as fuel in the transport or portable sector

(i) the capacity to produce hydrogen is limited,

(ii) there is currently *no* hydrogen infrastructure, and

(iii) the energy density of hydrogen is low.

The latter is illustrated in Figure 5, where the volume and weight of various hydrogen storage systems are compared for the same energy equivalent with those of diesel fuel, gasoline, methanol, and ethanol [20]. The data are normalized to the base case diesel fuel, *i.e.*, the values of diesel fuel are equal to 100%.

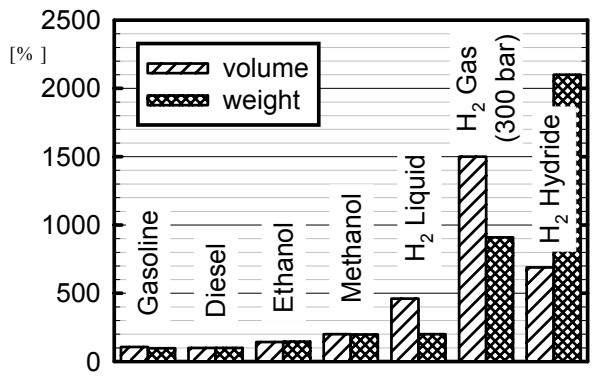

Figure 5: Volumes and weights of different fuels compared with those of hydrogen storage systems for the same equivalent energy. The data are normalized to those of diesel fuel [20].

Among the three different possibilities to store hydrogen, liquefied, gaseous, or stored in metal hydrides, liquid hydrogen may be the only "effective" method of storing hydrogen with relatively high specific energy and energy density. However, liquefaction consumes about 30% of the energy of hydrogen [13] and the storage of liquid hydrogen causes high boil-off losses. Therefore, on board storage of carbonaceous fuels is presently favorable, if large ranges or long periods of uninterrupted operation are required, *e.g.*, in cars.

The Reformate-fuelled PEFC

Because the storage of a sufficient amount of hydrogen causes space and weight problems, hydrogen could be derived from on board reformation systems using a primary carbonaceous fuel, such as, methanol. However, the additional reformer system presents problems of space, complexity, dynamics, cost, and overall system efficiency. In addition, the fuel cell has to operate on a reformate, which is primarily hydrogen but also contains carbon dioxide, nitrogen, and carbon monoxide. As mentioned in the section before, the PEFC is extremely sensitive to CO and thus the CO content needs to be lowered to 10-100 ppm to avoid serious deterioration of the cell performance [18].

The DMFC

In contrast to reformate-fuelled fuel cells, a carbonaceous fuel, methanol, is as mixture with water directly used as the anodic reactant in the DMFC akin to the H_2-fuelled PEFC. The advantages of a liquid-feed DMFC are that a humidification system, which is required for any vapor-feed PEFC, is not needed and, compared to reformate-fuelled PEFC's, a bulky and heavy reformation system can be avoided. Furthermore, the repetitive pitch per cell may be reduced considerably because the aqueous methanol solution may serve as coolant [21].

At present, however, the DMFC is still at an 'infant stage' [22] and its main disadvantages are its high price (because of its multiple noble metal loadings compared to the H_2-fuelled PEFC) and its relatively poor power density (in the range of 100 to 200 mW cm^{-2}, see *Chapter III*, pp. 37). The reasons lay in a number of challenging problems.

These mainly include

(i) enhancing the sluggish kinetics of the methanol oxidation,

(ii) reducing the methanol permeation across the membrane, and

(iii) improving the mass transport limitations at the anode and cathode.

4 Structure of the Thesis

Scope of the thesis

Although numerous studies have focused on the liquid-feed, high temperature[†] DMFC, as yet, the processes involved in operating DMFC's remain unclear. Large discrepancies are reported in terms of polarization characteristics, the optimum in operating conditions, and the degree and the effect of the methanol crossover.

Therefore, this work is devoted to a great deal to characterize the DMFC on a sound standing, consistent, experimental basis. The implications of the operating conditions on the DMFC performance and efficiency are identified on the basis of this data bank, approaches for improving the DMFC characteristics derived, two novel *in situ* methods for the characterization of mass-transfer related phenomena developed, and the potential of radiation-grafted membranes to reduce the methanol crossover are explored. In the following a short overview on the contents of the thesis is given.

Overview of thesis content

Chapter II deals with the fundamentals of the DMFC. The thermodynamics and the kinetics of DMFC's that are based on the PEFC concept are presented and the basics of the electrochemical components used in DMFC's are described.

The challenges of realizing DMFC's will be outlined in *Chapter III* and the strategies to bypass those troubles are expounded on the basis of a review of past and recent work in these areas. From these insights, approaches to improve the DMFC are derived.

Detailed experimental information about the effects of operating conditions on the polarization characteristics, the methanol crossover, and its consequences on the overall cell efficiency of "state of the art" DMFC's is provided in *Chapter IV*. Furthermore, the potential of radiation-grafted membranes to improve the DMFC polarization characteristics and to lower the methanol crossover will be discussed in detail.

[†] High temperature means close to or above 100°C.

The subsequent chapter, *Chapter V*, is devoted to methodical aspects of characterizing PEFC's. In the first part, a new type of method for the characterization of PEFC's will be introduced, which allows to visualize *in situ* the gas-liquid distribution within the flow field. This section is identical in part to a scientific article that is submitted to the journal *Fuel Cells*, Wiley-VCH, Weinheim (Germany) for publication. In the following section, a second novel *in situ* method is illustrated, which allows to measure the current distribution over the active area of a PEFC. The principle of measurement, experimental implications, proof of concept, and the impact of the operating conditions on the current distribution of a DMFC will be highlighted. This section is identical for the most part to a scientific paper that is prepared for publication. Finally, this chapter will conclude with a section that introduces the unique combination of these two *in situ* methods.

In the last chapter, *Chapter VI*, the overall conclusions of this work will be drawn and fields for further work identified.

This thesis is drafted in a way which allows the reader to extract only that part of work that is of interest, *i.e.*, each chapter is designed as quasi standalone. It has been tried to minimize redundancies to the most possible extent but repetitions were made where they improved the understanding.

5 References

[1] T.M. McDevitt, K.A. Stanecki, and P.O. Way, "World Population Profile: 1998 - With a Special Chapter Focusing on HIV/AIDS in the Developing World", Report WP/98, U.S. Bureau of Census, Washington, DC 1999.

[2] B. Geiger, Lehrstuhl für Energiewirtschaft und Anwendungstechnik, Technical University Munich, Germany, personal communication, 2002.

[3] A. Wokaun, *Erneuerbare Energien*, B.G. Teubner, Stuttgart / Leipzig, 1999.

[4] International Energy Agency, "CO_2 Emissions from Fuel Combustion - A New Basis for Comparing Emissions of a Major Greenhouse Gas", OECD / IEA, Paris, France, 1997.

[5] International Energy Agency, "World Energy Statistics from the IEA", 2001 Edition, IEA, Paris, France, 2001.

[6] "Our Common Future", The Report of the World Commission on Environment and Development, United Nations, 1987.

[7] "COP 3 report, document FCCC/CP/1997/7/Add.1", March 18, United Nations Framework Convention on Climate Change, 1998.

[8] N. Itoh, "New tricks for an old power source", IEEE Spectrum **9** (1990) 40-43.

[9] T. Ralph, and G.A. Hards, "Fuel Cells: clean energy production for the new millennium", Chem. & Ind. **9** (1998) 334-335.

[10] T.R. Ralph, and G.A. Hards, "Powering the cars and homes of tomorrow", Chem. & Ind. **9** (1998) 337-342.

[11] K. Ro, and S. Rahman, "Control of grid-connected fuel cell plants for enhancement of power system stability", Renewable Energy **28** (2003) 397-407.

[12] OECD, "Indicators for the integration of environmental concerns into transport policies part II", OECD, Paris, France, 1998.

[13] C.E. Borroni-Bird, "Fuel Cell Commercialization Issues for Light-duty Vehicle Applications", J. Pow. Sources **61** (1996) 33-48.

[14] K. Kordesch, and G. Simader, *Fuel Cells and Their Applications*, Wiley-VCH, Weinheim, 1996.

[15] EG&G Services Parsons Inc., and Science Applications International Corporation, *Fuel Cell Handbook, 5th Edition*, U.S. Department of Energy, Office of Fossil Energy, National Energy Technology Laboratory, Morgantown, USA, 2000.

[16] K. Ledjeff (Ed.), Brennstoffzellen: Entwicklung, Technologie, Anwendung, C.F. Müller, Heidelberg, 1995.

[17] T. Gilchrist, "Fuel Cells to the fore", IEEE Spectrum **11** (1998) 35-40.

[18] L. Gubler, "Operating Polymer Electrolyte Fuel Cells with Reformed Fuel", ETH Zurich, Dissertation, *Diss ETH No. 13954*, 2001.

[19] W. Dönitz, "Fuel Cells for mobile applications, status, requirements and future application potential", Int. J. Hydrogen Energy **23** (1998) 611-615.

[20] J. Fabri, W. Dabelstein, and A. Reglitzki, "Motor Fuels", in *Ullmann's Encyclopedia of Industrial Chemistry*, Ed. by B. Elvers, S. Hawkins, M. Ravenscroft, and G. Schulz, VCH, Weinheim (1989) 719-753.

[21] X. Ren, P. Zelenay, S. Thomas, J. Davey, and S. Gottesfeld, "Recent advances in direct methanol fuel cells at Los Alamos National Laboratory", J. Pow. Sources **86** (2000) 111-116.

[22] C. Lamy, J-M. Léger, and S. Srinivasan, "Direct Methanol Fuel Cells: From a Twentieth Century Electrochemist's Dream to a Twenty-first Century Emerging Technology", in *Modern Aspects of Electrochemistry*, Ed. by J.O'M. Bockris, B.E. Conway, and R.E. White, Kluwer Academic / Plenum Publishers, New York (2001) 53-118.

Chapter II

The Fundamentals of the DMFC

1 INTRODUCTION 18

2 THERMODYNAMICS 20

3 KINETICS 22

3.1 Contributions to the Electrode Overpotential 23

3.2 Methanol Oxidation Reaction 26

3.3 Oxygen Reduction Reaction 28

4 DMFC EFFICIENCY 30

5 THE ELECTROCHEMICAL COMPONENTS OF THE DMFC 32

6 REFERENCES 34

1 Introduction

In alkaline electrolytes the carbonate formation is a serious problem, particularly at the current densities regarded as commercially attractive [1]. Therefore, an acidic electrolyte is necessary which allows to reject the CO_2 produced by the electro-oxidation of methanol (Equation 1). Considerable advances in the development of direct methanol fuel cells (DMFC) were made by the introduction of a proton-conducting membrane (solid polymer electrolyte), which acts as an acidic medium and as a barrier for reactants / products between the anode and the cathode (Figure 1). Thus, the "electrochemical heart" of the DMFC consists of a proton conducting membrane, which is sandwiched between two porous electro-catalytic electrodes, each consisting of a porous backing and an active layer (Figure 1).

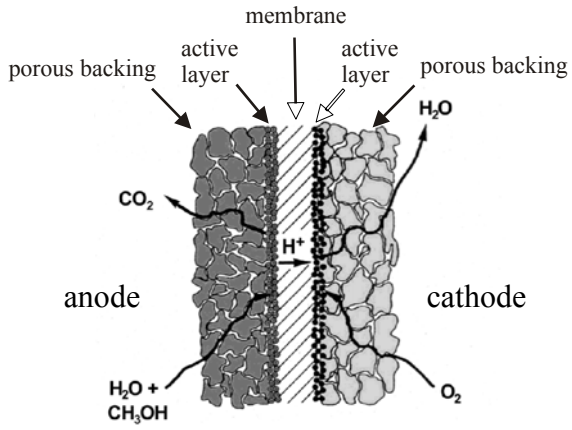

Figure 1: Expanded view of the membrane electrode assembly (MEA). The MEA consists of a solid polymer electrolyte onto either side porous electro-catalytic electrodes (each consisting of a porous backing and an active layer) are attached.

Separated by the membrane two different half-cell reactions occur at the interface electrode / electrolyte. An aqueous methanol solution is fed to the anode (left side of Figure 1), where the methanol is oxidized to carbon dioxide, six electrons and six protons.

$$CH_3OH + H_2O \longrightarrow CO_2 + 6H^+ + 6e^- \qquad (1)$$

Consequently, the anode is the negative electrode of the cell. The protons are transported through the membrane, while the electrons have to flow via the external circuitry, where they can deliver power to an external device, to the cathode. The half-cell reaction on the cathode side (Equation 2) is the electrochemical reduction of oxygen. Therefore, the cathode corresponds to the positive electrode of the cell.

$$\tfrac{3}{2}O_2 + 6H^+ + 6e^- \longrightarrow 3H_2O \tag{2}$$

The overall cell reaction is thus identical to the catalytic combustion of methanol with oxygen to water and carbon dioxide.

$$CH_3OH + \tfrac{3}{2}O_2 \longrightarrow CO_2 + 2H_2O \tag{3}$$

Because all these electrochemical conversions are isothermal, the limitation of Carnot's theorem, which is intrinsically combined with the conventional energy conversion devices (*i.e.*, heat engines), does not apply for fuel cells.

$$\eta_{Carnot} = 1 - \frac{T_o}{T} \tag{4}$$

where T refers to the absolute temperature of the isothermal expansion, whereas T_o is the lower temperature and referes to the absolute temperature of the isothermal compression.

This chapter aims to provide an overview of the DMFC fundamentals. However, it is only based on a few excellent text books [1-3], literature with a special focus on fuel cells [4, 5] and scientific reviews of the DMFC [6-8], which can be consulted for further details.

2 Thermodynamics

Under reversible conditions, the maximum electrical work available from a chemical reaction is described by the change of the Gibbs free energy ΔG. At a constant pressure and temperature, ΔG is related to the enthalpy change ΔH and to the entropy ΔS by the Gibbs-Helmholtz equation

$$\Delta G = \Delta H - T\,\Delta S \tag{5}$$

where T denotes the absolute temperature. Under these conditions, *i.e.*, reversible conditions, the change of the Gibbs free energy of the electrochemical reaction is related to the reversible cell potential, the electromotive force E

$$\Delta G = -z\,F\,E \tag{6}$$

where z is the number of electrons transferred in the reaction and F is the Faraday's constant. The change with the temperature of the electromotive force E can be derived at a constant pressure from Equations 5 and 6.

$$\left.\frac{\partial E}{\partial T}\right|_{p=const.} = \frac{\Delta S}{zF} \tag{7}$$

Furthermore, the Gibbs free energy depends on the chemical potential μ_i of species i that participate in the cell reaction and therefore, ΔG can be written as a function of the activities a_i:

$$\Delta G = \sum_i \upsilon_i \mu_i = \Delta G^o + \Re T \sum_i \upsilon_i \ln a_i \tag{8}$$

where ΔG^o represents the standard-state Gibbs free energy, $\Re$ is the ideal gas constant, and υ_i refers to the stoichiometric factor of component i, which is positive for oxidized and negative for reduced species. The electromotive force, which is the difference between the electrode potentials ε of the two half-cell reactions, can thus be related to the activities of the reactants and products by a general form of the Nernst equation.

$$E = \varepsilon_{red} - \varepsilon_{ox} = E^{\circ} + \frac{\Re T}{zF} \ln\left[\frac{\prod (a_{educt})^{\nu_{educt}}}{\prod (a_{product})^{\nu_{product}}}\right] \tag{9}$$

where the subscripts *red* and *ox* denote the respective half-cell reaction and a_{educt} and $a_{product}$ refer to the activities of the educt and the product, respectively. ν_{educt} and $\nu_{product}$ refer each to the corresponding stoichiometric factor of the educt or the product and $E°$ is the reversible cell potential at standard-state conditions.

The standard thermodynamic data for the overall DMFC reaction (Equation 3) are summarized in Table 1 together with the data corresponding to the cell reaction of the H_2-fuelled fuel cell. Because ΔS is negative, the reversible cell potential declines for both reactions with increasing temperature. Furthermore, almost identical reversible potentials ($E°$) are calculated from the thermodynamic quantities at standard-state conditions for both fuel options (Equation 6). In reality however, the open circuit voltage of the DMFC is significantly lower than 1.21 V and is more in the range of 0.75 V (cf. *Chapter IV*). This deviation from the theoretically reversible potential can be attributed to kinetic losses at both electrodes.

Table 1: Thermodynamic quantities at standard state conditions (T = 298 K, p = 1.013 bar_{abs}) for the DMFC reaction and the H_2-fuelled PEFC reaction.

quantity	$CH_3OH_{(sol)} + \frac{3}{2}O_2 \rightarrow CO_2 + 2H_2O_{(sol)}$	$H_2 + \frac{1}{2}O_2 \rightarrow H_2O_{(sol)}$	
ΔG^o	-702	-237	kJ mol^{-1}
ΔH^o	-726	-286	kJ mol^{-1}
ΔS^o	-80	-163	J mol^{-1} K^{-1}
$E°$	1.21	1.23	V

3 Kinetics

The reversible potential of each half-cell reaction can be calculated from Equation 6, which leads to an anodic reversible potential ε_{ox} of 0.016 V and for the cathode ε_{red} of 1.229 V under standard-state conditions. Methanol, in principle, should be spontaneously oxidized when the anode potential is above 0.016 V, with respect to the normal hydrogen electrode (NHE). Likewise, oxygen should be immediately reduced when the cathodic potential is below 1.229 V vs. NHE. In reality however, the reactions occurring at the electrodes are more complex and involve additional reactions (see section 3.3: *Oxygen Reduction Reaction*, p. 28), which cause the electrode potentials to deviate from their ideal thermodynamic values.

Therefore, a substantially lower open circuit voltage† (OCV) is measured in practice as shown in Figure 2. Furthermore, the cell voltage steadily decreases with an increase of the current production. The drop in the cell voltage U as a function of the current density i can be related to several processes:

$$U = U^{\circ} - \eta_{a,act} - \eta_{c,act} - \eta_{a,diff} - \eta_{c,diff} - iR_{ohm} \tag{10}$$

where U^{o} is the OCV, $\eta_{a,act}$ and $\eta_{c,act}$ refer to the activation overpotentials of the anode and cathode, respectively. $\eta_{a,diff}$ and $\eta_{c,diff}$ represent diffusion or concentration overpotentials and the last term of Equation 10 describes the voltage drop due to ohmic losses R_{ohm}, which are caused by the various ohmic resistances of the cell.

The various sources of deviation from the reversible cell voltage (see Equation 10) are reflected in the polarization characteristic of a cell, *i.e.*, in the current-voltage curve as illustrated in Figure 2.

† The cell voltage at zero current density.

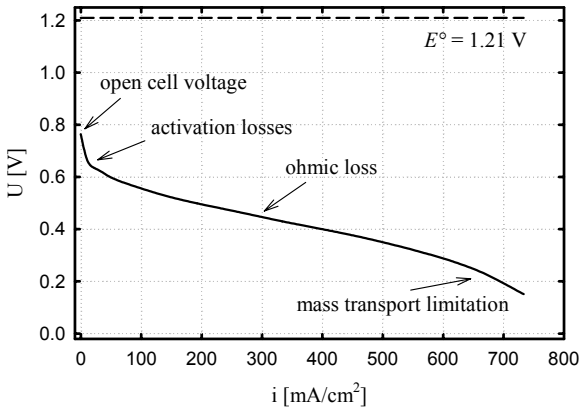

Figure 2: Characteristic current-voltage curve of a DMFC and its attributed losses by region. The reversible cell voltage at standard-state conditions (dashed line) is plotted for comparison.

Mainly, three different regions can be allocated in current-voltage curves, which essentially can be attributed to a single source of deviation as described below.

(i) Because of activation losses, a large drop of the cell voltage can be noted in Figure 2 at low current density.

(ii) The cell resistance and thus ohmic losses mainly predominate the shape of the polarization curve at medium current densities, which results in a more or less linear behavior.

(iii) Mass transport limitations of the reactants to the active sites become more evident at high current density and cause the steep decrease of the cell voltage.

3.1 Contributions to the Electrode Overpotential

A simple redox reaction of the form

$$Ox + ze^- \underset{k_f}{\overset{k_b}{\leftrightarrows}} Red \tag{11}$$

where k_b and k_f are the rate constants for the backward and the forward reaction, respectively. *Ox* and *Red* refer to the oxidized and reduced species participating in the redox reaction. The processes which are involved in such a reaction are several and include at least the following:

(i) Transport of species *Ox* to the surface.

(ii) Adsorption of *Ox* on the surface.

(iii) Charge transfer according to Equation 11.

(iv) Desorption of the species *Red* from the surface.

(v) Transport of *Red* off the surface.

The steps *(ii)* to *(iv)* are usually summarized to the activation overpotential, while the processes *(i)* and *(v)* contribute to the diffusion or concentration overpotential.

Generally, the rate constants k_b and k_f depend on the free activation energy ΔG_{act} and a quantitative relation can be derived from chemical kinetics.

$$k \propto \exp\left(-\frac{\Delta G_{act}}{\Re T}\right) \tag{12}$$

By convention, the current, which generally describes the reaction rate of an electrochemical reaction, is positive when it flows from the electrode into the solution and vice versa. The net current density of an electrode is then given by the summation of the anodic current density i_{ox} and cathodic current density i_{red}, which can themselves be related to the rate constants of the backward and forward reaction and the concentrations of the oxidized c_{ox} and reduced species c_{red}, respectively.

$$i = i_{ox} + i_{red} = zF\left(k_b c_{red} - k_f c_{ox}\right) \tag{13}$$

Furthermore, the rate constants depend on the driving force and consequently, are related to the electrode overpotential, the composition of the solution at the electrode-electrolyte interface, and the temperature. A correlation between the net current density i of a reaction and the overpotential η can be derived from Equation 12 and Equation 13 and is frequently called Butler-Volmer-Equation.[†]

$$i = i_{\circ}\left\{\exp\left(\frac{\alpha zF\eta}{\Re T}\right) - \exp\left(-\frac{(1-\alpha)zF\eta}{\Re T}\right)\right\} \tag{14}$$

[†] A complete derivation of the Butler-Volmer-Equation can be found in one of the electrochemistry textbooks, *e.g.*, in reference [9].

where α is a kinetic parameter of the charge transfer reaction that may be termed "apparent transfer coefficient" [3] and i_o is the exchange current density. The latter strongly depends on the composition at the electrode-electrolyte interface and on the temperature. If the reaction conditions are known, the overpotentials can be calculated as a function of the current density according to Equation 14. Based on the three different regions, which can be observed in a current-voltage curve (see Figure 2), the various losses are discussed in the following.

Activation overpotential

The activation overpotential is the difference between the actual electrode potential and its equilibrium potential under redox reaction conditions if any concentration gradients between the bulk and the electrode-electrolyte interface can be excluded. In Equation 14, the best measure of the degree of the kinetic limitations is given by the exchange current density. The latter is determined when the redox reaction is at its equilibrium potential, *i.e.*, η is equal to zero and the currents for the oxidation and the reduction reaction are equal in magnitude to each other and to i_o. At a fixed current density, a small activation overpotential is obtained for a large value of i_o, which frequently is referred to as a fast reaction. Therefore, i_o is an important measure for the characterization of electrocatalysts for redox reactions.

The methanol oxidation reaction on Pt-based catalysts is at least three to four orders of magnitude slower than the electro-oxidation of hydrogen[†] [6]. In addition, the exchange current density of the oxygen reduction reaction is about five orders of magnitude smaller compared to the i_o of the hydrogen oxidation reaction. Therefore, high activation overpotentials are obtained for the anode *and* the cathode of a DMFC, which explains the steep decrease in Figure 2 at low current density.

Diffusion overpotential

If the mass transport of the reactants to the electrode-electrolyte surface limits the reaction rate, then the concentrations of the reactants at the electrode-electrolyte

---

[†] The exchange current density on smooth platinum is for the hydrogen oxidation reaction about 8 10^{-4} A cm^{-2} [10].

interface approach zero. The relation between the diffusion overpotential η_{diff} and the current density i can then be expressed by

$$\eta_{diff} = \frac{\Re T}{zF} \ln\left(1 - \frac{i}{i_L}\right) \tag{15}$$

where i_L is the limiting current density, which is the current density at a reactant concentration of zero at the electrode-electrolyte interface. The limiting current density describes the transport of the reactants to the electrode-electrolyte interface.

Ohmic resistance

The limited proton conductivity of the electrolyte, the resistances inherent in the electrodes and bipolar plates plus any contact resistances sum up to an overall resistance of a cell R_{ohm}. The latter causes a voltage drop according to Ohm's law whose effect can best be seen in Figure 2 by the more or less linear decrease of the cell voltage with an increase of the current density.

In contrast to Equations 1 and 2, the actual reaction mechanisms of the half-cell reactions are much more complex and involve several intermediates. An introduction into the methanol oxidation and oxygen reduction reaction will be given in the following.

3.2 Methanol Oxidation Reaction

The electro-oxidation of methanol to carbon dioxide (Equation 1) involves the transfer of six electrons. However, it is unlikely that these six electrons are transferred simultaneously. On the contrary, the reaction mechanism of the methanol electro-oxidation on a Pt surface is believed to take place through a sequence of electron transfer steps as schematically depicted in Figure 3 [1, 6, 11].

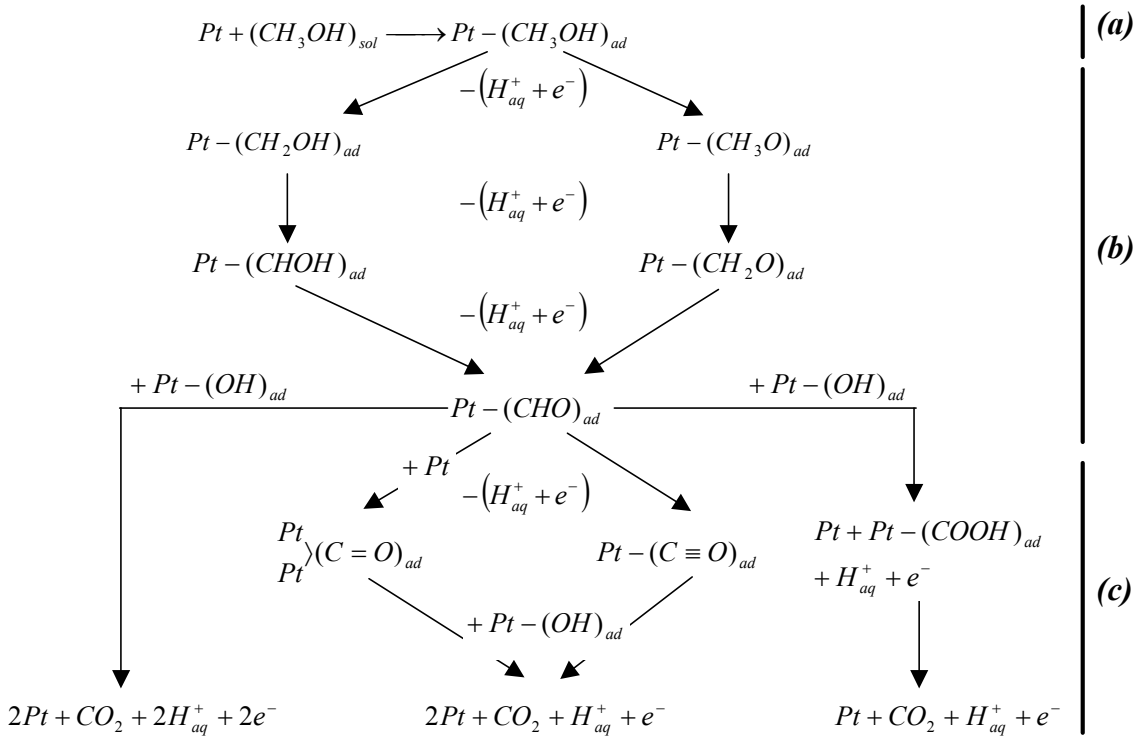

Figure 3: Possible pathways of the electro-oxidation of methanol on a Pt-surface in a sulphuric acid electrolyte [6, 8, 11, 12]: ***(a)*** methanol adsorption; ***(b)*** deprotonation; ***(c)*** CO electro-oxidation.

In principle, the electro-oxidation of methanol (Figure 3) can be summarized in three separate processes:

(a) Methanol adsorption on the Pt catalyst.

(b) Sequential proton and electron stripping, which includes several adsorbed intermediates, leading to adsorbed carbon monoxide (preferred intermediate).

(c) Oxidation of the adsorbed CO species with Pt-OH, which comes from the dissociation of water (the oxidation of the Pt-$(CHO)_{ads}$ with Pt-$(OH)_{ads}$ occurs only at small rates).

The rate limiting step in the methanol electro-oxidation is the oxidation of the adsorbed CO species that inhibit the adsorption of further intermediates on these active sites [1]. For the oxidation of the adsorbed CO species oxygenated species arising from the dissociation of water are needed. However, the dissociation of water on Pt only takes place at a significant rate for potentials greater than 0.45-0.5 V (vs. NHE) [1, 8, 13].

Secondary materials such as Ru can enhance the overall reaction rate. However, the nature of the promoting metals is, as yet, not too well understood. For Pt-Ru catalysts it is known that the water discharging with the formation of Ru-OH groups is possible at considerably lower electrode potential (0.2 V vs. NHE) [6]. Moreover, the Pt-C bond may be weaker in Pt-Ru alloys than at pure Pt at low potentials [14]. Furthermore, Ru seems to increase the activity of Pt at high potentials (above 0.45 V vs. NHE) by promoting the formation of Pt-$(OH)_{ads}$ [15].

3.3 Oxygen Reduction Reaction

In the overall reaction at the cathode, the oxygen reduction reaction (ORR) is written as a direct reduction in a four-electron step to water (in an acidic medium). Under thermodynamic equilibrium conditions (298 K, 1.013 bar_{abs}) a cathodic potential of 1.229 V should be obtained.

$$O_2 + 4H^+ + 4e^- \leftrightarrows 2H_2O \qquad E° = 1.229\ \text{V} \quad (16)$$

In practice, an electrode potential around 1 V is measured, which basically expresses the various reaction pathways possible for the ORR at metal surfaces. The various possible reactions of the ORR are summarized in Figure 4 as given in reference [16] and are based on a modified scheme as proposed by reference [17].

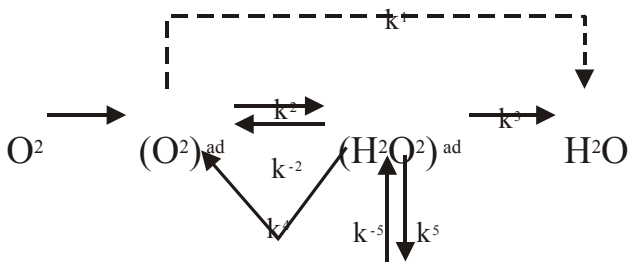

Figure 4: Reaction scheme for the ORR [16, 17].

In principle, oxygen can be electrochemically reduced either on a direct pathway to water (Equation 14) with the rate constant k_1 or H_2O_2 may be produced as intermediate with a rate constant k_2 along the sequential pathway. Subsequently, the adsorbed

hydrogen peroxide can be electrochemically reduced to water with the rate constant k_3, desorbed (k_5), or catalytically decomposed on the electrode surface (k_4) [16].

The thermodynamic equilibrium potential of the reduction of oxygen to H_2O_2 is, for instance, 0.695 V vs. NHE. Therefore, a mixed potential will be, most probably, obtained in an ORR and may explain the cathodic potential of about 1 V at OCV of a H_2 / O_2 fuel cell. However, the cathodic potential is even lower under DMFC conditions. Because of the methanol crossover through the electrolyte an additional reaction occurs at the cathode, probably the combination of the two half-cell reactions of the DMFC (see Equation 3, p. 20) [18], which further reduces the cathodic potential. The negative effects of the methanol crossover on the overall cell efficiency will be discussed in section 5 of this chapter (p. 32).

4 DMFC Efficiency

The maximum efficiency of an electrochemical energy converter is given by its thermal efficiency η_{th}, which is defined as the ratio of the maximum amount of useful energy to the total energy that was needed.

$$\eta_{th} = \frac{\Delta G}{\Delta H} \tag{17}$$

Therefore, the ratio of the Gibbs free energy change of the reaction ΔG to its enthalpy change ΔH represents the maximum efficiency that can be achieved by an ideal electrochemical converter. From Equation 17, a η_{th} of 83% (liquid product water) and 97% (gaseous product water) is calculated for the H_2 / O_2 fuel cell and the DMFC, respectively. In practice however, the efficiency of an electrochemical energy conversion is lower because of the losses discussed in the kinetic section of this chapter (section 3, pp. 22) just before. Conveniently, the fuel cell efficiency η_{fc} can be related to the voltage efficiency η_V and thus to the practically observed cell voltage. Therefore, η_{fc} can be expressed by

$$\eta_{fc} = \eta_{th}\eta_V = \eta_{th}\frac{U}{U^o} \tag{18}$$

Equation 18 may be of use for the H_2 / O_2 fuel cell to describe the overall cell efficiency. Applied for the DMFC however, the considerable methanol losses to the cathode would be ignored, which of course affects the cell efficiency. Therefore, a fuel efficiency η_{fuel} has to be added to Equation 18, which is a measure for the amount of fuel that is used to produce electrical work per the total amount of fuel needed.

$$\eta_{fuel} = \frac{\dot{n}_{electricity}}{\dot{n}_{x-over} + \dot{n}_{electricity}} = \frac{i}{i_{x-over} + i} \tag{19}$$

where $\dot{n}_{electricity}$ and $\dot{n}_{x-over}$ correspond to the amount of fuel that is used to produce electrical work and to the quantity of methanol that is lost to the cathode, respectively. Equation 19 can also be written in terms of a current density ratio because the mole flux is directly proportional to the corresponding current density. i is then the macroscopic

current density that is withdrawn from the cell and $i_{x\text{-}over}$ is the methanol leakage current density that would be produced by the total oxidation of all permeated methanol[†]. Therefore, the overall cell efficiency of a DMFC can be expressed by

$$\eta_{DMFC} = \eta_{th} \frac{U}{U^o} \frac{i}{i_{x-over} + i} \tag{20}$$

Because the thermal efficiency of the DMFC is close to one, η_{th} was not taken into account for the calculation of an overall cell efficiency throughout this work. When comparing efficiencies with the H_2 / O_2 fuel cell, the effect of the thermal efficiency on the overall cell efficiency should, however, be considered.

[†] $i_{x\text{-}over}$ is a fictive current!

5 The Electrochemical Components of the DMFC

The solid polymer electrolyte

The "electrochemical heart" of the DMFC is the MEA consisting of the membrane sandwiched between the electrodes as schematically illustrated in Figure 1 (p. 18). The membrane serves as electrolyte, which provides the proton conductivity, simultaneously functions as electrical insolator, and acts as a barrier for the reactants. Usually, the polymer electrolyte is based on a fluorinated backbone, which may be cross-linked and has side chains with sulfonic acid groups attached. The hydration of the membrane leads to a dissociation of the sulfonic acid groups, *i.e.*, into H^+ and immobilized SO_3^- covalently bonded to the polymer side chains. The proton conductivity of perfluorosulfonated membranes, such as Nafion (for further details on Nafion membranes see *Chapter IV*, section 3, pp. 72), is a function of its water content and thus a good hydration of the membrane must be guaranteed. Fortunately, the liquid-feed DMFC, which is the object of this study, ensures the full hydration of the membrane as was shown in the literature by measuring *in situ* the membrane resistances at various operating conditions and electrical loads [19-21].

The free miscibility of methanol and water results in a methanol uptake of the membrane in addition to the uptake of water [22]. However, it is highly undesirable to have methanol transport across the membrane for operating a DMFC because it would be spontaneously oxidized at the cathode and additionally cause a depolarization of the cathode. Therefore, the methanol crossover affects the overall cell efficiency in three ways:

(i) All methanol permeated to the cathode is lost fuel because it is oxidized to CO_2,

(ii) the cell voltage is lowered considerably because a mixed potential is established at the cathode, and

(iii) additional oxygen has to be supplied to the cathode because of the extra oxygen needed due to the cathodic oxidation of the permeated methanol.

Detailed information about the membrane structure and its behavior under DMFC operating conditions will be given in *Chapter IV* (pp. 49).

Electrodes

The electrodes have to fulfill two principal tasks:

(i) Providing a high electrochemically active surface area to lower the effective current density per active surface area and

(ii) enabling a high mass flow of the reactants to the active area while effectively removing the reaction products.

Usually, a gas / liquid diffusion electrode consists of several layers of different function. A porous carbon support (backing) acts as the electronic connection between the flow field and the electrochemically active area. In addition, the backing serves as gas / liquid diffusion layer, which may contain PTFE to adjust its wetting properties. Carbon papers or woven carbon cloths are commonly used as backing materials with a thickness in the order of 300 µm. A carbon / PTFE layer is spread onto its surface to fill the pores of the backing before applying the electrochemically active area. Typically, the electrochemically active area consists of highly dispersed precious alloys, which are deposited on high surface area carbon. PTFE and / or Nafion solution is used as binder as well as wetting agent. The incorporation of Nafion into the electrochemically active area is important to extent the three-phase boundary (see Figure 5), *i.e.*, to increase the interfacial area, where electronic and ionic conductivity *and* access of the reactants is simultaneously present. In this way, the three-phase boundary can be extended into the active layer, therefore, more catalyst particles are ionically connected and consequently, higher catalyst utilizations can be achieved.

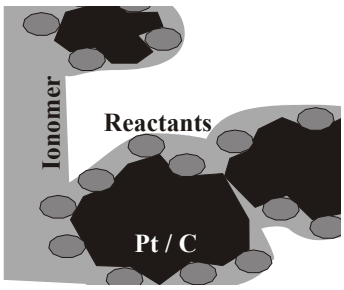

Figure 5: Schematical illustration of the three-phase boundary where the electrochemical reaction takes place.

6 References

[1] C. Lamy, J-M. Léger, and S. Srinivasan, "Direct Methanol Fuel Cells: From a Twentieth Century Electrochemist's Dream to a Twenty-first Century Emerging Technology", in *Modern Aspects of Electrochemistry*, Ed. by J.O'M. Bockris, B.E. Conway, and R.E. White, Kluwer Academic / Plenum Publishers, New York (2001) 53-118.

[2] A.J. Bard, and L.R. Faulkner, *Electrochemical Methods: Fundamentals and Applications*, 2nd edition, Wiley, New York, 2001.

[3] J.S. Newman, *Electrochemical Systems*, 2nd edition, Prentice Hall, Englewood Cliffs, 1991.

[4] K. Kordesch, and G. Simader, *Fuel Cells and Their Applications*, Wiley-VCH, Weinheim, 1996.

[5] EG&G Services Parsons Inc., and Science Applications International Corporation, *Fuel Cell Handbook, 5th Edition*, U.S. Department of Energy, Office of Fossil Energy, National Energy Technology Laboratory, Morgantown, USA, 2000.

[6] A.S. Aricò, S. Srinivasan, and V. Antonucci, "DMFCs: From Fundamental Aspects to Technology Development", Fuel Cells **1** (2001) 133-161.

[7] S. Wasmus, and A. Küver, "Methanol oxidation and direct methanol fuel cells: a selective review", J. Electroanal. Chem. **461** (1999) 14-31.

[8] M.P. Hogarth, and G.A. Hards, "Direct Methanol Fuel Cells", Platinum Metals Rev. **40** (1996) 150-159.

[9] C.H. Hamann, and W. Vielstich, *Elektrochemie*, 3rd edition, Wiley-VCH, Weinheim, 1998.

[10] J.O`M. Bockris, and A.K.N. Reddy, *Modern Electrochemistry*, Plenum Press, New York, 1970.

[11] B. Beden, C. Lamy, and J-M. Léger, "Electrocatalytic Oxidation of Oxygenated Aliphatic Organic Compounds at Noble Metal Electrodes", in *Modern Aspects of Electrochemistry*, Ed. by Bockris J.O`M., B.E. Conway, and R.E. White, Plenum Press, New York (1992) 97-264.

[12] V.S. Bagotsky, Yu.B. Vasiliev, and O.A. Khazova, "Generalized scheme of chemisorption, electrooxidation and electroreduction of simple organic compounds on platinum group metals", J. Electroanal. Chem. **81** (1977) 229-238.

[13] A. Hamnett, and G.L. Troughton, "Electrocatalysis and the Direct Methanol Fuel Cell", Chemistry & Industry **13** (1992) 480-483.

[14] T. Iwasita, F.C. Nart, and W. Vielstich, "An FTIR Study of the Catalytic Activity of a 85-15 Pt-Ru Alloy for Methanol Oxidation", Ber. Bunsenges. Phys. Chem. **94** (1990) 1030-1034.

[15] A. Hamnett, B.J. Kennedy, and S.A. Weeks, "Base metal oxides as promotors for the electrochemical oxidation of methanol", J. Electroanal. Chem. **240** (1988) 349-353.

[16] N.M. Markovic, T.J. Schmidt, V. Stamenkovic, and P.N. Ross, "Oxygen Reduction Reaction on Pt and Pt Bimetallic Surfaces: A Selective Review", Fuel Cells **1** (2001) 105-116.

[17] Halina S. Wroblowa, Yen-Chi-Pan, and Gerardo Razumney, "Electroreduction of oxygen a new mechanistic criterion", J. Electroanal. Chem. **69** (1976) 195-201.

[18] X. Ren, W. Henderson, and S. Gottesfeld, "Electro-osmotic Drag of Water in Ionomeric Membranes: New Measurements Employing a Direct Methanol Fuel Cell", J. Electrochem. Soc. **144** (1997) L267-L270.

[19] S. Gottesfeld, S.J.C. Cleghorn, X. Ren, T.E. Springer, M.S. Wilson, and T.A. Zawodzinski, "Polymer electrolyte direct methanol fuel cells: an option for transportation applications", Fuel Cell Seminar, Extended Abstract, November 17-20 (1996) 521-524.

[20] X. Ren, M.S. Wilson, and S. Gottesfeld, "High Performance Direct Methanol Polymer Electrolyte Fuel Cells", J. Electrochem. Soc. **143** (1996) L12 - L15.

[21] X. Ren, M.S. Wilson, and S. Gottesfeld, "On direct and indirect methanol fuel cells for transportation applications", in: *Proc. First International Symposium on Proton Conducting Membrane Fuel Cells I*, Ed. by S. Gottesfeld, G. Halpert, and A. Landgrebe, Chicago, IL, USA, PV 95-23 (1995) 252-260.

[22] A.B. Geiger, J. Newman, and J.M. Prausnitz, "Phase Equilibria for Water-Methanol Mixtures in Perfluorosulfonic-Acid Membranes", AIChE J. **47** (2001) 445-452.

Chapter III

The Status of the DMFC Development

1 INTRODUCTION 37

2 ELECTROCHEMISTRY 38

2.1 Methanol Oxidation 38

2.2 Methanol Crossover 39

3 PROCESS ENGINEERING 43

3.1 Mass-transport 43

3.2 Operation parameters 44

4 CONCLUSIONS 46

5 REFERENCES 47

1 Introduction

Compared to other types of fuel cells (cf. *Chapter I*), the direct methanol fuel cell (DMFC) is currently still at an "infant stage" [1] because of its high cost and relatively low power density in the range of 100 to 200 mW cm^{-2}. At present, the cost of a DMFC system is mainly determined by its high catalyst loadings, which consist primarily of noble metals, and the use of DuPont's Nafion membranes[†] [2, 3]. Furthermore, the power density of a DMFC is relatively poor because of a number of unresolved challenges in view of the catalyst design, the electrolyte development, and the process engineering.

This chapter intends to identify the challenges that are combined with the realization of DMFC's and aims to give an overview of the various research programs that have been undertaken to tackle those. Although these problems are largely interconnected, they can basically be distinguished into two separate areas:

(i) Difficulties that are directly related to the electrochemistry of the DMFC, *e.g.*, the methanol oxidation or the methanol crossover. They will be discussed in section 2 of this chapter

(ii) Problems that arise from the technical realization of the DMFC (see section 3), *e.g.*, mass-transfer limitations.

This differentiation draws the outline of this chapter. First the fundamental questions of the DMFC will be addressed. A brief overview of the activities in the development of electrocatalysts to enhance the methanol oxidation in an acidic medium will be given (section 2.1). In addition, the work, which has been done to minimize the effect of the methanol crossover (advanced solid polymer electrolytes and methanol tolerant electrocatalyst for the oxygen reduction reaction), will be summarized in section 2.2. The following section, *Process Engineering*, deals with the technological aspects of the DMFC and summarizes the most important findings in this area.

[†] For details on Nafion membranes see *Chapter IV*, section 3: Nafion 117, pp. 72.

2 Electrochemistry

2.1 Methanol Oxidation

The sluggishness of the DMFC performance is, among others, the result of the relatively poor kinetics of the methanol oxidation, which is much more complex than its half-cell reaction suggests. As outlined in the previous chapter within the *Kinetics* section *(Methanol Oxidation Reaction*, Figure 3, p. 27*)* the oxidation of methanol on a Pt surface is a multi-step process, which demands at last the oxidation of CO species, which are adsorbed on the Pt surface.

Unfortunately, Pt is not a sufficiently active catalyst for the methanol oxidation to be commercially useful. Therefore, there has been an intensive search for more active materials over the past years. Such catalysts should allow for the oxidation of methanol at low overpotential and thus must have the ability to simultaneously adsorb methanol and water at low potentials [4]. Because platinum appears to be one of the most efficient catalysts for the sequential deprotonation of methanol in an acidic medium, various alloy combinations with Pt have been studied. Intense effort were devoted to the development of binary Pt alloys containing Ru, Rh, Re, or Sn, *e.g.*, references [5, 6]. Among these binary alloys Pt-Ru and maybe Pt-Sn seem to be the most promising catalysts for the methanol oxidation [7-9].

Temperature dependence studies on Pt-Ru catalysts in 0.5 M methanol suggest that the rate limiting step at ambient temperature is either the methanol adsorption or the sequential electron and proton stripping, while at higher temperature the reactions which involves adsorbed OH species become rate limiting [10]. Therefore, ternary alloys were investigated, which were based on the Pt-Ru system. The third component should add the functionality to either weaken the bonding of the adsorbed CO-species or to improve the oxidation of the methanolic residues [11]. Various elements such as Os [12], Mo [13], Rh, Ir, W, and Sn, *e.g.*, references [14, 15], were studied in combination with Pt-Ru. As yet, enhanced activity of ternary alloys could be shown for the Pt-Ru catalyst in combination with Mo [13], Os [12], and W [15] compared to the binary Pt-Ru catalyst.

Recently, quaternary catalysts such as Pt-Ru-Os-Ir [16, 17] have also been suggested as catalysts for the methanol oxidation. It has been claimed that the performance of $Pt_{47}Ru_{29}Os_{20}Ir_4$ is significantly superior to Pt-Ru catalyst with an atomic ratio of 1:1 [17].

Though, all these catalysts screenings are encouraging, however, one should note most of these investigations were carried out with an liquid electrolyte in half-cell measurements. Thus, the superior performance of some catalyst alloys compared to Pt-Ru has still to be proven in cell tests.

2.2 Methanol Crossover

Proton-conducting membranes

At present, membranes based on fluoropolymers containing sulfonic acid groups, such as Nafion (registered trademark of *E.I. DuPont de Nemours & Co., Inc.* for perfluorocarbon sulfonate membranes) are most commonly used in DMFC's. The chemical structure of Nafion is depicted in Figure 1, where the value of m is equal to one [18] and k varies from about 5 to 12 depending on the equivalent weight (EW) of the Nafion membrane [19].

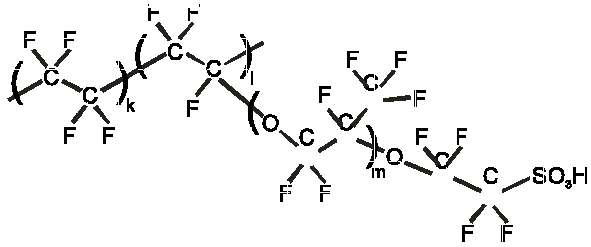

Figure 1: Schematic diagram of the structure of Nafion. The value of m may be as low as 1 [18] and the value of k ranges between 5 and 12 [19].

The morphology of the perfluorosulfonate membranes and their proton transport mechanism have been the subject of many studies. From rheological investigations of Nafion and X-ray diffraction patterns, Yeo *et al.* [20] suggested that most of the sorbed water exists in aqueous ion clusters within the membrane, which are, as first proposed by Gierke *et al.* [21] interconnected by channels. This picture of an ion-cluster-network

model, as illustrated in Figure 2, has become a well-accepted feature of Nafion, confirmed by other researchers, e.g., in reference [22].

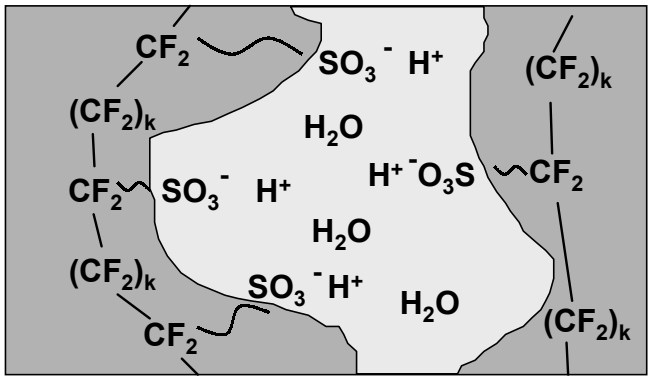

Figure 2: Cluster-network model of Nafion [21]. Channels interconnect the aqueous ion clusters.

Unfortunately, these membranes are quite permeable to methanol, which can well be understood by the cluster-network model (Figure 2), leading to methanol crossover to the oxygen/air cathode. Unfortunately, this causes lost fuel and depolarizes the cathode. In addition, more oxygen is needed to be supplied to the cathode to maintain effective reaction conditions. In consequence, the overall efficiency of a DMFC system is lowered considerably. Therefore, it is a major concern to develop solid polymer electrolytes with low methanol permeation.

Up to the present day, various strategies have been followed to minimize the methanol permeation across the membrane. Mostly, the methanol crossover has been tried to minimize by increasing the thickness of the Nafion membrane. Thus, Nafion 117, which has a nominal thickness of 7 mils and an average equivalent weight of 1100 g mol^{-1}, or even thicker membranes are commenly used in the DMFC [23, 24]. Alternatively, increasing the equivalent weight of the Nafion membrane can minimize the methanol crossover as reported by Narayanan *et al.* [23] and Ren *et al.* [25].

Furthermore, it has been tried to modify Nafion by various methods to lower the methanol crossover. Among other things, the surface modification of Nafion by plasma etching [26], the coating of Nafion with a metallic layer [26-28], the doping with Cs^+-ions [29], the *in-situ* polymerization of Nafion with poly(1-methylpyrrole) [30], and

membranes based on recast Nafion containing different additives, such as, silica [31, 32], aerosil [33], or molybdophosphoric acid [33] have been proposed. Other approaches included the synthesis of novel membranes based on acid-base polymer blends [34, 35], zeolites [36], or acid-doped polybenzimidazole [37-40]. Moreover, radiation-grafted membranes based on fluorinated, partly- and non-fluorinated polymer substrates were prepared with the objective to improve the DMFC performance [41].

So far, present research has been focused on finding more advanced barrier materials to lower the fuel crossover. It is important to realize that the permeation rates of methanol to the cathode could mostly be reduced. However, the mechanical properties, the chemical stability, or the conductivity of the membrane was also severely affected by all methods proposed [26-41] and thus, there is still a lack of optimized membranes for use in the DMFC.

Methanol-tolerant electrocatalysts for the oxygen reduction reaction (ORR)

Ideally, the cathodic half-cell reaction, *i.e.*, the ORR, of a DMFC and the one of a H_2-fuelled PEFC would be identical. In fact, the catalyst (Pt) employed at present for the ORR of a DMFC is mostly similar to the one used for the H_2-fuelled PEFC. In reality however, the cathodic half-cell reaction of a DMFC differs significantly from the ORR occurring in the H_2-fuelled PEFC because of the methanol permeation across the membrane. The latter arises from the permeability of all currently available solid polymer electrolytes towards methanol (see discussion above: *Proton-conducting membranes*).

Unfortunately, platinum catalysts are active at cathodic potentials towards of both oxygen reduction and methanol oxidation. Therefore, a mixed potential occurs at the cathode, resulting in a lower cathodic potential and thus reducing the overall cell performance. Besides the development of new proton-conducting membranes with a significantly lower methanol crossover, an alternative or maybe additional approach is the development of electroactive materials, which are selective for the ORR. That means the methanol permeation across the membrane is not hindered but electrocatalysts are used on the cathode, which “simply” do not oxidize methanol. In

this way, a mixed potential could not be established and thus neither the cell voltage would be reduced nor would fuel losses occur.

Various materials have been investigated as methanol tolerant electrocatalysts for the ORR such as heat-treated transition metal macrocycles [42-44] or molybdenum-ruthenium based chalcogenides [45-47]. So far, all these catalysts are significantly less active for the ORR than Pt catalysts. However, in the presence of methanol their overpotential of the ORR is less affected than that of a Pt catalyst. Therefore, these catalysts may be superior to Pt catalysts for the ORR in the presence of methanol. However, those investigations were carried out in half-cell measurements comprising an liquid electrolyte. If the methanol tolerant electrocatalysts can give superior performance in the DMFC has not been proven yet.

3 Process Engineering

3.1 Mass-transport

In addition to the slow kinetics of the methanol oxidation and the problem of methanol crossover, the performance of the DMFC is affected by mass-transport limitations. On the oxidation of methanol, the reaction product is carbon dioxide, which is evolved as a gas in the cell leading to a two-phase flow at the anode. On the cathode side, the two-phase flow develops from liquid water as reaction product and air as oxidant. Water droplets may accumulate within a channel of the flow field and flood it partly, thus blocking the channel from the supply with air. In addition, the supply of a liquid fuel at the anode leads to a higher swelling of the membrane of a DMFC. Therefore, excessive amounts of water are transported across the membrane to the cathode by diffusion and electro-osmosis presumably making the water removal at the cathode of a DMFC even more important than in a H_2-fuelled PEFC [48].

Little attention has been paid to the degree and the effect of two-phase flows on the performance of a DMFC up to the present. On the anode, gas bubbles within the electrode superimpose physical processes, such as micro convection, to the electrochemical processes and thus interfere with the operation of the electrode. Some progress has been made by improving the characteristics of the backing and the diffusion layer in terms of composition, structure, and thickness [49-52].

Furthermore, large amounts of carbon dioxide may accumulate in the channels of the flow field and hinders the supply of reactants to the electrode already in the flow field. However, the two-phase distribution in the flow channels cannot be easily measured with standard electrochemical methods, *e.g.*, current-voltage curves, and depends on the interaction of numerous parameters, such as flow field and electrode design, material properties, and operating conditions. Because of this rather complex system, visual information of product-rich areas in the flow field is highly desirable to obtain during operation of the DMFC. Recent investigations have been focused on this topic [53-55]. Unfortunately, the two-phase flow is difficult to study *in situ* because the cell design (see Figure 4, *Chapter I*, p. 10) prevents us from any visual access. If the cell design is

modified to allow for visual access, then, the experimental method, however, may change the temperature, pressure, or current distribution and cause unwanted feedbacks on the two-phase distribution in the flow channels as was reported by Argyropoulos *et al.* [53]. Thus, the effect of CO_2 clusters on the performance of a DMFC remains, at present, uncertain (cf. *Chapter V*, pp. 133).

In this context, the design of the flow field was explored in a few studies [52, 56, 57]. Optimized mass transport in the channels (anodic and cathodic) of a flow field is an important electrochemical engineering issue. On one side the supply of the reactants (fuel and oxidant) across the active area of the cell has to be considered to ensure a most homogeneous current density and temperature distribution. On the other side an optimal pressure drop along the flow field has to be utilized to remove reaction products, *i.e.*, water at the cathode side or CO_2 at the anode side, and at the same time has to allow minimal power losses in the auxiliary mass flow components, such as pumps or compressors. Usually, the flow field patterns, which are employed in DMFC's, consist of one or more channels in serpentine configuration and are adopted from the H_2-fuelled PEFC's. A different approach for the design of the anodic flow field is an interdigitated design [52, 56], which forces the flow through the backing layer. It could be shown that this pattern can enhance the mass transfer characteristics significantly, however, these beneficial effects are only observed at high current densities, *i.e.*, at a low cell voltage (below 0.4 V) [56].

3.2 Operation parameters

Different applications, such as portables or on the other hand vehicular applications require different power densities, which result in different operating temperatures and DMFC designs. In addition, the design of the cell is also dependent on the DMFC type; a vapor-feed DMFC requires a different system design as a liquid-feed DMFC [58, 59].

The DMFC performance strongly depends on operating parameters (see *Chapter IV*) such as:

- methanol concentration,
- cell temperature,

- pressure, and
- methanol and air stoichiometry.

At present, it is very difficult to compare the polarization characteristics of DMFC's reported in the literature mainly because of different operating conditions. However, some general remarks can be made:

In general, the highest power densities, which are in the range between 100 to 200 mW cm^{-2} have been observed in the presence of a 0.5 to 2 M anodic methanol concentration and were always obtained at temperatures close to 100°C or above [4, 60-62]. If air is used as oxidant, lower methanol concentrations are preferable to reduce the effects of the methanol crossover on the cathode polarization. At ambient conditions and with air as oxidant, the power density of a DMFC goes currently down to less than one-tenth of that at high temperature [11].

A high cathodic backpressure of 3 bar or higher is desirable to enhance the ORR in the presence of methanol. In addition, high cathodic backpressure may be necessary to prevent the membrane from drying out if the DMFC is operated at high temperature (close to or above 100°C). On the other side, the water removal at the cathode of a DMFC is a critical issue because excessive amounts of water permeate through the membrane if a liquid aqueous methanol solution is supplied to the anode. Therefore, balance must be maintained between suitable ORR rates and a sufficiently humidified membrane. Typically, backpressures up to five bars are applied on the cathodic compartment, *e.g.*, references [4, 60-62].

Generally, high airflow rates, *i.e.*, high air stoichiometries of 5 to 60, result in a better performance of a DMFC, especially, if high methanol concentrations are used on the anode. So far, most polarization characteristics[†] published in the literature are measured from the point of view to achieve highest power density. That means somewhat "unrealistic" air stoichiometries of 10 or higher were used to achieve the high power densities frequently reported [4, 60-62].

[†] Not to say all.

4 Conclusions

As outlined in the sections 1 to 3 of this chapter, there are various challenges to overcome before the cost and the power density of a DMFC will be competetive to the other fuel cell types. At present, stack costs of 30 \$ kW^{-1} or below are the technical targets for the H_2-fuelled PEFC for automotive applications [63]. About this cost target would also apply to the DMFC. Because of the very high noble metal loadings of the DMFC, which are usually at least four times higher than in the H_2-fuelled PEFC, this cost target will be even more difficult to reach for the DMFC. Furthermore, high power densities, *i.e.*, 200 to 300 mW cm^{-2}, have to be reached at high cell voltage (around 0.5V) and under realistic operating conditions, primarily at a low air stoichiometry of 2 or below.

Clearly, improving the methanol oxidation reaction, *i.e.*, the activity of the catalyst towards the methanol oxidation has to be raised and the noble metal loading has to be reduced. Furthermore, diminishing the methanol crossover to the cathode is essential to achieve. The latter has been focused on in *Chapter IV*.

With a reduction of the kinetic and ohmic limitations, the effects of mass-transport limitations on the DMFC performance are getting more important. However, there are only few diagnostic methods, such as, current-voltage curves and AC-impedance, available to study such effects. All of these methods do only give an integral understanding of the processes occuring in the cell but do not allow to assess mass-transfer phenomena locally. Therefore, there is a lack of *in situ* diagnostic methods that allow to map the processes occurring in the DMFC. This problem will be addressed in *Chapter V*.

5 References

[1] C. Lamy, J-M. Léger, and S. Srinivasan, "Direct Methanol Fuel Cells: From a Twentieth Century Electrochemist's Dream to a Twenty-first Century Emerging Technology", in *Modern Aspects of Electrochemistry*, Ed. by J.O'M. Bockris, B.E. Conway, and R.E. White, Kluwer Academic / Plenum Publishers, New York (2001) 53-118.

[2] S. Wasmus, and A. Küver, "Methanol oxidation and direct methanol fuel cells: a selective review", J. Electroanal. Chem. **461** (1999) 14-31.

[3] B.D. McNicol, D.A.J. Rand, and K.R. Williams, "Direct methanol-air fuel cells for road transportation", J. Pow. Sources **83** (1999) 15-31.

[4] A. Hamnett, "Mechanism and electrocatalysis in the direct methanol fuel cell", Catalysis Today **38** (1997) 445-457.

[5] B. Beden, F. Kadirgan, C. Lamy, and J-M. Léger, "Electrocatalytic oxidation of methanol on platinum-based binary electrodes", J. Electroanal. Chem. **127** (1981) 75-85.

[6] M. Watanabe, M. Uchida, and A. Motoo, "Preparation of highly dispersed Pt + Ru alloy clusters and the activity for the electrooxidation of methanol", J. Electroanal. Chem. **229** (1987) 395-406.

[7] R. Parsons, and T. VanderNoot, "The oxidation of small organic molecules ; A survey of recent fuel cell related research", J. Electroanal. Chem. **257** (1988) 9-45.

[8] A.S. Aricò, V. Antonucci, N. Giordano, A.K. Shukla, M.K. Ravikumar, A. Roy, S.R. Barman, and D.D. Sarma, "Methanol oxidation on carbon-supported platinum-tin electrodes in sulfuric acid", J. Pow. Sources **50** (1994) 295-309.

[9] J-M. Léger, and C. Lamy, "The Direct Oxidation of Methanol at Platinum Based Catalytic Electrodes: What is New Since Ten Years?" Ber. Bunsenges. Phys. Chem. **94** (1990) 1021-1025.

[10] H.A. Gasteiger, N. Markovic, P.N. Ross Jr., and E.J. Cairns, "Temperature-Dependent Methanol Electro-oxidation on Well-Characterized Pt-Ru Alloys", J. Electrochem. Soc. **141** (1994) 1795-1803.

[11] A.S. Aricò, S. Srinivasan, and V. Antonucci, "DMFCs: From Fundamental Aspects to Technology Development", Fuel Cells **1** (2001) 133-161.

[12] K.L. Ley, R. Liu, C. Pu, Q. Fan, N. Leyarovska, C. Segre, and E.S. Smotkin, "Methanol Oxidation on Single-Phase Pt-Ru-Os Ternary Alloys", J. Electrochem. Soc. **144** (1997) 1543-1548.

[13] A. Lima, C. Coutanceau, J-M. Léger, and C. Lamy, "Investigation of ternary catalysts for methanol oxidation", J. Appl. Electrochem. **31** (2001) 279-386.

[14] G.L. Troughton, and A. Hamnett, Bulletin of Electrochemistry **7** (1991) 488.

[15] M. Götz, and H. Wendt, "Binary and ternary anode catalyst formulations including the elements W, Sn and Mo for PEMFCs operated on methanol or reformate gas", Electrochim. Acta **43** (1998) 3637-3644.

[16] B. Gurau, R. Viswanathan, R. Liu, T.J. Lafrenz, K.L. Ley, E.S. Smotkin, E. Reddington, A. Sapienza, B.C. Chan, T.E. Mallouk, and S. Sarangapani, "Structural and Electrochemical Characterization of Binary, Ternary, and Quaternary Platinum Alloy Catalysts for Methanol Electro-oxidation", J. Phys. Chem. B **102** (1998) 9997-10003.

[17] E. Reddington, A. Sapienza, B. Gurau, R. Viswanathan, S. Sarangapani, E.S. Smotkin, and T.E. Mallouk, "Combinatorial Electrochemistry: A Highly Parallel, Optical Screening Method for Discovery of Better Electrocatalysts", Science **280** (1998) 1735-1737.

[18] R.S. Yeo, "Dual cohesive energy densities of perfluorosulphonic acid (Nafion) membrane", Polymer **21** (1980) 432-435.

[19] W. Grot, "Use of Nafion Perfluorosulfonic Acid Products as Separators in Electrolytic Cells", Chem. -Ing. -Techn. **50** (1978) 299-301.

[20] S.C. Yeo, and A. Eisenberg, "Physical properties and supermolecular structure of perfluorinated ion-containing (Nafion) polymers", J. Appl. Pol. Sci. **21** (1977) 875-898.

[21] T.D. Gierke, G.E. Munn, and F.C. Wilson, "The Morphology in Nafion Perfluorinated Membrane Products, as Determined by Wide- and Small-Angle X-Ray Studies", J. Pol. Sci. **19** (1981) 1687-1704.

[22] J. Halim, F.N. Büchi, O. Haas, M. Stamm, and G.G. Scherer, "Characterization of Perfluorosulfonic Acid Membranes by Conductivity Measurements and Small-Angle X-ray Scattering", Electrochim. Acta **39** (1994) 1303-1307.

[23] S.R. Narayanan, H. Frank, B. Jeffries-Nakamura, M. Smart, W. Chun, and G. Halpert, "Studies on Methanol Crossover in liquid-feed direct methanol PEM fuel cells", in: *Proc. Proton Conducting Membrane Fuel Cells I*, Ed. by S. Gottesfeld, G. Halpert, and A. Landgrebe, Chicaga, IL, USA, PV 95-23 (1995) 278-283.

[24] X. Ren, T.A. Zawodzinski Jr., F. Uribe, H. Dai, and S. Gottesfeld, "Methanol Cross-over in Direct Methanol Fuel Cells", in: *Proc. Proton Conducting Membrane Fuel Cells, 1*, Ed. by S. Gottesfeld, G. Halpert, and A. Landgrebe, Chicago, IL, USA, PV 95-23 (1995) 284-298.

[25] X. Ren, T.E. Springer, and S. Gottesfeld, "Water and Methanol Uptakes in Nafion Membranes and Membrane Effects on Direct Methanol Cell Performance", J. Electrochem. Soc. **147** (2000) 92-98.

[26] Won Choon Choi, Ju Dam Kim, and Seong Ihl Woo, "Modification of proton conducting membrane for reducing methanol crossover in a direct methanol fuel cell", J. Pow. Sources **96** (2001) 411-414.

[27] C. Pu, W. Huang, K.L. Ley, and E.S. Smotkin, "A Methanol Impermeable Proton Conducting Composite Electrolyte System", J. Electrochem. Soc. **142** (1995) L119-L120.

[28] S.R. Yoon, G.H. Hwang, W.I. Cho, I.-H. Oh, S.-A. Hong, and H.Y. Ha, "Modification of polymer electrolyte membranes for DMFCs using Pd films formed by sputtering", J. Pow. Sources **106** (2002) 215-223.

[29] V. Tricoli, "Proton and Methanol Transport in Poly(perfluorosulfonate) Membranes Containing Cs^+ and H^+ Cations", J. Electrochem. Soc. **145** (1998) 3798-3801.

[30] N. Jia, M.C. Lefebvre, J. Halfyard, Z. Qi, and P.G. Pickup, "Modification of Nafion Proton Exchange Membranes to Reduce Methanol Crossover in PEM Fuel Cells", Electrochemical and Solid-State Letters **3** (2000) 529-531.

[31] A.S. Aricò, P. Cretì, P.L. Anonucci, and V. Antonucci, "Comparison of Ethanol and Methanol Oxidation in a Liquid-Feed Solid Polymer Electrolyte Fuel Cell at High Temperature", Electrochemical and Solid-State Letters **1** (1998) 66-68.

[32] P.L. Antonucci, A.S. Aricò, P. Cretì, E. Ramunni, and V. Antonucci, "Investigation of a direct methanol fuel cell based on a composite Nafion(R)-silica electrolyte for high temperature operation", Solid State Ionics **125** (1999) 431-437.

[33] P. Dimitrova, K.A. Friedrich, U. Stimming, and B. Vogt, "Recast Nafion-Based Membranes for Direct Methanol Fuel Cells", in: *Proc. First European Fuel Cell Forum*, Ed. by Felix N. Buechi, Guenther G. Scherer, and Alexander Wokaun, Lucerne, Switzerland, 2 - 6 July (2001) 97-107.

[34] L. Jörissen, V. Gogel, J. Kerres, and J. Garche, "New membranes for direct methanol fuel cells", J. Pow. Sources **105** (2002) 165-171.

[35] J. Kerres, A. Ullrich, F. Meier, and T. Haring, "Synthesis and characterization of novel acid-base polymer blends for application in membrane fuel cells", Solid State Ionics **125** (1999) 243-249.

[36] Z. Poltarzewski, W. Wieczorek, J. Przyluski, and V. Antonucci, "Novel proton conducting composite electrolytes for application in methanol fuel cells", Solid State Ionics **119** (1999) 301-304.

[37] J.-T. Wang, J.S. Wainright, R.F. Savinell, and M. Litt, "A direct methanol fuel cell using acid-doped polybenzimidazole as polymer electrolyte", J. Appl. Electrochem. **26** (1996) 751-756.

[38] J.-T. Wang, S. Wasmus, and R.F. Savinell, "Real Time Mass Spectrometric Study of the Methanol Crossover in a Direct Methanol Fuel Cell", J. Electrochem. Soc. **143** (1996) 1233-1239.

[39] R. Savinell, E. Yeager, D. Tryk, U. Landau, J. Wainright, D. Weng, K. Lux, M. Litt, and C. Rogers, "A Polymer Electrolyte for Operation at Temperatures up to 200°C", J. Electrochem. Soc. **141** (1994) L46-L48.

[40] J.S. Wainright, J.-T. Wang, D. Weng, R.F. Savinell, and M. Litt, "Acid-Doped Polybenzimidazoles: A New Polymer Electrolyte", J. Electrochem. Soc. **142** (1995) L121-L123.

[41] K. Scott, W.M. Taama, and P. Argyropoulos, "Performance of the direct methanol fuel cell with radiation-grafted polymer membranes", J. Mem. Sci. **171** (2000) 119-130.

[42] S. Gupta, D. Tryk, S.K. Zecevic, W. Aldred, D. Guo, and R.F. Savinell, "Methanol-tolerant electrocatalysts for oxygen reduction in a polymer electrolyte membrane fuel cell", J. Appl. Electrochem. **28** (1998) 673-682.

[43] R. Holze, I. Vogel, and W. Vielstich, "New oxygen cathodes for fuel cells with organic fuels", J. Electroanal. Chem. **210** (1986) 277-286.

[44] D.A. Tryk, S.L. Gupta, W.A. Aldred, and E.B. Yeager, "Approaches to methanol-tolerant air cathodes for methanol-air fuel cells", in: *Proc. Electrode Materials and Processes for Energy Storage and Conversion*, Ed. by S. Srinivasan, D.D. Macdonald, and A.C. Khandkar, San Francisco, CA, USA, PV 94-23 (1994) 294-301.

[45] T.J. Schmidt, U.A. Paulus, H.A. Gasteiger, N. Alonso-Vante, and R.J. Behm, "Oxygen Reduction on $Ru_{1.92}SeO_4$, Ru/Carbon, and Pt/Carbon in Pure and Methanol-Containing Electrolytes", J. Electrochem. Soc. **147** (2000) 2620-2624.

[46] O. Solorza-Feria, K. Ellmer, M. Giersig, and N. Alonso-Vante, "Novel low-temperature synthesis of semiconducting transition metal chalgenide electrocatalyst for multielectron charge transfer: molecular oxygen reduction", Electrochim. Acta **39** (1994) 1647-1653.

[47] N. Alonso-Vante, H. Tributsch, and O. Solorza-Feria, "Kinetics studies of oxygen reduction in acid medium on novel semiconducting transition metal chalcogenides", Electrochim. Acta **40** (1995) 567-576.

[48] X. Ren, and S. Gottesfeld, "Electro-osmotic Drag of Water in Poly(perfluorsulfonic acid) Membranes", J. Electrochem. Soc. **148** (2001) A87-A93.

[49] S.C. Thomas, X. Ren, and S. Gottesfeld, "Influence of ionomer content in catalyst layers on direct methanol fuel cell performance", J. Electrochem. Soc. **146** (1999) 4354-4359.

[50] M. Neergat, and A.K. Shukla, "Effect of diffusion-layer morphology on the performance of solid-polymer-electrolyte direct methanol fuel cells", J. Pow. Sources **104** (2002) 289-294.

[51] Z. Wei, S. Wang, B. Yi, J. Liu, L. Chen, W. Zhou, W. Li, and Q. Xin, "Influence of electrode structure on the performance of a direct methanol fuel cell", J. Pow. Sources **106** (2002) 364-369.

[52] X. Ren, P. Zelenay, S. Thomas, J. Davey, and S. Gottesfeld, "Recent advances in direct methanol fuel cells at Los Alamos National Laboratory", J. Pow. Sources **86** (2000) 111-116.

[53] P. Argyropoulos, K. Scott, and W.M. Taama, "Gas evolution and power performance in direct methanol fuel cells", J. Appl. Electrochem. **29** (1999) 661-669.

[54] P. Argyropoulos, K. Scott, and W.M. Taama, "Carbon dioxide evolution patterns in direct methanol fuel cells", Electrochim. Acta **44** (1999) 3575-3584.

[55] K. Scott, P. Argyropoulos, P. Yiannopoulos, and W.M. Taama, "Electrochemical and gas evolution characteristics of direct methanol fuel cells with stainless steel mesh flow beds", J. Appl. Electrochem. **31** (2001) 823-832.

[56] A.S. Aricò, P. Cretì, V. Baglio, E. Modica, and V. Antonucci, "Influence of flow field design on the performance of a direct methanol fuel cell", J. Pow. Sources **91** (2000) 202-209.

[57] K. Scott, W.M. Taama, and P. Argyropoulos, "Material aspects of the liquid feed direct methanol fuel cell", J. Appl. Electrochem. **28** (1998) 1389-1397.

[58] M. Hogarth, P. Christensen, A. Hamnett, and A. Shukla, "The design and construction of high-performance direct methanol fuel cells. 2. Vapour-feed systems", J. Pow. Sources **69** (1997) 125-136.

[59] M. Hogarth, P. Christensen, A. Hamnett, and A. Shukla, "The design and construction of high performance direct methanol fuel cells. 1. Liquid-feed systems", J. Pow. Sources **69** (1997) 113-124.

[60] X. Ren, M.S. Wilson, and S. Gottesfeld, "High Performance Direct Methanol Polymer Electrolyte Fuel Cells", J. Electrochem. Soc. **143** (1996) L12 - L15.

[61] S.R. Narayanan, W. Chun, T.I. Valdez, B. Jeffries-Nakamura, H. Frank, S. Surampudi, G. Halpert, J. Kosek, C. Cropley, A.B. LaConti, M. Smart, Quin-Ji Wang, G. Surya Prakash, and G. Olah, "Recent Advances in High-Performance Direct Methanol Fuel Cells", in: *Proc. Fuel Cell Seminar*, Ed. by Courtesy Associates, Orlando, Florida, USA, November 17 (1996) 525-528.

[62] M. Baldauf, and W. Preidel, "Experimental results on the direct electrochemical oxidation of methanol in PEM fuel cells", J. Appl. Electrochem. **31** (2001) 781-786.

[63] H. Schmidt, P. Buchner, A. Datz, K. Dennerlein, S. Lang, and M. Waidhas, "Low-cost air-cooled PEFC stacks", J. Pow. Sources **105** (2002) 141-147.

Chapter IV

Solid Polymer Electrolytes

1 INTRODUCTION 52

2 EXPERIMENTAL 54

2.1 DMFC Testing Facility 54

2.2 Cell Hardware 58

2.3 Electrochemical Components 60

2.4 Parameters & Process Variables 62

2.5 Cell Assembly & Operation 65

3 NAFION 117 72

3.1 Introduction to Nafion 72

3.2 Cell Performance of Nafion Based MEA's 74

3.3 Discussion of the Nafion-Cell Results 87

3.4 Summary & Conclusions 92

4 RADIATION-GRAFTED MEMBRANES 93

4.1 Preparation of Radiation-Grafted Membranes 93

4.2 Characterization of FEP-Membranes in the DMFC 97

4.3 Summary 118

5 COMPARISON OF FEP-MEMBRANES WITH NAFION 117 120

6 CONCLUSIONS 124

7 OUTLOOK 126

8 REFERENCES 128

1 Introduction

Direct methanol fuel cells (DMFC) using solid polymer electrolytes could provide an attractive alternative to fuel cells operating on hydrogen derived from on board reformation systems using a primary fuel such as methanol. Besides functioning as an acidic electrolyte, the membrane separates the fuel from the oxidant gas and allows operating the DMFC with high-pressure differentials across the membrane. Today, membranes based on fluoropolymers containing sulfonic acid groups, such as Nafion (registered trademark of *E.I. DuPont de Nemours & Co., Inc.* (Wilmington, USA) for perfluorocarbon sulfonate membranes) are most commonly used in DMFC's. However, these membranes are quite permeable to methanol, leading to methanol crossover to the oxygen/air cathode, which causes losses in terms of fuel and depolarization at the cathode. In consequence, the overall efficiency of a DMFC system is lowered considerably. Furthermore, commercially available proton-conducting membranes are a significant cost factor for fuel cell stacks and thus the material cost of polymer electrolytes has to be decreased from presently about 600 US$ m^{-2} to as low as 20 US$ m^{-2} [1]. Therefore, it is a major concern to develop inexpensive polymer electrolytes with low methanol permeation.

Up to the present day, various strategies have been followed to either minimize the methanol permeation across the membrane or to reduce the cost of the polymer electrolyte. Among other things, the surface modification of Nafion by plasma etching [2], the coating of Nafion with a metallic layer [2-4], the doping with Cs^+-ions [5], the *in-situ* polymerization of Nafion with poly(1-methylpyrrole) [6], and membranes based on recast Nafion containing different additives, such as, silica [7, 8], aerosil [9], or molybdophosphoric acid [9] have been proposed. Other approaches included the synthesis of novel membranes based on acid-base polymer blends [10, 11], zeolites [12], or acid-doped polybenzimidazole [13-16]. Moreover, radiation-grafted membranes based on fluorinated, partly- and non-fluorinated polymer substrates were prepared with the objective to improve the DMFC performance [17].

Although promising results were shown for some of the strategies mentioned before, an improved cell performance could not be demonstrated yet. The reduction of the methanol permeation across the membrane was most often targeted. However, the mechanical properties, the chemical stability, or the conductivity of the membrane were also severely affected by all methods proposed [2-17] and thus there is still a lack of optimized membranes for use in the DMFC.

Based on the experience gained for the preparation of radiation-grafted membranes for the hydrogen polymer electrolyte fuel cell (PEFC) at the Paul Scherrer Institut (PSI), *e.g.*, references [18, 19], a characterization study was started to learn about the effects of various PSI-membrane properties on the DMFC performance. The results of this characterization study as well as the cell data obtained for the "state of the art" membrane, Nafion 117, mostly used in the DMFC literature, will be presented within this chapter. Furthermore, the effects of different operating conditions on the polarization characteristics, the methanol crossover, and its consequence on the overall cell efficiency will be highlighted.

This chapter will start with a detailed description of the experimental setup, the electrochemical components, and an overview of the different operating parameters. In the following, the cell performances obtained for the various types of membranes will be discussed separately: In section 3, the cell data obtained for membrane electrode assemblies (MEA's) based on Nafion 117 will be shown and compared to data available from the literature where possible. Additionally, the effect of operating parameters on the DMFC performance will be discussed. The cell data obtained for MEA's based on in-house prepared membranes will be presented in section 4 and the effect of various membrane properties on the polarization characteristics and the methanol permeation across the membrane will be discussed. In the last section, section 5, the experimental results obtained for MEA's based on Nafion 117 will be compared with the cell data obtained for MEA's based on the in-house developed membranes. Finally, we will conclude this chapter with a summary of the achievements in this area.

2 Experimental

For a thorough investigation of the DMFC behavior and characterization of various polymer electrolytes in the DMFC, new testing facilities were planned and installed. The technical layout was similar to test benches used for PEFC's operating on hydrogen and was designed for unattended operation. A detailed description of the experimental set-up will be given within this experimental section. Hereon, the cell hardware and the cell assembly will be introduced and their benefits and limits discussed. The experimental section will conclude with an overview of the various process variables and cell parameters which may affect the DMFC performance. The parameters chosen to vary will be discussed in short.

2.1 DMFC Testing Facility

For the investigation of the DMFC behavior under variable load and operating conditions, new testing facilities were installed. The test stands were dimensioned for small-scale single cells of 30 cm^2 active area and enable well-defined operation of liquid-feed DMFC's up to a temperature of 120°C at a pressure of 3 bars absolute. Furthermore, the test stands allow controlling and monitoring of all relevant process parameters, such as temperatures, pressures, reactant flows, the oxidant humidification, or the electrical load of the cell. In addition, the CO_2 content of the effluent gas stream at the cathode is monitored as a measure for the methanol permeation across the membrane for a precise membrane characterization in the DMFC. The design of the testing facilities installed for this purpose is given in Figure 1 as a schematic diagram.

Cathode gas processing

The layout of the cathodic measurement and control technology is similar to the design of hydrogen test stands as shown in Figure 1. The flow rate of the oxidant, air or oxygen, is regulated by mass flow controllers of the 5850s series from *Brooks Instrument B.V.* (Veenendaal, The Netherlands), which were dimensioned for an oxidant flow equivalent to a stoichiometry of 2 at a current density of 1 A cm^{-2}. The mass flow controllers are directly connected to the in-house gas supply. Pressure regulators positioned in upstream to the mass flow controllers compensate for any pressure

fluctuations on the in-house gas lines. Downstream to the mass flow controllers, the oxidant is humidified by bubbling through a heated water vessel (*Trabold & Co AG*, Bern, Switzerland). The oxidant is then fed through a heated gas pipe to the fuel cell to prevent condensation.

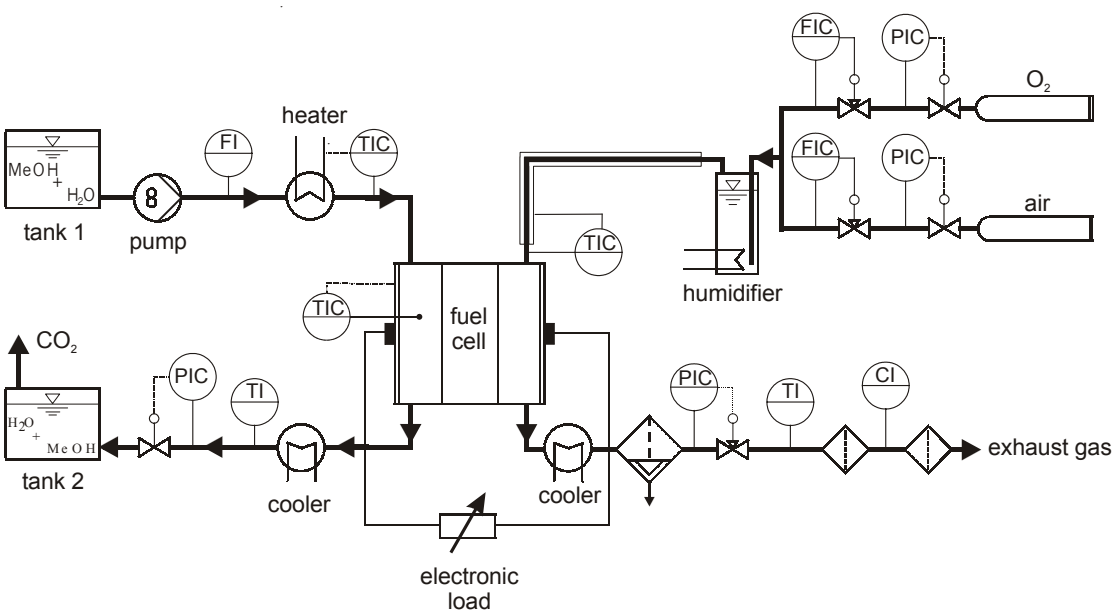

Figure 1: Schematic diagram of the DMFC test stand. The measurement and control technology is indicated in the following manner: First letter: F flow, T temperature, P pressure, C concentration. Second letter: I indicator. Third letter: C controller.

Downstream to the fuel cell, the gas is cooled to room temperature by an air cooler and subsequently, the condensate is collected in a liquid separator (F.33 8MY, *Bachofen AG*, Uster, Switzerland). Hereon, the gas is expanded to ambient pressure by a pressure controller in upstream configuration of the 5860s series from *Brooks Instrument B.V.*. The CO_2 concentration of the cathode gas stream is monitored by an IR sensor obtained from *Vaisala Oy* (GMM 12B, Helsinki, Finland), whose in- and outlet are protected by particle filters (7 micron, *Swagelok Co.*, Solon OH, USA) to prevent the incorporation of particles into the sensor head. Additionally, the inlet temperature of the gas into the IR sensor is monitored to compensate for temperature effects on the concentration signal. At last, the gas is fed to the in-house exhaust gas line. On the cathode side, all tubing and fittings (*Swagelok Co.*) were made of stainless steel 316.

Anodic loop

In contrast, all tubing and fittings were made of PFA (*Swagelok Co.*) to prevent any corrosion in the anodic loop, which may occur because of the use of deionized water and methanol. Consequently, all other materials in contact with the anodic feed were made of titanium, PTFE, PP, graphite, or other non-corroding materials. The only exception was the pump head (ZP-181, *Micropump USA*, Vancouver WA, USA) of the gear pump, which was made of stainless steel 316. As shown in Figure 1, the aqueous methanol solution is conveyed by a gear pump (propulsion: ISM 405, *Ismatec SA*, Glattbrugg-Zürich, Switzerland) from tank 1 to the DMFC anode. The gear pump has a nominal flow range of 0-250 ml min^{-1} at equivalent pressures at in- and outlet. The maximum pressure at the outlet of the pump head is 6 bars. Since the DMFC is operated at variable pressures and thus the flow rate varies at a constant pump speed, the exact flow rate has to be either calibrated by a speed-pressure-flow rate diagram or the pump speed has to be controlled by measuring the flow rate. In the realization of the test stands a combination of both methods was used. At a flow rate lower than 15 ml min^{-1}, the flow rate was regulated by the speed of the pump, which was calculated from the speed-pressure-flow rate diagram. At an operating point requiring a flow rate exceeding 15 ml min^{-1}, the flow rate was measured by a pelton wheel flow meter from *Kobold-Messring GmbH* (DPL, Hofheim-Ts., Germany) and the pump speed was computer-controlled via a PID software tool. A flow heater (*Heat Systems*, Marienheide, Germany) was used to preheat the methanol-water mixture prior feeding it to the fuel cell.

A recirculation of the aqueous methanol solution combined with a dosing of the consumed methanol was omitted for the sake of a reproducible methanol concentration. In addition, the accumulation of any by-products, which may or may not occur in such an anodic loop, was avoided in that way. Therefore, the feed is cooled by an air cooler to ambient temperature downstream to the DMFC. For safety, the feed temperature after the cooler is monitored to avoid damaging the following backpressure controller. The pressure over the DMFC anode is controlled by a backpressure controller of the type FDV.-31 KP Z from *KNF-Neuberger AG* (Balterswil, Switzerland). At last, the water-methanol-carbon dioxide mixture is fed to a wastewater tank (tank 2 in Figure 1). The

wastewater tank also serves as gas-liquid separator and thus is connected to the in-house exhaust gas line.

Measurement & Control

A 150 W programmable electronic load from *Hewlett-Packard* (mainframe HP 6050A; load module HP 60501B, Palo Alto CA, USA) allows operating the cell in constant current / voltage / resistance mode. Because only limited current can be drawn by the electronic load when operated at voltages below 3 V, a DC power supply (RAX 5-35K, *Kepco Inc.*, Flushing NY, USA) with a constant voltage output of about 3 V is connected in series to the fuel cell and the electronic load to raise the voltage level. The voltage of the cell is measured separately with shielded sensing cables, which are connected to a 20-channel armature multiplexer plug-in module (HP 34901A) installed in a mainframe (HP 34979A), both from *Hewlett-Packard*. Furthermore, the plug-in module was also connected to a number of thermocouples for the monitoring of system temperatures. All heaters were controlled by temperature controllers of the model Jumo dTron 16.1 from *M.K. Juchheim* (Fulda, Germany). All thermocouples were of the K type (NiCr – Ni).

The control software was based on LabView from *National Instruments* and allowed to fully control the test benches. All devices were connected to the control computer by a GPIB, RS-232, or a RS-485 interface. Via the latter, the temperature controllers were linked to an interface card (AT-485/2, *National Instruments*, Austin TX, USA) of the control computer. A master-slave protocol (Modbus) was used for the communication to the temperature controllers. The flow rate and the pressure of the oxidant are controlled by a programmable controller (WMR 12, *Westphal Mess- und Regeltechnik*, Ottobrunn, Germany), which is connected to the GPIB interface card (PCI-GPIB, *National Instruments*) of the control computer. On the same bus, the multiplexer and the electronic load are also linked to the control computer. Finally, the pumps are controlled via the RS-232 interface and are connected in series, which allowed a quasi-bus topology of the pumps.

A number of safety features are included into the design of the test stands to enable unattended operation of the DMFC test benches. Among other things, the automatic

shutdown of a test bench in case of major leakages or an overflow of its wastewater tank, a polarization protection of the fuel cell, an inherently safe flow heater, a dry run protection of the pump at flow rates exceeding 15 ml min^{-1}, etc. were implemented into the technical layout of the testing facilities.

2.2 Cell Hardware

The DMFC tests were performed in single cells of the conventional filter press type with an active area of 30 cm^2. The MEA was sandwiched between two flow-field plates, which were clamped together by outer stainless steel plates of grade 316 L as illustrated in Figure 2. The latter were 15 mm thick and pressed together by 12 screws with the flow-field plates and the MEA in between. The flow-field plates were made of graphite (Diabon NS 2, *SGL Carbon Group*, Meitingen, Germany), which featured high temperature resistance and low electrical resistivity.

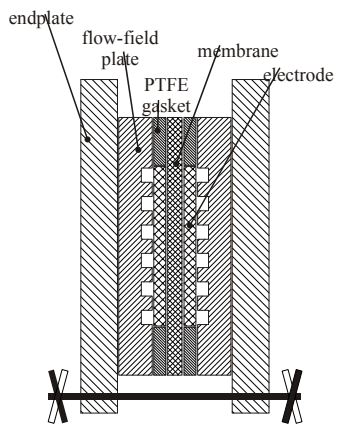

Figure 2: Schematical drawing of the fuel cell arrangement.

A single flow channel was machined in serpentine configuration into the graphite plates for the supply of the reactants and the removal of the products. Its structure and the dimensions of the flow channel are depicted in Figure 3. The cross-section of the flow channel was one by one millimeter with a one-millimeter gap between two adjacent channels. Moreover, the flow-field plates were quite thick (each 15 mm) to compensate for the deflection of the endplates and thus, to accomplish a homogenous pressure distribution over the active area. PTFE gaskets of about 0.25 mm thickness were used for sealing the cell.

The choice of a single channel configuration for the anode and, as the mirror image of Figure 3, also on the cathode was based on the following considerations. On the oxidation of methanol, carbon dioxide is evolved as a gas in the cell. The carbon dioxide may accumulate in the flow field and block the active sites from the supply of reactants. Therefore, a single channel flow field was chosen to enable a forced liquid flow through all parts of the flow field and thus, avoiding the accumulation of any gas clusters. Very little has been published on the effect of the flow field on the DMFC performance. Only recently, some research groups have picked up on this subject [20-22] and as a first summary, they all favored a forced flow configuration on the anode. Different thoughts lead to the choice of this flow field structure for the cathode. In the DMFC, excessive amounts of water permeate through the membrane to the cathode and thus the cathode electrode and flow channels are highly flooded (as shown later in this chapter, pp. 82). In a multi-channel flow field, water may accumulate in one of the channels and block this channel for the supply of oxidant. Consequently, part of the active area would suffer from oxygen depletion resulting in a lower cell performance. For these reasons, the single channel configuration was chosen as flow field for the anode and the cathode.

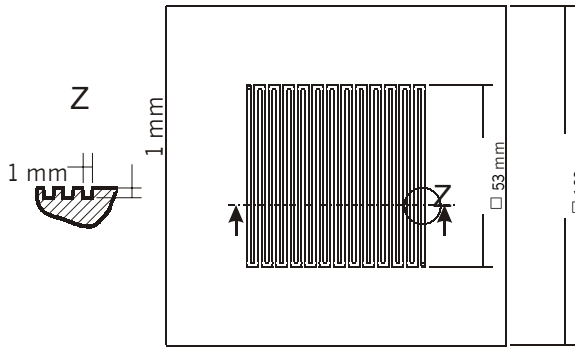

Figure 3: Schematic of the flow field used for the characterization of the DMFC on the anode as well as on the cathode. The flow field comprises a single channel in serpentine configuration. The channel was one millimeter wide and one millimeter deep. The distance between two flow channels was one millimeter (see detail Z on the right side).

A typical pressure distribution obtained for one of the experimental cells with a pressure measuring film (Super Low, *Fuji Photo Film Co.*, Tokyo, Japan) is shown in Figure 4. The pressure distribution was measured at room temperature in a cell including the MEA and all gaskets. All screws were tightened with a torque of 4 Nm. In general, the

intensity of the gray coloration of the image in Figure 4 indicates the degree of contact pressure in a certain area. The dark areas in Figure 4 equal regions of high contact pressure while light areas show zones of relatively low pressure. Not surprisingly, the highest pressure is obtained in the sealing area where the gaskets and the membrane overlap as shown in Figure 4. Moreover, the serpentine structure of the flow field can nicely be seen. Obviously, the pressure onto the electrode is small along the flow channels. However, the gray coloration along the webs is moderately uniform and indicates a reasonably homogeneous pressure distribution over the entire active area as depicted in Figure 4. From the gray intensity of Figure 4, a contact pressure exceeding 2.5 MPa is found in the sealing area, while a lower pressure of about 2 MPa is applied to the active area.

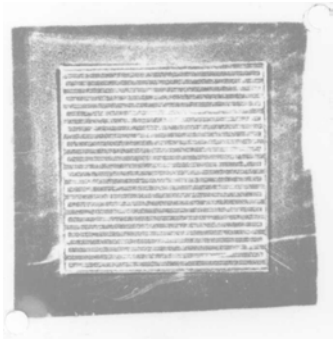

Figure 4: The pressure distribution in the experimental cell (active area 30 cm^{-2}). Dark colors indicate high pressure, bright areas low pressure.

2.3 Electrochemical Components

Membrane

The "electrochemical heart" of the DMFC is the MEA consisting of the membrane sandwiched between the electrodes. The membrane serves as electrolyte, which provides the proton conductivity, simultaneously functions as electrical isolator, and acts as a barrier for the reactants. Usually, the polymer electrolyte is based on a fluorinated backbone, which may be cross-linked and has side chains with sulfonic acid groups attached. The hydration of the membrane leads to a dissociation of the sulfonic acid groups, *i.e.*, into H^+ and immobilized SO_3^- covalently bonded to the polymer side chains. The proton conductivity of perfluorosulfonated membranes, such as Nafion, is a function of its water content and thus a good hydration of the membrane must be

guaranteed. Fortunately, the liquid-feed DMFC, which is the object of this study, ensures the full hydration of the membrane as was shown in the literature by measuring *in situ* the membrane resistances at various operating conditions and electrical loads [23-25].

The free miscibility of methanol and water results in a methanol uptake of the membrane in addition to the uptake of water [26]. However, it is highly undesirable to have methanol transport across the membrane for operating a DMFC because it would be spontaneously oxidized at the cathode and additionally cause a depolarization of the cathode. Therefore, the methanol crossover affects the overall cell efficiency in three ways: *(i)* All methanol permeated to the cathode is lost fuel, *(ii)* the cell voltage is lowered considerably because of the formation of a mixed potential at the cathode, and *(iii)* more oxygen has to be supplied to the cathode because of the additional oxygen needed at the cathode due to the oxidation of permeated methanol.

In this study, various polymer electrolytes were characterized in the DMFC. As a commercially available standard, which is mostly used in the DMFC literature, MEA's based on Nafion 117 were investigated. In addition, MEA's based on in-house developed membranes of different thickness, degree of cross-linking, and degree of grafting were studied under realistic DMFC operating conditions. A more detailed view of the structure of these membranes will be given each in its own chapter, *i.e.*, for Nafion 117 in section 3.1 and for the PSI-membranes in section 4.1.

Electrodes

The electrodes have to fulfill two principal tasks: *(i)* to provide a high electrochemically active surface area and *(ii)* to enable a high mass flow of the reactants to the active area while effectively removing the reaction products. Usually, a gas / liquid diffusion electrode consists of several layers of different function. A porous carbon support (backing) acts as the electronic connection between the flow field and the electrochemically active area. In addition, the backing serves as gas / liquid diffusion layer, which may contain PTFE to adjust its wetting properties. Carbon papers or woven carbon cloths are commonly used as backing materials. A carbon / PTFE layer is spread onto its surface to fill the pores of the backing before applying the electrochemically

active area. Typically, this layer consists of highly dispersed precious alloys, which are deposited on high surface area carbon. PTFE and / or Nafion solution is used as binder as well as wetting agent. The incorporation of Nafion into the electrochemically active area is important to extent the three-phase boundary and thus, to achieve high catalyst utilizations.

Throughout these measurements, commercially available electrodes with an active area of 30 cm^2 were used in the cell tests. Pt-Ru electrodes were used on the anode with platinum and ruthenium loading of about 1 and 0.5 mg cm^{-2} (atomic ratio 1:1), respectively. On the cathode, platinum electrodes were used with a metal loading of about 4 mg cm^{-2}. The electrodes were employed in the MEA's "as received".

2.4 Parameters & Process Variables

Process variables

The characterization of the DMFC is a very open field, which leaves at present all degrees of freedom to the experimenter. Different applications, such as portables or on the other hand vehicular applications require different power densities, which result in different operating temperatures and DMFC designs. In addition, the testing facilities and the design of the cell are also dependent on the DMFC type. A vapor-feed DMFC requires a different fuel processing as a liquid-feed DMFC as well as a different cell design [27, 28]. Therefore, this characterization study is restricted to only one part, nevertheless, highly interesting area of the DMFC: the high-power, liquid-feed DMFC.

Even with the focus on the high-power, liquid-feed DMFC the process variables, which may affect the DMFC performance, are numerous as summarized below:

- Cell temperature T_{Cell},
- methanol concentration c_{MeOH},
- oxidant (air or oxygen),
- pressure p,
- degree of humidity (temperature of dew point, T_{Dew}) of the oxidant,
- anode and cathode inlet temperature (T_{MeOH} and T_{Ox}), and
- methanol and air stoichiometry (λ_{MeOH} and λ_{air}).

Table 1 summarizes all these parameters and in its diagonal, the number for meaningful variations of the specific parameter is given, *e.g.*, four different cell temperatures or three different methanol concentrations. The numbers in Table 1 show clearly that numerous experiments (1152) have to be done to fully characterize a single MEA-type not accounting for any experiments to be performed for the sake of reproducibility. For the characterization of various polymer electrolytes in the DMFC, this would mean a lifework. Therefore, only specific process variables were selected and their effect on the performance of the DMFC was studied. The selection made is indicated by the signs in Table 1, where "+" means that all variations of this parameter combination were investigated, "o" states that the interplay of these two parameters was only investigated for a single temperature, pressure, or concentration, and "-" indicates that this parameter combination was not studied. Furthermore, Table 1 shows only the parameter combinations, which were studied on Nafion based MEA's. For the characterization of membranes with different properties Table 1 includes still too many parameters. Therefore, the two process variables with the largest effect on the DMFC performance were determined from the study of Nafion based MEA's. Only these two were varied in the characterization study of radiation-grafted membranes.

Table 1: Overview of the various process variables, which may affect the DMFC performance. The numbers refer to the quantity of meaningful variations for the respective variable. Other signs used: "+" all combinations of these two variables were investigated; "o" the interplay of these two parameters was only investigated for one temperature / pressure / concentration; "-" not studied.

	T_{Cell}	c_{MeOH}	Oxidant	p	T_{Dew}	T_{MeOH}	T_{Ox}	λ_{MeOH}	λ_{Ox}
T_{Cell}	4	+	-	+	o	o	o	o	o
c_{MeOH}	+	3	-	+	o	o	o	o	o
Oxidant	-	-	2	-	-	-	-	-	-
p	+	+	-	2	o	o	o	o	o
T_{Dew}	o	o	-	o	3	o	o	o	+
T_{MeOH}	o	o	-	o	o	1	o	o	o
T_{Ox}	o	o	-	o	o	o	1	o	o
λ_{MeOH}	o	o	-	o	o	o	o	2	+
λ_{Ox}	o	o	-	o	+	+	o	+	4

Additional parameters

Generally, the DMFC can be operated in two different flow configurations, such as co- or counter flow as illustrated in Figure 5. In co-flow, the methanol concentration and thus the methanol permeation across the membrane, decreases with the oxygen concentration along the flow channels (the structure of the flow field is given in Figure 3). At the highest methanol concentration, the highest oxygen concentration is at the cathode and thus the methanol crossover may be compensated best. However, if the methanol crossover is high and the air stoichiometry low, total oxygen depletion on the cathode may occur close to the outlet, which may result in a very inhomogeneous current distribution.

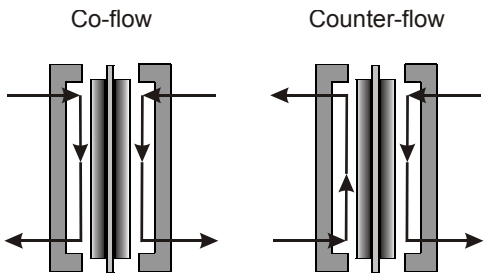

Figure 5: The principal flow concepts in fuel cells.

In contrast to co-flow, the counter flow mode could result in a more homogeneous current distribution over the active area at low air stoichiometry. At the oxidant inlet, the methanol concentration and thus the methanol crossover may be the lowest and consequently, less oxygen is consumed. That is why, the distribution of oxygen and thus the current distribution over the active area may be more homogeneous in counter flow mode at a low air stoichiometry. A discussion of its effect on the current distribution over the electrode area will follow in *Chapter V* (pp. 161).

Since the objective of this study is to characterize DMFC's under realistic operating conditions, *i.e.*, at a low air stoichiometry, the counter flow operation was chosen for all DMFC tests. Moreover, the inlet of the aqueous methanol solution was in all cell tests at the bottom of the flow field and thence the outlet was at the top.[†]

[†] This measure was taken to avoid clogging of CO_2 in the last channel of the flow field. In addition, liquid water may be easier removed from the cathodic flow field with the help of gravity.

Especially for portable applications, the position of the cell, *e.g.*, upright or horizontal, is as an additional parameter, which has to be considered. The cell position may affect the cell performance because *(i)* the CO_2 removal from the cell may be more or less effective or *(ii)* the cathode flooding is affected, which limits or enhances the oxygen transport to the active sites. For no other reason as for consistency with earlier investigations and comparable results to literature data, the upright position was chosen for this characterization study.

2.5 Cell Assembly & Operation

MEA Hot-pressing & Cell Assembly

Different to Nafion membranes, the PSI-membrane was coated with a small amount of Nafion solution (EW 1100, *Solution Technology*, USA) prior assembling the MEA by hot pressing the electrodes onto the membrane. The impregnation procedure was the following. The membranes were dried under vacuum for about an hour at 120°C prior to immersing the membrane in a 0.5% Nafion solution for another hour. Afterwards, the membrane was allowed to dry at ambient temperature and subsequently, transferred to an oven at 120°C. For at least two hours, the Nafion layer was allowed to cure at this temperature before the membranes were hot pressed.

In contrast to the Nafion membranes, the PSI membranes were hot pressed in their dry state while Nafion 117 membranes were hot pressed in their fully swollen state. A frame made of reinforced PTFE (*Maag Technic*, Dübendorf ZH, Switzerland) was used for precisely positioning the electrodes and to avoid a compaction of the backing structure during the hot pressing of the MEA. A schematic drawing of the positioning device is shown in Figure 6. It consists of two plastic foils of about 0.25 mm thickness, which are glued together at the edge of one side. Two diagonally opposite corners position an electrode, while the second electrode is put into the correct position by the other two corners. In this way, the force is lead over the plastic frame after a fully compaction of the MEA, while the membrane is not jammed between the plastic foils. Therefore, MEA's could be produced with precisely lined up electrodes while the membrane was less subjected to mechanical stresses during the hot pressing procedure.

Slightly different temperatures were chosen in the hot pressing procedure for the Nafion and the in-house developed membranes. For the latter, a temperature of about 115°C was sufficient to reach adhesion of the electrodes on the membrane, while for Nafion based MEA's higher temperatures (120-125°C) were needed. However, the heat was applied for an equal period of time (3 minutes) for all MEA's, just as the pressure, which was always within the range of 35 to 40 bars. The latter was determined by a pressure measuring film with a range from 1 to 5 MPa (Medium, *Fuji Photo Film Co.*).

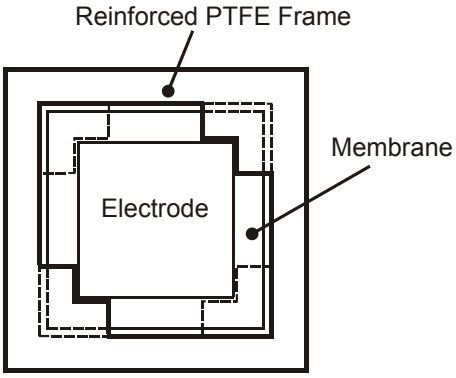

Figure 6: Centering device for hot pressing MEA's. The frame was made of reinforced PTFE to avoid compaction of the electrodes during the hot pressing procedure. The geometry of the centering device minimizes the mechanical stress applied on the membrane during the hot pressing.

After hot pressing, the MEA was allowed to cool to ambient temperature and assembled in the cell hardware. All screws were tightened with a torque of about 4 Nm resulting in a contact pressure of about 2 MPa in the active area as measured by a pressure measuring film. As depicted in Figure 4, higher contact pressure is obtained in the sealing zone, which on the one hand ensures a gas-tight cell but on the other hand makes high demands on the mechanical stability of the membrane. Because of the enormous swelling of the membrane when in contact with liquids, the membrane is highly subjected to mechanical stress at the interface gasket / active area. Moreover, the experimental cells use PTFE gaskets, which further increase the demands on the membrane. Because of the inflexibility of this material it will not compensate for any swelling or drying of the membrane during operation.

Start-up procedure

After assembling the MEA in the cell hardware, the cell was installed in the testing facility. At open circuit voltage (OCV), the supply of the reactants was started at room temperature and ambient pressure. A mixture of methanol (pro analysis GC grade, *Merck*, Dietikon ZH, Switzerland) and deionized water of a methanol concentration of 0.5 M and air were used as the reactants for the anode and the cathode, respectively. The flow rate of the aqueous methanol solution was constant at 12 ml min^{-1} as well as the airflow rate, which was held constant at 200 mlN min^{-1}.

As soon as the OCV of the cell stabilized, which was usually within the first hour, the cell was set to potentiostatic operation at 0.3 V and heated to 90°C. Likewise, the aqueous methanol solution and the air were fed to the cell preheated at 90°C. Furthermore, the pressure on the anode and the cathode was adjusted to equal pressure of 3 bar_{abs} to avoid on the one hand the vaporization of methanol at the anode side and on the other hand a pressure difference between anode and cathode side, which may affect the membrane's lifetime. While the anodic supply was continued in the constant flow mode, the air supply was set to a stoichiometry of 2. However, the minimum airflow rate was 200 mlN min^{-1}, which corresponds to an air stoichiometry of 2 at a current density of 200 mA cm^{-2} for cells of this size. This airflow rate of 200 mlN min^{-1} is required by the IR sensor used to determine the CO_2 concentration in the effluent cathode stream.

The only difference in the start-up procedure between Nafion based MEA's and MEA's based on PSI-membranes was the air humidification. Nafion MEA's were fed with almost dry air (dew point 35°C), while air with a dew point of 60°C was supplied to cells equipped with PSI-membranes. The latter was done for no other reasons as for consistency with previous measurements. All cells were operated continuously under these conditions for at least 12 hours before collecting data.

Operation

The DMFC was characterized at the different operating conditions by galvanostatic driven polarization curves and simultaneously measuring the methanol permeation across the membrane. Data of the polarization curves were recorded starting from the

OCV and increasing incrementally the current of the cell until the cell voltage dropped below a given cut-off value. The current increments were 2 A, however, the first current interval was subdivided into four steps to account for the activation overvoltage regime. Thus, the polarization curve was measured with a higher resolution in this regime. Each data point of the polarization curves and the corresponding methanol crossover curves was measured at the end of an equilibration time of 6 minutes per single current step. Additionally, the membrane resistance ($R_{membrane}$) was determined *in situ* by the current pulse technique, explained in detail in reference [29]. The membrane resistance was determined before and after measuring a polarization curve at a current density of 400 mA cm^{-2}.

The polarization curves are subject to some experimental errors due to

- the measurement of the cell current (up to 6 A: 0.1% ± 80 mA, above 6 A: 0.1% ± 350 mA),
- the measurement of the cell voltage (better 1 mV),
- variations in the fuel supply (gas: ± 2%, liquid: ± 1 ml),
- pressure fluctuations (gas: ± 0.5%, liquid: ± 50 mbar),
- variations in the methanol concentration, and
- the precision of the temperature measurement (± 1 K).

While all these errors are small, there is no obvious way of estimating their impact on the polarization curves quantitatively.

Determination of the methanol crossover

Since the methanol permeation rate across the membrane is an important factor not only affecting the DMFC performance but also the efficiency of the DMFC system, the methanol leakage rates across the membrane were determined by monitoring the CO_2 concentration in the effluent cathode stream [30-32]. It was assumed that methanol which permeates across the membrane to the cathode is completely oxidized to CO_2 at the cathode[†] and that the membrane is impermeable for any CO_2.

[†] In practice, methanol is not completely oxidized at the cathode. However, it is neglected here because it is in the range of a few percent of the total methanol crossover [7] and thus comparable to the accuracy of the IR-sensor [33].

There are two experimental indications, which support the latter assumption:

- First, no CO_2 bubbles (permeated through the membrane from the cathode) are observed in the anodic fuel outlet at OCV up to a temperature of 120°C, an anodic flow rate of 6 ml min^{-1} and high CO_2 concentrations at the cathode (6 vol.%). Therefore, all CO_2, which permeates through the membrane, must be dissolved in the aqueous methanol solution. The resulting CO_2 flux across the membrane (Nafion 117, FEP 25, and FEP 75) calculated from the solubility of CO_2 in water at 120°C and 3 bar [34] can therefore be at most 5.5 10^{-7} mol s^{-1}. This CO_2 flux would correspond to an experimental error of about 10% at a methanol leakage current of 3 A (equals to 100 mA cm^{-2} for a 30 cm^2 active area).

- Second, if the aqueous methanol solution is supplied at a constant flow rate and the current load of the cell is incrementally increased, the methanol concentration at the anode is reduced. Simultaneously, the CO_2 concentration at the anode raises steadily with the current load of the cell. Nevertheless, a decrease of the methanol crossover is experimentally determined as depicted in Figure 7 by the squares.

Of course, one may argue that the methanol crossover data may also include attributes from anodic CO_2. However, if the membrane is permeable to carbon dioxide, this method[†] should result in a virtual increase of the methanol leakage when the methanol concentration at the anode is held constant while increasing the current load of the cell. Nevertheless, in the experiment such a behavior could not be observed as illustrated in Figure 7 by the triangles. Because of this experimental finding, the experimental error ignoring the permeability of the membrane towards CO_2 is small and thus is not taken into account.

In the following, methanol leakage rates will be presented in current densities (*e.g.*, Figure 7) that correspond to the current produced by total electro-oxidation of the permeated methanol at the cathode. In terms of molar flux across the membrane, a

---

[†] The measurement of the cathodic CO_2 as a measure for the methanol crossover.

methanol leakage current density of 200 mA cm^{-2} is equivalent to a specific molar methanol flux of 1.24 mmol $h^{-1}cm^{-2}$, *i.e.*, 37 mmol h^{-1} for an active area of 30 cm^2.

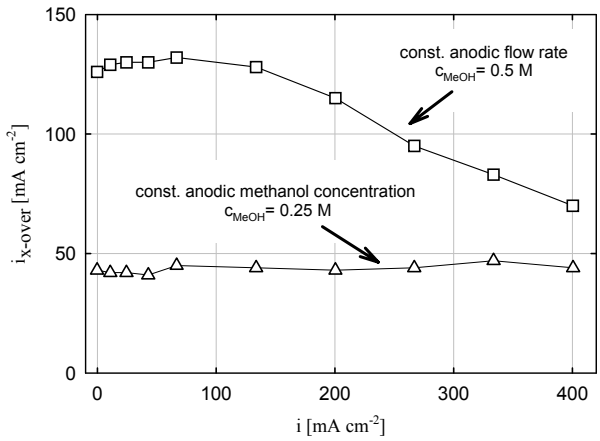

Figure 7: Experimental support for the assumption of an CO_2 impermeable membrane (see text above). Experimental conditions: T_{Cell} = 100°C, Nafion 117.

Water permeation measurements

For a further assessment of a membrane's characteristic, the water flux across the membrane was measured. Therefore, the DMFC was operated at a constant current and the entire water of the cathode effluent was collected over a certain period. An equal backpressure of 3 bar_{abs} was applied on the anode and cathode compartment as under "normal" experimental conditions. The schematic of the experimental setup is given in Figure 8. The cathode effluent was cooled to ambient temperature and subsequently the water was removed in a water separator. Because the volume of the water separator was limited, the accumulated water was drained partly into a separate vessel at regular intervals (each time 10 ml). Any water, which was left in the cathode effluent, was trapped in an adsorber filled with a drying agent ($CaCl_2$). In addition, the outlet of the 'water collector' was connected to the adsorber to prevent water losses of the vessel during the measurement. The methanol leakage across the membrane was determined by measuring the CO_2 concentration of the cathode effluent stream using an IR sensor (in Figure 8 indicated as CI). Water was collected for at least 5 hours at high current density and up to 50 hours at low current density to accumulate sufficiently large amounts of water to minimize the experimental error. The amount of water collected in such a measurement was determined by the mass difference of the water collector and the adsorber before and after the measurements, respectively.

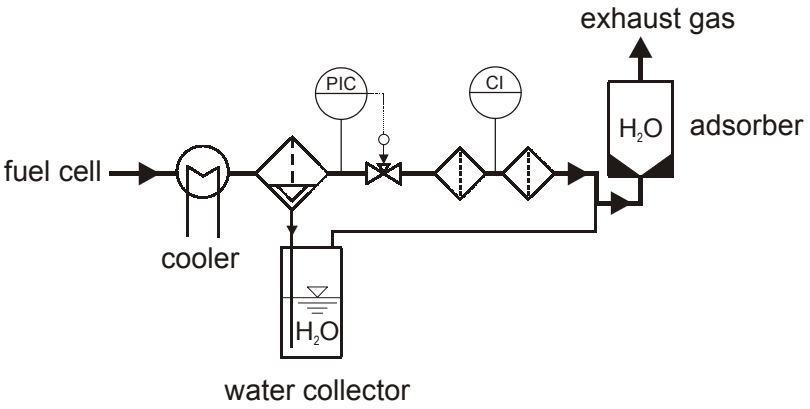

Figure 8: Experimental setup used for the measurement of the water permeation across the membrane.

The measurements were corrected for the water electrochemically produced due to the charge passed and the methanol leakage determined. Presumably, Reaction 1 and Reaction 2 take place at the cathode of a DMFC. Reaction 1 is the reduction of oxygen occurring at the cathode of a DMFC, whereas Reaction 2 is a combination of the two electrochemical half-processes and probably describes the recombination of oxygen and methanol at the cathode [35].

$$4\,H^+ + O_2 + 4\,e^- \leftrightarrows 2\,H_2O \qquad (1)$$

$$CH_3OH + {}^3/_2\,O_2 \leftrightarrows 2\,H_2O + CO_2 \qquad (2)$$

Reaction 1 allows calculating the water produced from the cell current passed, whereas the water produced by methanol crossover is given by Reaction 2. The latter is calculated from the CO_2 concentration in the cathode effluent stream.

3 Nafion 117

Typically, Nafion 117 is used as electrolyte in most DMFC research reported in the literature, *e.g.*, references [28, 36, 37]. Studies employing thinner membranes of the Nafion series, such as Nafion 115 or Nafion 112, revealed a strong dependency of the methanol crossover on the membrane's thickness [31, 32]. At a sufficiently high oxidant stoichiometry an increase of the cell voltage at a fixed current density can be noted for thinner membranes as Nafion 117, however, the methanol permeation across thinner membranes is significantly higher [31]. The latter overbalances the comparable small gain in polarization characteristics that can be achieved by the use of thinner membranes in the DMFC. Furthermore, the equivalent weight of the membrane affects both the current-voltage curve and the methanol crossover [31, 36]. However, a higher equivalent weight reduces both the methanol permeation across the membrane as well as the polarization characteristics. For this reason, Nafion 117 was mostly employed in the literature and therefore, it was used to assess the cell hardware, the electrodes, and the operating conditions. Furthermore, the effects of various process variables on the cell performance were investigated with Nafion 117 because of its availability at large scale with only minimal property variations. Besides, the Nafion data served as an internal standard to compare the results obtained with MEA's based on radiation-grafted membranes (see section 4 and 5 of this chapter). In the following, the Nafion membranes will be introduced and the knowledge of this membrane will be summarized in short. The cell results obtained with MEA's based on Nafion 117 will be given within this section, compared to data from the literature where possible and discussed.

3.1 Introduction to Nafion

In the late sixties, the Nafion series was developed by the *DuPont Company* for use as separators in electrochemical processes. The Nafion membrane features an extraordinary high chemical stability combined with high temperature stability and good processibillity [38]. Nafion membranes are made by copolymerizing sufonyl vinyl ether with tetrafluorethylene (PTFE) to form a polymer *DuPont* calls XR Resin [38]. This high-molecular-weight polymer can be melted or extruded into various forms such as sheets or tubes. By hydrolyzing the sulfonyl fluoride group to the ionic sulfonate

form, the XR Resin is converted into Nafion. The chemical structure of Nafion is depicted in Figure 9, where the value of m may be equal to one [39] and k varies from about 5 to 12 depending on the equivalent weight (EW) of the Nafion [40].

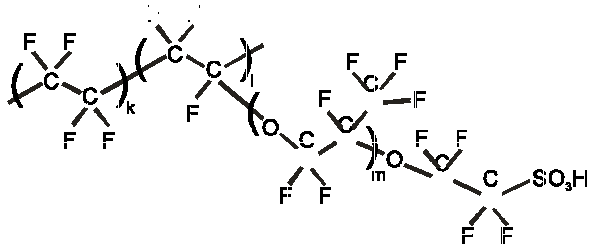

Figure 9: Schematic diagram of the structure of Nafion. The value of m may be as low as 1 [39] and the value of k ranges between 5 and 12 [40].

The morphology of the perfluorosulfonate membranes and their proton transport mechanism have been the subject of many studies. From rheological investigations of Nafion and X-ray diffraction patterns, Yeo *et al.* [41] suggested that most of the absorbed water exists in aqueous ion clusters within the membrane, which are, as first proposed by Gierke *et al.* [42], interconnected by channels. This picture of an ion-cluster-network model, as illustrated in Figure 10, has become a well-accepted feature of Nafion, confirmed by other researchers, *e.g.*, in reference [43].

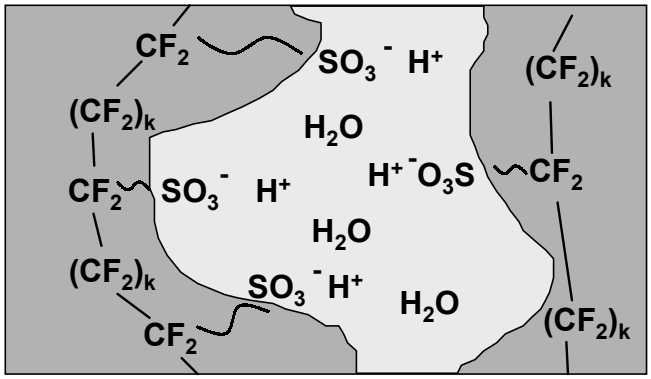

Figure 10: Cluster-network model of Nafion [42]. Channels interconnect the aqueous ion clusters.

Protons migrate through the membrane, if a current is drawn from the cell. From Figure 10, the electro-osmotic drag of water molecules becomes obvious, as most of the water exists in aqueous ion clusters and thus are dragged with the protons to the

cathode. Surely, the size of the clusters depends on the temperature, which affects the swelling of the membrane.

In this section, the DMFC characteristics of MEA's based on Nafion 117 are reported. These membranes have a nominal thickness of 7 mils, *i.e.*, about 175 µm, an average equivalent weight of 1100 g mol^{-1}, and an average density of 1.9 kg m^{-3} at ambient temperature in the dry condition [44]. Prior to the use in the DMFC, the membrane was boiled in a solution of concentrated nitric acid and deionized water (50 / 50 by volume) at a temperature of 90°C for two hours to remove impurities and to exchange any sodium ions with protons. Afterwards, the membrane was washed free of acid by boiling it repeatedly in deionized water. The membrane was stored in deionized water at room temperature before use in the DMFC.

3.2 Cell Performance of Nafion Based MEA's

The effect of the different process variables given in Table 1 on the DMFC performance was evaluated with MEA's based on Nafion 117 membranes. In general, a good reproducibility of the cell data was obtained. This indicates that the properties of the electrodes and the membrane vary only marginally over different batches. The key results of this extensive survey are presented within this subsection. If not stated otherwise, the data were obtained at the following standard operating conditions: The aqueous methanol solution was supplied preheated at cell temperature to the anode at a constant flow rate of 12 ml min^{-1}. The DMFC was operated with air at a stoichiometry of 3. However, a minimum airflow rate of 200 mlN min^{-1} was required, resulting in higher stoichiometric values for current densities below 130 mA cm^{-2}. The air was humidified at 35°C and fed preheated at cell temperature to the cathode. An equal backpressure of 3 bar_{abs} was applied on the anode and cathode, respectively.

Cell temperature

First, the effect of a variation of the cell temperature on the DMFC performance was evaluated. At constant operating conditions, polarization curves were recorded in the range between 90 and 120°C and simultaneously the methanol crossover was measured.

The result of this study is shown exemplarily for a methanol concentration of 0.5 M in Figure 11.

In general, a better polarization characteristic can be observed when increasing the cell temperature. Most notably at current densities above 100 mA cm^{-2}, the cell voltage is shifted to higher potentials with an increase of the cell temperature. At 270 mA cm^{-2}, the cell voltage increases from around 0.4 V at 90°C to almost 0.5 V at 120°C while the OCV rises in the same temperature range from about 740 mV to approximately 790 mV at 120°C as shown in Figure 11a. However, the improvements of the polarization characteristics get smaller for each temperature rise. While for the first temperature increment from 90 to 100°C the polarization characteristics improved considerably (at 200 mA cm^{-2} from around 450 mV to almost 500 mV), the improvement was smaller for the next temperature step, and a further increase of the cell temperature above 110°C resulted in no significant improvement of the polarization curve for the operating conditions chosen.

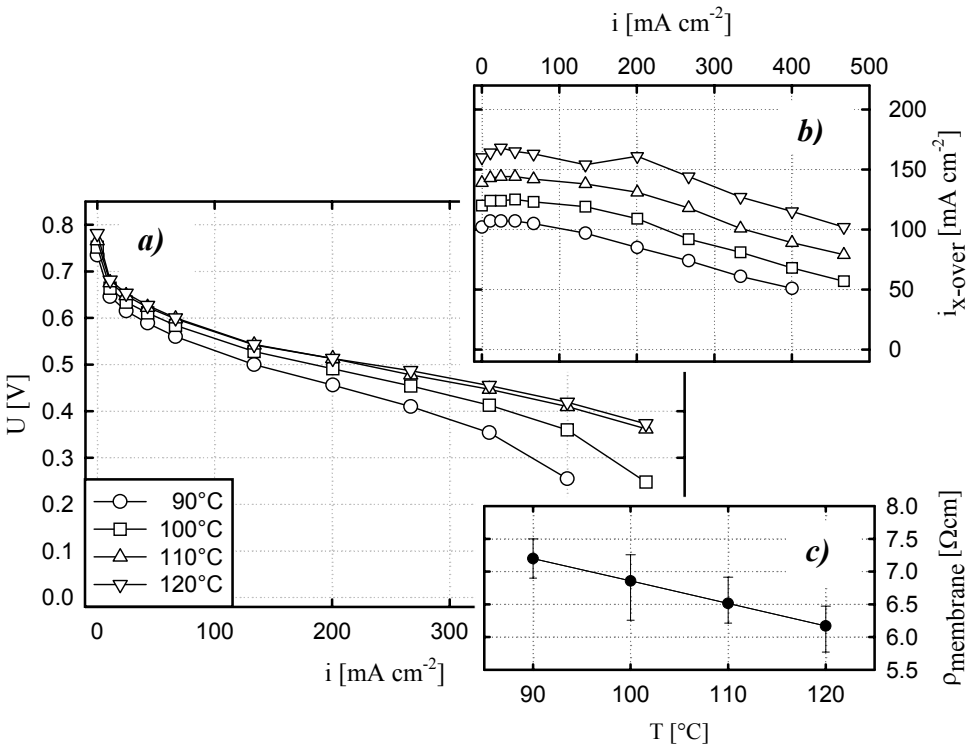

Figure 11: The effect of the cell temperature on the polarization characteristics (Figure 11a), the methanol permeation across the membrane (Figure 11b), and the membrane resistivity as shown in the Figure 11c. The cell data were obtained at the standard operating conditions and a methanol concentration of 0.5 M.

Unfortunately, the methanol permeation across the membrane is directly proportional to the cell temperature. As depicted in Figure 11b, the methanol leakage current density, $i_{x\text{-}over}$, steadily increases with a temperature rise of the cell. While the methanol leakage current density at OCV and 90°C (round data points in Figure 11b) is around 100 mA cm^{-2}, the methanol crossover at 120°C is 60 % higher, *i.e.*, about 160 mA cm^{-2} (triangles in Figure 11b). The shape of the methanol leakage curves derives from the methanol depletion at the anode of the DMFC with increasing current load. Please recall, the DMFC is operated at the standard operating conditions with a constant flow rate of the methanol-water mixture, *i.e.*, the methanol stoichiometry is variable along the polarization curve.

In general, some measurement artifacts are included in the method used to measure the methanol permeation across the membrane. As shown in Figure 11b, the methanol crossover slightly increases in the range between zero to 33 mA cm^{-2} (cell current). Because the measurements of the polarization curves were always started from potentiostatic operation at 0.3 V, the difference in the CO_2 concentration of the effluent gas stream was highest between operation at 0.3 V and OCV (starting point of the current-voltage curve). Therefore, the delay-time of the CO_2-sensor to reach full signal for the starting point of the current-voltage curve was the longest and thus the measurement interval (6 min) was too short to reach full signal for the first data point. Moreover, a deviation of a single point from the general trend of a methanol permeation curve can sometimes be noted, *e.g.*, the data point at 130 mA cm^{-2} of the methanol leakage curve measured at 120°C (Figure 11b). This sudden drop of the methanol leakage can be explained by the experimental set-up. The CO_2 sensor was located after the backpressure controller on the cathodic loop. Any regulations of the backpressure controller increase or decrease the airflow rate through the valve until the set point of the pressure is reached. However, if the tuning takes too long, the airflow rate through the backpressure controller (and thus through the CO_2 sensor) is not equal to the airflow rate through the mass flow controller, which is located before the cell, at the end of the six minutes interval. Therefore, the methanol permeation data calculated from the momentary CO_2 concentration and the momentary airflow as obtained by the mass flow controller explains this measuring error.

As depicted in Figure 11c, the membrane resistivity, $\rho_{membrane}$, decreases linearly with an increase of the cell temperature. The values of the cell resistivities are derived from a frequency distribution of all measurements at each temperature and the most frequent values are plotted in Figure 11c. These data are in a quantitatively good agreement to values reported in the literature [24, 25]. In contrast to the H_2-fuelled PEFC, the membrane is fully hydrated under liquid-feed DMFC operating conditions and thus its membrane resistance remains nearly constant over the entire polarization range (data not shown). In the literature the membrane resistivity was reported to be constant up to a current density of 1 A cm^{-2} under DMFC operating conditions [24].

Methanol concentration

Another key variable to enhance the DMFC performance significantly is the anodic methanol concentration. In Figure 12, the polarization curves and the corresponding methanol crossover are depicted at a cell temperature of 110°C for a methanol concentration of 0.5, 1, and 2 M, respectively. Under the standard operating conditions (see p. 74), the best polarization characteristic is found at a methanol concentration of 0.5 M. Higher anodic methanol concentrations result in a drastic decrease of the cell voltage, *e.g.*, the OCV is lowered by about 100 mV (2 M). Simultaneously, the methanol permeation across the membrane increases almost linearly with the increase of the anodic methanol concentration as illustrated in Figure 12b. At OCV, the methanol leakage current density at 0.5 M is around 130 mA cm^{-2}, 240 mA cm^{-2} at 1 M, and 560 mA cm^{-2} at 2 M methanol concentration, respectively.

In addition, the effect of the air stoichiometry may be foreseen from the polarization curves at 1 and 2 M methanol concentration as depicted in Figure 12a. The latter was recorded at a three times higher airflow rate as the polarization curve obtained at 1 M methanol. The methanol permeation across the membrane is roughly doubled for the 2 M-methanol concentration compared to the data obtained for 1 M (see Figure 12b). However, the effective air stoichiometry, which takes the methanol crossover into account (Equation 2, p. 70), is still higher for the polarization curve recorded at 2 M. Therefore, the polarization curves recorded for 1 and 2 M methanol concentration intersect at "higher" current density (at about 70 mA cm^{-2}) in Figure 12a. Both polarization curves terminate at 130 mA cm^{-2}, presumably, because of oxygen depletion

at the cathode. At this current density, the air stoichiometry is about 1.1 for the 1 M-polarization curve and approximately 1.7 for the 2 M-polarization curves.

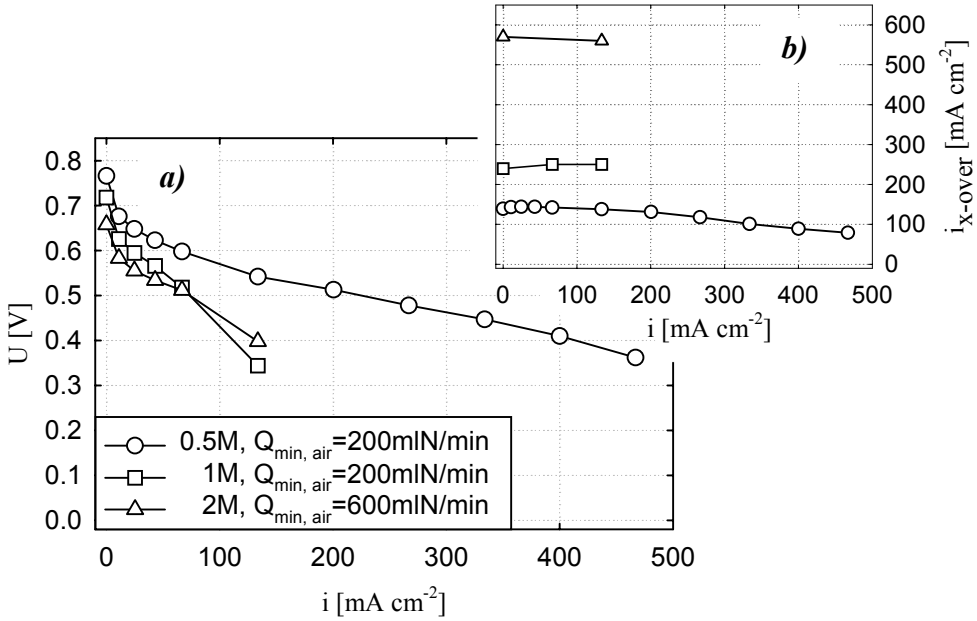

Figure 12: Variation of methanol concentration and its effect on the polarization curves (Figure 12a), as well as on the methanol crossover (Figure 12b). The data were measured at a cell temperature of 110°C and the standard operating conditions.

Air stoichiometry

The compression of gases requires a considerable amount of energy and thus the air stoichiometry is a crucial point for the design of any mobile application based on air-breathing fuel cells. In contrast to the H_2-fuelled PEFC, the DMFC operates usually at a higher pressure ($3bar_{abs}$ or higher), which further increases the parasitic energy demand of the compressor. Therefore, it is of utmost importance to assess the impact of the air stoichiometry on the polarization characteristic of a DMFC.

The effect of various air stoichiometries on the current-voltage curve of a DMFC is shown in Figure 13 for a methanol concentration of 0.5 M at a cell temperature of 100°C. All other process variables were kept at the standard operating conditions as described in the beginning of this section (p. 74).

From Figure 13, a slight shift to higher current densities at a fixed cell voltage can be noted with an increase of the air stoichiometry. At a cell voltage of 0.5 V, the current density is shifted from about 210 mA cm^{-2} at λ_{air} equals to two to around 260 mA cm^{-2} for air stoichiometries of five or higher. Moreover, the current-voltage curves obtained for the different air stoichiometries are in a good agreement up to a current density of about 130 mA cm^{-2}. The higher airflow shows its beneficial effect only in the higher current density region and results in a 10 to 20 mV raise only. However, the yield is small and thus, does not compensate for the additional energy required to supply the extra airflow.

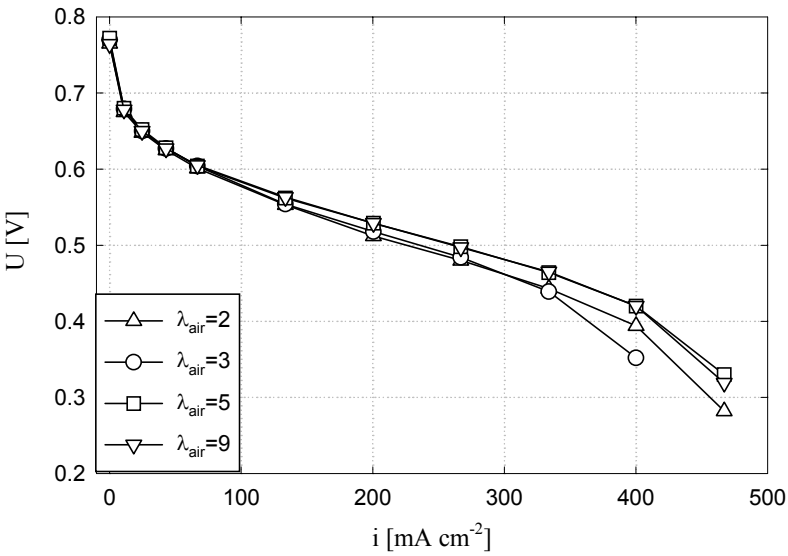

Figure 13: Variation of the air stoichiometry at 100°C, a methanol concentration of 0.5 M and standard conditions.

A different picture is drawn, if the DMFC is operated at a higher methanol concentration. As shown in Figure 12 by the intersection of the polarization curves measured for a 1 and 2 M methanol concentration, a higher airflow improves the polarization curve significantly because of the higher methanol permeation across the membrane. However, even with a three times higher airflow, the polarization characteristic at 2 M is significantly lower in the potential range of interest (≥ 0.4 V) than the one obtained for the 0.5 M aqueous methanol feed as illustrated in Figure 12.

Methanol stoichiometry

So far, all cell data presented were measured with a constant flow rate of the aqueous methanol solution and thus the methanol stoichiometry is large in the low current density range, *e.g.*, at a methanol concentration of 0.5 M and an anodic flow rate of 12 ml min^{-1}, the methanol stoichiometry is about 19 at a current density of 100 mA cm^{-2}. However, methanol depletion occurs for low methanol concentrations at high current densities. Under the same operating conditions as just mentioned before, the methanol stoichiometry is at a current density of 500 mA cm^{-2} just about 4. Therefore, the stoichiometric operation of the anodic feed is a necessity and can generally be realized in two ways:

(i) By varying the methanol concentration at a constant flow rate.

(ii) by regulating the flow rate at a constant methanol concentration.

The latter was investigated and the cell results are shown in Figure 14. Unfortunately, a minimum flow rate of 6 ml min^{-1} was required in these experiments to maintain a constant inlet temperature of the aqueous methanol solution. Therefore, the effect of a stoichiometric supply of the aqueous methanol solution can be seen in Figure 14, for a methanol stoichiometry of 7 not until a current density of about 130 mA cm^{-2}. Likewise, stoichiometric operation of the anodic feed is introduced for a methanol stoichiometry of 5 and 3 not until a current density of 200 and 330 mA cm^{-2}, respectively. In addition, the cell data for a constant anodic flow rate of 12 ml min^{-1} (gray triangles) are included in Figure 14, which is used under standard operating conditions. All cell data shown in Figure 14 were obtained at a methanol concentration of 0.5 M and an air stoichiometry of 3.

Interestingly, no significant improvement of the polarization curves can be observed up to a current density of about 330 mA cm^{-2} as depicted in Figure 14a. Solely an earlier mass transport limitation can be noted in the polarization curve obtained for low methanol stoichiometries, such as 3. Furthermore, it seems that a methanol stoichiometry of 7 helps to avoid early mass transport limitations and extends the polarization curve to slightly higher current densities (see Figure 14a unfilled triangles).

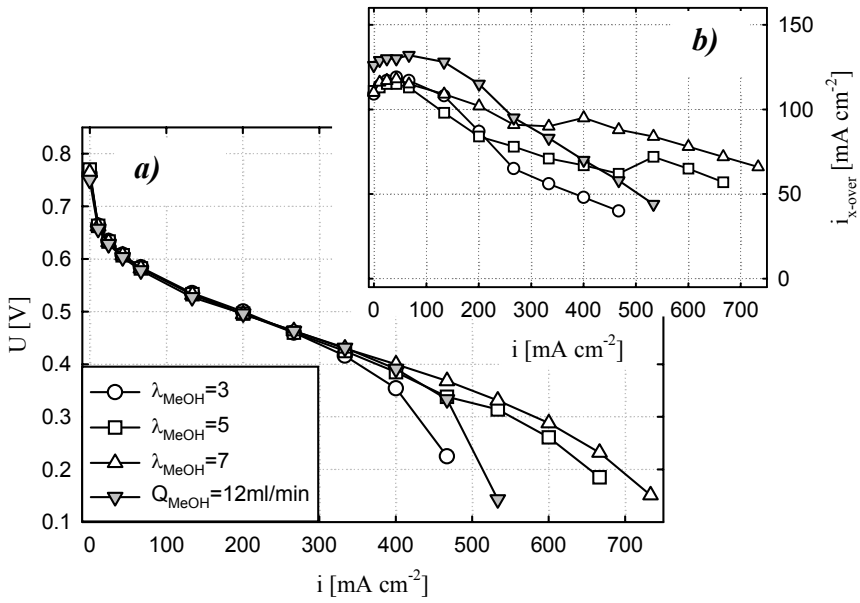

Figure 14: The effect of the methanol stoichiometry on the polarization characteristics and the methanol crossover (inset). The data were obtained for a methanol feed of 0.5 M at 100°C and an air stoichiometry of 3.

While the effect of stoichiometric operation of the anodic feed on the polarization curve is small, the methanol crossover is reduced significantly. It can be minimized up to about one third at a current density of 200 mA cm^{-2} as plotted in Figure 14b. Furthermore, the starting points of the stoichiometric operation of the anodic feed can be seen in Figure 14b. At a current density of 200 mA cm^{-2}, the methanol stoichiometry is just about 5 and thus the anode flow rate was incrementally raised with each further increase of the current load. As expected, the methanol leakage decreases at a constant methanol stoichiometry more slowly with an increase of current density and remains almost constant at the crossover level at which the methanol stoichiometry of five was first reached (at 200 mA cm^{-2}). Furthermore, the methanol leakage curve obtained for the constant flow rate of 12 ml min^{-1} intersect with the curves measured for a methanol stoichiometry of 7 and 5 at a current density, where the methanol stoichiometry for the constant-flow-rate curve is equal to 7 and 5, respectively. This demonstrates nicely the high reproducibility of the results obtained with the test benches entirely built during this work.

The bumps in the methanol leakage curves, which can be seen for a methanol stoichiometry of 7 at a current density of 400 mA cm^{-2} and for a methanol stoichiometry

of 5 at 530 mA cm^{-2} in Figure 14b, are related to the flow rate control of the testing facility. At these points, the regulation of the flow rate is switched from a constant-speed control to PID control (cf. section 2.1: *anode loop*, p. 56). Presumably, the flow rate was slightly too high under PID control because the flow meter has the highest error at low flow rate (at 15 ml min^{-1} about 16%). Thus, the methanol stoichiometry was slightly too high at this point.

A different approach to regulate the methanol stoichiometry is to vary the methanol concentration. However, the dynamic change of the methanol concentration in the anodic feed was not implemented into the technical layout of the testing facilities and thus two polarization curves obtained for 0.5 and 1 M may serve as an indication for the effect of a variation of the methanol concentration. Current-voltage curves of the two methanol concentrations are given in Figure 15 at a cell temperature of 90°C. At higher cell temperature and an air stoichiometry of 3, polarization curves could not be measured for cell current densities above 130 mA cm^{-2} at methanol concentrations of 1 M or higher because of oxygen depletion (cf. this section: *Methanol concentration*).

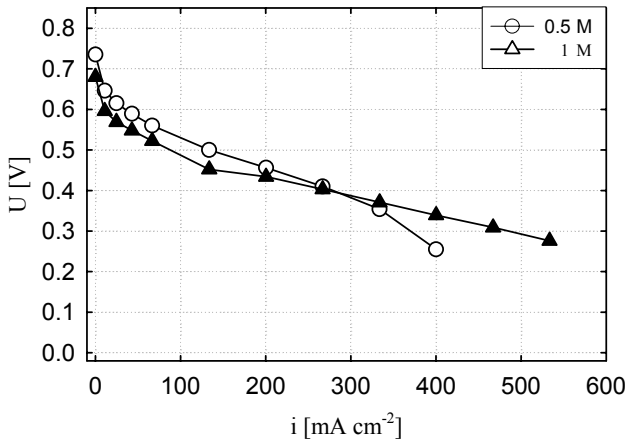

Figure 15: Cell data measured at 90°C and standard conditions for a 0.5 and 1 M methanol concentration, respectively.

Once more, the current-voltage plot obtained for the 1 M-methanol concentration is well below the one measured at 0.5 M in the current density region between 0 and 270 mA cm^{-2}. However, the curves intersect where a methanol stoichiometry of 7 is reached for a methanol concentration of 0.5 M and a flow rate of 12 ml min^{-1} (at about

270 mA cm^{-2}). At higher current densities, an anodic feed with a 1 M-methanol concentration results in a superior polarization performance.

Dew point of air

As a further parameter, the impact of the air humidification on the polarization characteristics was studied. The results of this study are summarized in Figure 16, which shows cell data obtained for a variation of the dew point of air between 35 and 90°C at the standard operating conditions (corresponding to a mole fraction of water in air of 1.9 and 23.4 %, respectively). In addition, the humidification study was carried out for different air stoichiometries and its result is given in Figure 16a for an air stoichiometry of 2 and in Figure 16b the data are shown for an air stoichiometry of 7. A minimum airflow rate of 200 ml min^{-1} was required to maintain a constant air temperature at the cathode inlet. Therefore, effects of an air stoichiometry of 2 and 7 cannot be seen in Figure 16a and Figure 16b until a current density of 200 and 60 mA cm^{-2}, respectively.

Fortunately, air humidification is not an issue for operating a DMFC as shown in Figure 16a. The supply of air saturated with water at 60 or 90°C leads even to a decrease of the polarization curve at an air stoichiometry of 2, which is likely related to a flooding of the cathode side. This is supported by *in situ* measurements of the gas-liquid distribution in the cathodic flow field. These studies revealed that parts of the cathodic flow channels are severely flooded (cf. *Chapter V*, section 2: *In situ Visualization*, pp. 135). If the membrane would dry out at high air stoichiometry such as 7, the polarization curves for the low (35°C; circles in Figure 16) and the high air humidification (90°C; triangles in Figure 16) should differ considerably. However, the current-voltage plots measured at the three different degrees of humidification are in good agreement at an air stoichiometry of 7 as illustrated in Figure 16b. Therefore, we allow to conclude that the membrane is not dried, even at an air stoichiometry of 7.

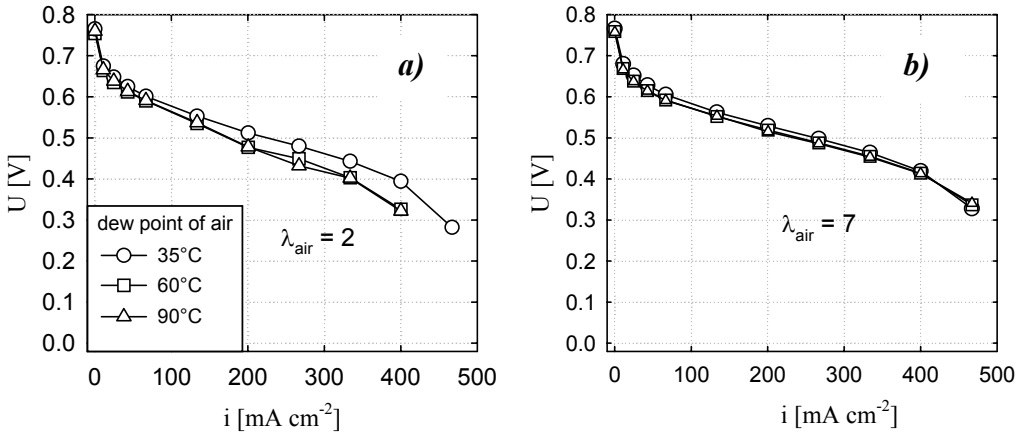

Figure 16: The effect of the dew point of air on the polarization curves at air stoichiometries of 2 ***(a)*** and 7 ***(b)***. The DMFC was operated at a methanol concentration of 0.5 M with a constant flow rate of 12 ml min^{-1}. The cell temperature was 100°C.

Water crossover

At last, the water permeation across the MEA was investigated. The entire water of the effluent gas stream of the cathode was collected over 5 to 50 hours. All water crossover data were corrected for the water introduced to the cell because of the humidification of the air (T_{Dew}= 35°C) and for the water produced. The latter was calculated from the charge passed and from the methanol permeation measurement (see p. 70). The water fluxes across the MEA were determined for cell temperatures of 90 and 110°C each at a methanol concentration of 0.5 and 1 M. The DMFC was operated at the standard operating conditions for the 1 M aqueous methanol feed (λ_{air}=3); however, the data obtained at the lower methanol concentration were measured at an air stoichiometry of 2 for consistency with data, which will be presented later in section 4 of this chapter. The resulting water fluxes at the different operating conditions are summarized in Figure 17 and given as function of the cell current density.

From Figure 17, it is obvious that the liquid-feed DMFC suffers from an extensive flooding of the cathode side. For comparison, the water flux across a Nafion 117 membrane in a H_2-fuelled PEFC was found to be around 0.3 g h^{-1} cm^{-2} at a cell temperature of 80°C independently of the current withdrawn (up to a current density of 700 mA cm^{-2}) [35].

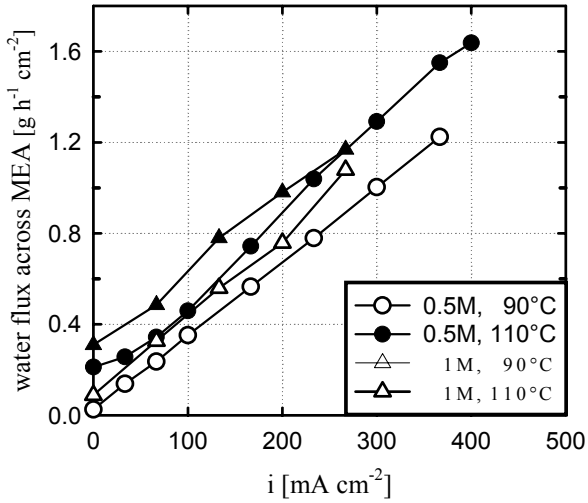

Figure 17: Water fluxes across a Nafion 117 membrane at different cell temperatures and methanol concentrations. The DMFC was operated at standard conditions and an air stoichiometry of 3 for the 1 M-methanol feed. The data shown for the 0.5 M methanol concentration are obtained for an air stoichiometry of 2.

Furthermore, an increase of the water flux across the membrane can be noted in Figure 17 by two ways. A temperature rise results in a higher water crossover, as seen by comparison of the data obtained at the same methanol concentration in Figure 17 (compare circles with circles or triangles with triangles) or by an increase of the methanol concentration. The latter can be seen in Figure 17 by comparison of the unfilled or filled data points. These observations are not too unexpected as from liquid-uptake studies in Nafion 117 an increase of the water uptake of the membrane with higher temperature is known [26, 45]. In addition, a stronger swelling of the membrane is reported when methanol is present in the equilibrating solution [26]. A higher liquid uptake will probably result in a higher liquid content of the micro-pores and thus, more water is transported to the cathode due to the electro-osmotic drag.

From the data reported in Figure 17, the water drag coefficients (number of methanol molecules per proton) at the different operating conditions may be calculated. At high current density, the water flux across the membrane may be mainly driven by the electro-osmotic drag. If one assumes that the electro-osmotic drag coefficient is independent of current density, then the water flux plotted *vs.* the current density should yield a straight line crossing the origin. As illustrated in Figure 17, except for the data obtained at a cell temperature of 110°C and a methanol concentration of 1 M (filled

triangles in Figure 17), the curves show this linear dependence at high current density. Since the water permeation across the MEA is not exclusively driven by the electro-osmotic drag but also by diffusion, a water flux across the MEA can be determined at zero current. The water drag coefficients calculated from the experimental data shown in Figure 17 are summarized in Table 2.

Table 2: Water drag coefficient obtained from the data reported in Figure 17.

T_{Cell} / c_{MeOH}	90°C	110°C
0.5M	5.1	6.4
1M	6	-

From the water measurements two conclusions can be drawn: *(i)* the membrane conductivity will be maintained at a high level even at high current densities and operating temperatures above 100°C, however, *(ii)* with the penalty of a significant water loss to the cathode presumably resulting in severe flooding of its electrode structure at high current density. The latter may be illustrated in the following armchair experiment.

Figure 18 summarizes the various water flows occurring in the cathodic porous electrode structure of a DMFC. Besides the water permeation across the membrane $\dot{m}_{mem}$ water is electrochemically produced due to the oxygen reduction because of the charge passed through the cell $\dot{m}_{charge}$ and the methanol crossover $\dot{m}_{x-over}$ (cf. *Section 2* of this chapter: *Water permeation measurements*, p. 70).

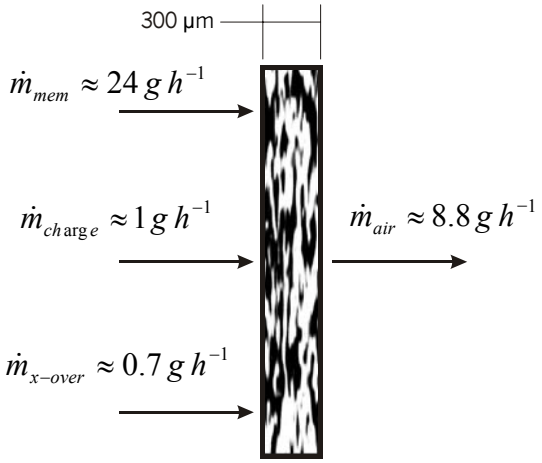

Figure 18: Typical water mass flows occuring at a cell current of 6 A, an anodic methanol concentration of 0.5 M and a cell temperature of 110°C. The values are valid for the Nafion 117 membrane.

It will be assumed that the air is completely free of water at the entrance of the cell and exits it completely saturated. Furthermore, an electrode thickness of roughly 300 µm, an area of 30 cm^2, and a pore volume of 50% are assumed. The DMFC may be operated at a cell temperature of 110°C, an aqueous methanol concentration of 0.5 M, and a current of 6 A may be withdrawn from the cell (corresponding to a current density of 200 mA cm^{-2}). The methanol crossover may be equivalent to 4 A (corresponding to about 130 mA cm^{-2}; see Figure 11b at 110°C). These assumptions result in the water fluxes as given in Figure 18. It is evident from Figure 18 that a flooding of the electrode structure must occur because a considerably larger amount of water is fed to the electrode as can be removed by the air stream. Therefore, a complete flooding of the electrode structure occurs within roughly one and a half minutes starting from a water-free electrode and assuming that all pores of the porous electrode (50% pore volume corresponding to a free volume of 0.45 cm^3) can be filled with water.

3.3 Discussion of the Nafion-Cell Results

From the experimental results given in section 3.2 of this chapter, we learned that the cell temperature and the methanol concentration have the highest impact on the cell performance of a liquid-feed DMFC as illustrated in Figure 11 and Figure 12. Both the cell voltage and the methanol crossover are functions of the cell temperature (Figure 11). The best polarization curve can be obtained at a cell temperature around

110°C, because at a higher cell temperature the methanol crossover limits a further improvement of the polarization curve. In principle, the same finding applies to the effect of the methanol concentration on the DMFC performance (Figure 12). An increase of the methanol concentration from 0.5 M to 1 M lowers the polarization curve because the methanol crossover is doubled.

The increase of the methanol crossover with a temperature rise as well as with an increase of the methanol concentration can be well explained by the cluster-network model shortly introduced in section 3.1. Because methanol is miscible with water and both molecules are of comparable size and similar physical properties, *e.g.*, dipole moment, the aqueous ion-clusters also include methanol molecules, which are also dragged by protons to the cathode if charge is passed through the cell. In addition, the concentration gradient between the anode and cathode compartment accounts for the methanol crossover at OCV. Since the methanol is oxidized at the cathode, the concentration gradient across the MEA is determined only by the anodic methanol concentration. Thus, a higher methanol concentration results in a higher concentration gradient across the MEA resulting in a higher methanol flux to the cathode. The latter can be seen by comparison of the methanol leakage rates at OCV given in Figure 12b. A doubling of the methanol concentration amounts to a doubling of the methanol leakage at OCV. The cell temperature affects the swelling of the membrane and thus the cluster size. However, larger aqueous ion-clusters allow larger methanol diffusion to the cathode and increase the number of methanol molecules dragged by protons as seen in Figure 11b. The latter could also be shown in the measurements of the water fluxes across the membrane. The water drag coefficient increased with a cell temperature rise as well as with an increase of the methanol concentration.

A high air stoichiometry improves the polarization characteristic as depicted in Figure 13. However, the yield in power is small compared to the extra energy needed to supply air at the higher stoichiometry. This may be demonstrated on the basis of the following example. The best a technical compressor can achieve is described by an isentropic compression:

$$P_s = \dot{m}\, w_s\,, \tag{3}$$

where P_s refers to the power, $\dot{m}$ to the mass flow of air, and w_s describes the energy needed to compress isentropic one kilo of gas. Under the experimental conditions used in this work, *i.e.*, a pressure of 3 bar_{abs} and air, w_s is calculated to 1.1 10^{-5} J kg^{-1}. Since the compressor power is directly proportional to the mass flow of air, any variation in airflow directly affects the power demand of the compressor. An example may illustrate that an increase in air stoichiometry is hard to justify. An air stoichiometry of 2 requires for this size of cell an airflow of 400 mlN min^{-1} (. 8.6 10^{-6} kg s^{-1}) at a current density of 400 mA cm^{-2}. Likewise, an airflow of 600 mlN min^{-1} (. 1.3 10^{-5} kg s^{-1}) is needed for an air stoichiometry of 3 at the same current density. According to Equation 3 and our operating conditions, this would mean the cell voltage has to be at least 40 mV higher at the stoichiometry of 3 compared to the stoichiometry of 2 to justify the higher airflow. Therefore, a low air stoichiometry is needed for operation of a DMFC at low methanol concentration (0.5 M). If the DMFC is operated at a higher methanol concentration, an increase of the airflow through the cell would probably result in a more significant rise of the cell voltage. However, a methanol concentration of 1 M doubles the methanol flux across the membrane compared to a 0.5 M aqueous methanol feed as illustrated in Figure 12b and thus the operation of the DMFC with a concentration of 1 M is only suitable at higher current density (above 300 mA cm^{-2}, see Figure 15).

In principle, the supply of methanol at a constant stoichiometry can be realized by regulating either the methanol concentration of the aqueous solution or its flow rate. The latter was shown in Figure 14. While the effect of the methanol stoichiometry on the polarization curve is small, reducing the methanol stoichiometry can minimize the methanol permeation across the MEA. Eventually, using an even more diluted aqueous methanol solution, such as 0.25 M and adjusting the flow rate if high current density is required can further minimize the methanol crossover. The other possibility, varying the methanol concentration in the anodic feed as suggested by Narayanan *et al.* [46], requires *(i)* a very accurate and fast methanol dosing to the anodic feed and *(ii)* the rapid change of the methanol concentration present in the cell / stack to allow for dynamic operation of the DMFC. Therefore, 'just' regulating the anodic flow rate and keeping the methanol concentration at a constant level is most probably the easier way to realize.

The measurement of the water flux across the MEA (Figure 17) confirmed the observation of the adversely effect of air humidification on the DMFC performance as depicted in Figure 16. Furthermore, the water permeation measurements yielded that the water flux increases considerably with an increase of either the cell temperature or the methanol concentration.

For benchmarking of the electrochemical components and the cell hardware, the cell results given in Figure 11 were compared to the best cell data available in the literature so far. At a cell temperature of 90 and 110°C, the cell voltage at a current density of 200 mA cm^{-2} is given for two references [24, 47] and for this work in Figure 19.

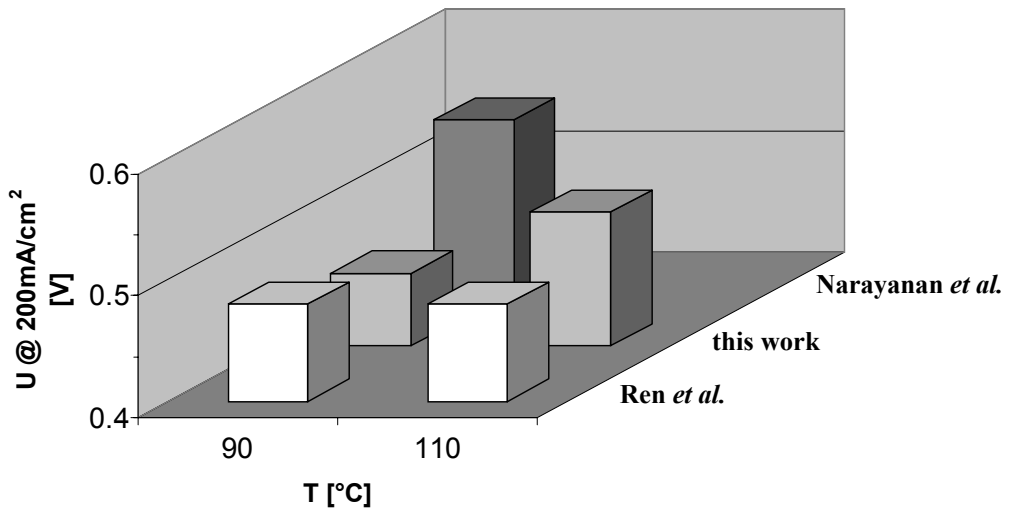

Figure 19 Evaluation of the cell results obtained in this work with the best data reported in the literature (based on Nafion 117). The cell voltage measured in this work at a current density of 200 mA cm^{-2} is given at a cell temperature of 90 and 110°C, respectively. The data from Narayanan *et al.* are taken from reference [47]; the data from Ren *et al.* are from reference [24].

Fortunately, the cell results presented within this work are in a good agreement with literature data as shown in Figure 19. However, please recall that the data presented in Figure 19 have only the membrane and the cell temperature in common. Besides catalyst loadings and the electrode structure, the operating conditions, *e.g.*, air stoichiometry or methanol concentration, differ quite considerably from the conditions used in this work. The data presented by Ren *et al.* [24] were obtained at an air stoichiometry of 36, a methanol concentration of 1 M, and a differential pressure of 1.2 bars were applied between the anode and cathode compartment. Similar operating

conditions were used by Narayanan *et al.* [47]. Air supplied at a stoichiometric flow rate of 60 compensated the adverse effect of the 1 M methanol solution and thus, a cell voltage of 0.54 V could be achieved. Unfortunately, both authors do not report the reasons for these 'extreme' operating conditions. In contrast to these energy demanding operating conditions, the cell results of this work are obtained at an air stoichiometry as low as 3.

A few research groups have also measured the methanol permeation across Nafion 117. While the methanol leakage data presented in this work are in reasonable agreement with data presented by Valdez *et al.* [48] at OCV, the decay of the methanol leakage with current density is different. However, the methanol crossover depends on the methanol stoichiometry (Figure 14) and thus is influenced by the anodic flow rate, which unfortunately is not stated in reference [48]. The methanol crossover measured by Dohle *et al.* [49] is in complete disagreement to the values reported in this study. A methanol leakage current of around 90 mA cm^{-2} is given in reference [49] for a DMFC at OCV operating on a 1 M aqueous methanol solution at 85°C. For comparison, a methanol leakage of about 230 mA cm^{-2} was measured in this work at OCV. One explanation for the very low methanol crossover reported by Dohle *et al.* may be the PTFE-loading of his electrodes (5% on anode and 30% on cathode), which may affect the methanol leakage.

By the same author, water fluxes across a MEA based on Nafion 117 were measured [50]. Once more, the water drag coefficient found by Dohle results in lower values as found in this work. At 110°C and a methanol concentration of 1 M, a water drag coefficient of 4.3 is reported in reference [50], which is even lower as the one of approximately 5.1 reported here for a methanol concentration of 0.5 M at 90°C. A substantially lower water drag coefficient was also found by Ren *et al.* [35]. At a methanol concentration of 1 M and 90°C, a water drag coefficient of 3.7 was determined. Once more, the electrode structure and its PTFE loading of the anode as well as of the cathode play a role in the water transport from the anode to the cathode and may account for these variations of the water drag coefficient. Unfortunately, neither the PTFE-loading of the electrodes used in this work nor the PTFE-loading of the electrodes used in reference [35] are known. Therefore, this lack of information

prevents us from evaluating the effect of the electrode hydrophobicity on the water crossover.

3.4 Summary & Conclusions

The cell tests based on Nafion membranes allowed assessing the behavior of the electrochemical components and the cell hardware under various operating conditions. The cell results obtained showed a reasonably good agreement with cell data published and are the benchmark for the characterization study of radiation-grafted membranes reported in the following section.

In contrast to the literature, the DMFC was operated at low air stoichiometry. Thus, best DMFC performance was obtained at low methanol concentration (0.5 M). Moreover, this study pointed out the process variables with the most relevance to the polarization characteristic as well as to the methanol crossover. These parameters were the cell temperature and the methanol concentration of the anode feed. Therefore, the effect of these two variables on the DMFC performance was chosen to investigate in the characterization study of radiation-grafted membranes.

A variation of the other process variables, such as air humidification, showed only a minor improvement of the DMFC performance or a variation of a specific parameter (*e.g.*, airflow) is just out of question in practice. However, introducing a stoichiometric operation of the anode flow makes a significant improvement in reducing the methanol crossover. Unfortunately, maintaining a constant inlet temperature for the anode feed is difficult and thus for the sake of reproducible cell results the stoichiometric supply of the anodic fuel will not be considered in the following characterization study of radiation-grafted membranes.

4 Radiation-Grafted Membranes

The cell performance of several radiation-grafted membranes based on poly(tetrafluor-ethylene-co-hexafluorpropylene) (FEP) was explored over a wide graft level range under DMFC operating conditions. The main goals of this characterization study can be summarized as follows:

(i) Evaluation of the polarization characteristic and methanol permeation across FEP based membranes,

(ii) correlation of these findings with their membrane properties, and

(iii) determination of the membrane with the best properties for use in the DMFC under the operating conditions investigated here.

This section is drafted in the following way:
A general description of the preparation of radiation-grafted membranes will be given in the next section (section 4.1) to introduce the reader to the key parameters affecting the properties of radiation-grafted membranes. This introduction to FEP membranes will be followed by the presentation of their cell results and discussion in section 4.2. At last, the findings of section 4.2 will be summarized and the main conclusions are drawn.

4.1 Preparation of Radiation-Grafted Membranes

Starting from commercially available FEP-foils, ion-conducting polymer films were prepared by the radiation-grafting technique, *e.g.*, reference [51]. A schematic of the process including the sulfonation and swelling of the membrane is depicted in Figure 20. The key steps of this process are the following:

(i) Irradiation of the polymer substrate by an electron-beam to generate free radicals within the polymer as illustrated in Figure 20b.

(ii) Upon immersion of the membrane in a solution of styrene and divinylbenzene, a radicalic polymerization is initiated by these radicals to form cross-linked polystyrene in the membrane as depicted in Figure 20c.

(iii) At last, the polystyrene is sulfonated and the membrane swollen with water as shown in Figure 20d.

With this procedure, an ion-conducting polymer of similar morphology to Nafion, in the broadest sense, is obtained. The material consists of two parts, an inert, hydrophobic FEP-backbone and highly hydrophilic, proton-conducting, sulfonated polystyrene side chains.

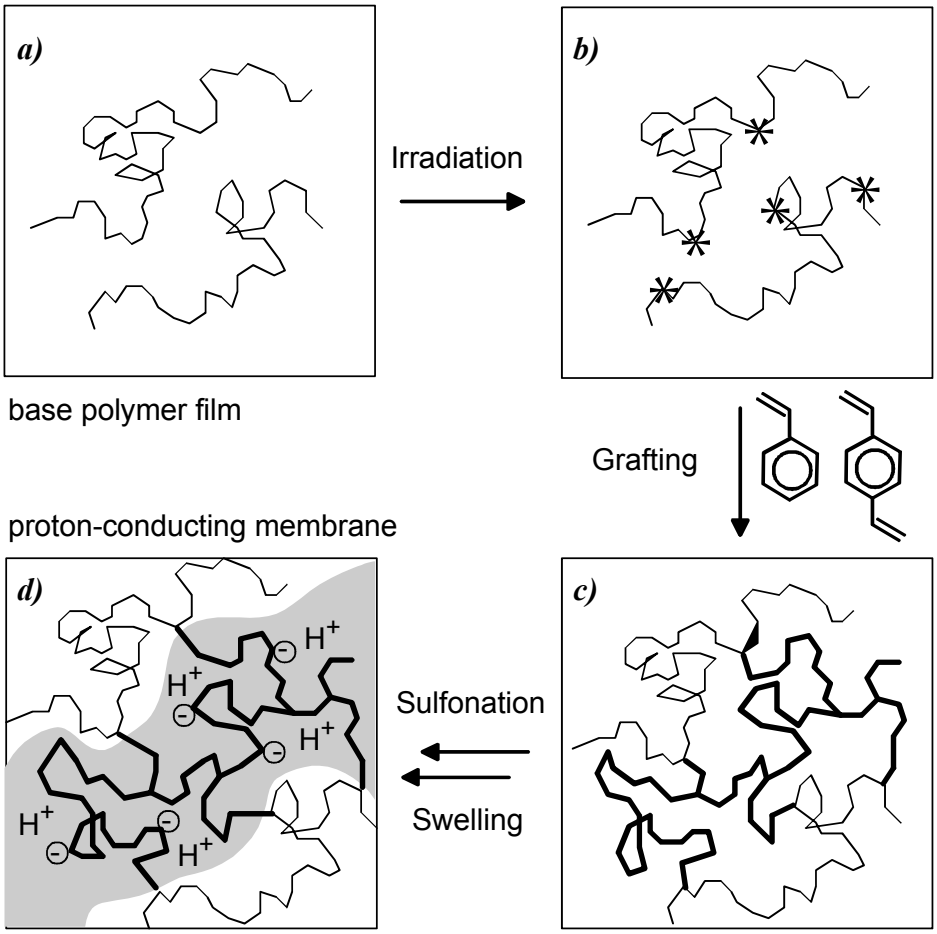

Figure 20: Schematic of the preparation of radiation-grafted membranes (illustration from *T. Rager*).

The conversion of a low-cost commodity polymer film with relatively simple chemical reactions and without any film forming process directly into a cross-linked, proton-conducting membrane is the advantage of this process. However, the membrane properties can be influenced by numerous reaction parameters, such as irradiation dose, thickness of the base polymer film, styrene to divinylbenzene ratio, and the degree of grafting, *i.e.*, the percentage by weight of the polystyrene to the base material.

Some experimental errors may arise from the radiation-grafting process itself:

If the polymer base film does not swell in the grafting solution, the grafting process occurs by a grafting front mechanism as illustrated in Figure 21.

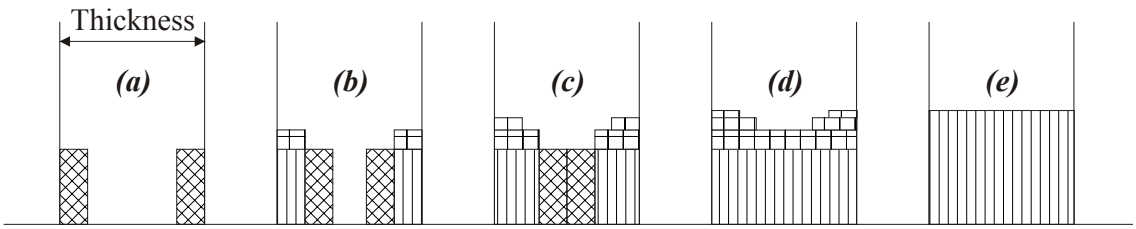

Figure 21: Grafting front mechanism. Illustration according to reference [19].

Because the base material cannot swell, grafting starts only at its surface (Figure 21a), which is in good contact with the grafting solution. The grafted surface region can then swell and thus the monomer can diffuse further into the polymer base material and can react ***(b)***. The two grafting fronts continue until they meet ***(c)***. Since ions should be conducted from one side of a membrane to the other when used as a solid polymer electrolyte in a fuel cell, the proton conductivity is determined by this middle layer (see Figure 21d). Thus, it is highly desirable to proceed until a homogeneous grafting level is achieved throughout the thickness ***(e)*** [18, 19]. Unfortunately, the grafting front mechanism as well as an inhomogeneous grafting over the membrane area may affect the reproducibility of this characterization study. At present, these variations are unknown.

For this study, FEP foils of two thicknesses (25 µm (FEP 25) and 75 µm (FEP 75)) were used as starting materials to prepare differently cross-linked membranes with varying degree of grafting (DG). The degree of cross-linking (DC) of a membrane is given by the styrene-to-divinylbenzene ratio by volume (S/DVB) of its grafting solution. Its effect on the cell performance was studied on membranes based on FEP 25. Three differently cross-linked FEP 25 membranes were investigated: low cross-linked FEP 25 membranes with a styrene-to-divinylbenzene ratio of 9 to 1 (S/DVB = 9:1), a medium cross-linkage of a styrene-to-divinylbenzene ratio of 8 to 2 (S/DVB = 8:2), and highly cross-linked FEP 25 membranes were prepared from a grafting solution with a styrene-to-divinylbenzene ratio of 7 to 3 (S/DVB = 7:3). Membranes based on FEP 75 were

only investigated low cross-linked (S/DVB = 9:1). Table 3 summarizes the various membrane types and their range of the DG, which were tested in the DMFC.

In the following section, the cell performances obtained for the different membranes as given in Table 3 will be shown and the effect of the DG and DC on the DMFC performance will be highlighted.

Table 3 Overview of the different membranes investigated.

Polymer Substrate	Degree of Cross-linking [S/DVB]	Degree of Grafting [wt%]
FEP 25	9 / 1	8, 10, 12, 15, 17, and 21
FEP 25	8 / 2	10, 12, 14, and 19
FEP 25	7 / 3	16
FEP 75	9 / 1	8, 13, 15, 19, 22, and 23

4.2 Characterization of FEP-Membranes in the DMFC

Let us shortly recall the findings of section 3: The highest impact on the DMFC performance was found to be the cell temperature and the methanol concentration. All other process variables had only a minor effect on the cell performance or their large variation is just out of question looked at from a technical point of view, *e.g.*, the airflow. Therefore, the cell data of each MEA were obtained at operating temperatures of 90, 100, and 110°C each at a methanol concentration of 0.5 and 1 M, respectively. All MEA's were investigated with air as oxidant humidified at 60°C at a stoichiometry of 2 (the minimum airflow was 200 mlN min^{-1}). The flow rate of the aqueous methanol solution at the anode was held constant and was about 12 ml min^{-1} (at a current density of 200 mA cm^{-2} a flow rate of 12 ml min^{-1} of a 0.5 M aqueous methanol solution is equivalent to a stoichiometry of about 9.7). An equal backpressure of 3 bar_{abs} was applied on the anode and cathode compartment. Subsequently, the standard operating conditions will refer to this set of process variables.

In the following, the cell data will be presented in three large blocks. Preceding these, however, the reproducibility of the cell results will be considered because of its utmost importance on all considerations and discussions. Afterwards, the cell results will be presented by the membrane type, starting with the low cross-linked FEP 25 membrane.

Reproducibility

A major goal of this characterization study was to establish a reliable data source for the performance of FEP based membranes under DMFC operating conditions. Therefore, at least two MEA's of each membrane batch were prepared and tested in the DMFC to gain confidence in the cell data. In addition, the DMFC performance of membranes with similar properties but of different batches was randomly checked. Exemplarily for all cell tests, Figures 22 to 24 shall demonstrate the reproducibility of the cell data obtained for the different membrane types. Any data measured at a cell temperature of 100°C were omitted in these Figures to improve the clarity of the diagrams. In the following, the reproducibility of the low cross-linked membranes will be discussed first.

As shown in Figure 22, the cell data of two different low cross-linked membrane batches of similar DG (12 wt%) result in close polarization characteristics and similar methanol permeation. The variation of the cell voltages over the entire current density range is only 20 mV at maximum as shown in Figure 22a. The methanol leakage data obtained for the different membrane batches are given at a cell temperature of 110°C in Figure 22b. As shown, the methanol crossover curves agree nicely over the measuring range and vary only around 10 to 20 mA cm^{-2}.

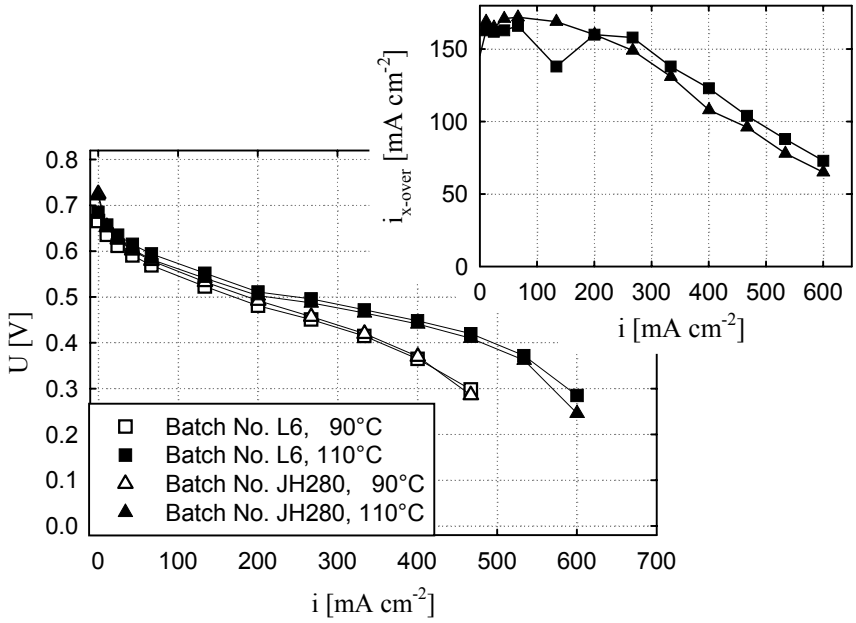

Figure 22 Reproducibility of the cell data obtained from MEA's based on FEP 25 membranes with a DG of 12 wt%. The data are given at a methanol concentration of 0.5 M and the standard operating conditions.

The polarization curves and the methanol leakages of low cross-linked FEP 75 membranes with a DG around 22 wt% are given in Figure 23 for different membrane batches. Once more, a good reproducibility can be noted for the polarization curves (Figure 23a) as well as for the methanol permeation across the membrane (Figure 23b). Except for the deviation of the polarization curves at high current density and 90°C, a close agreement and a variation of 20 mV at most can be found for the current voltage plots of FEP 75 membranes. In addition, the methanol crossover of both MEA's agrees reasonably as shown in Figure 23b. Solely, the methanol leakage data at 90°C differ by about 20 mA cm^{-2} in the low current density region. The reason for this deviation of the methanol leakage data is presently not known but might be related to some

measurement artifact. However, the methanol leakage data at 110°C are in a good agreement, as shown by comparison of the filled data points in Figure 23b.

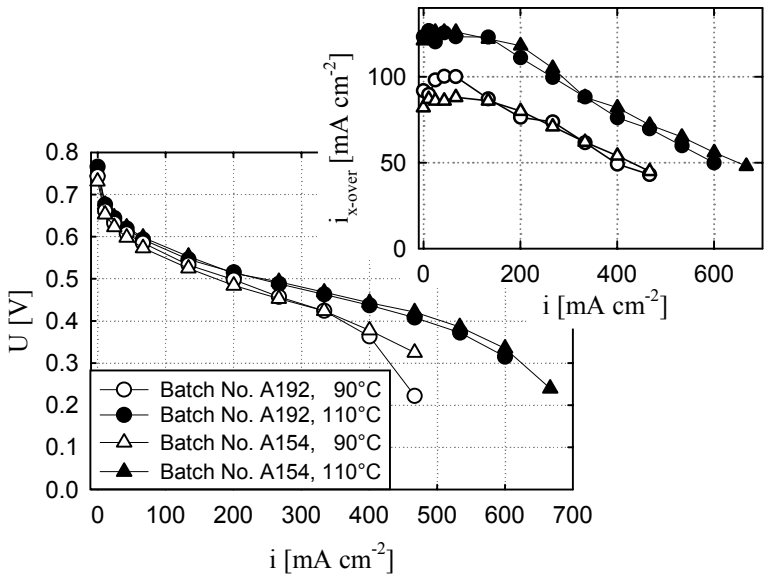

Figure 23 The reproducibility of cell performance data obtained for FEP 75 membranes. The polarization and methanol leakage curves are shown for a membrane with a DG of about 22 wt% at a cell temperature of 90 and 110°C. The data are given at a methanol concentration of 0.5 M and the standard operating conditions.

A comparison of the DMFC performance obtained from MEA's made of medium cross-linked membranes with a DG of 14 wt% is shown in Figure 24. The data are given for MEA's based on the same membrane batch. Unfortunately, the polarization curves of these MEA's differ quite considerably. At a current density of 200 mA cm^{-2} and a cell temperature of 110°C a difference of 50 mV can be found in the current-voltage curves, as shown in Figure 24. Additionally, the methanol permeation data of these membranes (Figure 24b) vary notably. Since other cell tests of medium cross-linked membranes show the same disagreement in the polarization curves and in the methanol crossover, although different electrode batches were used, an effect of the electrodes on these results is unlikely. Therefore, only the better of both cell tests performed per single membrane batch will be given in the following for membranes of medium DC.

The reproducibility of the cell results was exemplarily shown in Figures 22 to 24 each for a certain membrane type. A good agreement of the cell results can be found for low cross-linked membranes as demonstrated in Figures 22 and 23 and was found to be

about the same as obtained within single membrane batches. The reproducibility of the polarization curves of these membranes under DMFC operating conditions is in the same range as in the H_2-fuelled PEFC. In contrast, the medium cross-linked membranes showed only poorly reproducible cell data as depicted in Figure 24. Presumably, the higher cross-linkage of the membrane resulted in inhomogeneous membrane properties within a single membrane batch. Therefore, the variation of the cell data has to be beard in mind, when interpreting the cell results of medium cross-linked membranes: Only the better data set available for the same DG are given in the following figures.

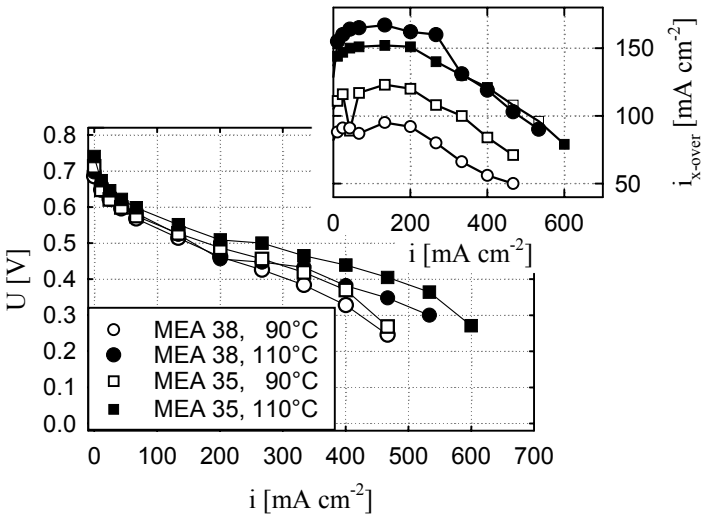

Figure 24 Cell data of MEA's based on the same membrane batch of medium cross-linked FEP 25 membranes (DG=14 wt%). The cell temperatures are indicated in the legend. The data were measured at a methanol concentration of 0.5 M and the standard operating conditions.

Cell data of high cross-linked membranes were not presented here because a complete data set could not be obtained for this membrane type. All attempts to assemble MEA's based on high cross-linked membranes resulted in cracks in the membrane either during hot pressing the MEA or during the start-up of the cell. Therefore, cell data of high cross-linked membranes will not be shown in the following.

Membrane resistivity

The degree of grafting of a membrane is determined as the weight ratio of polystyrene to the base material (cf. *Preparation of Radiation-Grafted Membranes*, p. 93). Because the content of the sulfonic acid groups in a membrane depends on the polystyrene

available within the membrane, the degree of grafting is an indication for its conductivity. A high DG translates into a higher polystyrene content in the membrane and thus an increased number of sulfonic acid groups are available within the membrane. Therefore, a higher DG results in a better conductivity and thus lower membrane resistivity (and unfortunately brittle membranes). On the other hand, a low DG gives membranes of good mechanical properties but of high membrane resistivity. Therefore, the membrane resistivity was measured *in situ* by the current-pulse technique [29] to gain further information about the membrane.

In Figure 25, the membrane resistivities of the three different membrane types are given for approximately similar DG (13±1 wt%) as a function of the cell temperature. For the standardization of the data, a thickness of 35 and 90 µm was used, which was measured with a thickness measuring gauge in the fully swollen state at room temperature for the FEP 25 and FEP 75 membrane, respectively. Henceforth, these thicknesses will be assumed for all calculations of resistivities, no matter of which DG the membranes are. As shown in section 3.2 (*Water crossover*, p. 84), the Nafion membrane tends to swell more in the presence of an increased methanol concentration and thus the membrane resistivity is lowered. Therefore, the membrane resistivities obtained at a methanol concentration of 1 M are included in Figure 25 in addition to the data obtained at 0.5 M to study the effect of the methanol concentration on the membrane resistivity.

Once again, a larger scatter of the cell resistivities can be noted for the data of the medium cross-linked membrane while the membrane resistivities of MEA's based on low cross-linked membranes show only a marginal variation, which is within the experimental error. Furthermore, a higher membrane resistivity can be noted for an increased cross-linking (S/DVB = 8:2, squares) of the membrane. An increase of the thickness of low cross-linked membranes does not affect the membrane resistivities as shown in Figure 25. Please note, *resistivities* are given in Figure 25, *i.e.*, the membrane resistance of low cross-linked membranes is at the same DG about three times higher for the FEP 75 membrane as for the FEP 25 membrane. The slightly lower membrane resistivity of the FEP 75 membrane compared to the low cross-linked FEP 25 membrane may be related to the higher DG or to the thicknesses assumed for calculating the resistivities (see paragraph before). The membrane thickness was

measured at room temperature in the swollen condition. However, the membrane's thickness after hot pressing the MEA and assembling it in the cell is an uncertainty for which the variations in the membrane resistivities may be accounted for.

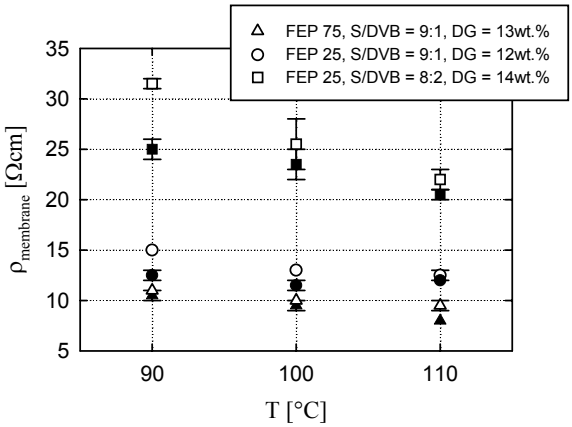

Figure 25: The membrane resistivity of low and medium cross-linked FEP 25 and FEP 75 membranes as function of the cell temperature. The membranes are of a similar DG around 13 wt% (±1 wt%). The error bars indicate the scatter in the experimental data of a single experiment. The membrane resistivities are given at a 0.5 M aqueous methanol feed (unfilled data points) and at 1 M (filled data points), respectively.

In general, a lower membrane resistivity is found for the methanol concentration of 1 M as shown in Figure 25. The decrease of the membrane resistivity is presumably related to a stronger swelling of the membrane, which increases its proton conductivity. However, it seems the higher methanol concentration affects especially the higher cross-linked membrane, which is surprising because the higher cross-linkage shall prevent excessive swelling of the membrane. On the other hand, the large difference may also be related to a better bonding of the membrane to the electrodes during operation (although stable cell performance, *i.e.*, constant power output, was observed at the end of the start-up procedure). This process is known to happen in the H_2-fuelled PEFC when the MEA is not hot pressed and may take up to several days [52]. The cell data were first obtained at a methanol concentration of 0.5 M starting from 90°C. Subsequently, the data at the higher methanol concentration were measured. The latter would be in agreement with the speculation that the surface of the membrane changes with a higher content of the cross-linking agent [53] and thus an intimate bonding of the MEA may not be reached in the hot pressing process.

In this characterization study, membranes based on FEP polymer films with different thickness, DC, and DG were investigated. The various membranes studied are summarized in Table 3 (p. 96) and their cell performances are given in Figure 26 and Figure 27 for a 0.5 and 1 M aqueous methanol feed, respectively. The general trends found for radiation-grafted membranes based on FEP polymer foils will be exemplarily illustrated based on these two Figures.

All cell data shown in Figure 26 are given for a methanol concentration of 0.5 M and a cell temperature of 110°C. Because of the better cell performance, cell data obtained with a 1 M aqueous methanol feed are depicted for a cell temperature of 90°C in Figure 27. In the "a" figures of Figure 26 and Figure 27, the cell performances of MEA's based on FEP 75 membranes (S/DVB = 9:1) are displayed. The cell data obtained for FEP 25 membranes (S/DVB = 9:1) are given in the "b" figures and the cell characteristics of medium cross-linked FEP 25 membranes (S/DVB = 8:2) are depicted in the "c" figures. The insets in these figures show the data measured for the methanol permeation of each membrane.

Low cross-linked FEP 25 membranes

As depicted in Figure 26b, the best polarization curve could be obtained for a low cross-linked FEP 25 membrane with a DG of 12 wt% at a 0.5 M aqueous methanol feed. - Please note the data shown for the membranes with a DG of 8 and 21 wt% were obtained at a higher minimum airflow (300 mlN min^{-1}), *i.e.*, the air stoichiometry was 3 at a current density of 200 mA cm^{-2}. - MEA's based on FEP 25 membranes with a higher DG, 17 or 21 wt%, have a higher methanol permeation as shown in the inset of Figure 26b, which is likely to be the cause for the reduction of the cell voltage compared to the polarization curve obtained for the best MEA (DG=12 wt%). The slightly lower membrane resistivity of the membrane with a DG=17 wt% ($\rho_{membrane}$ = 11 Ω cm, resistivity data not shown) compared to the membrane resistivity of the best membrane (DG=12 wt%, $\rho_{membrane}$ = 13 Ω cm) does not compensate the adverse effect of the increased methanol permeation across the membrane. On the other hand, the lowest grafted FEP 25 membrane (DG=8 wt%) reduces the methanol crossover up to a current density of 430 mA cm^{-2} as shown in the inset of Figure 26b

(circles). However, its membrane resistivity was considerably higher ($\rho_{membrane}$ = 20 Ω cm) resulting in a somewhat sluggish polarization curve.

At a 1 M aqueous methanol fuel feed, an increase of the DG of a membrane worsens its polarization curve considerably as seen in Figure 27b. The lowest grafted membrane shows the best polarization curve, because of its lower methanol permeation as depicted in Figure 26b. Please note, the methanol permeation data of the membranes with a DG of 12 and 17 wt% are constant up to a current density of 200 mA cm^{-2} as plotted in the inset of Figure 27b, because of the limited range of the CO_2 sensor. At low cell current density, the CO_2 concentration of the effluent stream is higher than the maximum range of reading of the CO_2 sensor. At a current density around 270 mA cm^{-2}, the airflow rate is raised for the first time from the minimum air flow rate of 200 mlN min^{-1} and thus the CO_2 concentration was diluted. Therefore, a sudden rise of the methanol crossover was measured for the membrane with a DG=12 wt% as seen in the inset of Figure 27b (triangles). Because the cell data of the membranes with a DG of 8 and 21 wt% were measured at a higher minimum airflow (300 mlN min^{-1}) the effective CO_2 concentration in the gas stream was lower. Therefore, a kink in the polarization curves of these membranes was not observed.

Similar to Nafion membranes best polarization characteristics are obtained at an aqueous methanol feed of 0.5 M. Furthermore, the methanol permeation across low cross-linked FEP 25 membranes directly scales with the DG. On the other hand, the membrane resistivity decreases with increasing DG. Therefore, an optimum in the polarization characteristics is obtained for a DG of 12 wt%, which represents the best compromise between the adverse effect of the methanol crossover and the membrane's proton conductivity. Since the methanol crossover is twice for doubling the methanol concentration of the anode feed as shown in the section before (section 3.2: *Methanol concentration*), the optimum polarization curve is shifted to lower DGs in the cell voltage range of interest (≥ 0.4 V).

Medium cross-linked FEP 25 membranes

A further possibility to limit the methanol losses to the cathode may be by increased cross-linking of the membrane. In this way, the swelling of the membrane should be

reduced, which should result in a reduction of the methanol permeation across the membrane. However, as reported before in the subsection *Reproducibility* (p. 97) of this section, the cell performances of MEA's based on medium cross-linked FEP 25 membranes were difficult to reproduce. Therefore, only the best cell data obtained for these membranes are shown in the Figure 26c and Figure 27c.

Once more, there is a trade-off between methanol permeation across the membrane (inset of Figure 26c) and the membrane resistivity (data not shown) at a 0.5 M methanol-water mixture. The methanol permeation across medium cross-linked membranes directly scales with the DG as depicted in the inset of Figure 26c. However, the membrane resistivities decrease with increasing DG from 48 Ω cm (DG=10 wt%) to 22 Ω cm (DG=14 wt%) to 20 Ω cm for the membrane with a DG=19 wt%. Combining the effects of the membrane resistivity and of the methanol crossover leads to an optimum in the polarization characteristics for a MEA based on the membrane with a DG of 14 wt%.

A comparison of the low cross-linked FEP 25 membranes (Figure 26b) with the medium cross-linked FEP 25 membranes (Figure 26c) shows comparable polarization characteristics of the best MEA's but a slightly reduced methanol leakage across medium cross-linked FEP 25 membranes as shown by comparison of the insets of these figures.

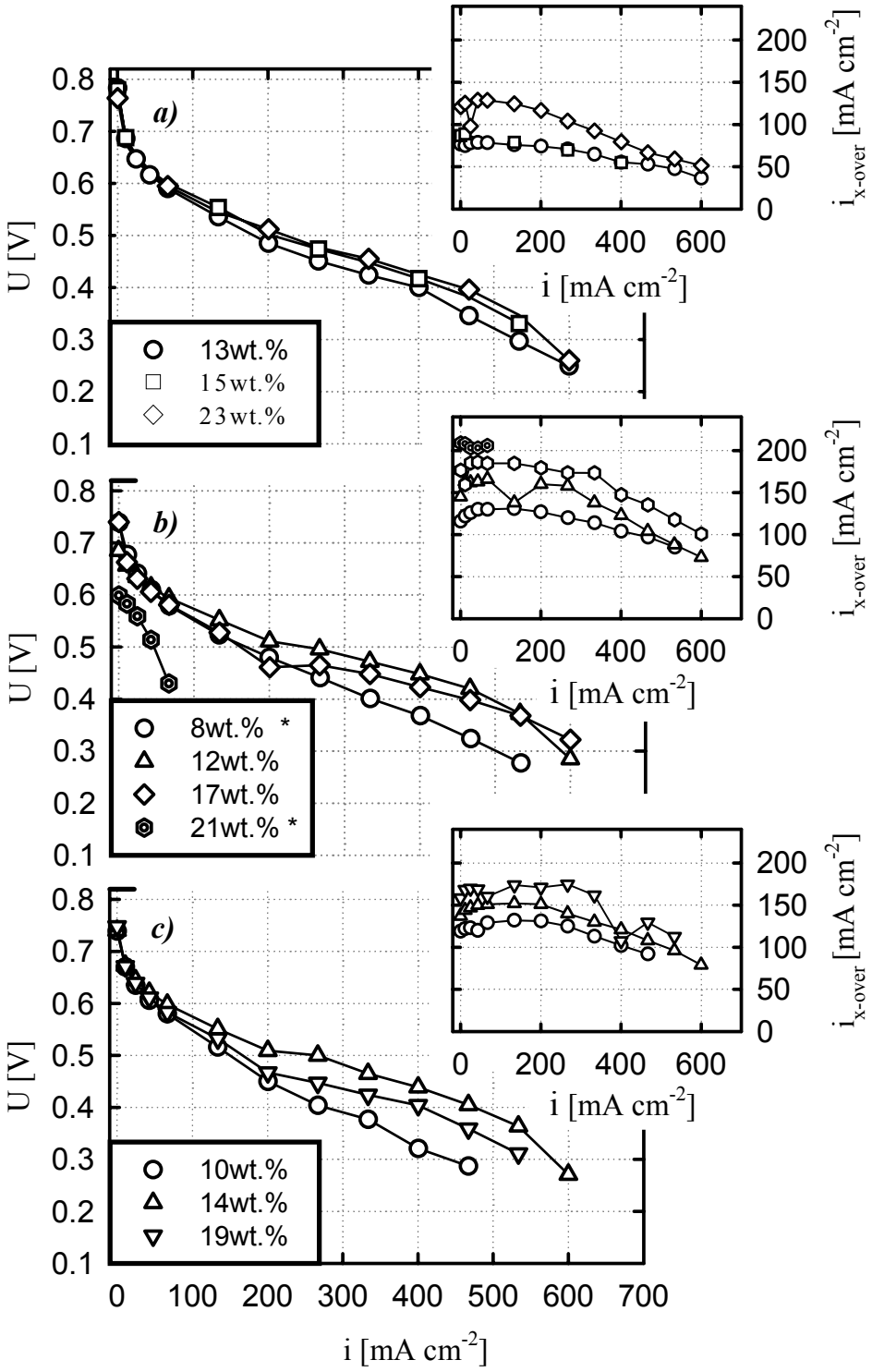

Figure 26: The effect of the degree of grafting on the polarization curves and the methanol permeation across the membrane (insets) at a cell temperature of 110°C and a 0.5 M methanol feed. In Figure 26a, the polarization curves and the methanol permeation across the membrane are given for low cross-linked FEP 75 membranes, in Figure 26b, the data are shown for low cross-linked FEP 25 membranes, and in Figure 26c, the cell data are given for medium cross-linked FEP 25 membranes. The star in the legends indicates a higher minimum airflow of 300 mlN min^{-1}.

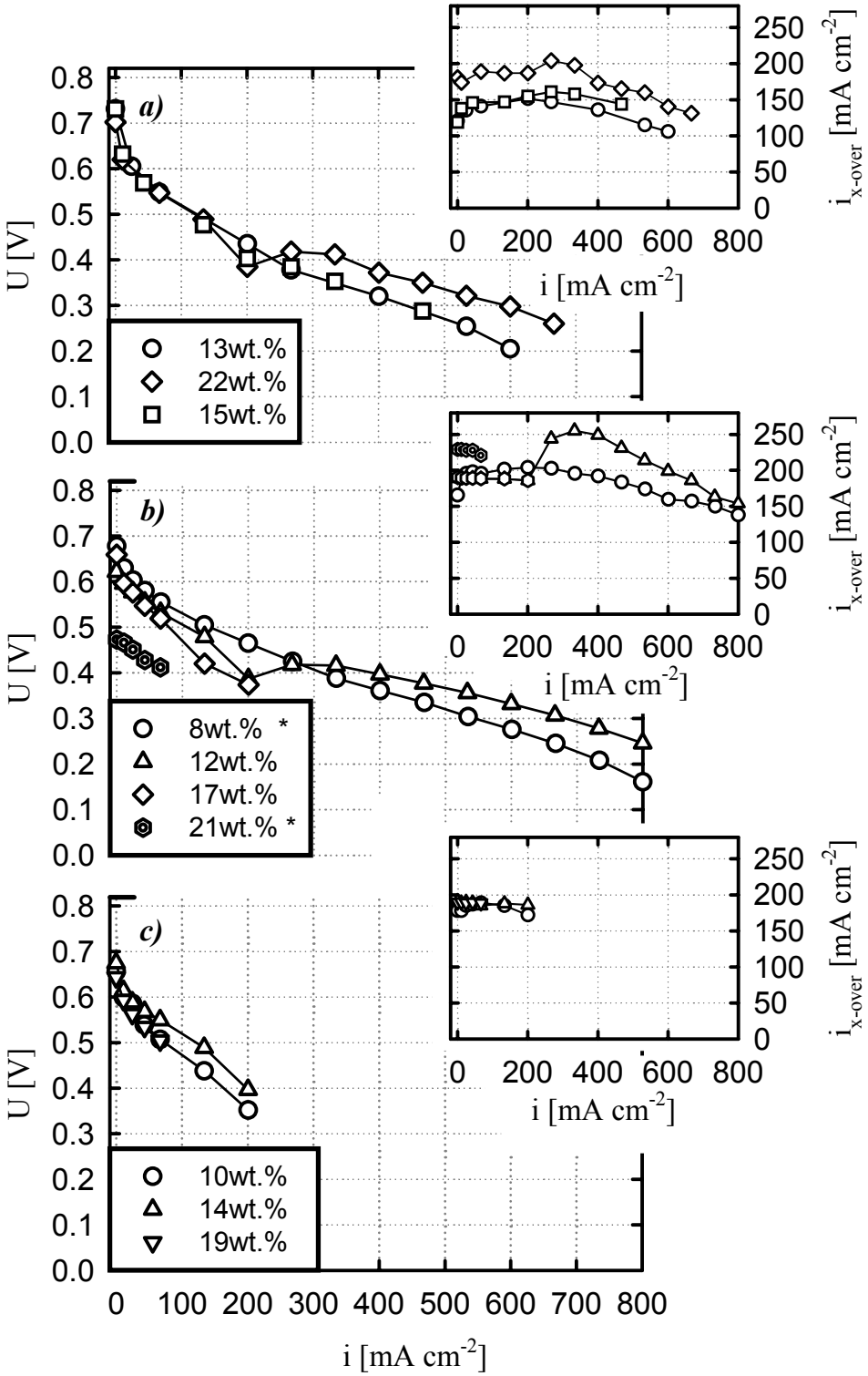

Figure 27: The effect of the degree of grafting on the polarization curves and the methanol permeation across the membrane (insets) at a cell temperature of 90°C and a 1 M aqueous methanol feed. In Figure 27a, the polarization curves and the methanol permeation across the membrane are given for low cross-linked FEP 75 membranes, in Figure 27b, the data are shown for low cross-linked FEP 25 membranes, and in Figure 27c, the cell data are given for medium cross-linked FEP 25 membranes. The star in the legends indicates a higher minimum airflow of 300 mlN min^{-1}.

Surprisingly, the polarization curves of the medium cross-linked FEP 25 membranes do not scale with the DG at a methanol concentration of 1 M as shown in Figure 27c. Presumably, the high membrane resistivity of the lowest grafted FEP 25 membrane overbalances its reduced methanol permeation as indicated from the measurements at 0.5 M (Figure 26c) and thus the MEA based on the membrane with a DG=14 wt% shows the better polarization characteristics. Once more, the close match of the methanol leakage currents at low current density as depicted in the inset of Figure 26c is a measurement artifact and is related to the maximum CO_2 concentration of the IR-sensor. Nevertheless, the methanol leakage can be estimated from the measurements at a methanol concentration of 0.5 M. Assuming a linear scaling of the methanol crossover with the methanol concentration at the anode, which was shown for the Nafion membrane in section 3.2 of this chapter, a methanol crossover between 200 and 270 mA cm^{-2} would be obtained at 1 M for the lowest and highest grafted membrane, respectively. These values are in good agreement with the polarization curves measured at 1 M. As shown for the current-voltage curve of the highest grafted membrane in Figure 27c (triangles down), data could not be obtained for higher current densities as 70 mA cm^{-2}. Assuming a methanol crossover of about 270 mA cm^{-2}, the air stoichiometry would be a little lower than one at the next data point (at 133 mA cm^{-2}) of the polarization curve. Therefore, oxygen depletion occurred at the cathode at higher current load of the cell resulting in a voltage drop below the cut-off value of 0.2 V.

Eventually, the methanol crossover data could be validated in that way. At a constant current, the airflow is reduced stepwise while monitoring the cell voltage. When the cell voltage becomes instable, an air stoichiometry of one is likely reached and the methanol leakage current may be estimated from the airflow and the charge passed through the cell.

FEP 75 membranes

The cell data obtained for the differently grafted FEP 75 membranes are shown in Figure 26a for a 0.5 M and in Figure 27a for a 1 M aqueous methanol fuel feed. Unfortunately, the cell data of MEA's based on the FEP 75 membrane with a DG=8 wt% could not be obtained because of its high membrane resistivity (560 Ω cm;

corresponding to a voltage loss of about 420 mV at 5 A) and thus are not included in Figure 26a and Figure 27a.

As depicted in Figure 26a, an optimum in polarization characteristics can be achieved for the highest grafted FEP 75 membrane (DG=23 wt%, diamonds in Figure 26a) at a 0.5 M aqueous methanol fuel feed. However, the methanol permeation across FEP 75 membranes also increases with the DG as shown in the inset of Figure 26a and is highest for the highest grafted FEP 75 membrane. Furthermore, the methanol leakage across the membranes with a DG=23 wt% is considerably higher than the methanol crossover of the lower grafted FEP 75 membranes. Nevertheless, the methanol leakage of a FEP 75 membrane is lower than the methanol leakage of a FEP 25 membrane of similar DG as seen by comparison of the insets of the plots in Figure 26 and Figure 27. For that reason, the MEA's based on FEP 75 membranes give comparable polarization characteristics to MEA's based on FEP 25 membranes, although they have an inherent higher membrane resistance. The membrane resistivities measured for MEA's based on FEP 75 membranes varied between 8 Ω cm (DG=23 wt%) to 18 Ω cm (DG=13 wt%) at a cell temperature of 110°C and are in the same range as the cell resistivities obtained for low cross-linked FEP 25 membranes (cf. *Membrane resistivity* of this section, p. 100).

An increase of the methanol concentration to 1 M affects the polarization curves and the methanol permeation data of the FEP 75 membranes considerably as depicted in Figure 27a. The methanol permeation across the lowest grafted FEP 75 membrane (DG=13 wt%; triangles up) is only slightly increased as seen by comparison of the insets of Figure 26a and Figure 27a because of the lower cell temperature of 90°C. Once again, the methanol leakage data of the highest grafted membrane are too low at a current density below 200 mA cm^{-2} because of the limited range of the CO_2 sensor. As expected, the polarization curves of these membranes are highly dependent on the DG at a methanol concentration of 1 M as shown in Figure 27a. The best polarization characteristics of FEP 75 membranes can be obtained for MEA's based on the lowest grafted membranes (DG of 13 or 15 wt%). The polarization characteristic of the highly grafted FEP 75 membrane shows a steep voltage drop in the low current density region (≤ 200 mA cm^{-2}) because of oxygen depletion at the cathode. Up to a current density of

200 mA cm^{-2}, the airflow was constant at 200 mlN min^{-1}, which corresponds to an air stoichiometry of 2 at a current density of 200 mA cm^{-2}. However, the methanol crossover is highest in this range (about 200 mA cm^{-2} as calculated from methanol leakage data measured at a methanol concentration of 0.5 M) and thus the effective air stoichiometry for the DMFC is close to one at 200 mA cm^{-2}.

Overall cell efficiencies

For a better comparison of the different membranes, the efficiency of a cell along its polarization curve was calculated. In contrast to the H_2-fuelled PEFC, the voltage efficiency cannot be used by itself to describe the cell efficiency of a DMFC because the methanol losses to the cathode are not taken into account. Therefore, the overall cell efficiency was defined as

$$\eta_{overall} = \eta_{voltage}\, \eta_{fuel}\,, \tag{1}$$

with

$$\eta_{voltage} = \frac{U}{U^{\circ}}\,, \tag{2}$$

and

$$\eta_{fuel} = \frac{\dot{n}_{electr.}}{\dot{n}_{x-over} + \dot{n}_{electr.}} = \frac{i}{i_{x-over} + i}\,, \tag{3}$$

where $\eta_{voltage}$ refers to the voltage efficiency and η_{fuel} is the fuel efficiency, which accounts for the methanol losses through the membrane per produced electricity. U is the actual cell voltage, U° refers to the thermodynamic cell voltage at standard state conditions, $\dot{n}_{electr.}$ is the molar methanol flux that contributes to the production of electricity, $\dot{n}_{x-over}$ is the methanol mole flux across the membrane, i is the actual cell current density, and i_{x-over} is the methanol leakage current density. The principal trends of fuel, voltage and overall efficiency are plotted in Figure 28. The fuel efficiency increases with higher current load of the cell because the methanol concentration at the anode is diminished and thus less methanol is lost to the cathode. Because of the reverse trends of fuel and voltage efficiency an optimum in the overall efficiency is obtained (Figure 28).

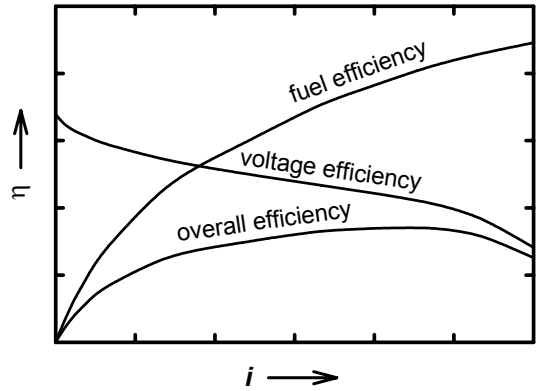

Figure 28: Schematic of the efficiency curves. The reverse trend of fuel efficiency and voltage efficiency results in an optimum of the overall efficiency.

This optimum in overall cell efficiency is reported in Figure 29 as function of the DG for all membrane types at a methanol concentration of 0.5 M. The efficiencies at 90, 100, and 110°C are given in Figure 29a to Figure 29c, respectively. Additionally, the power density at the best overall cell efficiency of each membrane is depicted in the corresponding bar chart of Figure 29.

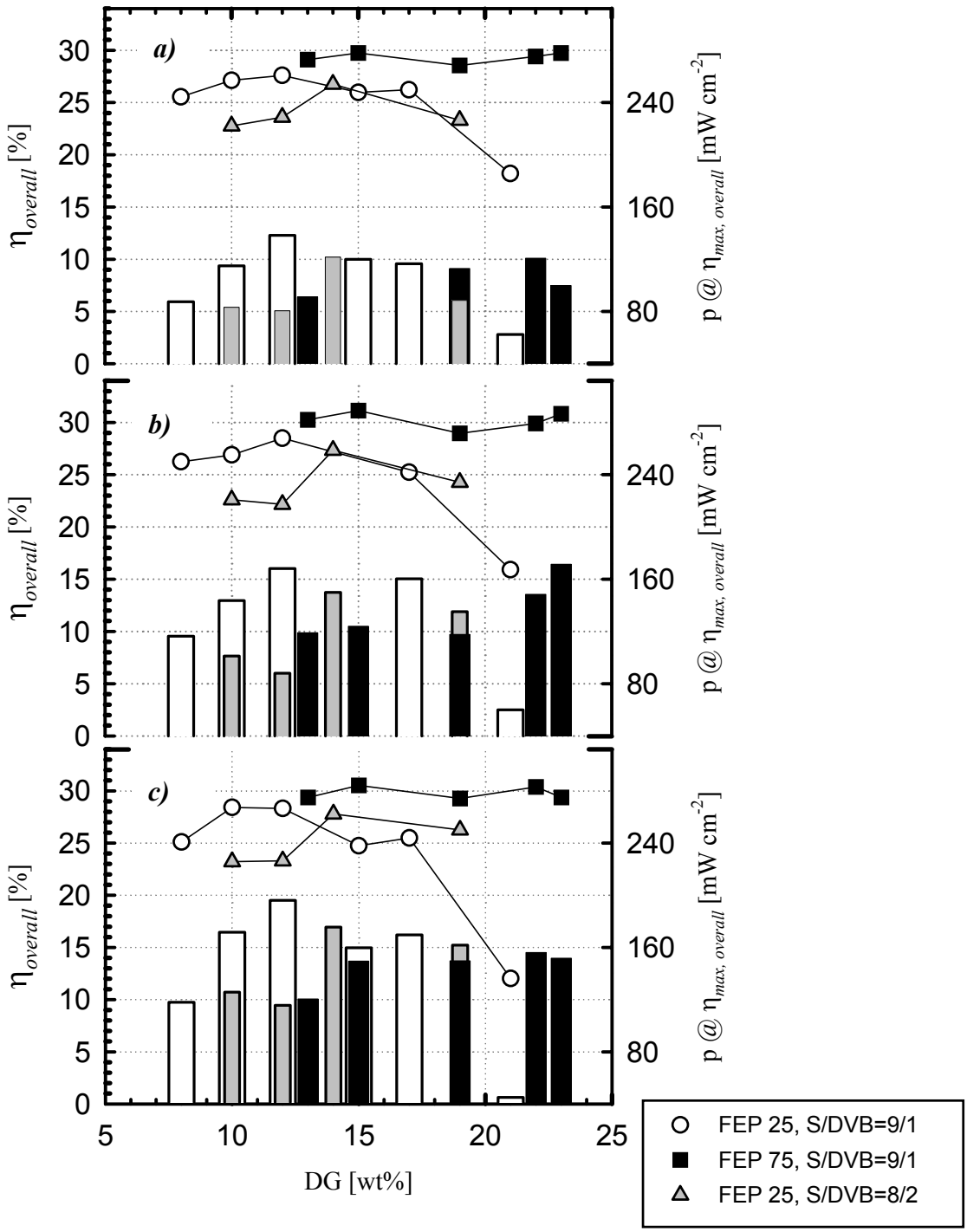

Figure 29: Best overall cell efficiencies as function of the degree of grafting for the different membrane types at a methanol concentration of 0.5 M. The data in the "a" Figure are given at a cell temperature of 90°C; in the "b" Figure at 100°C; and in the "c" Figure at 110°C. The overall cell efficiency was calculated according to Equation 1. Additionally, the power density at the maximum cell efficiency of each membrane is depicted in the bar chart.

The various trends of Figure 29 are summarized below:

- As shown in Figure 29, overall cell efficiencies around 30% can be obtained for the FEP 75 membranes at all cell temperatures. Moreover, the DG of FEP 75 membranes hardly affects the cell efficiency and the power density in the range between 15 to 22 wt%. However, the cell temperature does affect the power density but not the overall cell efficiency as seen by comparison of the black bars and squares in Figure 29.

- The thinner membranes show more clearly an optimum of the DG with respect to the overall cell efficiency. At 90°C, the best overall cell efficiency is obtained for FEP 25 membranes at a DG of 12 wt% for a low cross-linked membrane and a similar efficiency is achieved for a medium cross-linked FEP 25 membrane at a DG of 14 wt%.

- Furthermore, Figure 29 shows that a DG above 15 wt% of low cross-linked FEP 25 membranes adversely affects the overall cell efficiency at high temperature as shown by the circles in Figures "b" and "c". Moreover, a shift of the optimum of the overall cell efficiency to lower DG's can be noted for low cross-linked FEP 25 membranes at 110°C. Although the best overall cell efficiency of low and medium cross-linked FEP 25 membranes is in close agreement, the highest power density at maximum cell efficiency is observed for the low cross-linked FEP 25 membrane in Figure 29 at all temperatures.

- The optimum in overall cell efficiency for the medium cross-linked FEP 25 membrane is around 14 wt% at all temperatures. The high membrane resistance measured for a low DG counterbalances the reduced methanol crossover and thus, even at high temperature, the membrane with a DG of 14 wt% shows the best compromise between methanol crossover and membrane resistance. The power density obtained at maximum overall cell efficiency is comparable to those obtained for the FEP 75 membranes. However, their overall cell efficiency is about 4% lower than the best value obtained for the FEP 75 membrane.

In general, the FEP 75 membrane shows the best overall cell efficiency at all three cell temperatures as depicted in Figure 29. The advantage in the overall cell efficiency of the thicker membrane can be attributed to a lower methanol loss to the cathode (Figure 26 and Figure 27), which decreases the adverse effect of the methanol on the cathode overvoltage and thus compensates for the inherent higher membrane resistance of a thicker polymer electrolyte. For the same reason, the thicker membranes have clear advantages at low current density (part load region) as illustrated in Figure 30. While the thinner membrane shows a clear optimum in its overall cell efficiency, the curve of the FEP 75 membrane basically remains constant over almost 200 mA cm^{-2} at maximum cell efficiency. Surely, the latter is highly desirable to design an efficient DMFC system.

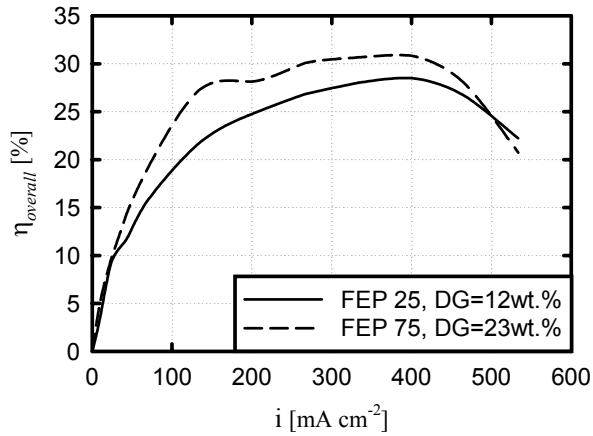

Figure 30: Trends of the overall cell efficiency illustrated for a thin and a thick membrane, which have a comparable power performance. The data are given at a cell temperature of 100°C and a 0.5 M aqueous methanol feed.

Water flux across FEP membranes

For the Nafion membrane, high water fluxes across the MEA were measured (cf. section 3.2: *Cell Performance of Nafion Based MEA's*, pp. 74). However, the methanol crossover and the water flux across the membrane are dependent variables if charge is passed and thus the water crossover of the FEP membranes may be different from the one measured for MEAs based on Nafion 117.

The water permeation across two FEP-membranes of similar DC (S/DVB = 9:1) and DG (FEP 25: DG=12 wt%; FEP 75: DG=15 wt%), but different thickness is shown in

Figure 31. The water fluxes were measured at a cell temperature of 90°C and a 0.5 M aqueous methanol feed. The water crossover data were corrected for the water produced, both calculated from the charge passed and from the methanol permeation measurement.

Surprisingly, very similar water fluxes were obtained for both membranes as shown in Figure 31. At OCV, the water flux across both membranes corresponds closely to the amount of water a fully saturated air stream can absorb. Similar to Nafion, the water fluxes across the MEA's increase linearly with the charge passed resulting in about two molecules of water dragged to the cathode per single proton. The latter indicates hydration shells of similar size for both FEP membranes. A comparison with the water fluxes across MEA's based on Nafion 117 membranes will be given in the next section of this chapter.

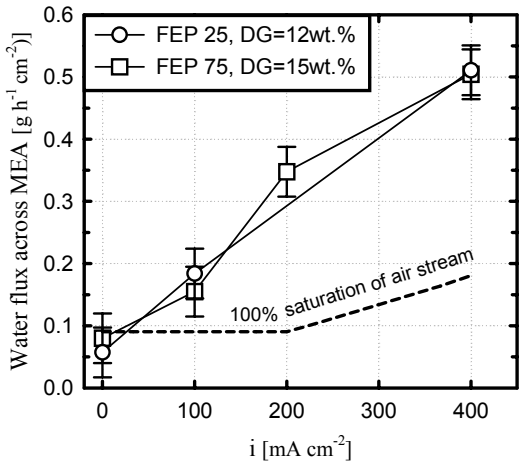

Figure 31 Water flux across two different FEP membranes under standard DMFC operating conditions at a cell temperature of 90°C and an aqueous methanol feed of 0.5 M. The dashed line refers to the amount of water fully saturated air stream can absorb at a pressure of 3 bar_{abs}. The air was fed humidified with water at 35°C to the cathode.

At OCV, water crossover to the cathode occurs only due to a concentration gradient. Therefore, a thicker membrane should decrease the amount of water permeating across the membrane. However, the membrane's thickness is probably not the parameter which limits the water flux across the membrane at OCV. Even a five time higher airflow at

OCV resulted in higher but still similar water fluxes across both membranes (data not shown) and corresponded again well with the amount of water absorbed by a fully saturated air stream. Therefore, either the structure of the cathode electrode limits the water flux across the membrane or the interface membrane/electrode may regulate the water flux.[†] The latter may be similar for both membrane types because of similar DC and DG of the membranes. However, because both explanations are possible, the similar water fluxes cannot be attributed solely to either of the two explanations described before at the current state of knowledge.

Long-term experience with PSI-membranes

All observations discussed so far in this chapter were based on short-term cell investigations, *i.e.*, an operation time of about 80 hours per cell test. The long-term behavior of the components used here at cell temperatures in the range from 90 to 110°C is unknown. Therefore, a long-term test of a MEA based on a FEP 25 membrane (DG = 12wt.%, low DC) was initiated to explore the potential lifetime of the components used here. The cell was operated continuously for almost 600 hours (about 150 hours at 90°C and 450 hours at 110°C) at a constant cell voltage of 0.3 V. At different operating times current-voltage curves were taken as a measure for the cell performance (see Figure 32a). In addition, the membrane resistivity was measured (Figure 32b) to unveil membrane degradation.

The first polarization curve measured at a cell temperature of 110°C (operating time: 50 hours) serves as a standard for subsequent current-voltage curves. This standard is given in Figure 32a (round data points) together with two polarization curves measured at runtimes of 170 and 540 hours, respectively. Unfortunately, the cell was operated twice for about an hour at a cell temperature of 150°C in the period between 70 and 150 hours of runtime. As a consequence, the polarization characteristics measured at a runtime of 170 hours (triangles in Figure 32a) is slightly (10 to 20 mV) shifted to lower cell

[†] Please note, the different methanol fluxes across these membranes are not contradictory, because the methanol is oxidized at the interface membrane/cathode electrode and thus the structure of the cathode electrode does not play a role for the methanol crossover.

voltage at the same current density as seen in Figure 32a by comparison of the current-voltage curves measured at 50 and 170 hours.

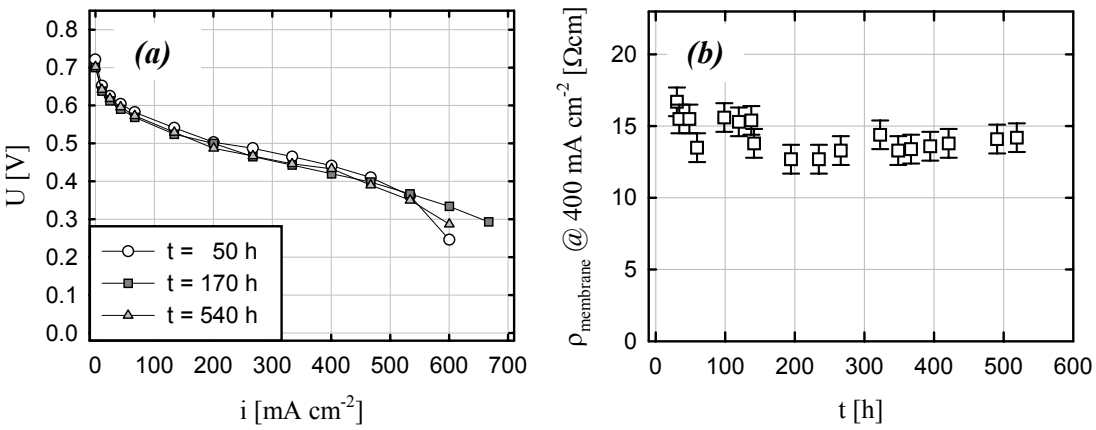

Figure 32: 600 hours test of a cell with a FEP 25 based MEA (DG = 12 wt.%, low DC); ***(a)*** polarization curves recorded at various operation times at a cell temperature of 110°C ***(b)*** membrane resistivity as function of runtime at 400 mA cm^{-2}. The cell was operated exclusively on a 0.5 M aqueous methanol solution and standard operating conditions (see p. 97).

Interestingly, the membrane seems to be unaffected by this harsh temperature treatment as illustrated (Figure 32b). The lowest membrane resistivity within the first 100 hours of runtime in Figure 32b was measured at a cell temperature of 110°C and is essentially the same as measured, *e.g.*, at a runtime of 200 hours. Therefore, the slight deterioration of the polarization curves could be attributed to losses of the catalyst activity. Fortunately, a further cell degradation cannot be observed within the time frame of this long-term study as seen in Figure 32a by the almost identical current-voltage curves at 170 and 540 hours. Furthermore, a significant change of the membrane resistivity with time (Figure 32b) cannot be observed either.

This study demonstrated nicely the potential lifetime of FEP membranes under DMFC operating conditions (150 hours at 90°C and 450 hours at 110°C). The losses in polarization characteristics were small and occurred within the first 200 hours of operation - most likely because of two thermal runaways. However, it should be emphasized at this point that this test has not been reproduced yet.

4.3 Summary

Radiation-grafted, cross-linked membranes were successfully short-term tested in the DMFC at 90, 100, and 110°C. In principle, similar polarization characteristics can be obtained by either of the three membrane types. Cell data of the fourth membrane type, the high cross-linked FEP 25 membrane, could not be shown here. Unfortunately, the brittleness of this membrane type prevented us from obtaining any cell data.

In the voltage region of interest (0.4 – 0.6 V), significant differences in the polarization characteristics could not be achieved for MEA's based on FEP membranes. Nevertheless, the variation of the membrane properties affects considerably the methanol crossover. Only minor methanol retention can be realized by increased cross-linking of the membrane. However, an increased cross-linking of the membranes results in a lower reproducibility of the data and thus might be an indication for inhomogeneous membrane properties. Tripling the membrane's thickness, however, decreases significantly the methanol permeation. Therefore, the OCV of these membranes is considerably higher (around 40 mV) as seen by comparison of the current-voltage plots in Figure 26a and Figure 26b.

The potential lifetime of FEP 25 membranes (DG = 12 wt.%, low DC) was explored under DMFC operating conditions. Only minor degradation of the cell performance was found within 600 hours of operation (150 hours at 90°C and 450 hours at 110°C). The losses in polarization characteristics occurred mainly within the first 200 hours of operation - most likely because of two thermal runaways. However, this test has to be regarded as "feasibility study" as these results have not been reproduced yet.

A water drag coefficient of about two was found for a low cross-linked FEP 25 membrane with a DG of 12 wt% at 90°C and a 0.5 M aqueous methanol feed. The same value was also obtained for a low cross-linked FEP 75 membrane with a DG of 15 wt% under the same conditions. There are two possible explanations for this observation; either the cathode limits the water flux or the interfaces membrane / electrode regulate the transport of water to the cathode. Because both explanations are likely, the similar water fluxes cannot be attributed solely to either of the two explanations described before at the current state of knowledge.

The best overall cell efficiency of about 31% was found for a FEP 75 membrane with a DG of 15 wt% at an aqueous methanol feed of 0.5 M. Furthermore, FEP 75 membranes are superior in their overall cell efficiency to any FEP 25 membrane because of their low methanol losses to the cathode.

5 Comparison of FEP-Membranes with Nafion 117

In the following, the cell performance obtained for MEA's based on FEP membranes are compared with the cell data measured for MEA's based on Nafion 117 under the same operating conditions. Since MEA's based on FEP 75 membranes show comparable polarization characteristics to MEA's based on FEP 25 membranes but significantly lower methanol permeation, only FEP 75 membranes are compared to Nafion 117 in Figure 33. These data are given for a methanol concentration of 0.5 M because of the heavily increased methanol crossover at higher methanol concentrations for the Nafion as well as for the FEP membranes. This higher methanol crossover results in poor polarization characteristics at an air stoichiometry of two. For the same reason, the data are given at a cell temperature of 100°C in Figure 33 because at this cell temperature, the best compromise between methanol crossover and power density was found (cf. *Overall cell efficiencies* in section 4.2, p. 110).

Only the "extreme" examples of MEA's based on FEP 75 membranes (DG of 15 and 23 wt%) are included in Figure 33. The best polarization curves of FEP 75 membranes were obtained for the membrane with a DG=23 wt% with the disadvantage, however, of a high methanol permeation across the membrane (inset of Figure 26a). On the other side, the MEA's based on the FEP 75 membrane with a DG=15 wt% show a fair polarization characteristic but significantly reduced methanol crossover. For these reasons, the cell data of the MEA's based on these FEP 75 membranes were included in Figure 33 in addition to the Nafion data.

Fortunately, the MEA's based on FEP 75 membranes (DG=23 wt%, circles) can achieve the same polarization characteristics as MEA's based on Nafion 117 (gray triangles). However, the methanol permeation across the highly grafted FEP 75 membrane is only slightly reduced compared to the data obtained for Nafion 117 as shown in the inset of Figure 33. On the other hand, the polarization curve of the lower grafted FEP 75 membrane (DG=15 wt%) is about 20 mV below the polarization curve obtained for Nafion 117 at a current density of 200 mA cm^{-2}. However, the methanol flux across the low grafted FEP 75 membrane is only half of the methanol permeation

across the Nafion 117 at low current density. In addition, the water flux across the FEP 75 membrane is lower than for Nafion as depicted in Figure 34, and the ohmic resistances of both membranes are in the same range as shown in Figure 35. Therefore, the question arises why the polarization curve of the FEP 75 membrane with a DG of 15 wt% does not show a superior performance to the one of the Nafion 117 membrane.

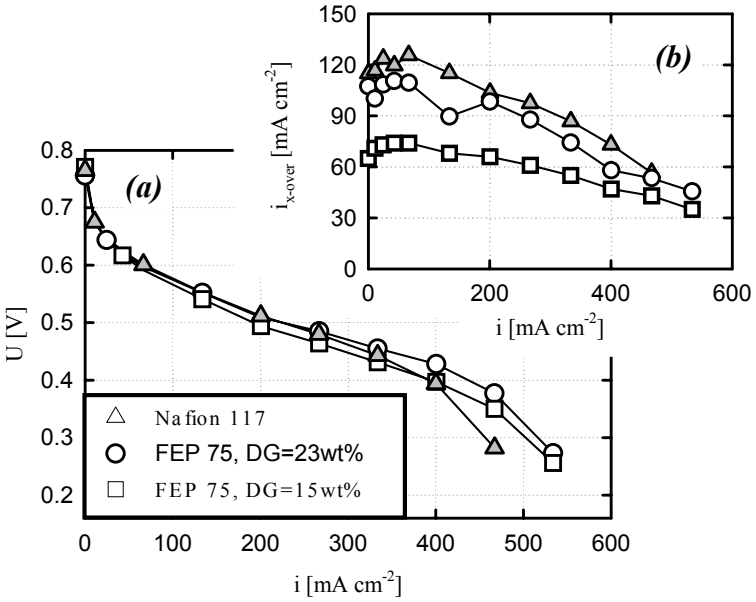

Figure 33: Comparison of cell performance data obtained for the best PSI-membranes with Nafion 117 under the same operating conditions; ***(a)*** polarization characteristics, ***(b)*** methanol leakage data. The data are given for a cell temperature of 100°C and a 0.5 M aqueous methanol fuel feed.

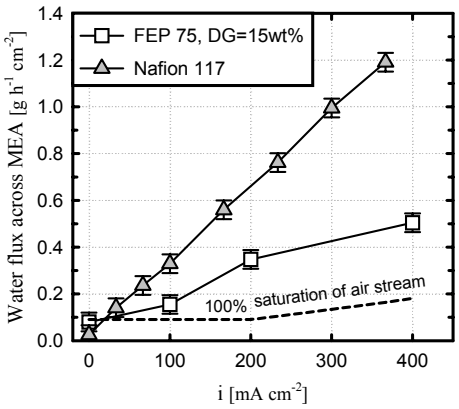

Figure 34: The water fluxes across FEP and Nafion membranes. The data are given at a cell temperature of 90°C, an aqueous methanol feed of 0.5 M, and an air stoichiometry of 2.

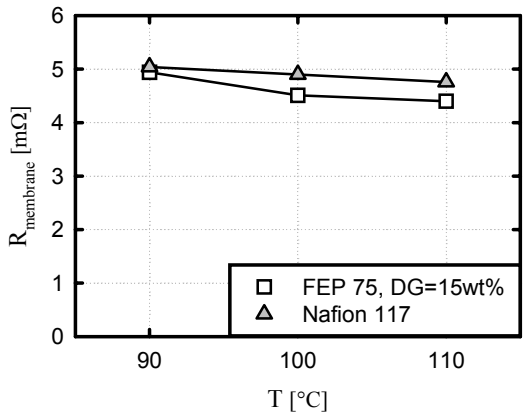

Figure 35: Membrane resistance of FEP and Nafion membranes determined *in situ* by current-pulse measurements.

Figure 36 may answer that question. The methanol concentration of the "permeate" was calculated from the water flux across the MEA as depicted in Figure 34 and from the methanol crossover as given in the inset of Figure 33. Except at very low current density, the methanol concentration of the "permeate" is essentially the same for both membranes as shown in Figure 36. Only at OCV and very low currents, the calculated methanol concentrations of the "permeates" differ for the Nafion and the FEP membrane, respectively. However, the experimental error is highest in this region and thus the strong deviation of the methanol concentration curves in this region may be not too meaningful.

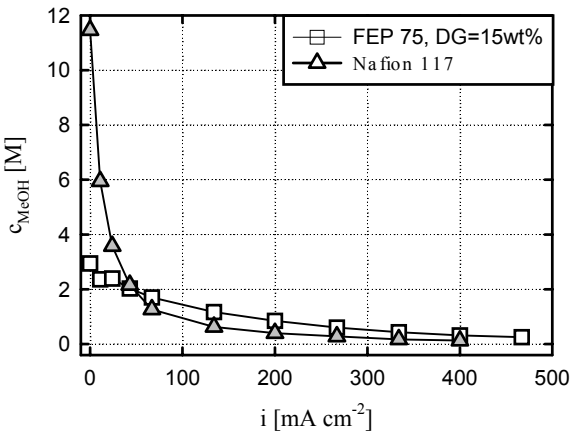

Figure 36: Methanol concentration of permeate as calculated from the CO_2 concentration of the effluent cathode stream and the water flux measurements. The data are valid for a methanol concentration of 0.5 M at the anode and a cell temperature of 90°C.

However, if the methanol concentration and not the absolute amount of "permeate" is the decisive factor for the mixed potential established at the cathode, which is suggested in reference [54], then the similar polarization characteristics measured for the FEP 75 membrane and the Nafion 117 can be explained. Similar has been concluded in the literature. Arico *et al.* [55] reported that the methanol present at the cathode causes only a minor Pt site-blocking effect besides establishing a mixed potential. A similar conclusion was drawn by Ren *et al.* [24] who suggested from the similarity of IR-corrected polarization curves of MEA's based on differently thick membranes (Nafion 112, 115, and 117) that the cathode is highly tolerant to variations in the methanol flux. Likewise, Küver *et al.* [56, 57] concluded that variations of the methanol flux across the membrane do not necessarily change the cathode depolarization. Therefore, Figure 36

may give a plausible explanation for the similarity of the polarization curves obtained for these membranes.

Cell efficiency

The relative insensitivity of the cathode to the methanol flux does not indicate, however, that the overall cell efficiency is unaffected. Therefore, the overall cell efficiency ($\eta_{overall}$) of both membrane types was calculated from Equation 1 (p. 110) and is given as function of the charge passed in Figure 37a. Generally, a higher overall cell efficiency is obtained for the low grafted FEP 75 membrane compared to Nafion 117. The highest overall cell efficiency of about 31% was obtained for the FEP 75 membrane at a current density around 270 mA cm^{-2}. However, the best overall cell efficiency of Nafion 117 is only two percentages below the one of the FEP 75 membrane. Nevertheless, the FEP 75 membrane has a clear advantage over the Nafion 117 membrane in the part load region as shown in Figure 37a. For a better understanding of the curve shape of the overall efficiencies, the trends of the voltage efficiency $\eta_{voltage}$ and the fuel efficiency η_{fuel} of the low grafted FEP 75 membrane and Nafion 117 are depicted in Figure 37b. From there, it is clear that the overall efficiency is mainly affected in the part load region by the fuel efficiency.

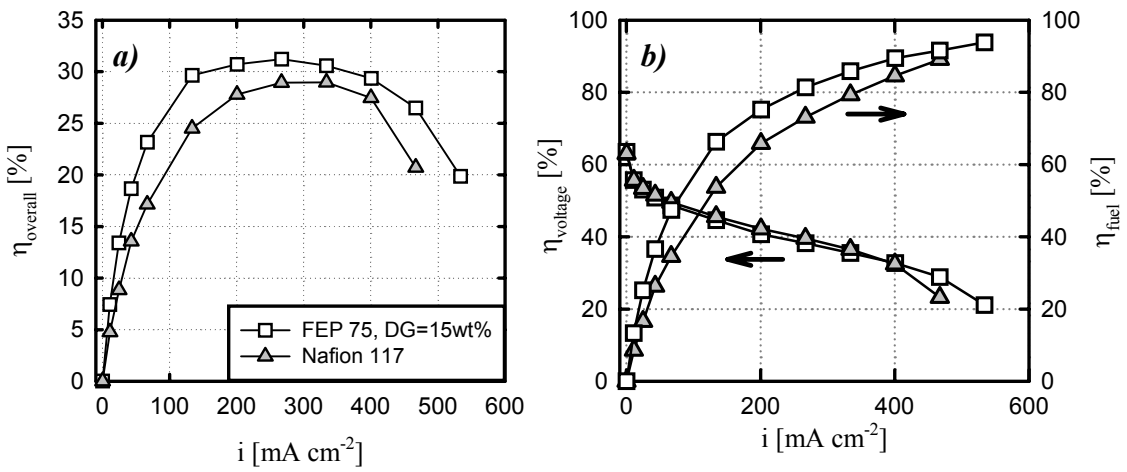

Figure 37: Calculated efficiencies from the cell data shown in Figure 33 for the FEP 75 membrane (S/DVB = 9:1, DG=15 wt%) and for Nafion 117 ***(a)*** overall DMFC efficiencies, ***(b)*** corresponding trends of voltage and fuel efficiency.

6 Conclusions

The cell tests based on Nafion membranes allowed assessing the behavior of the electrochemical components and the cell hardware under various operating conditions. The cell results obtained showed a reasonably good agreement with the cell data published. Moreover, the cell tests based on Nafion membranes pointed out the process variables with the most relevance to the polarization characteristic as well as to the methanol crossover. These parameters were the cell temperature and the methanol concentration of the anodic feed. A variation of the other process variables, such as air humidification, showed only a minor effect on the DMFC performance. Introducing a stoichiometric operation of the anodic fuel supply may make a significant improvement. However, maintaining a constant inlet temperature for the anodic feed was difficult with the current testing facilities.

The characterization study of radiation-grafted membranes revealed that similar polarization characteristics can be obtained by any of the three FEP based membrane types. Unfortunately, the brittleness of the fourth type, the highly cross-linked FEP 25 membrane, prevented us from obtaining any cell data for this membrane. In the voltage region of interest (0.4 – 0.6 V), huge differences in the polarization characteristics could not be achieved for MEA's based on FEP membranes. Nevertheless, the variation of the membrane properties affects the methanol crossover considerably. Only minor methanol retention can be realized by increased cross-linking of the membrane. In addition, the cell tests based on higher cross-linked membranes had a significantly lower reproducibility which might be an indication for inhomogeneous membrane properties. Tripling the membrane's thickness, however, decreased the methanol permeation significantly.

A comparison of MEA's based on Nafion 117 and on FEP 75 membranes showed under the same operating conditions that similar polarization characteristics can be achieved. Although the methanol and water flux across the FEP 75 membrane (DG=15 wt%) is decreased considerably (by about 50%) compared to Nafion 117, a similar methanol concentration of the "permeate" was calculated for the Nafion and the FEP 75 membrane. The latter could explain well the identical polarization characteristics of

both membranes. However, the overall cell efficiency of MEA's based on the FEP 75 membrane (DG=15 wt%) is higher in the part load region than data obtained from MEA's based on Nafion 117. Furthermore, the effect of the methanol crossover on the overall efficiency was highlighted and finally, an overall efficiency of roughly 31% was shown for MEA's based on the FEP 75 membrane with a DG=15 wt%.

Based on this extensive characterization study, it seems that the methanol concentration could be the decisive factor for the depolarization of the cathode and not the absolute amount of permeate. Furthermore, it appears that the water and methanol flux across the membrane are coupled, which results in similar methanol concentrations of the "permeate" for different membranes. Then, the depolarization of the cathode is the same, even for membranes with minimized methanol flux. However, if the ratio of methanol to water flux is fixed, it will be difficult to minimize the mixed potential established at the cathode of a DMFC by membranes of similar proton conductivity mechanism to Nafion. Nevertheless, the membrane does influence the water flux to the cathode and can minimize the losses of methanol to the cathode.

7 Outlook

The challenges in realization of the DMFC are numerous and highly interconnected. Many new interesting subjects arose in the course of this study and may serve as guides for future work. As demonstrated, advances in the DMFC may be approached on very different areas. Therefore, future studies should be also concerned with work on a wide basis, which may include the following issues.

Surely, the water permeation mechanism of PSI-membranes deserves further attention. The issues that could be addressed are:

(i) What does limit the water flux across the membrane and

(ii) how does the DG or the DC affect the water permeation.

Presumably, the development and validation of ex situ measurements of water and methanol flux across a membrane would be of great help for precise characterization of the membrane's properties.

This study showed clearly that thick membranes are advantageous for use in the DMFC. Therefore, even thicker membranes than FEP 75 should be investigated. Furthermore, it may be of interest to explore the potential of PSI-membranes at low operating temperature. The latter would be required for most applications in the mobile sector.

Furthermore, the effect of the electrode structure on the water flux and the methanol permeation across the membrane would be worth studying. The effect of the PTFE content of the backing, its porosity, and the amount of pore filler on the liquid / gas flux on the one hand and on the ohmic resistance on the other hand is surely an interesting research field of high potential. Eventually, the methanol crossover to the cathode can be diminished by the structure, porosity, and hydrophobicity of the anode electrode. In contrast, the cathode electrode may be designed to ease the flooding of the electrode or to prevent the permeation of excessive amounts of water.

In section 4.2 (*Medium cross-linked FEP 25 membranes*), a method to estimate methanol crossover data from the airflow was discussed in short. In practice, this

method would be of great help because the validation of methanol crossover data would be possible. Furthermore, it would allow to estimate the methanol crossover even if other measuring instruments are not available.

This work has illustrated that the operating conditions have great impact on the DMFC performance. Because the supply of a liquid at variable flow rates but at constant temperature makes high demands on the dynamics of the heater, the impact of the methanol stoichiometry on the DMFC performance has been mostly forgotten in the literature. Therefore, it would be worth exploring the potential of the methanol stoichiometry. First results indicated that a stoichiometric operation of the methanol flow reduces the methanol crossover but results in a somewhat limited polarization curve in the high current density range.

8 References

[1] H. Schmidt, P. Buchner, A. Datz, K. Dennerlein, S. Lang, and M. Waidhas, "Low-cost air-cooled PEFC stacks", J. Pow. Sources **105** (2002) 141-147.

[2] Won Choon Choi, Ju Dam Kim, and Seong Ihl Woo, "Modification of proton conducting membrane for reducing methanol crossover in a direct methanol fuel cell", J. Pow. Sources **96** (2001) 411-414.

[3] C. Pu, W. Huang, K.L. Ley, and E.S. Smotkin, "A Methanol Impermeable Proton Conducting Composite Electrolyte System", J. Electrochem. Soc. **142** (1995) L119-L120.

[4] S.R. Yoon, G.H. Hwang, W.I. Cho, I.-H. Oh, S.-A. Hong, and H.Y. Ha, "Modification of polymer electrolyte membranes for DMFCs using Pd films formed by sputtering", J. Pow. Sources **106** (2002) 215-223.

[5] V. Tricoli, "Proton and Methanol Transport in Poly(perfluorosulfonate) Membranes Containing Cs^+ and H^+ Cations", J. Electrochem. Soc. **145** (1998) 3798-3801.

[6] N. Jia, M.C. Lefebvre, J. Halfyard, Z. Qi, and P.G. Pickup, "Modification of Nafion Proton Exchange Membranes to Reduce Methanol Crossover in PEM Fuel Cells", Electrochemical and Solid-State Letters **3** (2000) 529-531.

[7] A.S. Aricò, P. Cretì, P.L. Anonucci, and V. Antonucci, "Comparison of Ethanol and Methanol Oxidation in a Liquid-Feed Solid Polymer Electrolyte Fuel Cell at High Temperature", Electrochemical and Solid-State Letters **1** (1998) 66-68.

[8] P. L. Antonucci, A. S. Aricò, P. Cretì, E. Ramunni, and V. Antonucci, "Investigation of a direct methanol fuel cell based on a composite Nafion(R)-silica electrolyte for high temperature operation", Solid State Ionics **125** (1999) 431-437.

[9] P. Dimitrova, K.A. Friedrich, U. Stimming, and B. Vogt, "Recast Nafion-Based Membranes for Direct Methanol Fuel Cells", in: *Proc. First European Fuel Cell Forum*, Ed. by Felix N. Buechi, Guenther G. Scherer, and Alexander Wokaun, Lucerne, Switzerland, 2 - 6 July (2001) 97-107.

[10] L. Jörissen, V. Gogel, J. Kerres, and J. Garche, "New membranes for direct methanol fuel cells", J. Pow. Sources **105** (2002) 165-171.

[11] Jochen Kerres, Andreas Ullrich, Frank Meier, and Thomas Haring, "Synthesis and characterization of novel acid-base polymer blends for application in membrane fuel cells", Solid State Ionics **125** (1999) 243-249.

[12] Z. Poltarzewski, W. Wieczorek, J. Przyluski, and V. Antonucci, "Novel proton conducting composite electrolytes for application in methanol fuel cells", Solid State Ionics **119** (1999) 301-304.

[13] J.-T. Wang, J.S. Wainright, R.F. Savinell, and M. Litt, "A direct methanol fuel cell using acid-doped polybenzimidazole as polymer electrolyte", J. Appl. Electrochem. **26** (1996) 751-756.

[14] J.-T. Wang, S. Wasmus, and R.F. Savinell, "Real Time Mass Spectrometric Study of the Methanol Crossover in a Direct Methanol Fuel Cell", J. Electrochem. Soc. **143** (1996) 1233-1239.

[15] R. Savinell, E. Yeager, D. Tryk, U. Landau, J. Wainright, D. Weng, K. Lux, M. Litt, and C. Rogers, "A Polymer Electrolyte for Operation at Temperatures up to 200°C", J. Electrochem. Soc. **141** (1994) L46-L48.

[16] J.S. Wainright, J.-T. Wang, D. Weng, R.F. Savinell, and M. Litt, "Acid-Doped Polybenzimidazoles: A New Polymer Electrolyte", J. Electrochem. Soc. **142** (1995) L121-L123.

[17] K. Scott, W.M. Taama, and P. Argyropoulos, "Performance of the direct methanol fuel cell with radiation-grafted polymer membranes", J. Mem. Sci. **171** (2000) 119-130.

[18] B. Gupta, and G.G. Scherer, "Proton Exchange Membranes by Radiation-Induced Graft Copolymerization of Monomers into *Teflon*-FEP Films", Chimica **48** (1994) 127-137.

[19] H-P. Brack, and G.G. Scherer, "Modification and Characterization of Thin Polymer Films for Electrochemical Applications", Macromol. Symp. **126** (1997) 25-49.

[20] A.S. Aricò, P. Cretì, V. Baglio, E. Modica, and V. Antonucci, "Influence of flow field design on the performance of a direct methanol fuel cell", J. Pow. Sources **91** (2000) 202-209.

[21] K. Scott, P. Argyropoulos, P. Yiannopoulos, and W.M. Taama, "Electrochemical and gas evolution characteristics of direct methanol fuel cells with stainless steel mesh flow beds", J. Appl. Electrochem. **31** (2001) 823-832.

[22] K. Scott, W.M. Taama, and P. Argyropoulos, "Material aspects of the liquid feed direct methanol fuel cell", J. Appl. Electrochem. **28** (1998) 1389-1397.

[23] S. Gottesfeld, S.J.C. Cleghorn, X. Ren, T.E. Springer, M.S. Wilson, and T.A. Zawodzinski, "Polymer electrolyte direct methanol fuel cells: an option for transportation applications", Fuel Cell Seminar, Extended Abstract, November 17-20 (1996) 521-524.

[24] X. Ren, M.S. Wilson, and S. Gottesfeld, "High Performance Direct Methanol Polymer Electrolyte Fuel Cells", J. Electrochem. Soc. **143** (1996) L12 - L15.

[25] X. Ren, M.S. Wilson, and S. Gottesfeld, "On direct and indirect methanol fuel cells for transportation applications", in: *Proc. First International Symposium on Proton Conducting Membrane Fuel Cells I*, Ed. by S. Gottesfeld, G. Halpert, and A. Landgrebe, Chicago, IL, USA, PV 95-23 (1995) 252-260.

[26] A.B. Geiger, J. Newman, and J.M. Prausnitz, "Phase Equilibria for Water-Methanol Mixtures in Perfluorosulfonic-Acid Membranes", AIChE J. **47** (2001) 445-452.

[27] M. Hogarth, P. Christensen, A. Hamnett, and A. Shukla, "The design and construction of high-performance direct methanol fuel cells. 2. Vapour-feed systems", J. Pow. Sources **69** (1997) 125-136.

[28] M. Hogarth, P. Christensen, A. Hamnett, and A. Shukla, "The design and construction of high performance direct methanol fuel cells. 1. Liquid-feed systems", J. Pow. Sources **69** (1997) 113-124.

[29] F.N. Büchi, A. Marek, and G.G. Scherer, "*In situ* Membrane Resistance Measurements in Polymer Electrolyte Fuel Cells by Fast Auxialiary Current Pulses", J. Electrochem. Soc. **142** (1995) 1895-1902.

[30] D.L. Maricle, B.L. Murach, and L.L. van Dine, "Direct Methanol Fuel Cell Stack Development", in: *Proc. Spring Meeting of the Electrochemical Society Extended Abstracts*, Ed. by The Electrochemical Society, San Francisco, CA, USA, (1994) abstract 35.

[31] S.R. Narayanan, H. Frank, B. Jeffries-Nakamura, M. Smart, W. Chun, and G. Halpert, "Studies on Methanol Crossover in liquid-feed direct methanol PEM fuel cells", in: *Proc. Proton Conducting Membrane Fuel Cells I*, Ed. by S. Gottesfeld, G. Halpert, and A. Landgrebe, Chicaga, IL, USA, PV 95-23 (1995) 278-283.

[32] X. Ren, T.A. Zawodzinski Jr., F. Uribe, H. Dai, and S. Gottesfeld, "Methanol Cross-over in Direct Methanol Fuel Cells", in: *Proc. Proton Conducting Membrane Fuel Cells, 1*, Ed. by S. Gottesfeld, G. Halpert, and A. Landgrebe, Chicago, IL, USA, PV 95-23 (1995) 284-298.

[33] A.S. Aricò, S. Srinivasan, and V. Antonucci, "DMFCs: From Fundamental Aspects to Technology Development", Fuel Cells **1** (2001) 133-161.

[34] P. Scharlin, contributors: R.W. Cargill, J.J. Carroll, H. Lawrence Clever, R. Crovetto, J.Chr. Gjaldbaek, I. Labádi, D.M. Mason, A.E. Mather, K.R. Thornton, T. Tominaga, D.A. Wiesenburg, Y.P. Yampol'skii, and C.L. Young, Carbon Dioxide Solubilities in Water and Aqueous Electrolyte Solutions (IUPAC Solubility Data Series), Oxford University Press, Oxford, 1996.

[35] X. Ren, W. Henderson, and S. Gottesfeld, "Electro-osmotic Drag of Water in Ionomeric Membranes: New Measurements Employing a Direct Methanol Fuel Cell", J. Electrochem. Soc. **144** (1997) L267-L270.

[36] G. Luft, K. Mund, K. Pantel, G. Starbeck, and M. Waidhas, "Construction of a Direct Methanol Fuel Cell Stack", Final Report, JOUE - CT91 - 0074, 31.05.1993, Siemens AG, Corporate Research and Development, Erlangen, Germany 1993.

[37] M. Baldauf, and W. Preidel, "Experimental results on the direct electrochemical oxidation of methanol in PEM fuel cells", J. Appl. Electrochem. **31** (2001) 781-786.

[38] W. Grot, "Perfluorierte Ionenaustauscher-Membrane von hoher chemischer und thermischer Stabilität", Chem. -Ing. -Techn. **44** (1972) 167-169.

[39] R.S. Yeo, "Dual cohesive energy densities of perfluorosulphonic acid (Nafion) membrane", Polymer **21** (1980) 432-435.

[40] W. Grot, "Use of Nafion Perfluorosulfonic Acid Products as Separators in Electrolytic Cells", Chem. -Ing. -Techn. **50** (1978) 299-301.

[41] S.C. Yeo, and A. Eisenberg, "Physical properties and supermolecular structure of perfluorinated ion-containing (Nafion) polymers", J. Appl. Pol. Sci. **21** (1977) 875-898.

[42] T.D. Gierke, G.E. Munn, and F.C. Wilson, "The Morphology in Nafion Perfluorinated Membrane Products, as Determined by Wide- and Small-Angle X-Ray Studies", J. Pol. Sci. **19** (1981) 1687-1704.

[43] J. Halim, F.N. Büchi, O. Haas, M. Stamm, and G.G. Scherer, "Characterization of Perfluorosulfonic Acid Membranes by Conductivity Measurements and Small-Angle X-ray Scattering", Electrochim. Acta **39** (1994) 1303-1307.

[44] D. Nandan, H. Mohan, and R.M. Iyer, "Methanol and Water Uptake, Densities, Equivalental Volumes and Thicknesses of Several Uni- and Divalent Ionic Perfluorosulphonate Exchange Membranes (Nafion-117) and their Methanol-Water Fractionation Behaviour at 298 K", J. Mem. Sci. **71** (1992) 69-80.

[45] J.T. Hinatsu, M. Mizuhata, and H. Takenaka, "Water Uptake of Perfluorosulfonic Acid Membranes from Liquid Water and Water Vapor", J. Electrochem. Soc. **141** (1994) 1493-1498.

[46] S.R. Narayanan, T.I. Valdez, and W. Chun, "Design and Operation of an Electrochemical Methanol Concentration Sensor for Direct Methanol Fuel Cell Systems", Electrochemical and Solid-State Letters **3** (2000) 117-120.

[47] S.R. Narayanan, A. Kindler, B. Jeffries-Nakamura, W. Chun, H. Frank, M. Smart, S. Surampudi, and G. Halpert, "Performance of PEM Liquid-Feed Direct Methanol-Air Fuel Cells", in: *Proc. Proton Conducting Membrane Fuel Cells I*, Ed. by S. Gottesfeld, G. Halpert, and A. Landgrebe, (1995) 261-266.

[48] T. Valdez, and S. Narayanan, "Recent Studies on Methanol Crossover in Liquid-Feed Direct Methanol Fuel Cells", in: *Proc. Second International Symposium on Proton Conducting Membrane Fuel Cells II*, Ed. by S. Gottesfeld, and T.F. Fuller, Boston, USA, November 1-6 (1998) 380-387.

[49] H. Dohle, J. Divisek, J. Mergel, H.F. Oetjen, C. Zingler, and D. Stolten, "Recent developments of the measurement of the methanol permeation in a direct methanol fuel cell", J. Pow. Sources **105** (2002) 274-282.

[50] H. Dohle, "Entwicklung und Modellierung von Direkt-Methanol-Brennstoffzellen", Forschungszentrum Jülich, Dissertation, 2000.

[51] G.G. Scherer, F.N. Büchi, and B. Gupta, EP667983, Paul Scherrer Institut, CH, 1993.

[52] L. Gubler, "Operating Polymer Electrolyte Fuel Cells with Reformed Fuel", ETH Zurich, Dissertation, *Diss ETH No. 13954*, 2001.

[53] T. Rager, Paul Scherrer Institut, Villigen, Switzerland, unpublished results, 2002.

[54] C. Lamy, J-M. Léger, and S. Srinivasan, "Direct Methanol Fuel Cells: From a Twentieth Century Electrochemist's Dream to a Twenty-first Century Emerging Technology", in *Modern Aspects of Electrochemistry*, Ed. by J.O'M. Bockris, B.E. Conway, and R.E. White, Kluwer Academic / Plenum Publishers, New York (2001) 53-118.

[55] A.S. Aricò, V. Antonucci, V. Alderucci, E. Modica, and N. Giordano, "A.C.-Impedance Spectroscopy Study of Oxygen Reduction at Nafion(R) Coated Gas-Diffusion Electrodes in Sulfuric-Acid - Teflon Loading and Methanol Cross-over Effects", J. Appl. Electrochem. **23** (1993) 1107-1116.

[56] A. Küver, and K. Potje-Kamloth, "Comperative study of methanol crossover across electropolymerized and commercial proton exchange membrane electrolytes for the acid direct methanol fuel cell", Electrochim. Acta **43** (1998) 2527-2535.

[57] A. Küver, and W. Vielstich, "Investigation of methanol crossover and single electrode performance during PEMDMFC operation A study using a solid polymer electrolyte membrane fuel cell system", J. Pow. Sources **74** (1998) 211-218.

Chapter V

Characterizing Mass Transfer Phenomena

1 INTRODUCTION 133

2 *IN SITU* VISUALIZATION 135

2.1 Introduction 135

2.2 Experimental 136

2.3 Investigation of Two-phase Flows in DMFC's 146

2.4 Present Limitations 158

2.5 Conclusions & Outlook 159

3 CURRENT DISTRIBUTION IN THE DMFC 161

3.1 Introduction 161

3.2 Technology of Measurement 162

3.3 The effect of operating conditions on the CD of a DMFC 170

3.4 Conclusions 177

3.5 Outlook 178

4 COMBINATION OF *IN SITU* METHODS 182

4.1 Introduction 182

4.2 Experimental 182

4.3 Results & Discussion 186

4.4 Conclusions and Outlook 191

5 CONCLUSIONS ON DMFC CELL DESIGN 193

6 REFERENCES 195

1 Introduction

Direct methanol fuel cells (DMFC's) have recently attracted renewed attention because a complex fuel processing as it is required for reformate-fuelled PEFC's can be avoided and maintaining an adequate water content of the membrane is intrinsincally given. Thus, humidifaction problems of vapor-feed PEFC systems can be circumvented. Their operating temperature in the range between room temperature to 130°C suits this type of fuel cell particularly well for portable power sources and vehicular applications. Despite the appealing simplicity of a DMFC system (see just before), however, the electrochemical conversion of an alcohol of low molecular weight with oxygen to carbon dioxide and water is demanding [1]. In addition to the hassles of the electrochemical oxidation of methanol and the higher demands on the polymer electrolyte (cf. *Chapter IV*), a gas-liquid two-phase flow has to be managed on the anode side *and* on the cathode side of a DMFC (see discussion later in this chapter).

On the oxidation of methanol, the reaction product is carbon dioxide, which is evolved as a gas in the cell leading to a two-phase flow at the anode. On the cathode side, the two-phase flow develops from liquid water as reaction product and air as oxidant. Water droplets may accumulate within a channel of the flow field and flood it partly, thus blocking the channel from the supply with air. In addition, the supply of a liquid fuel at the anode leads to a higher swelling of the membrane of a DMFC. Therefore, excessive amounts of water are transported across the membrane to the cathode by diffusion and electro-osmosis, presumably making the water removal at the cathode of a DMFC even more important than in a H_2-fuel cell [2].

Surprisingly, little attention has been paid to the degree and the effect of two-phase flows on the performance of a DMFC up to the present. In general, processes occurring at gas-evolving electrodes differ significantly from those taking place at electrodes without gas evolution. On the anode, gas bubbles within the electrode superimpose physical processes, such as micro convection or mass transport limitations, to the electrochemical processes and thus interfere with the operation of the electrode. On the one hand, gas bubbles shield the active sites from the supply of reactants. However, the

growth of gas clusters at the boundary layer, on the other hand, may also cause a beneficial micro flow in the electrode, which enhances the transport of reactants to the electrochemical active sites [3]. Furthermore, large amounts of carbon dioxide may accumulate in the channels of the flow field and may hinder the supply of reactants to the electrochemically active area already in the flow field [4-6].

The effect of the degree of bubble coverage on the operation of electrolyzers has been extensively studied in the past, *e.g.*, [7-10]. However, these studies apply only in part on the operation of DMFC's. In the DMFC, adhering gas bubbles only affect the supply of reactants to the active sites but do not prevent the catalyst from contact with the solid polymer electrolyte. Therefore, gas-covered electrode surfaces of DMFC's are still electrochemically active but are limited by mass transport in contrast to systems with liquid electrolytes which are adversely affected by mass transport and variation in the ohmic resistance of the electrolyte. Unfortunately, the impact of the two-phase flow on the performance of a DMFC cannot be easily assessed with standard electrochemical methods, *e.g.*, polarization curves. Therefore, a thorough investigation of this rather complex system asks for additional "real-time" and *in situ* methods to give a better understanding of mass transport related phenomena in DMFC's.

In the following, two novel *in situ* methods will be presented, which allow to characterize the mass transfer in DMFC's in detail. The first gives visual information about the gas-liquid distribution in the flow channels and allows to observe the accumulation of gas clusters in the flow field of a DMFC. This method will be introduced in section 2 where the principle of measurement and the experimental setup will be explained. In the experimental part of this section, the effect of operating conditions, such as flow rate and flow direction, on the carbon dioxide distribution will be discussed. The second *in situ* method, which is introduced in section 3, allows the "real-time" mapping of the current distribution (CD) over the entire electrode area. The effect of the operating conditions, *e.g.*, air stoichiometry, on the CD will be outlined within this section. In the following section, the combination of these two *in situ* methods will be highlighted and first results of these measurements will be given. At last, this chapter will conclude with a summary and interesting areas for future work will be addressed.

2 *In situ* Visualization

2.1 Introduction

Optimized mass transport in the flow field channels (anodic and cathodic) of a bipolar plate is an important electrochemical engineering issue. On one side the supply of reactants (fuel and oxidant) across the active area of the cell has to be considered to ensure a most homogeneous current density and temperature distribution. On the other side an optimal pressure drop along the flow field has to be utilized to remove reaction products, *i.e.*, water at the cathode side or CO_2 at the anode side of a DMFC, and at the same time it has to allow minimal power losses in the auxiliary mass flow components, such as pumps or compressors.

However, the two-phase distribution in the flow channels cannot be easily measured and depends on the interaction of numerous parameters, such as flow field and electrode design, material properties, and operating conditions. Because of this rather complex system, visual information of the reactant / product distribution in the flow field is highly desirable to obtain during the operation of the DMFC to optimize the mass transport in the flow field.

In the past, various strategies have been followed to visualize *in situ* two-phase flows. An ultrasonic doppler method was used by Hilgert [11] to characterize the gas flow in a bubble column. However, the spatial resolution of this method is too low to resolve the two-phase distribution occurring in filigree structures such as flow fields. Others employed optical methods such as high-speed camera systems to investigate two-phase flows [3-6]. While the latter have clear advantages in simplicity and spatial / temporal resolution, the optical methods have the disadvantage that the cell has to be modified to allow optical access. However, this modification can affect, for instance, the current distribution across the electrode and thus may result in unwanted feedbacks on the two-phase distribution in the flow channels as was reported by Argyropoulos *et al.* [4].

A different approach to access *in situ* the two-phase distribution in a DMFC is neutron radiography. As described below, neutron radiography is well suited to visualize the

two-phase flow of a gas and a liquid *in situ* and in "real time". In the past, this method was already applied in fuel cell research by Bellows *et al.* [12] to determine the water gradient across the polymer electrolyte in an operating H_2-fuel cell. According to their studies, the water diffusivity in the membrane may be higher than commonly assumed. Others used neutron radiography to determine either the gas velocity [13] or the void fraction in various media and applications, *e.g.*, [14-16].

Within this section, the principle of measurement will be explained, the various detector systems available introduced and the experimental setup described. In the experimental part, the consequences of the flow direction and the flow rate on the gas-liquid distribution in anodic flow fields of a DMFC will be addressed. At the end, the current limitations of this method will be outlined, further improvements discussed, and an outlook for future investigations will be given. In addition, the experimental observations will be summarized and their impact on DMFC systems will be considered.

2.2 Experimental

Principle of measurement

In principle, neutron transmission radiography is similar to X-ray radiography, and is complementary to the nature of information supplied. However, the interaction mechanisms of neutrons and X-rays with matter are significantly different. While X-rays interact with the electron cloud surrounding the nucleus of an atom, neutrons interact with the nucleus itself. Therefore, neutrons are particularly sensitive to some light elements (*e.g.*, hydrogen) that have a much higher interaction probability with neutrons than with X-rays. In contrast, the interaction probability of neutrons with metals is comparatively lower and thus allows quite high penetration depths into the material. A general overview of the mass attenuation coefficients of thermal neutrons, low energetic and high-energetic X-rays is given in Figure 1 for various elements.

In general, three different processes can occur if neutrons interact with matter:

(i) Neutrons can get *absorbed*, *i.e.*, the intensity of the neutron beam is reduced but its direction remains unchanged.

(ii) A *scattering* of the neutron beam can occur, *i.e.*, its intensity as well as its direction of the neutron beam is changed.

(iii) Neutrons can only be *refracted*.

The mass attenuation coefficient as plotted in Figure 1 summarizes all these processes and gives a measure for the reduction of the flux density by a specific element.

The combination of high sensitivity to hydrogen and the relatively low neutron attenuation of metals, as seen in Figure 1, goes very well with the materials used in polymer electrolyte fuel cells (PEFC's). Because thermal neutrons are used, which have very low energy (2 - 100 meV), negative effects such as damages of the electrochemical components can be avoided. In addition, the experimental setup of the neutron radiography is analogous to the X-ray radiography and thus allows the investigation of large samples. Therefore, neutron radiography is an *in situ* method of high potential for the fuel cell research.

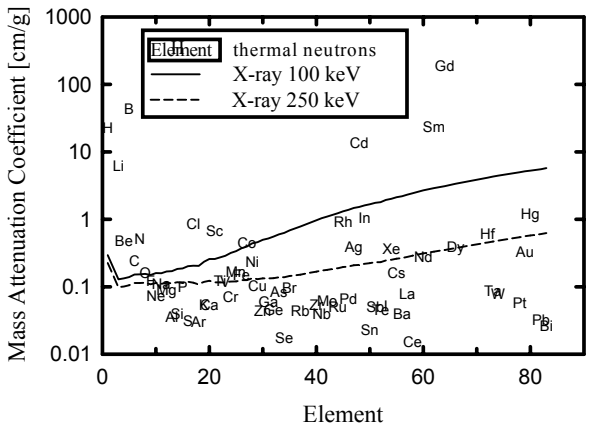

Figure 1: Comparison of the attenuation coefficients of X-rays [17] with the attenuation coefficients of thermal neutrons at various elements [18].

Figure 2 shows the principle of the neutron radiography. The neutron beam is guided by a collimator to the fuel cell, attenuated by the elements with high neutron attenuation coefficients and finally, the transmitted neutrons are collected by a detector system. The result is a two-dimensional image of the object with light areas indicating sections of lowest neutron attenuation. The dark areas show regions of highest neutron attenuation.

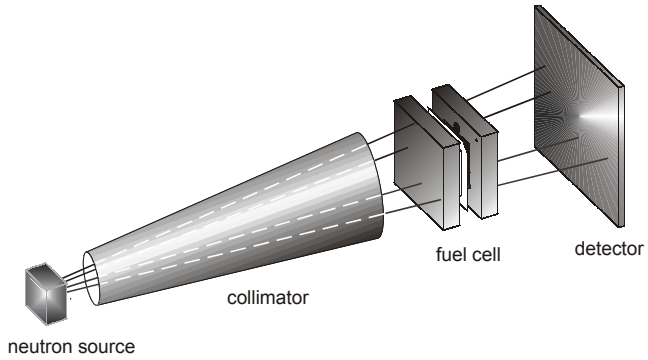

Figure 2: The principle of measurement of neutron radiography.

Experimental setup at the neutron source

The fuel cells were investigated at the neutron radiography facility (NEUTRA) of the Paul Scherrer Institut (PSI). A schematic diagram including the outer dimensions of the experimental setup at NEUTRA is shown in Figure 3. The whole radiography facility is contained in a heavy concrete shielding that encloses an area of 2.2 by 2.5 m^2 for the setup of the radiography measurements. A fuel cell test bench was placed next to the sample holder (indicated in Figure 3 as position 2) to operate the fuel cell under controlled conditions. Both the CCD-camera system as well as the fuel cell test bench were remotely controlled from the outside. Fortunately, the useful beam diameter is large (Ø 35 cm) and thus allows the investigation of fuel cells of technical interest.

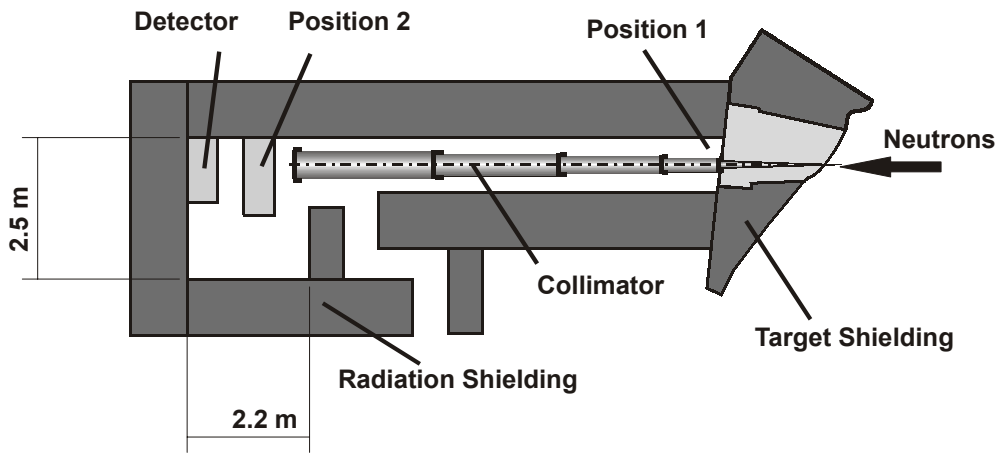

Figure 3: Experimental setup at NEUTRA. A neutron beam is extracted from the neutron source (not shown) and guided in a collimator to one of the two measuring stations (position 1 or 2). The schematic illustrates the experimental setup for measurements at position 2. The entire area is enclosed in a radiation shielding for safety.

In general, experiments can be performed at two different positions in the beam line as illustrated in Figure 3.† Position 1 is the closest to the target block and thus has the highest specific neutron flux but also the highest divergence of the beam. The latter is described by the L/D-ratio, where L is the distance between the point of measurement to the orifice of the beam and D is the diameter of the orifice (about 2 cm). The second position is located at the end of the collimator. Therefore, this position features a quasi-parallel beam with the detriment of a lower specific neutron flux. Table 1 summarizes some properties in addition to the assets and drawbacks of both positions.

Table 1: Pros and cons of the two different measuring position available at NEUTRA. The neutron flux is normalized to a proton beam of 1 mA strength [19].

	Position 1	Position 2
+	• Highest neutron flux ($1.6\ 10^{7}$ cm^{-2} s^{-1} mA^{-1})	• Relatively spacious • Quasi-parallel beam (L/D = 550) • Lowest gamma background
–	• Very limited amount of space • Divergent beam (L/D = 200) • Higher gamma background	• Lower neutron flux ($3\ 10^{6}$ cm^{-2} s^{-1} mA^{-1})

Unfortunately, both positions have their drawbacks (see Table 1). While position 1 allows shorter exposure times because of its higher neutron flux, position 2 has the better image quality (larger L/D-ratio). Furthermore, position 2 facilitates the installation of a bulky experimental setup inside the shielded area. In the following, measurements performed at both positions are shown and their profit and loss for visualization of two-phase flows are discussed.

Detector systems

The "real-time" visualization of two-phase flows in PEFC's makes high demands on the neutron detector system. The width of a flow channel, which is usually in the order of

† In principle, measurements can also be done in a mid-position at NEUTRA, which is usually called position 2. Because this position is not of interest for these investigations, the original position 3 is renamed in this work to position 2 for consistency.

one millimeter, requires neutron radiography images with a high spatial resolution (see section 2.3, *Evaluation of the method*). In addition, the flow rate in the channels demands to obtain the images in a continuous process at very short exposure times (better than 1 s) to resolve time-dependent processes. An example may illustrate the latter:

Assuming the same flow rate to active-area ratio as used in *Chapter IV*[†], *i.e.*, to keep the stoichmetric factor constant at a fixed current density, gives an anodic flow rate of 40 ml min^{-1} for an active area of 100 cm^2. The latter corresponds to a superficial velocity in the flow channel of about 0.7 m s^{-1} (one channel, area of channel cross-section: 1 mm^2). Furthermore, the total channel length of such a single-channel configuration is presumably in the order of 5 m (50 channels, each 10 cm long with a gap between two adjacent channels of 1 mm). Therefore, the average residence time of the liquid is calculated to about 7 s. This example illustrates that time-dependent processes can only be observed in the DMFC if the exposure time is at most in the order of one second.

Unfortunately, the requirement of a low exposure time does not match very well the demand of high-resolution images. In fact, a high-resolution image requires typically an exposure time of several seconds to a few minutes rather than the tenth of a second. Because of this trade-off between time and spatial resolution the appropriate neutron detector is not obvious to choose. Therefore, among the various detectors available for neutron radiography [13], a digital camera system and the imaging plate technique were chosen for evaluation. While the first allows observing time dependent processes, images at a higher spatial resolution can be obtained by imaging plates.

Generally, the CCD-camera systems consist of five components (see Figure 4) *(i)* the CCD-camera (DV434, *Andor Technology*, Northern Ireland) *(ii)* a lens (NOKT 43 mm F 1.2, *Nikon*, Japan), *(iii)* a mirror, *(iv)* a scintillator, and *(v)* a light-tight box.

[†] Usually, an anodic flow rate of 12 ml min^{-1} was used in *Chapter IV*.

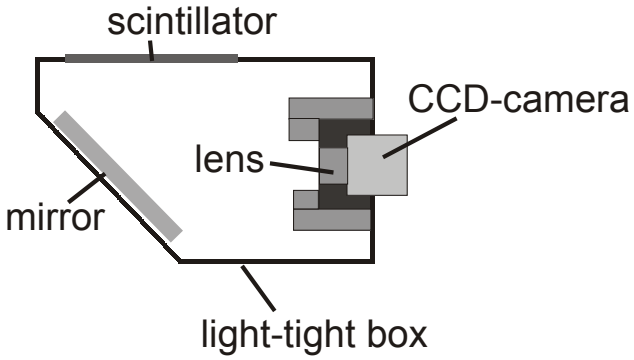

Figure 4: Schematic of the CCD-camera system [20].

A neutron sensitive scintillator emits light on the penetration of neutrons, which is reflected to the camera by a mirror and focused on the CCD-chip using a lens (Figure 4). Because of the indirect imaging method, the highly sensitive CCD-chip of the camera is protected from damages by neutrons. Furthermore, all components are not only enclosed in a light-tight box but also the electronics is shielded from radiation (neutron and γ-radiation). The information stored in the CCD-chip is read out from the camera to a connected computer (not shown in Figure 4). Further details are dispensed at this point and allowed to refer to references [20, 21] for a comprehensive discussion of the digital camera system.

In contrast to the CCD-camera system, the imaging plates are directly exposed to the neutron radiation. Imaging plates are two-dimensional neutron detectors[†] that are based on the mechanism of photostimulated luminescence. Gd (Gd_2O_3) is employed as neutron converter material, while $BaFBr:Eu^{2+}$ is used as an agent for the photostimulated luminescence. The nuclear reactions of neutrons with Gd produce γ-rays plus internal conversion electrons. The latter excite the $BaFBr:Eu^{2+}$. After transferring the imaging plate to an imaging plate scanner, this information is extracted, based on the principle of de-excitation by a laser and simultaneously recording the photostimulated luminescence emissions. Detailed insights into imaging plates, further aspects of their use, and the current status of development can be found in references [22-24].

[†] They are also available for X-, β-, γ-rays, and ultraviolet light.

The use and the limitations of these two neutron detector systems for the investigation of two-phase flows in DMFC's will be illustrated in the following.

Digital image analysis

Usually, digital image processing deals with arrays of numbers called picture elements or pixels (px) that are obtained by dividing images in horizontal grids. In mathematical terms, an image is represented by a two-dimensional array A of the type $m \times n$.

$$A = \begin{pmatrix} \alpha_{00} & \alpha_{01} & \cdots & \alpha_{0n} \\ \alpha_{10} & \alpha_{11} & \cdots & \alpha_{1n} \\ \vdots & \vdots & & \vdots \\ \alpha_{m0} & \alpha_{m1} & \cdots & \alpha_{mn} \end{pmatrix} \tag{1}$$

The location of each number in the array is described by its row number m and column number n. The pixel value corresponds to the degree of grayness at this location. Both neutron detectors generate grayscale images of 16 bit dynamic range, *i.e.*, each array element includes a number between 0 (black) and 65536 (2^{16}, white). Unfortunately, the gray color range of interest is fairly small in these studies and thus the images have to be post-processed as described below.

In a first step, the images have to be normalized to the "open beam" to compensate for fluctuations of the neutron flux during the measurement. Subsequently, the interesting range of gray colors has to be determined, cut out and scaled by some useful factor. For a qualitative evaluation of the images, "referenced" images may be necessary, *i.e.*, intensity ratio images calculated from images of two different operating conditions. Each image of a series is divided by a reference image, which is, of course, the flow field at open circuit voltage (OCV) because all flow channels are then liquid filled. If the state of the flow field has not changed compared to the reference image, the division of these two images is calculated to one for each pixel. In other words, any change in the state of the flow field will result in the intensity-ratio image in values unequal one in the region that has changed. By defining some meaningful threshold, the pixels below or above (depends on definition) this threshold refer to the gas-filled areas of the flow field. A qualitative analysis of the void fraction of the whole flow field area can be

given by summation of the gray colors of these pixels.† This number can now be related to the total amount of pixels that refer to the entire area of the flow channels‡.

However, the comparison of various flow fields is difficult because of the large error of the image analysis. The error derives from the algorithm itself and its source is illustrated in Figure 5. In principle, the histogram of a "referenced" image consists of two overlapping Gaussian distributions that originate from the noise-induced error. The curve with a mean value of about one derives from the liquid-filled channels plus the graphite matrix (no changes), and the second distribution with a mean value greater than one emerges from the gas-filled channels.

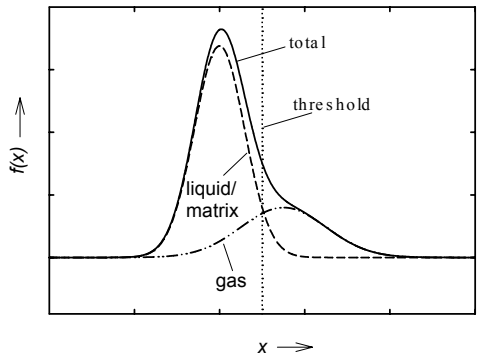

Figure 5: Typical histogram of a "referenced" image with gas-filled channels. The envelope is indicated with "total" in the diagram and consists basically of two Gaussian distributions derived from the liquid-filled and gas-filled channels, respectively. The threshold is indicated by the dotted line.

As easily seen in Figure 5, the threshold method results in pixel counts that include parts of the matrix, but also exclude a considerable amount of pixels that refer to gas-filled channels. As long as the Gaussian distribution that refers to the liquid / matrix does not change significantly, *i.e.*, as long as the same cell is used, this algorithm will

---

† Counting only the number of pixels above or below to the threshold (depends on definition) assumes that all these channels are completely gas-filled. By summation of their gray colors, partly gas-filled channels are taken into account, too.

‡ The number of pixels that refer to the total area of the flow channels cannot be counted from the reference image (completely liquid-filled flow channels) because of the small dynamic range and the limited spatial resolution. Therefore, this number is calculated from the spatial resolution of the image and the dimensions of the flow channels.

result in consistent results. Most probably, this algorithm will prevent us, however, from comparing different cell designs because of the variations of the Gaussian distribution representing the liquid / matrix. Results of such a comparison are given in the subsection *Flow field* (p. 157), where their significance is discussed.

Advanced image analysis has a large potential to improve the accuracy of its results to a great extent and is currently under development [25]. Various strategies are followed, which include, *e.g.*, pattern recognition, etch-detection, noise filters, and fitting Gaussian distributions. All of them target the accuracy of discrimination between liquid-filled channels, gas-filled channels, matrix and the reduction of the noise-induced error.

Cell design

The exposure time is a crucial point for "real-time" investigations by neutron radiography and is greatly influenced by the materials used. Therefore, appropriate materials have to be chosen according to their neutron attenuation coefficient and dimensioned as thin as possible. Figure 1 shows the thermal neutron attenuation coefficient of various elements. Thus, it gives a first hint, which components of the fuel cell that have to be dimensioned with care. Particularly critical components are the current collectors and the flow-field plates for these investigations. In many cases, the latter consist of graphite and the current collectors are usually made of copper. Fortunately, the neutron attenuation of aluminum is literally low and thus sufficiently thick endplates can be used to guarantee a homogenous pressure distribution.

Two different designs of fuel cell housings have been investigated by neutron radiography. One fuel cell housing was based on the "conventional" design of fuel cells used in the laboratory. It consisted of endplates made of aluminum, current collectors made of 1 mm thick gold-coated copper, and graphite (Diabon NS 2, *SGL Carbon* Group, Meitingen, Germany) based flow-field plates. The endplates and the flow-field plates had each a thickness of 15 mm and 5 mm, respectively.

The second fuel cell housing was optimized for low neutron attenuation and easier installation in the neutron beam. The cell housing also consisted of aluminum endplates

(each 15 mm) and current collectors made of gold-coated copper (1 mm). However, thinner flow-field plates (each 2.5 mm) were used to minimize their neutron attenuation. Besides, a graphite material (BMA 5, *SGL Carbon Group*) with a polymer filler of lower H-content (PVDF) compared to the cell described just before was chosen to further minimize the neutron attenuation. The cell design was also slightly modified for easier implementation into the experimental setup at the neutron source. In most cell designs the manifolds are positioned at the edges of the active area. However, this position is not useful for these investigations because parts of the active area are blocked by the feed lines and thus cannot be visualized. The latter is illustrated in Figures 8 and 11 by the black strip crossing the images in the upper half. In addition, the vibration of the tubing causes plentiful trouble in the digital image analysis and affects the significance of its result considerably. To avoid this problem the manifolds were positioned in some distance to the active area.

Both, the fuel cell based on the "conventional" approach as well as the "optimized" fuel cell, have been designed for an active area of 100 cm^2. To avoid any misunderstanding the cell design based on the "conventional" approach is referred to as type I in the following and the "optimized" cell design is called type II.

Flow-field design

Two different flow-field structures were analyzed in the flow visualization studies. The anodic structure of both flow-field designs is illustrated in Figure 6 and is the mirror image of the flow-field design used at the cathode side, respectively. A flow field comprising seven flow channels in serpentine configuration (Flow field A; Figure 6a) was chosen for the evaluation of its CO_2 management capabilities under DMFC conditions. The width of a channel was 1.5 mm and the depth was about 0.8 mm. In addition, the gas-liquid two-phase distribution was studied in a flow field of parallel design (Flow field B, Figure 6b). A main channel supplied the reactants to 50 small channels starting perpendicular from it. The reaction products were collected in the second main channel and removed from the cell through the manifold. The outer dimensions of the small channels were 1 mm in width and 1 mm in depth. The in- and outlets of the reactants/products were positioned at the utmost end of each main channel.

As mentioned before, both flow fields were of similar size and designed for an active area of 100 cm^2. The active area was of quadratic shape, *i.e.*, the dimensions were 10 by 10 cm^2.

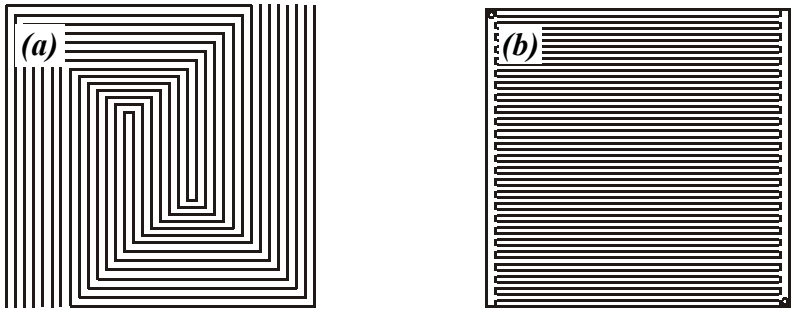

Figure 6: Schematic of the flow fields investigated in the visualization studies. The flow field in ***(a)*** (Flow field A; fuel cell type I) comprises seven flow channels in serpentine configuration. The cross-section of a channel is $1.5 \times 0.8\ mm^2$ (width × depth). The structure of the flow field schematically depicted in ***(b)*** (Flow field B; fuel cell type II) consists of 50 parallel channels, which are interconnected at each end by two main channels. The cross-section of the 50 channels is $1 \times 1\ mm^2$ (width × depth), respectively; the cross-section of the main channel is $1.5 \times 1\ mm^2$ (width × depth).

2.3 Investigation of Two-phase Flows in DMFC's

As mentioned before, the observation of a gas-liquid two-phase flow in filigree work such as the structure of a flow field of a fuel cell makes high demands on the detector system. Therefore, two different topics were addressed in the radiography imaging of two-phase flows in DMFC's. On the one side, the use of the two neutron detector systems and the benefits of both locations in the beam line for visualization of the processes occurring in the flow fields of DMFC's were evaluated. Moreover, strategies were developed to analyze the images qualitatively. On the other side, the gas distribution in the anodic flow field was studied as function of anodic operating conditions, *i.e.*, the flow rate and the flow direction.

Evaluation of the method

The performance of the two neutron detector systems was tested at position 2 (see Figure 3) with the fuel cell housing of type I and the flow field A (Figure 6a). The

potential range of spatial resolution was explored with the imaging plate technique because of its higher spatial resolution (up to 50 µm px^{-1}) compared to the CCD-camera system. The survey revealed that a resolution of at least 500 µm px^{-1} is required to visualize the two-phase flows in the flow fields.[†] Fortunately, this resolution is just within the range of the spatial resolution of the digital camera system whose highest resolution is 200 µm px^{-1}. Since the imaging plate technique prevents us from observing transient processes like the flow of gas bubbles in a liquid (the plate has to be changed manually after exposure), "real-time" measurements can only be done by the CCD-camera system. Therefore, all measurements, which are shown in the following, were carried out with the CCD-camera system.

At the same position (position 2), the exposure time needed to obtain an image of suitable quality[‡] could be reduced from 25 s with the imaging plate technique to as low as 1 s with the CCD-camera system. However, between the exposures of two images an interval of 0.5 seconds was required to read out an image from the camera, which results in a frame rate of about 0.7 frames per second (fps). Appropriate gray-scaled images were obtained as described in the section *Digital image analysis* (p. 142). Examples of such processed images are shown in Figure 8 (p. 149) for a DMFC operating at different current loads. The spatial resolution of these images is 270 µm px^{-1} and the exposure time was one second, *i.e.*, each image shows an averaged process over one second.

The advantage of position 1, the higher neutron flux, allowed to reduce the exposure time required for images of suitable quality by a factor of two to 0.5 s. Furthermore, the higher γ-background did not affect the image quality significantly. Only a minor increase of "white spots" (white areas in the image caused by γ-radiation) could be noted in the images recorded at position 1. However, the study revealed that the fuel cell housing of type I is less appropriate for measurements at position 1. The design of this fuel cell housing prevents us from locating the fuel cell close to the scintillator screen because the gas / liquid supply lines were connected to the fuel cell in such a way that

---

[†] The state of the channel (width 1 mm) is then given by only two pixels at a resolution of 500 µm px^{-1}.

[‡] Quality is used here in the sense of sufficient dynamic range for later post-processing.

same space was needed between the scintillator screen and the tubings. Therefore, the radiography images obtained for the fuel cell housing of type I have a higher blurring, which is characterized by a reduced sharpness of the edges and limited spatial detail.

The effect of image blurring is schematically illustrated in Figure 7. Neutrons are emitted completely at random, thus neutron radiation at the aperture is diffuse and needs to be collimated. However, because of the characteristic of a nonpoint source, radiography images have an inherent blurring independent from the detector system. As easily seen from Figure 7 the blurring depends on the distance *x* of the sample from the scintillator screen and the L/D ratio (see Table 1, p. 139).

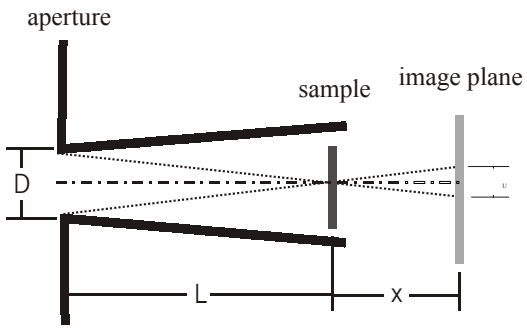

Figure 7: Schematic diagram illustrating the effect of blurring.

The inherent blurring *U* is independent of detector properties and can easily be calculated according to the intercept theorems to

$$U = \frac{x}{L/D}, \tag{2}$$

where *L* is the distance of the sample from the aperture and *D* refers to the aperture diameter (~2 cm at NEUTRA)[†]. For the fuel cell housing of type I, *x* was approximately 8 cm, which results in an inherent blurring of 0.4 mm at position 1. Since the channel width was only 1.5 mm of the "A" flow field, a qualitative analysis of the images is not meaningful at position 1 and thus only the radiography images of the "A" flow field obtained at position 2 ($U \approx 0.15$ mm) will be shown in the following. Because of the

[†] Typically, *L* is given as the distance between the aperture and the image plane. Because *x* is small the distance between aperture and sample is approximately *L* [26].

modified design, the fuel cell housing of type II could be placed closer to the image plane ($x \approx 3$ cm) resulting in an inherent blurring of 0.15 mm at position 1. Therefore, results will be given for the "B" flow field at position 1 in the following.

Flow direction

In contrast to vehicular applications, there is no fixed orientation of most portable products. Therefore, the fuel cell has to be able to operate - at least under stand-by conditions - in virtually any orientation and thus gravitation may play a role in the liquid-gas distribution in the flow field.

In the following study, this topic was addressed on the basis of two different flow directions and was studied on the flow field of type "A" (Figure 6a). In Figure 8a, the methanol-water mixture was fed into the flow field from the bottom. The inlet of the aqueous methanol solution was at the bottom of the left side and the outlet was located at the diagonally opposite side at the top of the right side (see the schematic of Figure 8a). The images given in Figure 8b depict the gas-liquid distribution in the flow field if the flow direction is reversed. Consequently, the outlet of the reaction products was at the bottom as illustrated in the sketch of Figure 8b (left side).

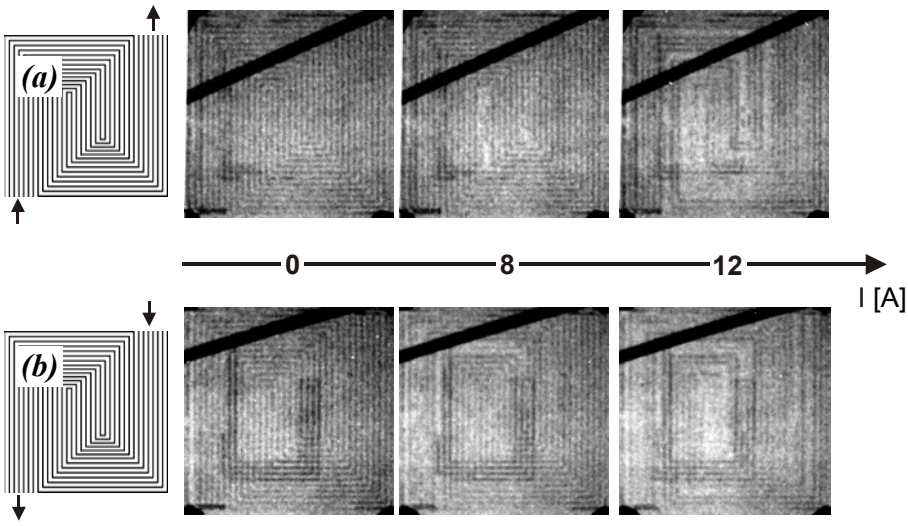

Figure 8: The effect of flow direction on the gas-liquid distribution in the anodic flow field of a DMFC ***(a)*** removal of the CO_2 with the help of buoyant force (at the outlet) ***(b)*** against buoyancy. The arrows in the schematics indicate the anodic flow direction. Liquid-filled channels result in dark regions; gas filled areas are bright. The experimental conditions were: $T_{Cell} = 45°C$, $c_{MeOH} = 0.5$ M, and constant fuel flow ($Q_{MeOH} = 24$ ml min^{-1}, $Q_{air} = 2$ lN min^{-1}).

In principle, both flow directions have areas of similar size for the given flow-field structure (Figure 6a) where gas has to be transported against buoyant force. Most probably these regions will be areas of high gas accumulation. However, in the flow direction of Figure 8b, the removal of the carbon dioxide through the manifold from the cell is against buoyancy. Therefore, the removal of carbon dioxide from the cell could be less efficient and could lead to a higher gas accumulation in the anodic flow field. All other operating parameters were essentially the same for both cases (see caption of Figure 8 for operating conditions).

The experimental procedure to obtain the images shown in Figure 8 was as follows: Prior to measuring a polarization curve, the DMFC was operated for several minutes at OCV. Meanwhile neutron radiography images of the anodic flow field were taken to ensure a completely liquid-filled flow field as illustrated in the images at OCV of Figure 8. Dark areas of the flow field indicate regions that are filled with liquid (high neutron attenuation). In contrast, gas filled channels have about the same neutron attenuation as the background noise and thus are indicated as bright areas (low neutron attenuation) in the neutron radiography images. Please note, the bright areas in the images at OCV of Figure 8 refer only to webs. Starting from a completely liquid-filled flow field and OCV, the polarization characteristic of the cell was measured and neutron radiography images of the flow field were taken along the polarization curve. Samples of these images are exemplarily given in Figure 8 at different load conditions of the cell (OCV, 8 and 12 A corresponding to 0, 80, and 120 mA cm^{-2}, respectively) and for both flow directions.

As shown by the uniform darkness of the images at OCV of Figure 8, a complete filling of the flow field could be achieved for this anodic flow rate (24 ml min^{-1}) for both flow directions. As soon as the DMFC is operated under a current load, carbon dioxide is produced and thus light areas can be seen in the images of Figures 8a and b at a current of 8 and 14 A. As expected, light areas are noted in Figure 8 where gas has to be removed against buoyancy, *i.e.*, gas clusters accumulate in the upward serpentines of the flow field. However, the gas accumulation in the flow channels was quite similar for both flow directions as seen by visual comparison of the images in Figure 8.

In addition to the gas-liquid distribution on the anode side, liquid water can be observed in the cathodic flow field as indicated by the darkest areas (highest neutron attenuation because of liquid water on both sides) in the images of Figure 8. Especially in Figure 8b, the flooded parts of the cathodic flow field can be seen very clearly and the locations of these areas are exemplarily indicated in Figure 9. Furthermore, the different pattern of the cathodic flow field (mirror image of anodic flow field) allows attributing dark areas indicating liquid to either the anodic or the cathodic flow field by their pattern. In the course of this study, liquid water has been observed in the cathodic flow field even at the highest cell temperature (110°C) investigated at a pressure of 3 bar_{abs} (data not shown). This observation is in consistency with the water crossover measurements as was reported in *Chapter IV* (p. 84). In *Chapter IV* it was concluded on the basis of a mass balance between the water actually removed from the cell and the water that could be removed by a fully saturated air stream that liquid water has to be carried out off the cell in addition to the water saturated air stream.

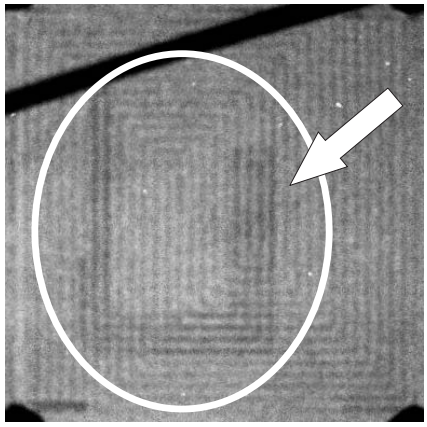

Figure 9: Regions of water accumulation on the cathode side. Cathodic liquid water is identified by its lower degree of grayness, *i.e.*, these areas are darker.

However, if liquid water is present in the cathodic flow field even at high temperatures, such as 110°C (at 3 bar_{abs}), then the design of the cathodic flow field is of outmost importance for the DMFC. Any droplet in a cathodic flow channel will increase the pressure drop of this channel and thus block this channel from the supply with air. With time oxygen depletion will occur and consequently this channel will only be filled with non-reactive nitrogen. Therefore, the active sites that are supplied with oxygen from this channel will not be able to contribute to the overall cell performance. In *Chapter IV*, this

problem was avoided by using a flow field comprising a single channel in serpentine configuration. Nevertheless, for any application where the pressure drop of the flow field results in a higher energy demand of the compressor a single channel flow field is unacceptable.

The visual impression of similar gas fractions for both flow directions Figure 8 is validated by the qualitative analysis of the gas clusters in the flow field as plotted in Figure 10, which shows the void fraction of gas, $\Theta_{Channel}$, as function of the current. The data were computed as described in the section *Digital image analysis* of this chapter. For clarity, a completely liquid-filled flow field, *i.e.*, at OCV, corresponds to a $\Theta_{Channel}$ of zero in Figure 10. Vice versa, a $\Theta_{Channel}$ of 100% refers to a flow field whose channels are solely gas-filled. The error bars in Figure 10 refer to the average deviation at each data point. Unfortunately, this range is large because of the blurring (see above, *Evaluation of the method*) and the low contrast between the matrix of the flow field and the liquid / gas-filled channels. Furthermore, the algorithm currently used for the qualitative analysis of the images causes an additional error. As outlined in the section *Digital image analysis* (p. 142), the "signal" of to the liquid-filled channels / matrix and the "signal" that corresponds to the gas-filled channels have both a Gaussian distribution that overlap (see Figure 5, p. 143). Thus, this method of image analysis (by defining a threshold) will result in a systematic error (see discussion in the section *Digital image analysis*, p. 142).

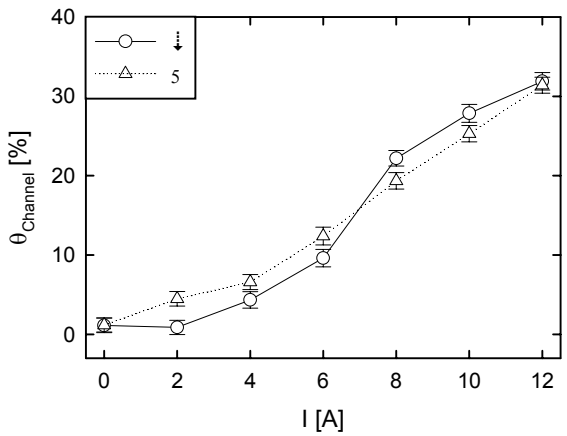

Figure 10: Void fraction of gas in the flow channels as function of the cell current. The diagram shows the qualitative analysis of Figure 8. A completely liquid-filled flow field corresponds to a $\Theta_{Channel}$ of zero or vice versa solely gas-filled channels refer to 100%. The error bars indicate the average deviation per single data point.

As nicely illustrated in Figure 10, an increase of the current results in a steadily gain of the void fraction of gas in the flow channels. Nevertheless, the void fractions agree well within the bounds of accuracy of the image analysis for both flow directions (circles refer to Figure 8a and squares to Figure 8b). The latter leads one to suppose that this specific pattern of a flow field seems to be insensitive to the flow direction of the anodic feed.

Flow rate

An effective gas removal from the flow field could be a critical issue for DMFC's, especially, if the flow rate of the aqueous methanol solution is varied. The latter is, for instance, of importance if a stoichiometric supply of the aqueous methanol solution is introduced to lower the methanol crossover as discussed in *Chapter IV*, section 3.2, *methanol stoichiometry* (p. 80).

At the same operating conditions as in Figure 8a, *i.e.*, the supply of the aqueous methanol solution from the bottom, the same cell temperature and airflow, images at OCV, 8, and 12 A of the anodic flow field are given at various flow rates in Figure 11. The image series *(a)* to *(d)* refer to an anodic flow rate of 36, 24, 12, and 6 ml min^{-1}, respectively. All images were obtained in the flow configuration as illustrated in the sketch on the left side of Figure 11, which is identical to the flow direction of Figure 8a.

As easily to be seen from the radiography images of Figure 11, a complete liquid-filling of the flow field of type A at OCV is difficult to achieve for flow rates below 12 ml min^{-1}. In addition, large parts of the flow field are gas-filled at low anodic flow rates under current load. These areas are mainly where gas has to be removed against the buoyant force. Moreover, a significant dependence of the gas fraction in the channels on the anodic flow rate can be noted by comparison of the images in the *(a)* to *(d)* series of Figure 11. A steady decrease of the gas fraction in the flow channels can be noted with an increase of the flow rate. Again, this visual impression is confirmed by the qualitative analysis of the image series given in Figure 11 and its result is plotted in Figure 12.

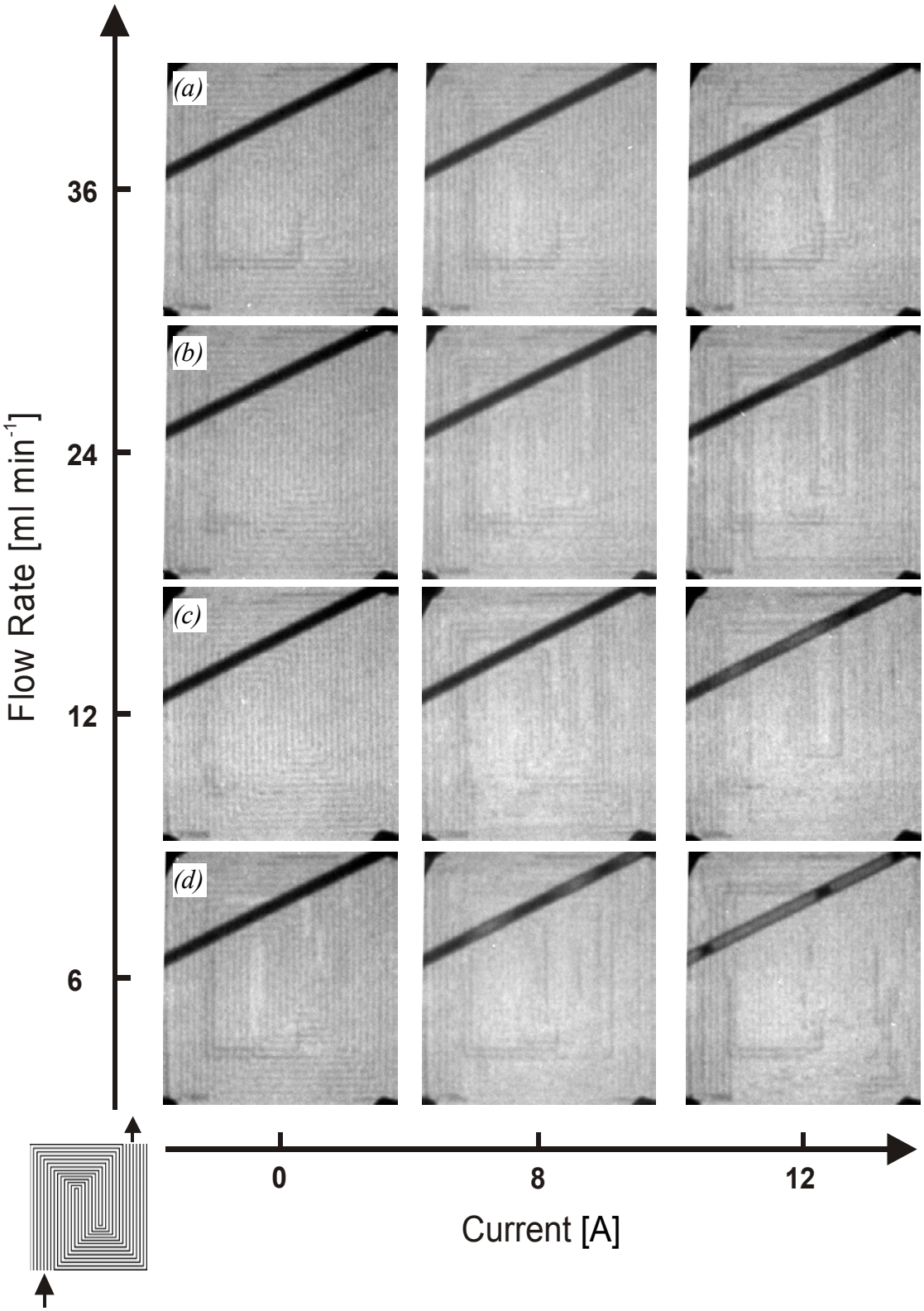

Figure 11: The gas-liquid distribution in the flow field as function of the anodic flow rate; ***(a)*** to ***(d)*** refer to an anodic flow rate of 36, 24, 12, and 6 ml min^{-1}, respectively. The operating conditions were identical for all images: $T_{Cell} = 45°C$, $c_{MeOH} = 0.5$ M, and $Q_{air} = 2$ lN min^{-1}.

There are two effects, which contribute to the reduced void fraction of gas in the flow channels at increased flow rates. Surely, an increase of the anodic flow rate increases the pressure drop over the entire flow field (theorem of Hagen-Poiseuille). Consequently, the pressure drop in a flow channel because of capillary forces becomes less important and thus the supply with liquid of each channel is more homogeneous. Therefore, gas can be removed more easily from the channels. However, quantifying the amount of CO_2 that is removed by this forced flow is difficult because

(i) the pressure distribution over the flow field is hard to assess experimentally and

(ii) modelling the pressure distribution is challenging because of the two-phase flow and the electrochemical processes involved.

Moreover, CO_2 is removed from the cell absorbed in the liquid phase. At higher flow rates more carbon dioxide can be absorbed in the liquid phase in a certain period of time and reducing in this way, the void fraction of gas in the flow field, too.

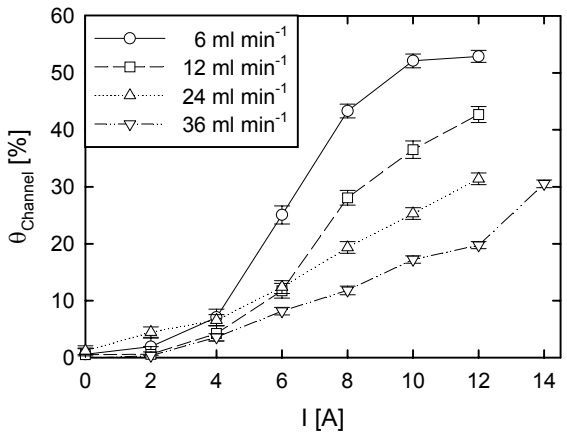

Figure 12: Void fraction of gas in the flow channels as function of the cell current at different anodic flow rates. The data are derived from a qualitative analysis of the image series of which examples are presented in Figure 11. A completely liquid-filled flow field corresponds to a $\Theta_{Channel}$ of zero. The error bars indicate the average deviation per single data.

However, there is currently no possibility to calculate the amount of carbon dioxide that is actually absorbed by the liquid phase in the flow field. Only the carbon dioxide absorbed in the liquid under equilibrium conditions can be calculated at present, which may or may not apply for the conditions predominant in an anodic flow field of a

DMFC[†]. Therefore, the quantity of gas that is removed from the cell by either the forced flow or by absorption in the liquid phase cannot be clearly attributed to either of them. Unfortunately, this lack of information prevents us from determining the length of stay of carbon dioxide in the flow field, which would be another useful characteristic for a flow field's carbon dioxide management ability.

In general, it is to conclude that the anodic flow rate has a large impact on the CO_2 content present in the flow field on the anode side. This may, for instance, be of relevance if a DMFC system is operated with a stoichiometric supply of the methanol-water mixture. In that case, the dynamics of the DMFC on large load demands may be rather slow because a considerable part of the flow field is gas-filled, which imposes mass-transport limitations on the load response of a DMFC. On the other side, the beneficial effect of gas-filled channels has also to be considered. The methanol permeation across the membrane will be significantly lower in parts of the anodic flow field that are gas-filled because of the phenomenon of a lower uptake of the membrane from a gas phase widely known as Schroeder's paradox [27]. In addition, the methanol concentration gradient across the membrane is significantly lower at anodic gas-filled areas.

Both, Schroeder's paradox and the lower methanol concentration gradient, will result in a reduced methanol concentration of the permeate and thus the cathodic potential could be less impaired. Surely, however, a lower methanol crossover will improve the DMFC efficiency considerably (cf. Section 4 of *Chapter IV*). Therefore, one might think about increasing the carbon dioxide content in the anodic flow field under part load conditions to lower the methanol crossover. However, if the gas is used as a barrier to limit the methanol permeation across the membrane, then the gas distribution in the flow field should be most homogeneous. Since buoyancy seems to be the driving force for the accumulation of gas clusters the cell should be operated in a horizontal position with the cathode side on top. In that way, a thin gas layer should develop above the liquid.

[†] The degree of the saturation of the liquid phase with CO_2 will also depend on the pattern of the flow field and its size. Both determine the average residence time of a gas bubble in the cell and its size and thus influence the degree of saturation reached in the cell.

Flow field

From the two studies above (*Flow direction* and *Flow rate*) we have learned that the pressure drop across the flow field and buoyancy affects the CO_2 distribution most. Both can also be influenced by the pattern of the flow field. Therefore, the void fraction of gas in the channels of a second flow field with different flow-field pattern (flow field B, Figure 6b) was investigated. In this study, the anodic flow field was fed from the upper left manifold and the outlet was at the bottom of the right main channel (as indicated in Figure 6b). Neutron radiography images of flow field B were obtained in the same way as with flow field A and subsequently analyzed to quantify the void fraction of gas at the different currents. In Figure 13, results of this study are plotted exemplarily together with the results obtained for the flow field A under similar operating conditions.

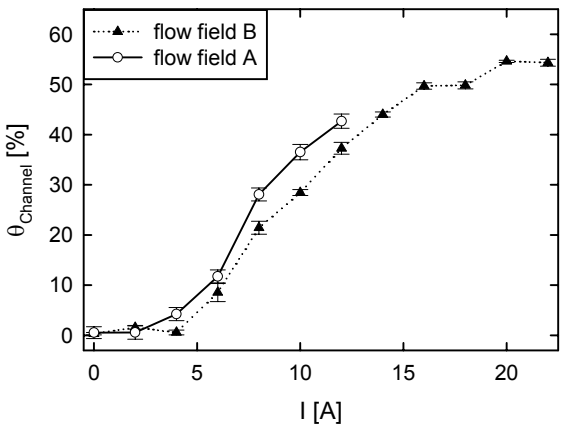

Figure 13: Consequences of anodic flow field patterns on the void fraction of gas in the channels at different currents. The circles refer to flow field A (Figure 6a); the triangles show data for the flow field B (Figure 6b). The error bars indicate the average deviation per single data point.

Surprisingly, large deviations of the void fraction of gas present in the anodic flow field between both types of flow fields cannot be observed in Figure 13. - However, Figure 13 is somewhat misleading. So far, the void fraction of gas, as given in Figure 13, is computed from 2-D information. Precisely, it is calculated from pixel counts and therefore, does not take the channel depth into account, *i.e.*, the void fraction of gas is a ratio of areas not of volumes. However, the total channel volume of the B flow field is about 11% larger than that of the A flow field, which would lead, if corrected for the total volume of the channels, to curves that would agree even better.

Unfortunately, any differences or agreements between the two curves in Figure 13 are not too meaningful because the error of the image analysis is large. A sensitivity analysis of the algorithm used revealed, not surprisingly, that the results highly depend on the threshold value. However, the use of different cell designs changes the variance of the Gaussian distributions, which directly affects the result of the image analysis (cf. *Digital image analysis*, p. 142). Unfortunately, there is no obvious way of estimating this error qualitatively. Therefore, only comparisons within the same flow field are possible at this time, *i.e.*, the comparison of void fractions at various operating conditions. The comparison of different flow fields causes inconsistent results. Therefore, all computed void fractions have to be regarded as qualitatively, but not quantitatively correct within the same flow field.

2.4 Present Limitations

Although this experimental method opens up exciting possibilities not only for DMFC but also for the H_2-PEFC research [28], this technique is currently limited by two problems:

(i) An increase of the spatial resolution will facilitate the qualitative analysis of the images to a great extent. In addition, its accuracy would be improved considerably.

(ii) A further reduction of the exposure time is necessary to observe fast processes in the flow channels more clearly.

Therefore, the investigation of PEFC's by neutron radiography is mainly limited by the performance of the neutron detector system. At present, high-resolution images can best be obtained by the image plate technique, but the exposure time is quite long and thus the processes occurring in the flow fields are averaged over about 20 seconds. Therefore, only a flow distribution in its steady state can be observed by the imaging plate technique.

The CCD-camera system is the method of choice because it allows the observation of time-dependent processes. The minimum exposure time required to obtain an image of suitable quality was about one second for the fuel cell of type I and approximately 0.5 s

for the type II fuel cell. However, the spatial resolution (about 250 μm px^{-1}) is a factor of five lower than the best resolution achievable by the imaging plate technique. In addition, the read-out rate from the camera to the computer is slow (~0.5 s per image) and prevents us from observing fast processes. Unfortunately, both limit the accuracy of the image analysis and allow us to regard its results only as qualitatively correct at present. That is why different flow fields can currently not be compared.

A higher frame rate would allow us to average the results over more images and a higher spatial resolution would enable us to distinguish better between the channel and its web. In addition, more pixels would describe the state of a channel in an image with a higher spatial resolution and therefore, the effect of the noise-induced error could be minimized. Ideally, the CCD-camera system should be able to obtain high-resolution images (50 μm px^{-1} or better) at very high frame rates (10 fps or better). Maybe these limitations are eliminated in future: The increase of the neutron flux of the neutron source at PSI [29] as well as further advances on neutron detector systems will improve the experimental conditions to observe gas evolution patterns and water condensation in the flow channels in a better temporal and spatial resolution.

2.5 Conclusions & Outlook

The results obtained so far have shown promising use of the neutron radiography for the investigation of DMFC's. At present, a sufficient[†] spatial resolution of the neutron radiography images is achieved; a reduction of the exposure time could be realized by the minimization of the neutron attenuation of the fuel cell (type B) and the blurring could be reduced by slightly modifying the cell design.

The consequences of the flow direction and the flow rate on the gas-liquid distribution in the anodic flow field of DMFC's were explored. Fortunately, the flow field of type A was completely insensitive to the two different flow directions. The latter can be explained by the similar size of the areas where gas has to be removed against buoyancy. Variations of the anodic flow rate revealed that the carbon dioxide content in

[†] Sufficient means that flow fields can be analyzed but one has to keep in mind that the accuracy is probably not very large.

the flow channels drastically depends on it. While at low current densities the gas accumulations may be used as barrier to minimize the methanol crossover to the cathode, large gas clusters may impose mass transport limitations on the anode at high current densities. However, the latter is still an effect whose impact on the cell performance is unknown. Although the methanol concentration in the gas phase is fairly low, methanol is surely transported from the liquid to the gas phase. Unfortunately, modeling the mass transport of methanol from the liquid phase through the gas phase to the active layer is under the highly undefined conditions of an operating DMFC a challenging task in which no one has yet succeeded.[‡]

The combination of visual information of the state of the anodic flow field and the current produced in areas of high gas accumulation could give a first hint on the importance of gas-filled channels. Therefore, a combination of this method with the *in situ* measurement of the CD of PEFC's, which is discussed in the next section, is highly desirable. In this way, the impact of the formation of carbon dioxide clusters in anodic flow fields of DMFC's can be investigated more thoroughly. A first outlook on the combination of these two *in situ* methods will be given in the last section of this chapter.

[‡] To the author's knowledge

3 Current Distribution in the DMFC

3.1 Introduction

While the benefits of polymer electrolyte fuel cells (PEFC's) as power sources for portable or mobile applications have widely been demonstrated in the past, the cost of the fuel cell system remains still the key hindrance for the commercialization of PEFC's [30]. Thus, most research effort is focused today on designing less costly and more efficient fuel cell systems. Besides the development of new materials, which either allow to simplify the fuel cell system or "simply" reduce the cost of a fuel cell stack, the optimization of the electrochemical activity over the whole electrode area is of prime importance to reach an optimum performance of each cell in a stack [31].

As inhomogeneities in fuel cell performance cannot be identified by the measurement of integral values like the cell voltage or cell current alone, real-time mapping of the current distribution (CD) covering the whole electrode area is highly desirable. For this purpose, a wide range of approaches has already been suggested, mainly applied to hydrogen-powered fuel cells [31-34] or to electrolysers [35, 36]. However, all of these methods suffer either from unknown interferences[†] of the diagnostic method with the processes occurring at the electrodes or cannot be implemented for measurements in fuel cell stacks.

Recently, Wieser *et al.* [37-39] presented a new method using a magnetic loop array for locally resolved measurement of currents in large scale PEFC's. A flow-field plate, which was divided into 40 electrical isolated segments, was used to avoid any lateral currents. The current sensors, consisting of Hall sensors fixed in the air gap of annular softmagnetic ferrites, were placed around a gudgeon of each flow-field segment. The latter was mounted in a mainframe, which was sealed gastight. The advantages of this method are:

[†] Because of corrosion, different pressure / temperature distribution, segmentation of the electrode, etc.

(i) No modifications on the membrane electrode assembly (MEA) are necessary (transversal currents within the backing are small and hence can be ignored, if the segment is sufficiently large [37]).

(ii) A combination of high spatial and time resolution can be achieved.

(iii) In principle, the integration into fuel cell stacks is possible.

However, the installation of Hall sensors into the flow-field plate makes any maintenance difficult and the investigation of several flow field structures pricey.

Therefore, a new method was sought which has the advantages of a magnetic loop array and allows an easy and highly adjustable implementation. This section will deal with our experience on a novel and simple to realize method for real-time current mapping of PEFC's. The principle of measurement and the feasibility of this approach will be discussed in the following subsection *Technology of Measurement*. Hereon, the impact of the operating conditions such as air stoichiometry or anodic flow rate on the CD of DMFC's will be shown in the subsection 3.3 and its consequences on technical cell will be considered. This section will conclude with a discussion of the methodical and experimental results and give an outlook on future improvements.

3.2 Technology of Measurement

A schematic of the experimental setup used to map the CD of PEFC's is depicted in Figure 14 and consists of the fuel cell and external circuitry for measuring the current. The different components of the experimental setup are described below in detail.

The fuel cell employed is of the conventional filter-press type consisting of a MEA sandwiched between two flow-field plates, which are clamped together by outer stainless steel plates. One of the flow-field plates is divided into electrical isolated sections, which themselves are electrically isolated against the stainless steel plate. The current flows through these segments are each measured by its own current sensor and connected to the same electrical load. For the other flow-field plate, the stainless steel plate serves as current collector, which is also connected to the electrical load. A 20-channel armature multiplexer plug-in module (HP 34901A) installed in a mainframe

(HP 34970A), both from *Hewlett Packard* (Palo Alto CA, USA), served as data acquisition unit to record the signal of each current sensor.

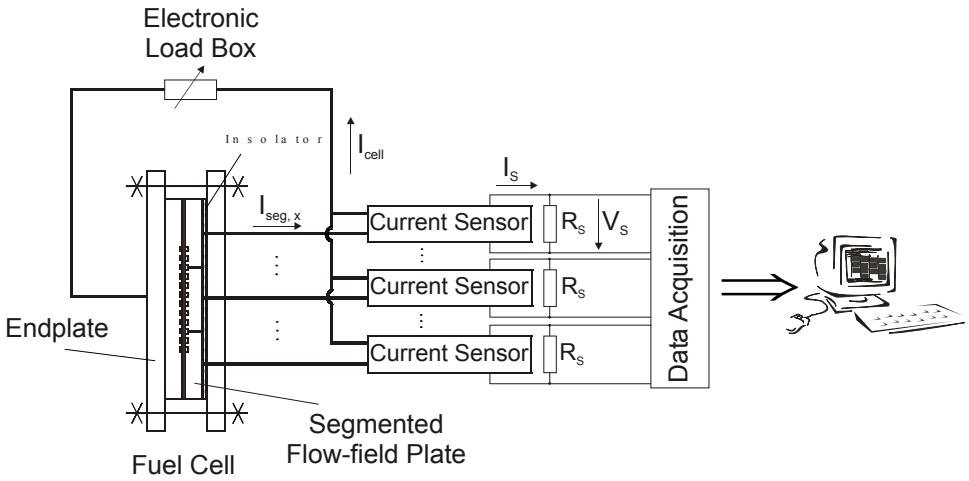

Figure 14: Experimental setup of the current distribution measurements. [40]

Current sensors

In contrast to the open-loop Hall effect sensors, that were used by Wieser *et al.* [37-39], closed-loop Hall Effect current sensors were used in this work for mapping the CD over the electrode area. These consist of five basic components (Figure 15), such as Hall generator, magnetic core, amplifier, driver circuit, and some windings around the magnetic core. The principle of measurement of "compensated" Hall Effect current sensors is shortly summarized in the following.

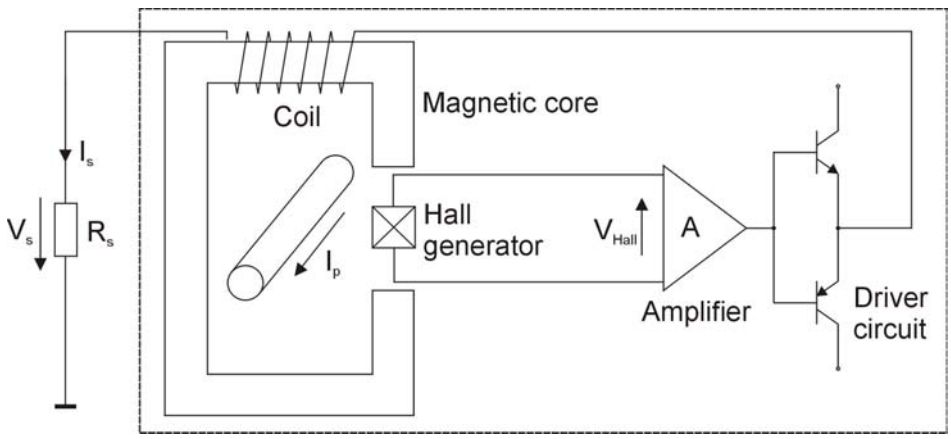

Figure 15: Block diagram of a closed-loop Hall Effect current sensor (within the dashed box) [41].

The magnetic field generated by the primary current, I_p, results in an output voltage of the Hall generator, which is proportional to the magnetic field and thus to I_P. This signal is boosted by an amplifier and fed to the driver circuit, which creates a canceling magnetic field that will drive the core to near zero flux. Therefore, the resultant secondary current, I_s, is a direct measure for the strength of the magnetic field being cancelled. This secondary current is measured using a resistor, R_S, which generates a voltage signal, V_S. The correlation between the primary current and the voltage being measured is then given as:

$$V_S = R_S \frac{1}{N} I_P, \tag{3}$$

where V_s refers to the voltage being measured and N states the number of turns of the coil [42].

In contrast to the open-loop Hall Effect current sensors used by Wieser *et al.*, the additional space needed for the electronics of the closed-loop Hall Effect sensors prohibit the integration of the sensors into the flow-field plate. Nevertheless, useful information could not be obtained by an integration of closed-loop Hall Effect current sensors. Only the open-loop Hall Effect current sensors allow to measure the current *and* the temperature distribution over the active area. Despite these drawbacks, however, there are several reasons for using closed-loop Hall Effect current sensors. The advantages of those sensors are

(i) high accuracy,
(ii) superior linearity, and
(iii) low temperature drift.

Furthermore, the installation of the current sensors outside the flow-field plate simplifies greatly any maintenance and calibration (no attention has to be paid to temperature effects on the current sensors because they can be held at ambient temperature). Therefore, the method illustrated in Figure 14 goes well with the demands of accuracy, low maintenance, and simplicity imposed on any diagnostic tool of practical importance.

In principle, shunt resistors could be used for this approach as well. However, the current sensors have the advantage of an inherent lower resistance (virtually zero) compared to shunts. The latter is important for the accuracy of these measurements, which may be illustrated by the block diagram in Figure 16.

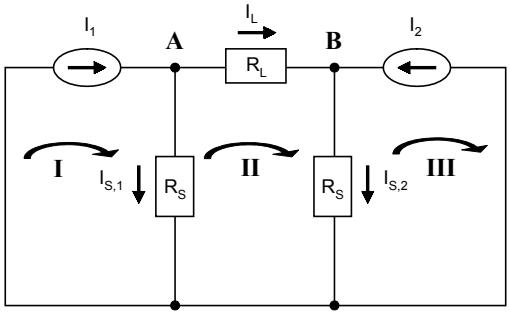

Figure 16: Simplified block diagram of a segmented fuel cell. I_1 and I_2 represent the current of each segment and I_L is the leakage current from one segment to the other. The current flows measured for each segment are indicated with $I_{S,1}$ and $I_{S,2}$. The resistance R_L refers to the lateral resistivity within the backing and R_S represents the resistance in the outer circuitry. It is assumed here that R_S is identical for all segments.

Generally, the different segments can be replaced by single current sources with a current I, *e.g.*, I_1 and I_2 for the segments 1 and 2. Because only the flow-field plate but not the diffusion layer is divided into electrically isolated sections, a leakage current from one segment to the other can occur. The latter is represented by the leakage current I_L and the corresponding resistance R_L in Figure 16. Finally, each circuit of a segment has an inherent resistance R_s that is the summation of all contact resistances, cable resistances, and additionally includes the resistance of the current sensor. Using the mesh current analysis, the following relationship of dependence can be derived from the example given in Figure 16.

$$I_L = \frac{I_1 - I_2}{\frac{R_L}{R_S} + 2} \tag{4}$$

As easily seen from Equation 4, the leakage current from one segment to the other is strongly influenced by the resistances inherent in the different circuits. Assuming a constant resistance of the diffusion layer R_L, it can be derived from Equation 6 that the leakage current depends on the resistances of each circuit. However, typical shunt

resistances are in the range of 100 mΩ compared to about 6 mΩ of the total circuit realized in this approach with current sensors. Therefore, lateral currents within the diffusion layer can best be minimized by using current sensors.

The considerations made above are only valid for small areas around the isolation layer between two adjacent segments. For an analysis on segment level or across the entire active layer, mutual interactions can be obtained by superposition. For a basic estimation, the model represented by the equivalent circuit is sufficient (Figure 16) and, at the same time, a coherence between leakage current and circuit reasistance can be derived without complex network analysis.

Commercially available closed-loop Hall Effect current sensors (LA 25-NP, *LEM*, Switzerland), that are designed for a primary current of 5 A at full scale, were chosen for the realization. Considering an active area of 30 cm^2 divided into nine segments of equal size (about 3.3 cm^2), a current density of 1.5 A/cm^2 can be measured at maximum per segment. For an application in the DMFC, which is subject of this study, this current range should be sufficient, even considering a highly inhomogeneous CD over the electrode area.

Each sensor was calibrated to increase its precision in the low current range. In this way, the maximum relative error was within 1% over the entire measuring range as summarized in Figure 17 (without calibration the relative error was at a primary current below 1 A in the range of a few percentage). Furthermore, any temperature effects can be safely ignored because the current sensors are installed outside the fuel cell and held at ambient temperature.

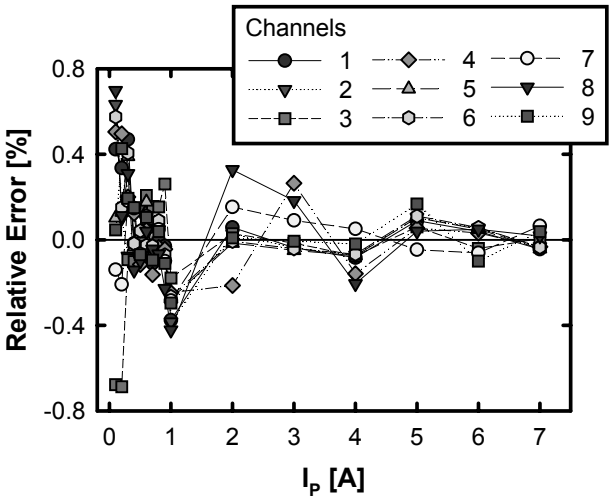

Figure 17: Relative Error of each current sensor (labeled as channels) as function of the primary current.

Flow field

The flow-field plates were made of graphite (Diabon NS 2, *SGL Carbon Group*, Meitingen, Germany), which featured high temperature resistance and low electrical resistivity. Two different flow-field structures were used on the anode side and the cathode side, respectively. While the anode flow-field comprised a parallel structure (Figure 18a) already known from the previous section *In situ Visualization* for the supply of the reactants and the removal of the products, a single flow channel was machined in serpentine configuration into the graphite plate used at the cathode (Figure 18b). Moreover, both flow-field plates were quite thick (15 mm) to compensate for the deflection of the endplates and thus to accomplish a homogeneous pressure distribution over the entire active area. The latter was experimentally verified for the segmented cell using a pressure measuring film (Super Low, *Fuji Photo Film Co.*, Tokyo, Japan) [40].

In this study, the anodic flow-field plate (Figure 18a) was segmented to avoid lateral currents in the graphite plate. The aim was to build a flow-field plate, which equates the "normal" flow-field plates in every respect. Therefore, the segmented flow-field plate must have identical physical properties, such as, thermal diffusivity, electrical resistivity, or mechanical characteristics. These constraints were met using the same graphite material (as already mentioned in the paragraph before) and embedding the segments in a resin of suitable properties.

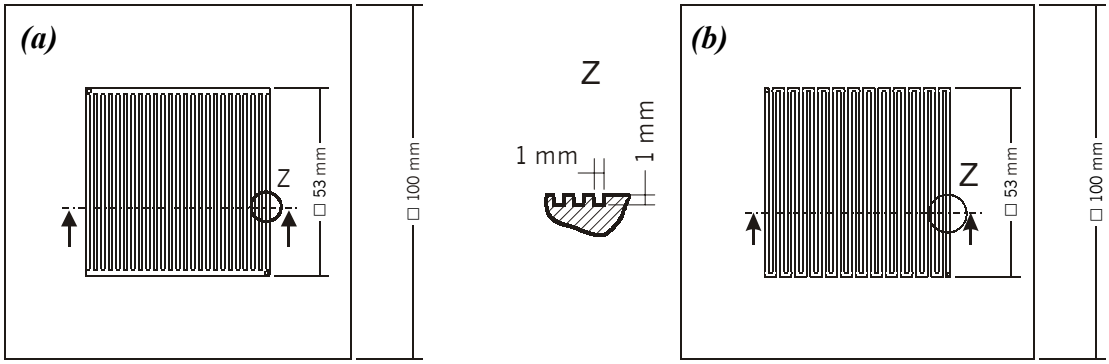

Figure 18: Schematics of the flow-field patterns used on the anode side ***(a)*** and the cathode side ***(b)***. In both flow patterns the channel was one millimeter wide and one millimeter deep. The width of the web between two adjacent channels was one millimeter (see detail Z in the middle).

However, this strategy makes high demands on the embedding material, which has to fulfill numerous requirements, such as

(i) high thermo stability for use in the DMFC (>120°C),

(ii) a similar thermal expansion to graphite,

(iii) good adhesion on the graphite,

(iv) good machining properties,

(v) excellent chemical stability in an acidic environment,

(vi) gas tightness, and

(vii) processible in small layers.

An extensive survey of numberless bonding agents revealed a two-component epoxy adhesive (ECCOBOND® 104, *Emerson & Cuming*, Billerica, MA, USA) as the most suitable for this application.

Manufacturing a segmented flow-field plate requires a multi-step process to achieve the same properties as non-segmented plates (see discussion above). Moreover, similar areas of each segment and defined positions are highly desirable. Therefore, a manufacturing process had to be developed, which is recounted below in short. A more detailed description of this process can be found in the diploma thesis of R. Eckl [40].

Three graphite bars of suitable size were made and glued together with the two-component epoxy resin. PTFE spacers were used to guarantee gaps of equal width. In this way, a thickness of the isolation layer of as low as 0.3 mm could be achieved. Therefore, negative effects of the non-conducting material on the electrochemical processes can be neglected. After curing these for six hours at 120°C, the glued plate was milled again into three bars perpendicular to the bonding surface and glued together with the spacer technique in the same way as described above. At last, the pattern of the flow-field was milled into the surface, resulting in a graphite plate comprising nine electrically isolated segments, each covering an active area of $18 \times 18\ mm^2$. The segmented flow-field plate in its final form is displayed in Figure 19, where the arrows indicate the position of the splices.

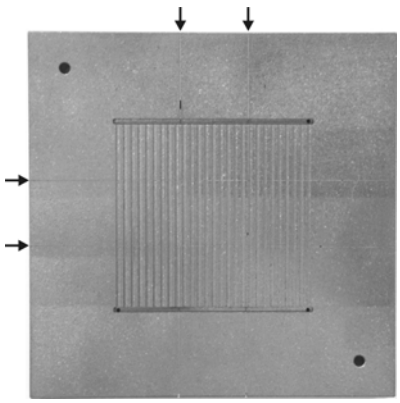

Figure 19: Segmented flow-field plate comprising a parallel flow pattern. The arrows indicate the locations of the bonding layers.

Contacting

Gold-coated copper sheets (thickness 1 mm) used as current collectors contacted each segment from the back. For precise positioning, these were attached on a silicon foil (thickness 0.5 mm), which served as gasket and as electrical isolation to the endplate. In this way, the cell could be assembled much the same as "normal" laboratory cells are put together.

An issue of utmost importance is the balance of the resistances inherent in the outer circuitry of each segment. The assumption of negligible lateral currents in the electrode is only valid for a quasi-isotropic flow-field plate (see discussion in *Current sensors* of

this section). However, any scatter in the contact resistances of the external circuitry or the cable resistances will result in an anisotropic flow-field plate or, metaphorically speaking, will create a flow-field plate of variable thickness. A 1 mΩ higher resistance of one segment compared to the others already results in an about 5% too low current reading for this segment [40]. Therefore, special attention has to be paid to match the overall resistance of each single circuit. The latter can be easily achieved by inserting trimming resistors into the respective circuit. In this way, the difference between the channel resistances could be compensated to about ±0.1 mΩ, which corresponds to a relative deviation from the average resistance of a single circuit of better than ±1%.

Electrochemical components & start-up procedure

In this study, a MEA consisting of a Nafion 117 membrane (*E.I. DuPont de Nemours & Co., Inc.*, Wilmington, USA) and commercially available electrodes were used. Pt-Ru electrodes were employed on the anode with platinum and ruthenium loading of 1 and 0.5 mg cm^{-2}, respectively. On the cathode, electrodes based on a platinum catalyst were used with a precious metal loading of about 4 mg cm^{-2}. The MEA was hot pressed prior assembling in the cell hardware. A more detailed overview of the electrochemical components and the cell assembly is given in the experimental section of *Chapter IV* (pp. 60) and thus details are dispensed at this point.

Prior the measurement, the DMFC was operated potentiostatically at a cell voltage of 0.3 V and a cell temperature of 90°C for at least 12 hours. An aqueous methanol solution of 0.5 M was fed preheated at cell temperature to the anode at a constant flow rate of 12 ml min^{-1}. Dry air was supplied at a stoichiometry of 3 to the cathode. An equal backpressure of 3 bar_{abs} was applied on the cathodic as well as on the anodic compartment. The latter ensured the supply of the aqueous methanol solution as liquid to the anode.

3.3 The effect of operating conditions on the CD of a DMFC

For the evaluation of this method, the effect of the air stoichiometry, the anodic flow rate, and the anodic methanol concentration on the CD of a DMFC was investigated. The results of this survey will be presented in the following. If not stated otherwise, the

data were obtained in the following manner, subsequently referred to as standard operating conditions.

An aqueous methanol solution was supplied preheated at cell temperature to the anode. The cell temperature was 110°C, which was also the inlet temperature of the air at the cathode. An equal pressure of 3 bar_{abs} was applied on the anodic and cathodic compartment. The cell was operated in counter-flow mode with air as oxidant.

Air stoichiometry

The airflow is one of the most important factors affecting the efficiency of a fuel cell system [43]. It is even more important for a DMFC than for a H_2-fuel cell system because these usually operate at high pressure (3 bar_{abs} and higher) and at high air stoichiometries (most often in the range between 5 and 60, *e.g.*, [44, 45]). Both, of course, increase considerably the parasitic energy demand of a compressor. However, understanding the phenomena involved in lowering the air stoichiometry is the basis to improve the DMFC performance at low air stoichiometry.

In principle, a single cell can be operated at constant cell voltage or under constant current conditions. However, in a fuel cell stack of the conventional filter press type a cell will always have to work under constant current conditions because the charge passing through each cell of the stack is the same, regardless if the stack itself is operated potentiostatically or galvanostatically [46]. Therefore, all CD's were measured under constant current conditions.

Furthermore, two different modes of fuel supply can be chosen *(a)* the feed of the reactants at a constant flow rate or *(b)* supplying the fuel stoichiometrically. In principle, stoichiometric operation of the cell is the one of technical relevance. However, the inlet temperature of the anodic fuel was, unfortunately, difficult to control for varying flow rates and thus constant flow rate conditions were chosen for the anode side (see discussion *Chapter IV*, p. 80). Whereas on the cathode side a constant inlet temperature of the air could be managed at varying flow rates and thus the stoichiometric supply of the oxidant was chosen for the cathode side.

Under these conditions, the DMFC was operated with a 1 M aqueous methanol solution at a constant flow rate of 14 ml min^{-1} and different air stoichiometries (from 3 to 9). The corresponding current distribution of the DMFC at a constant cell current of 10 A (330 mA cm^{-2}) is plotted in Figure 20 as function of the air stoichiometry. The current density of each segment is given as the deviation from the average current density (which is the one measured in polarization curves) at the respective air stoichiometry. The symbols correspond to the location of the segment in the flow field plate as indicated in the legend of Figure 20. In horizontal direction, the type of symbol refers to its horizontal position; in vertical direction, the filling of the symbol corresponds to its vertical location.

As easily to be seen in Figure 20, the CD of the DMFC highly depends on the air stoichiometry. In general, the inhomogeneity of the current distribution increases with decreasing air stoichiometry. At an air stoichiometry of 3, the segments close to the inlet of air (filled symbols) produce about three times as much current as segments located close to the outlet (open symbols). Middle segments (in vertical direction, dotted symbols) are basically unaffected by the air stoichiometry and show an almost constant current density of about 330 mA cm^{-2} (corresponding to a relative deviation from the average current density of 0% in Figure 20) for all air stoichiometries.

The enormous inhomogeneity of the current distribution at low air stoichiometry may surprise at first glance because at the lowest air stoichiometry still three times as much air is supplied as needed by the cell reaction. However, for the calculation of the air stoichiometries as given in Figure 20, the methanol crossover (approximately 200 mA cm^{-2} at a current density of 330 mA cm^{-2}, cf. *Chapter IV*, p. 77) was not taken into account. Therefore, the effective air stoichiometry is considerably lower as given in Figure 20. That means the air stoichiometries of 3, 4, 5 etc., as given in Figure 20, correspond to an effective air stoichiometry of 1.9, 2.5, 3.1, etc., respectively. The latter may explain the high inhomogeneity of the current distribution at low air stoichiometries.

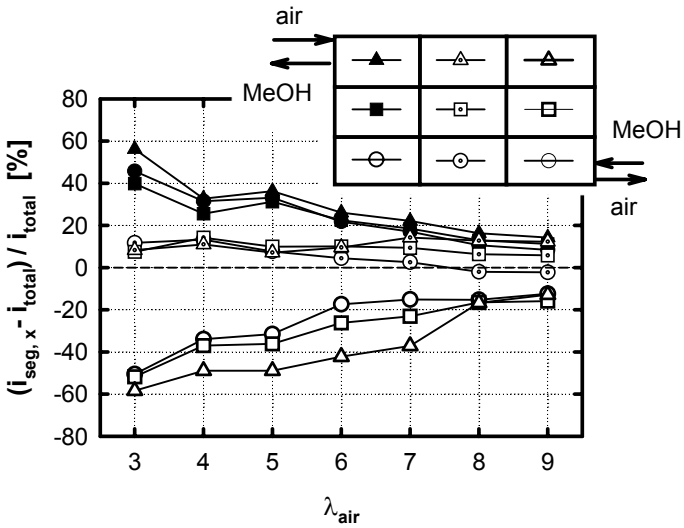

Figure 20: Current distribution vs. air stoichiometry at a cell current of 10 A, a methanol concentration of 1 M, a flow rate of 14 ml min^{-1} (corresponding to an anodic stoichiometry of 13.6), and standard operating conditions (see p. 170). The current density of each segment is given as the deviation from the average current density at the respective air stoichiometry.

Material inhomogeneities & flow rate

The impact of material inhomogeneities and the effect of the anodic flow rate on the CD were tested the following way:

(i) The cell was rotated 180°, *i.e.*, the flow direction is kept the same but the segments that were close to the inlet before are now at the outlet and vice versa.[†]

(ii) The anodic flow rate was reduced by a factor of two to demonstrate its effect on the CD.

The effect of the rotation of the cell as well as the impact of the reduction of the anodic flow rate on the CD is together illustrated in Figure 21.

[†] The flow-field patterns on the anode and cathode side are rotationally symmetric (see Figure 18).

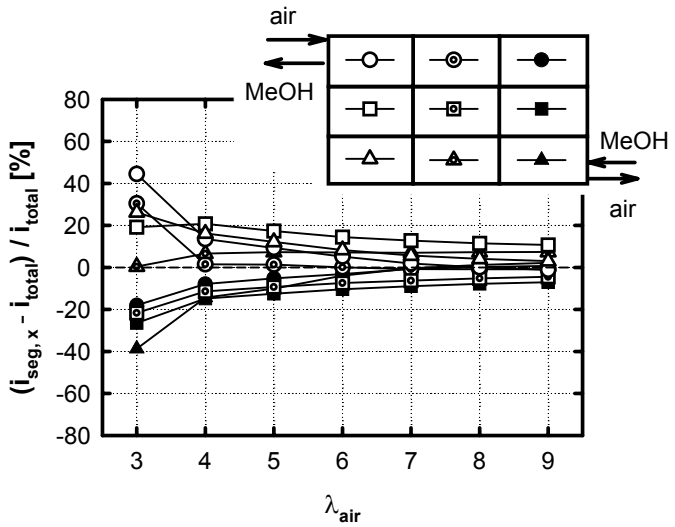

Figure 21: Current distribution as function of the air stoichiometry at a cell current of 10 A, a methanol concentration of 1 M, an anodic flow rate of 7 ml/min (corresponding to an anodic stoichiometry of 6.8), and standard operating conditions. The cell was rotated 180°. The current density of each segment is given as the deviation from the average current density at the respective air stoichiometry.

As easily to be seen by comparison of Figures 20 and 21, the segments that showed a negative deviation from the average current density in Figure 18 are better than the average in Figure 21 and vice versa. Only the segments in the middle (in vertical direction) show somehow unexpected behavior. Probably, their performance can be related to the lower anodic flow rate, which may result in an unequal liquid supply of each channel. In neutron radiography studies of such a parallel flow field (the data were not shown in section 2) it could be observed that gas clusters mostly accumulated in the middle at low anodic flow rates [28]. Although this may apply here, the actual gas-liquid distribution in the anodic flow field is not known. Nevertheless, these effects are not very large except for the deviation at an air stoichiometry of 3. Because of the experimental results plotted in Figure 21, it is concluded that major effects of material inhomogeneities such as catalyst distribution, contact resistances, or temperature gradients on these CD's can be excluded.

Finally, the comparison of Figures 20 and 21 seems to reveal a dependency of the CD on the methanol crossover. Cutting the anodic flow rate in half decreases the methanol stoichiometry by a factor of two (from 13.5 to 6.75) and thus affecting the methanol

crossover (cf. discussion and results of *Chapter IV*, section 3.2, pp. 80). Presumably, there are three effects that all influence the methanol crossover:

(i) As shown in section 2 of this chapter (see Figure 12, p. 155), the gas content in the anodic flow channels is higher at a lower anodic flow rate. Therefore, a larger area of the membrane may be in contact with vapor on the anode side, which would reduce the methanol crossover in these areas (cp. discussion on p. 156).

(ii) Decreasing the anodic flow rate means also to lower the pressure drop across the flow field. This may result in a less efficient removal of carbon dioxide off the electrode structure. Consequently, a gas layer would develop between the liquid phase and the membrane and thus the methanol crossover to the cathode side would be limited.

All these reasons will result in a lower methanol crossover and therefore, less oxygen will be consumed by the parasitic methanol oxidation on the cathode side. Consequently, the dependency of the CD on the air stoichiometry would be smaller.

Methanol Concentration

Generally, the methanol crossover can also be reduced by lowering the anodic methanol concentration. The resulting CD is depicted in Figure 21 at a methanol concentration of 0.5 M, a current of 6 A, and otherwise constant operating conditions (compared to Figure 20). Please note that in Figure 22 the values of the CD for an air stoichiometry of two are additionally included in contrast to Figure 21 and Figure 20.

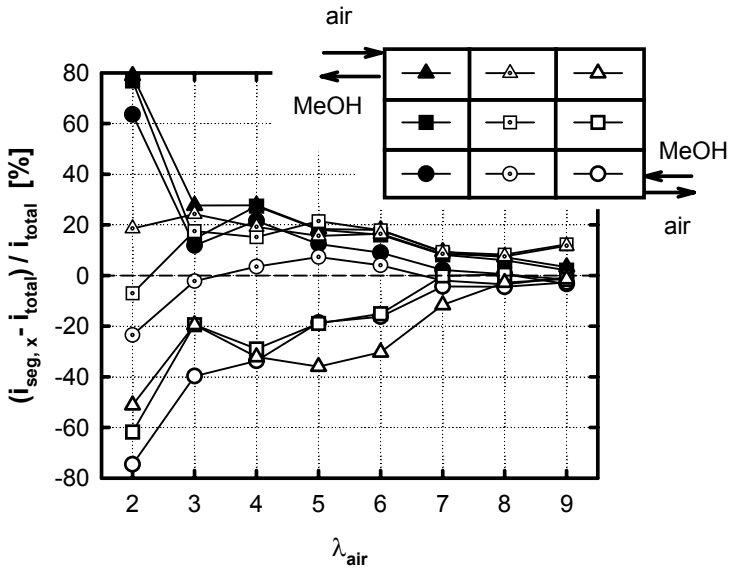

Figure 22: Current distribution vs. air stoichiometry at a cell current of 6 A, a methanol concentration of 0.5 M, a flow rate of 14 ml min^{-1} (corresponding to an anodic stoichiometry of 11.2), and standard operating conditions. The current density of each segment is given as the deviation from the average current density at the respective air stoichiometry.

So far, effects based on material inhomogeneities can be excluded and the influence of the flow rate and the methanol concentration was explored. Therefore, the general pattern of the deviation of each segment from the average current density can be explained in the following way.

Because of the flow pattern used on the cathode side (single channel in serpentines, see Figure 18b), the oxygen concentration is approximately identical in segments of the same vertical location. Furthermore, the oxygen concentration decreases from the inlet to the outlet, *i.e.*, oxygen depletion may occur at loci close to the outlet (filled symbols in Figure 20). Increasing the air stoichiometry influences the segments differently depending on their location in the flow field:

- Segments close to the inlet profit from a high oxygen concentration and from a good water removal off the electrode structure at low air stoichiometry. At very high airflow, however, the membrane will start to dry and thus the performance of these segments will be limited.
- Segments close to the outlet of air will mainly profit from a higher air stoichiometry because of a local increase of the oxygen concentration.

Furthermore, these segments will profit up to a certain air stoichiometry from a better water removal off the electrode.[†]

Although all these considerations are likely, the anodic gas-liquid distribution and its impact on the anode performance is an uncertainty, which also could affect the CD of a DMFC. Therefore, it is highly desirable to obtain visual information of the state of the flow field simultaneously with the measurement of the CD to explore the effect of carbon dioxide in the anodic flow field on the cell performance.

3.4 Conclusions

A novel approach to measure *in situ* the current distribution of PEFC's has been developed and the proof of concept could be given. The principle of measurement is based on measuring the current flow externally through different areas of a flow-field plate. The advantages of this method can be summarized as follows:

(i) High accuracy,
(ii) low cost,
(iii) relatively simple to realize,
(iv) easy to maintain, and
(v) capable of real-time current mapping.

Furthermore, it has already been proven that this method can be "upscaled" to fuel cells of technical interest and is adjustable to different cell designs [46], which shows its high flexibility. Even the integration into fuel cell stacks should be possible although challenging [40].

From the CD measurements it is concluded that the current distribution of a DMFC seems to depend highly on the distribution of the oxygen concentration present in the cathodic flow field. This dependency could be mainly related to the methanol crossover and thus can be influenced by a number of measures such as less methanol-permeable membranes or the operating parameters, *e.g.*, the air stoichiometry, the anodic methanol concentration, or the anodic flow rate. Consequently, higher homogeneity of the CD can

[†] Surely, at some point the membrane will be dried in these segments, too.

be achieved for the flow field patterns and electrochemical components used here at either high air stoichiometries such as 7, a low methanol concentration (0.5 M) on the anode side, or a low anodic flow rate.[†]

Unfortunately, a reduction of the anodic flow rate also imposes higher gas loads on the anodic flow channels (cf. section 2.3, *Investigation of Two-phase Flows in DMFC's* of this chapter). Therefore, it is not clear if the methanol crossover is just reduced by a smaller concentration gradient across the membrane or if carbon dioxide layers limit the methanol transport to the membrane. Therefore, visual information of the state of the flow channels in addition to the knowledge of the current distribution will greatly improve the understanding of the phenomena involved in operating a DMFC. First results of the combination of both *in situ* methods will be given in the next section of this chapter.

Improving the CD homogeneity does involve cell design issues as well. The flow-field pattern on the cathode side has, of course, a high impact on the distribution of the oxygen concentration over the active area. A cathodic flow field comprising a single channel in serpentine configuration avoids any channel flooding, however, as these studies nicely illustrated results in a highly inhomogeneous CD at an air stoichiometry of two to three. Therefore, the cathodic flow field has to be designed very carefully because, among others, membrane drying effects, the flooding of the cathodic channels (cf. the section *In situ Visualization* of this chapter), and high oxygen depletion along a channel have to be considered.

3.5 Outlook

Methodical improvements

On the basis of today's knowledge, some improvements can be made on the methodical side, which may include the following:

- A further decrease of the resistance inherent in each channel down to 2 mΩ is possible and increases the accuracy of measurement: Decreasing the resistance

[†] Each compared to the baseline, which is a methanol concentration of 1 M and an anodic flow rate of 14 ml min^{-1}.

of each circuit will further decrease the lateral currents from one segment to the other occurring within the backing and thus it will further increase the accuracy of measurement. The latter is even more important, if a "quasi-segmented" approach is used as described in the next section of this chapter and it would increase the accuracy of measurement considerably.

- Increasing the resolution, *i.e.*, the number of channels: Increasing the number of channels may be a tedious task for cells with small active area, e.g., 30 cm^2 and may be even counterproductive because then lateral currents from one segment to the other may not be ignored anymore. However, the nine channels currently available give only limited information for fuel cells of technical interest.

- Implementing a higher channel read-out (20 kHz per channel or higher): A higher channel read-out is required if one likes to tackle the CO_2 poisoning in fuel cells. At the moment, the bottle neck is the data acquisition, which is too slow (1 Hz scan rate). In addition, the signals are scanned sequentially. Both will limit the significance of the experimental results.

Besides the combination of this method with the *in situ* visualization of the state of the flow field, this method opens up the exciting possibility to combine it with impedance spectroscopy. At present, impedance spectroscopy can only access integral cell values such as cell current or cell voltage, which limits its analysis to an average of the whole cell. However, the combination of impedance spectroscopy with this method of measuring the CD would allow to obtain *local* information by impedance spectroscopy.

In principle, the experimental setup as illustrated in Figure 14 remains the same for the locally resolved impedance spectroscopy measurements, except that the electronic load is replaced by an impedance spectrum analyzer. With a data analyzer that is able to record simultaneously all signals of the current sensors in addition to the total cell current and the cell voltage at a frequency of at least 20 kHz per channel the phase shift per single channel can be computed. Furthermore, the impedance of the whole cell would also be obtained and eventually, effects that were seen in these data can be

related to the local impedance data. So far, preparatory work has been done and no contraindications for such a combination have been found [47].

Recommendations for future studies

This work has to be regarded as a basis for future studies, which could be concerned with the following questions:

(i) What is the influence of water droplets in cathodic flow fields on the cell performance?

(ii) What are the important parameters for an optimized cathodic flow pattern?

(iii) Does co-flow mode have any effects on the CD of a DMFC?

(iv) Can advanced membranes, that feature lower methanol and lower water crossover, improve the CD of a DMFC?

(v) What are the consequences of other anodic flow patterns on the CD of a DMFC?

So far, it was illustrated by the data in Figures 20 to 22 that employing a cathodic flow field comprising a single channel in serpentine configuration results in a highly inhomogeneous CD. However, how does an optimized cathodic flow-field pattern that allows a homogeneous CD at low air stoichiometry have to look like? In principle, multi-channel flow patterns, as used for H_2-fuel cells, provide a better distribution of the reactants and at the same time lower the pressure drop over the flow field considerably. Either would be highly desirable for any technical application.

As seen in section 2 of this chapter, *In situ Visualization*, liquid water occurs in the cathodic flow channels even at a cell temperature of 110°C at 3 bar_{abs}. However, a partial flooding of a channel will change the pressure distribution within a multi-channel flow field considerably (see discussion at the beginning of this chapter) and thus will alter the flow of the reactants. In the worst case, one channel will be blocked from the supply with air and with time this channel will be filled with non-reactive nitrogen. Although this effect is likely to occur, the degree and the impact of the cathodic channel flooding on the performance of a DMFC is unknown. If the flooding of the cathode leads to a severe deterioration of the cathodic performance, various strategies, such as

hydrophobic web walls, could be followed to facilitate the water removal from the flow field.

In this context, the consequences of co-flow conditions on the CD are surely worth exploring. In co-flow mode the methanol concentration decreases along the flow channel together with the oxygen content. In this way, the highest oxygen concentration would be available on the cathode side where the highest methanol crossover is to be expected and thus the effect of methanol crossover may better be compensated. Presumed that a depletion of methanol along the anodic flow channels occurs, the co-flow mode could lead to a more homogeneous CD. Therefore, the operation of DMFC's in co-flow mode could be advantageous over the counter-flow mode.

The effect of different membrane types on the CD may be interesting to study. In *Chapter IV*, lower methanol *and* lower water permeation across radiation-grafted membranes could be shown (p. 114). Presumably, either will lead to a more homogeneous CD. On the other side, the lower water crossover could also add another difficulty to the operation of a DMFC, because parts of the membrane (at the air inlet) could be dried. Therefore, the investigation of the impact of water crossover on the CD of DMFC will give further insights in the mass transport phenomena involved in operating a DMFC.

Up to the present day, little is known about the influence of various anodic flow field patterns such as multi- or interdigitated channels on the CD of DMFC's. Especially flow fields comprising interdigitated channels, which shall provide a better mass transfer to the catalytic sites on the anode [48], may prove to be particular critical on their impact on the CD. It may be supposed that a homogeneous fuel distribution in interdigitated flow fields will be a challenging task, in which knowledge of the CD will be of great use. Since the distribution of the cathodic oxygen concentration overlays any other effect, studies that deal with the impact of the anodic flow field on the CD should use pure oxygen as oxidant.

4 Combination of *In situ* Methods

4.1 Introduction

In the previous sections, *In situ Visualization* and *Current Distribution in the DMFC*, the effect of carbon dioxide clusters present in the anodic flow field on the DMFC performance could not be answered. It was shown in the *in situ* visualization studies (Section 2) that large parts of the anodic flow field can be gas filled. Furthermore, the current distribution measurements (Section 3) revealed large variations of the current density over the electrode area. Although each method on its own allows characterizing the DMFC more thoroughly than standard electrochemical methods, *e.g.*, current-voltage curves, the information of these methods is still an integral value that can only be attributed to some extent to the one or the other effect. Therefore, it is necessary to combine different *in situ* methods to get further insights in the cell processes. This section will describe the experimental effort to explore the mass transfer limitations imposed by CO_2 clusters in the anodic flow field on the performance of a DMFC. First experimental results will be shown herein, conclusions drawn, and recommendations for future work will be given.

4.2 Experimental

Principle of measurement

As stated before, the current distribution and the *in situ* visualization measurements could be combined to one powerful method to gain further insights into mass transfer related phenomena. However, the technology to measure the current distribution has to be modified for this combination. The fairly thick flow-field plates (each 15 mm) used for the current distribution studies would prevent us from obtaining a neutron radiography image of a flow field at a short exposure time. On the other side, the thin graphite flow-field plates used in the *in situ* visualization studies do not allow to divide them into electrical isolated sections with all the requirements a segmented flow-field plate has to fulfill (cp. discussion on pp. 167).

The solution was a “quasi-segmented” approach of the flow-field plate whose principle is schematically depicted in Figure 23. Since dividing the graphite plate into separate

sections was not possible, a thin flow-field plate based on graphite material (Sigracet BMA5, *SGL Carbon Group*, Meitingen, Germany) of low conductivity (100 μΩm [49]) was chosen. Similar to the CD method introduced in section 3, this graphite plate was contacted by 9 current collectors, which, in principle, present the individual segments.

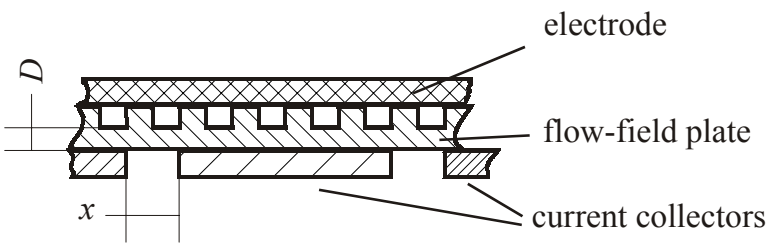

Figure 23: Schematic of the "quasi-segmented" flow field.

However, this method heavily relies on the thickness D of the graphite plate, its electrical conductivity ρ, and the gap x between two adjacent current collectors (see Figure 23). The conductivity of the graphite plate has to be low because the gap between two "segments" basically serves as "electrical isolation". In contrast to the earlier experiments outlined in section 3 of this chapter, the resistance R_L (see Figure 16) in this approach is significantly lower. In addition to the diffusion layer, lateral currents can also occur in this approach within the flow-field plate, which of course increases the leakage current from one "segment" to the other. Therefore, a high resistance of the graphite plate helps to minimize these leakage currents. For the graphitic material and the dimensions chosen (x = 2 mm, D = 1.5 mm) in this approach R_L is about 4 mΩ.

Nevertheless, this approach will result in less accurate measurements of the current distribution compared to those of section 3 of this chapter because lateral currents within the flow field cannot completely be avoided, *i.e.*, a "blurring" of the current distribution will be seen. A calculation based on the block diagram depicted in Figure 16 (p. 165) may illustrate this "blurring".

Assuming that the current produced by segment 2 is half of that of segment 1, $I_2 = 0.5\ I_1$. Then we can calculate according to Equation 4 the leakage current I_L from segment 1 to segment 2 and the actually measured currents $I_{S,1}$ and $I_{S,2}$ as given in

Equation 5. Furthermore, the actual values for the resistances are used, *i.e.*, R_S and R_L are equal to 6 and 4 mΩ, respectively.

$$I_L = \frac{3}{16} I_1 \quad \Rightarrow \quad \begin{cases} I_{S,1} = I_1 - I_L = \frac{13}{16} I_1 \\ I_{S,2} = I_2 + I_L = \frac{11}{16} I_1 \end{cases} \tag{5}$$

Equation 5 illustrates that the leakage current cannot be ignored and thus the error of this method is large. Consequently, the measured CD will be smoothed because of the leakage current. That means it has to be kept in mind, on the one hand, that small differences between two segments in the CD already indicate a significant difference. On the other hand, the values of the CD have to be regarded only as qualitative information.

Unfortunately, the error cannot be estimated from the calculation presented in Equation 5 because:

(i) The leakage current is only considered to one adjacent segment. However, in this approach each segment has at least two neighboring segments (see the next section for details on the technical layout). Therefore, the error will be even larger in practice.

(ii) The assumptions made for Equation 5 represent a "worst case scenario". It is assumed that the *entire* current of each segment *only* occurs at the edge of adjacent segments as depicted in Figure 24a. In reality, of course, a current distribution (Figure 24b) is more likely to occur and consequently, the current gradient across the "electrical isolation" is considerably smaller than assumed. Therefore, the leakage currents from one segment to the others will be considerably smaller.

However, an estimation of the error is not obvious and cannot be given here because the current distribution of each segment and the contact resistances are unknown.

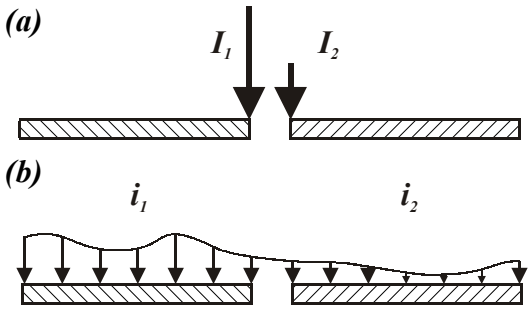

Figure 24: Schematics to illustrate the difference between the simplified approach made in Equation 5 ***(a)*** and the current distribution most likely to occur in reality ***(b)***. Assumption made: $I_2 = 0.5\ I_1$.

Nonetheless, the accuracy of this approach can be significantly increased by decreasing the resistance inherent in the outer circuitry. With an advanced system the resistance could be relatively easily reduced from currently 6 mΩ to as low as 2 mΩ. In the example given above, the leakage current I_L could then be reduced by about 40% to 0.1 I_1.

The "quasi-segmented" fuel cell

The cell used for these measurements is depicted in Figure 25 for illustration. The flow field used was flow field B (parallel flow field design) from section 2 of this chapter (Figure 6b, p. 146). It consisted of 50 channels in parallel arrangement with main channels on either side and was used on the anode as well as on the cathode side. Nine current collectors (gold-coated copper) were embedded in the anodic endplate to guarantee equal distances between the segments (on the upper left side in Figure 25). In contrast, the cathodic current collector consisted of a single gold-coated copper sheet. All current collectors were contacted from the backside through the endplate and connected according to the schematics given in Figure 14 of this chapter (p. 163). The contact resistances were minimized to the most possible extent by using gold-coated plug connectors (Multiarn "twisted", *Multi-contact AG*, Basel, Switzerland).

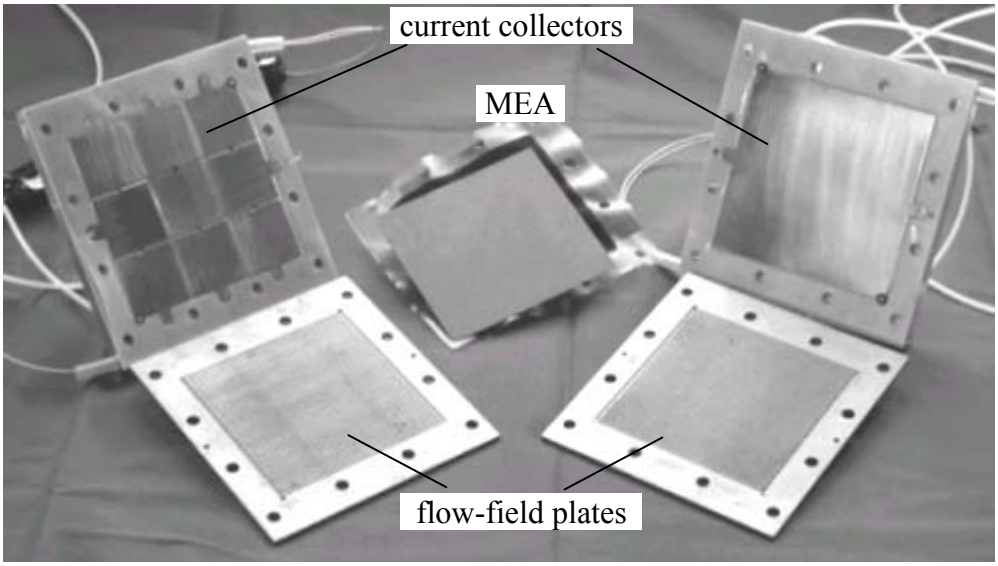

Figure 25: The cell used for the simultaneous measurement of the current distribution of the cell and the liquid-gas distribution in the anodic flow field.

4.3 Results & Discussion

The scope of this study was to explore the impact of gas accumulation in the anodic flow field on the performance of a DMFC. Therefore, neutron radiography images of the cell were taken at different anodic flow rates (6, 12, 24, and 50 ml min^{-1}) simultaneously with the measurement of the current distribution of the cell.

Operating conditions

Generally, varying the anodic flow rate resulted in the same relationship between the anodic flow rate and the gas content present in the anodic flow field as reported in Section 2 of this chapter: The void fraction of gas in the anodic flow channels recedes with an increase of the anodic flow rate (see subsection *Flow rate* of Section 2.3, p.153). In contrast, the general trend of the current distribution over the active area was unaffected by variations of the anodic flow rate. Therefore, only the experimental results obtained, for one flow rate will be given here exemplarily for the others. The data chosen to present below are based on the second lowest flow rate (12 ml min^{-1}) because of the higher gas accumulation in the channels at low anodic flow rate. In this way, the effect of gas clusters on the current distribution can be better observed.

As illustrated in the schematic of Figure 26, the DMFC was operated in co-flow mode with horizontal flow channels. The inlet of the aqueous methanol solution (0.5 M) and of air was at the upper left side and the outlet was located on the diagonally opposite side. Dry air was supplied to the cathode at a constant flow rate of 2 $\mathrm{lN\,min^{-1}}$ corresponding to an air stoichiometry of six at a current density of 200 $\mathrm{mA\,cm^{-2}}$. Similar to the CD measurements reported in section 3 of this chapter an equal backpressure of 3 $\mathrm{bar_{abs}}$ was applied on the anodic as well as on the cathodic compartment. The cell temperature and the supply temperatures of the reactants were constant at 70°C.

Experimental results

For a qualitative evaluation of the data, the neutron radiography images were segmentally analyzed with the algorithm described in Section 2 of this chapter (*Digital image analysis*, p. 142). Figures 26a to 26c display the gas fractions $\theta_{seg,x}$ present in the anodic channels for each segment x as function of the current density. Below each gas-fraction diagram the corresponding relative deviations from the average current density per segment are summarized (Figures 26d to 26e).

In general, the diagrams in Figure 26 refer to the three different vertical locations in the flow field. The symbols correspond to the location of the segment in the flow-field as indicated in the legend of Figure 26. In vertical direction, the type of symbol refers to its vertical position; in horizontal direction, the filling of the symbol corresponds to its horizontal location. The location of a segment is coded in its two-digit number consisting of row and column number, *e.g.*, the segment in the upper right edge is segment 13 (row 1, segment 3).

The segmental analysis of the neutron radiography images revealed that, in principle, the gas content increases vertically from the inlet to the outlet. The latter can be seen by comparison of Figures 26a to 26c. The only exception from this general trend is segment 11 (filled triangles in Figure 26a), which has a significantly higher gas content than the other two segments of the first row.

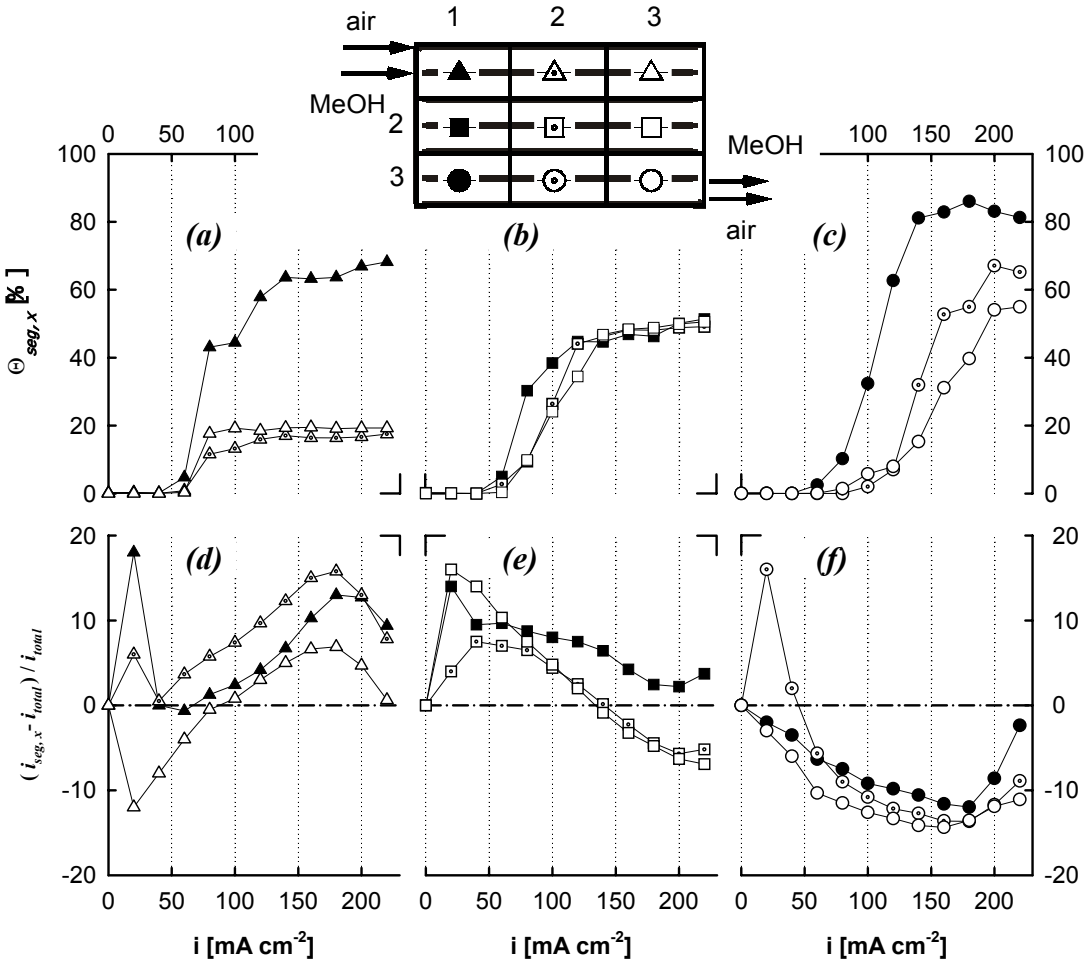

Figure 26: Void fractions of gas per single segment ***(a-c)*** and ***(d-e)*** the relative deviation of the current density of each segment from the average current density as function of the cell current. The cell conditions were as follows $T_{Cell} = 70°C$, $c_{MeOH} = 0.5$ M, $Q_{MeOH} = 12$ ml min^{-1}, $Q_{air} = 2$ lN min^{-1}, and p = 3 bar$_{abs}$.

However, a careful visual analysis of the neutron radiography images could explain this discrepancy. Because of buoyancy a large gas bubble had moved from the lower segments over the left main channel to segment 11. The latter can be seen in Figure 26a by the sudden rise of the gas content in segment 11 at a current density of 80 mA cm^{-2}. Furthermore, the visual analysis showed that the channel velocity in row 1 (triangles) was very slow and thus the gas bubble basically remained in segment 11 during the period of measurement.

In contrast to the vertical distribution of the gas content in the flow channels, a contrary deterioration of the current production from the top to the bottom can be observed by comparison of Figures 26d to 26f. The segments in row 1 have the highest positive

deviation from the average current density as to be seen by comparison of Figures 26d to 26f. The segments in the middle row (Figure 26e) perform about average, while all segments in row 3 (Figure 26f) have a negative deviation from the average current density.

Discussion

Nevertheless, it is *not* possible from Figure 26 to correlate the CD to the degree of gas content in the segments. In segment 11, for instance, more than 60 percentage of its channel area is gas-filled at a current density of 150 mA cm^{-2}. Nevertheless, this segment performs better than the average as illustrated in Figure 26d. Something similar is also observed for the segments of the middle row (squares). Although the channels of all three segments are filled with gas to about the same degree, segment 21 has a significantly better performance than the others. Again in row 3, the segment with the highest gas content within row 3, segment 31, performs about as well as the other two segments of this row as to be seen in Figure 26f.

From the experimental findings of Section 3, however, these CD data could be related to the cathodic air distribution. Presumably, the pressure drop over the cathodic flow field is too low to guarantee a homogeneous distribution of air. Therefore, the segments closest to the inlet of air (row 1, Figure 26d) have the best air supply and thus have the best performance. In contrast, the segments in row 3 are furthermost from the inlet of air. Therefore, less air may be supplied, and consequently, the segments of row 3 perform inferior to the segments in row 1.

This hypothesis would also explain the performance drop of the segments in row 1 and the performance increase of the segments in row 2 and 3 observed at current densities above 180 mA cm^{-2} as plotted in Figures 26d to 26f. If the supply of air to the channels is not homogeneous, which is also supported by the observation of liquid water in the cathodic flow field, then oscillations in the cathodic air distribution are possible. The latter could be caused by the formation of additional liquid water in the cathodic flow field and / or by the removal of liquid water from a cathodic flow channel. Both would result in drastic changes of the pressure distribution in the cathodic flow field and thus would affect the air distribution over the active area. Unfortunately, cathodic water

removal or the formation of additional liquid water in the cathodic flow field is difficult to observe under a current load. If only one flow field is liquid-filled the location of the liquid can be attributed neither to the cathodic nor to the anodic flow field.

Although the accumulation of carbon dioxide in the anodic flow channels was observed in these investigations the liquid distribution within the diffusion layer is unknown. Therefore, the impact of carbon dioxide on the CD remains an open question. Presumably, any effects of large CO_2 clusters in the anodic flow channels on the anodic performance could be better observed at a higher current density such as 500 mA cm^{-2}. Unfortunately, only low current densities could be studied here because the cells used were dramatically limited in their cell performance. The latter is illustrated in Figure 27, which gives a comparison of the polarization curves as obtained with a cell of 30 cm^2 (single-channel flow field, cf. *Chapter IV*) and the cell used here. Both cells were operated at the same temperatures / pressure and the identical electrochemical components were used.

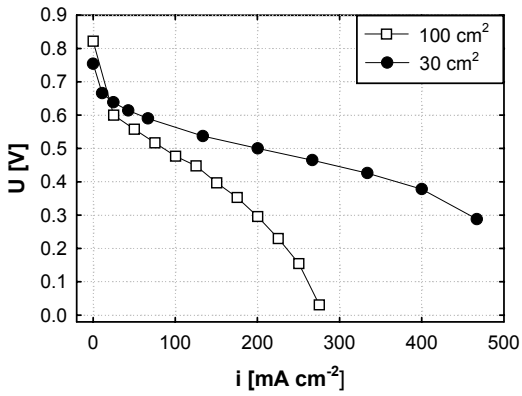

Figure 27: Comparison of the polarization characteristic of different cell sizes. The cell temperature and pressure were essentially the same (100°C, 3 bar_{abs}) and identical electrochemical components were used in both cells. The flow pattern of the small-scale cell was a single-channel flow field, whereas a parallel flow pattern was used in the large cell.

As easily to be seen from Figure 27, the scale up from laboratory single cells of 30 cm^2 size to cell with an active area of technical interest leads to inferior performance of the large-scale cell. Since identical electrochemical components were employed in both cells the difference in the polarization characteristic must originate from the different flow patterns. However, the reason for this difference is unknown so far. Inferior

performances of large scale cells are also reported in the literature, *e.g.*, in reference [4], about the effect, however, one can currently only speculate. Some experimental results suggest that the lower cell performance is related to the lower pressure drop of multi-channel flow fields [50]. Therefore, these flow patterns are hindered by the mass transport into the diffusion layer and thus to the catalytic sites.

4.4 Conclusions and Outlook

The results obtained so far have shown promising use of the combination of neutron radiography with the CD measurements for the investigation of DMFC's.[†] The consequences of the accumulation of carbon dioxide clusters in the anodic flow field of a DMFC on its CD were explored. At present, a correlation between product-rich areas in the anodic flow field and low current production in these areas could not be observed within the current density range. However, the gas-liquid distribution within the diffusion layer is unknown and may account for the insensibility of the CD on CO_2 clusters. Furthermore, these investigations could only be carried at low current density and thus any mass transport limitations imposed by the anodic carbon dioxide clusters may not be observed. Nevertheless, the general trend of the CD could be related to the oxygen distribution on the cathode side.

For future investigations, there are two major tasks:

(i) Improving the CD method for the application in the "quasi-segmented" cell approach.

(ii) Increasing the cell performance of large-scale cells.

Basically, an improvement of the CD method means to lower the resistances inherent in the outer circuitry. In this way, the lateral current occurring within the flow-field plate will be minimized and thus the accuracy of measurement in this "quasi-segmented" approach will increase considerably. A reduction of the ohmic resistance of the outer circuitry by 4 mΩ to 2 mΩ in total should be possible.

[†] It can also be applied on H_2-fuel cells and may give information on inhomogeneities during start up or shut down of the cell.

The cell performance of the large-scale cell has to be improved so that these investigations can be performed at higher current densities. Unfortunately, nothing has been published on the essential scale up factors for anodic flow patterns of DMFC's so far. Therefore, a fundamental understanding of the mass transfer phenomena involved in the processes occurring in anodic flow fields has to be developed. The latter will hopefully allow to come up with either improved operating parameters or a better anodic flow pattern, which allows operating the large scale cell at a higher current density, e.g., at 500 mA cm^{-2}.

5 Conclusions on DMFC Cell Design

Based on the experimental results of sections 2, 3, and 4 the following conclusions can be summarized:

(i) Two-phase flows occur on the anode as well as on the cathode side of a DMFC.

(ii) Increasing the anodic flow rate minimizes the gas-content in the anodic flow channels.

(iii) The CD of the DMFC is for the components used highly inhomogeneous at air stoichiometries of technical interest, *i.e.*, at an air stoichiometry of two or three.

(iv) The methanol crossover seems to be the key factor that influences the CD of a DMFC. Therefore, it can be influenced by optimizing the anodic operating conditions, *e.g.*, the flow rate or the methanol concentration.

(v) A correlation between gas-filled flow channels and a low current production in these areas could not be observed within the range of measurement (0-200 mA cm^{-2}).

(vi) The scale up from an active area of 30 cm^2 to 100 cm^2 results in severe performance losses.

Because of these six issues, the scale up of DMFC's from small-scale single cells to technical systems will differ significantly from that of H_2-fuel cells.

Considerations on the design of flow-field patterns

This work showed that special attention has to be paid to the design of the anodic flow pattern. Up to the present day, little is known about the influence of anodic flow patterns comprising multi- or interdigitated channels on the performance of DMFC's. It seems that a parallel flow field is considerable inferior to a single channel flow field. About the effect, however, one can currently only speculate. Experimental results (data were not shown) suggest that the lower performance of the parallel flow field is related to its lower pressure drop and thus the mass transport into the diffusion layer and therefore to the catalytic sites is impaired [50]. Consequently, flow fields comprising interdigitated channels, which shall provide an even better mass transfer to the catalytic

sites on the anode [48] may be the proper pattern for anodic flow fields of technical interest.

The choice of a flow pattern for the cathode side may be even more challenging than on the anode side for any cell of technical relevance. Because of the occurrence of water droplets in the cathodic flow field, a flow field comprising a single-channel is surely the most desirable. However, because of its inherent high-pressure drop, such a flow field is just not applicable in any technical realization. Therefore, multi-channel flow fields have to be used in a technical application using a DMFC. A blocking of the cathodic flow channels by liquid water could be anticipated or at least minimized by coating the channel walls with a hydrophobic layer and thus facilitate the water removal from the channels.

Considerations on the operating conditions

Minimizing the methanol permeation across the membrane for a given polarization characteristic is one of the biggest tasks in realizing DMFC's. As shown in section 3 of this chapter and also extensively discussed in *Chapter IV*, the methanol crossover not only affects the efficiency of a DMFC but, as shown in this chapter, also leads to significant inhomogeneities of the CD. However, reducing the anodic methanol concentration and lowering the anodic flow rate have both the potential to improve the CD of a DMFC greatly. Therefore, the stoichiometric supply of the aqueous methanol solution at a low methanol concentration is a necessity for operation of a DMFC system.

6 References

[1] M.P. Hogarth, and G.A. Hards, "Direct Methanol Fuel Cells", Platinum Metals Rev. **40** (1996) 150-159.

[2] X. Ren, and S. Gottesfeld, "Electro-osmotic Drag of Water in Poly(perfluorsulfonic acid) Membranes", J. Electrochem. Soc. **148** (2001) A87-A93.

[3] J. Eigeldinger, and H. Vogt, "The bubble coverage of gas-evolving electrodes in a flowing electrolyte", Electrochim. Acta **45** (2000) 4449-4456.

[4] P. Argyropoulos, K. Scott, and W.M. Taama, "Gas evolution and power performance in direct methanol fuel cells", J. Appl. Electrochem. **29** (1999) 661-669.

[5] P. Argyropoulos, K. Scott, and W.M. Taama, "Carbon dioxide evolution patterns in direct methanol fuel cells", Electrochim. Acta **44** (1999) 3575-3584.

[6] K. Scott, P. Argyropoulos, P. Yiannopoulos, and W.M. Taama, "Electrochemical and gas evolution characteristics of direct methanol fuel cells with stainless steel mesh flow beds", J. Appl. Electrochem. **31** (2001) 823-832.

[7] L. Müller, M. Krenz, and K. Rübner, "On the relation between the transport of electrochemical evolved Cl_2 and H_2 into the electrolyte bulk by convective diffusion and by gas bubbles", Electrochim. Acta **34** (1989) 305-308.

[8] F.N. Ngoya, and J. Thonstad, "On mass transfer effect due to electrolytically evolved gas", Electrochim. Acta **30** (1985) 1659-1664.

[9] H. Riegel, J. Mitrovic, and K. Stephan, "Role of mass transfer on hydrogen evolution in aqueous media", J. Appl. Electrochem. **28** (1998) 10-17.

[10] C.W. Tobias, "Effect of Gas Evolution on Current Distribution and Ohmic Resistance in Electrolyzers", J. Electrochem. Soc. **106** (1959) 833-838.

[11] W. Hilgert, "Charakterisierung der Gasphasenströmung in Blasensäulen mit Hilfe eines Ultraschall-Doppler-Messverfahrens", Friedrich-Alexander-Universität Erlangen-Nürnberg, Erlangen-Nürnberg, Germany, Dissertation, 1985.

[12] R.J. Bellows, M.Y. Lin, M. Arif, A.K. Thompson, and D. Jacobson, "Neutron Imaging Technique for In Situ Measurement of Water Transport Gradients within Nafion in Polymer Electrolyte Fuel Cells", J. Electrochem. Soc. **146** (1999) 1099-1103.

[13] E. Lehmann, H. Pleinert, T. Williams, and C. Pralong, "Application of new radiation detection techniques at the Paul Scherrer Institut, especially at the spallation neutron source", Nucl. Instr. and Meth. A **424** (1999) 158-164.

[14] K. Mishima, T. Hibiki, Y. Saito, H. Nakamura, and M. Matsubayashi, "The review of the application of neutron radiography to thermal hydraulic research", Nucl. Instr. and Meth. A **424** (1999) 66-72.

[15] Y. Saito, K. Mishima, T. Hibiki, A. Yamamoto, J. Sugimoto, and K. Moriyama, "Application of high-frame-rate neutron radiography to steam explosion research", Nucl. Instr. and Meth. A **424** (1999) 142-147.

[16] K. Mishima, T. Hibiki, Y. Saito, H. Nishihara, Y. Tobita, K. Koishi, and M. Matsubayashi, "Visualization and measurement of gas-liquid methanol two-phase flow with large density difference using thermal neutrons as microscobic probes", Nucl. Instr. and Meth. A **424** (1999) 229-234.

[17] J. H. Hubbell, and S. M. Seltzer, "Tables of X-Ray Mass Attenuation Coefficients and Mass Energy-Absorption Coefficients (version 1.03), [Online]", Available: http://physics.nist.gov/xaamdi [2002, June 7], National Institute of Standards and Technology, Gaithersburg, MD, USA 1997.

[18] "Table of simple integral neutron cross section data from JEF-2.2, ENDF/B-VI, JENDL-3.2, BROND-2, and CENDL-2", JEF Report, 14, Nuclear Energy agency organisation for economic co-operation and development, 1994.

[19] E. H. Lehmann, P. Vontobel, and L. Wiezel, "Properties of the Radiography Facility Neutra at SINQ and its Potential for Use as European Reference Facility", Nondestr. Test. Eval. **16** (2001) 191-202.

[20] H. Pleinert, E. Lehmann, and S. Körner, "Design of a New CCD-camera Neutron Radiography Detector", Nucl. Instr. and Meth. A **399** (1997) 382-390.

[21] S. Koerner, E. Lehmann, and P. Vontobel, "Design and optimization of a CCD-neutron radiography detector", Nucl. Instr. and Meth. A **454** (2000) 158-164.

[22] K. Takahashi, S. Tazaki, J. Miyahara, and Y. Karas, "Imaging Performance of Imaging Plate Neutron Detectors", Nucl. Instr. and Meth. A **377** (1996) 119-122.

[23] M. Thoms, "Neutron detection with imaging plates. Part II. Detector characteristics", Nucl. Instr. and Meth. A **424** (1999) 34-39.

[24] M. Thoms, D. Myles, and C. Wilkinson, "Neutron detection with imaging plates. Part I. Image storage and readout", Nucl. Instr. and Meth. A **424** (1999) 26-33.

[25] D. Kramer, Paul Scherrer Institut, Villigen, Switzerland, personal communication, 2002.

[26] S. Körner, "Digital Image Processing in Neutron Radiography", Technische Universität Wien, Wien, Austria, Dissertation, *HB 11209*, 2000.

[27] P. v. Schroeder, "Über Erstarrungs- und Quellungserscheinungen von Gelatine", Z. Phys. Chem. **45** (1903) 75-128.

[28] A.B. Geiger, A. Tsukada, E. Lehmann, P. Vontobel, A. Wokaun, and G.G. Scherer, "In Situ Investigation of Two-Phase Flow Patterns in Flow Fields of Polymer Electrolyte Fuel Cells by Neutron Radiography I: Opportunities, Limitations, and First Results", Fuel Cells, submitted (2002)

[29] G.S. Bauer, "Operating experience and development projects at SINQ", PSI-Report 98-04, Paul Scherrer Institut, Villigen 1998.

[30] T. Gilchrist, "Fuel Cells to the fore", IEEE Spectrum **11** (1998) 35-40.

[31] J. Stumper, S.A. Campbell, D.P. Wilkinson, M.C. Johnson, and M. Davis, "*In-situ* methods for the determination of current distributions in PEM fuel cells", Electrochim. Acta **43** (1998) 2772-2783.

[32] S.J.C. Cleghorn, C.R. Derouin, M.S. Wilson, and S. Gottesfeld, "A printed circuit board approach to measuring current distribution in a fuel cell", J. Appl. Electrochem. **28** (1998) 663-672.

[33] P.C. Rieke, and N.E. Vanderborgh, "Thin Film Electrode Arrays for Mapping the Current-Voltage Distributions in Proton-Exchange-Membrane Fuel Cells", J. Electrochem. Soc. **134** (1987) 1099-1104.

[34] B. Gupta, and G.G. Scherer, "Proton Exchange Membranes by Radiation-Induced Graft Copolymerization of Monomers into *Teflon*-FEP Films", Chimica **48** (1994) 127-137.

[35] L.R. Czarnetzki, and L.J.J. Janssen, "Electrode current distribution in a hypochlorite cell", J. Appl. Electrochem. **19** (1989) 630-636.

[36] C.J. Brown, D. Pletcher, F.C. Walsh, J.K. Hammond, and D. Robinson, "Local mass transport effects in the FM101 laboratory electrolyser", J. Appl. Electrochem. **22** (1992) 613-619.

[37] Ch. Wieser, A. Helmbold, and E. Gülzow, "A new technique for two-dimensional current distribution measurements in electrochemical cells", J. Appl. Electrochem. **30** (2000) 803-807.

[38] C. Wieser, A. Helmbold, and W. Schnurnberger, "Advanced Method to Measure Current Gradients in Polymer Electrolyte Fuel Cells", in: *Proc. Second International Symposium on Proton Conducting Membrane Fuel Cells II*, Ed. by S. Gottesfeld, and T.F. Fuller, Boston, November 1-6 (1998) 457-461.

[39] C. Wieser, and A. Helmbold, "Verfahren zur Bestimmung des Stoffumsatzes bei elektrochemischen Reaktionen und elektrochemische Einheit", *German Patent Application* DE 197 50 738 C 1, German Aerospace Center DLR, Germany, Nov. 15, 1997.

[40] R. Eckl, "Ortsaufgelöste Strommessung in Polymer-Elektrolyt-Brennstoffzellen", Technische Universität München, München, Germany, Diplomarbeit, 2001.

[41] H. Schaumburg (Ed.), *Werkstoffe und Bauelemente der Elektrotechnik 8 - Sensoranwendungen*, B.G. Teubner, Stuttgart, Germany, 1995.

[42] M.J. Caruso, T. Bratland, C.H. Smith, and R. Schneider, "A New Perspective on Magnetic Field Sensing", Sensors **15** (1998) 34-46.

[43] D. Xue, and Z. Dong, "Optimal fuel cell system design considering functional performance and production costs", J. Pow. Sources **76** (1998) 69-80.

[44] S.R. Narayanan, A. Kindler, B. Jeffries-Nakamura, W. Chun, H. Frank, M. Smart, S. Surampudi, and G. Halpert, "Performance of PEM Liquid-Feed Direct Methanol-Air Fuel Cells", in: *Proc. Proton Conducting Membrane Fuel Cells I*, Ed. by S. Gottesfeld, G. Halpert, and A. Landgrebe, (1995) 261-266.

[45] X. Ren, M.S. Wilson, and S. Gottesfeld, "High Performance Direct Methanol Polymer Electrolyte Fuel Cells", J. Electrochem. Soc. **143** (1996) L12 - L15.

[46] F.N. Büchi, A.B. Geiger, and R.P.C. Neto, "Current Distribution Measurements in PE Fuel Cell of Technical Relevance", PSI Annual Report / Annex V, ISSN 1423-7342, Paul Scherrer Institut, Villigen 2001.

[47] B. Andreaus, and A.B. Geiger, Paul Scherrer Institut, Villigen, Switzerland, unpublished results, 2001.

[48] A.S. Aricò, P. Cretì, V. Baglio, E. Modica, and V. Antonucci, "Influence of flow field design on the performance of a direct methanol fuel cell", J. Pow. Sources **91** (2000) 202-209.

[49] SGL Carbon Group, Technical Data Sheet BMA 5, 2002.

[50] D. Kramer, and A.B. Geiger, Paul Scherrer Institut, Villigen, Switzerland, unpublished results, 2002.

Chapter VI

Synopsis & Future Work

1 CONCLUSIONS 199

2 RECOMMENDATIONS FOR FUTURE WORK 201

2.1 Electrochemical Components 201

2.2 Process Engineering 202

2.3 Diagnostic methods 203

3 REFERENCES 205

1 Conclusions

Operating parameters

The cell results obtained showed a reasonably good agreement with published polarization characteristics (see p. 90, *Chapter IV*). The process variables with the most relevance to the polarization characteristic as well as to the methanol crossover were the cell temperature and the methanol concentration of the anode feed. As shown in *Chapter IV*, an aqueous methanol concentration of 0.5 M and high temperature (110 or 100°C) resulted in all cell tests in the best polarization characteristics. Furthermore, introducing a stoichiometric operation of the anodic fuel supply can improve the overall cell efficiency significantly (pp. 80).

FEP based membranes

The characterization study of radiation-grafted membranes revealed that similar polarization characteristics are obtained by any of the three FEP based membrane types (pp. 106). In the voltage region of interest (0.4–0.6 V), huge differences in the polarization characteristics could not be achieved for FEP based MEA's. However, the variation of the membrane properties affected the methanol crossover considerably. Only minor methanol retention could be realized by increased cross-linking of the membrane. In addition, the cell data of the medium cross-linked membranes (styrene / DVB = 8 / 2) were less reproducible, which could be an indication for inhomogeneous membrane properties. Unfortunately, it turned out that the mechanical properties of the highly cross-linked (styrene / DVB = 7 / 3) FEP 25 membrane were insufficiently and thus prevented us from obtaining any cell data for this membrane. Tripling the membrane's thickness (FEP 75), however, reduced the methanol permeation significantly. A comparison of MEA's based on Nafion 117 and FEP 75 membranes showed that similar values along a current-voltage curve could be achieved under the same operating conditions. However, the methanol and water flux across the FEP 75 membrane is significantly lower (about half) compared to Nafion 117 (p. 121). Thus, the overall cell efficiency (best value 31%) of MEA's based on the FEP 75 membrane (DG=15 wt%) is higher, especially in the part load region.

Methanol crossover

Based on water and methanol permeation measurements presented in *Chapter IV* (pp. 121), it seems that the methanol concentration is the decisive factor for the depolarization of the cathode in these studies, *i.e.*, for the components used here, and not the absolute amount of permeate. Furthermore, it appears that the water and methanol flux across the membrane are coupled, which results in similar methanol concentrations of the permeate for different membranes. Therefore, the depolarization of the cathode because of the methanol crossover is the same (if it is dependent on the methanol concentration of the permeate), regardless what membrane is used. The membrane however, does affect the flooding of the cathode considerably and can minimize the losses of methanol to the cathode. Therefore, the membrane does influence the overall cell efficiency of a DMFC greatly (see *Chapter VI*, section 5, pp. 120).

Furthermore, the current distribution measurements (section 3 of *Chapter V*, pp. 161) were for the electrochemical components used in this work highly inhomogeneous at air stoichiometries of technical interest, *i.e.*, at an air stoichiometry of two or three. It seems that the methanol crossover is the key factor, which affects the current distribution of a DMFC (see pp. 173). Therefore, optimizing the anodic operating conditions, *e.g.*, the flow rate or the methanol concentration, can influence it significantly.

Mass transport

From the water permeation measurements, which were presented in *Chapter IV*, p. 85, and the *in situ* visualization data illustrated in *Chapter V*, p. 151, it is to conclude that two-phase flows occur on the anode *and* on the cathode side of a DMFC. On the anode side, a direct relation between the gas content in the channels of the flow field and the flow rate was observed (p. 152). Increasing the anodic flow rate minimized the void fraction of gas in the flow channels. However, a correlation between gas-filled flow channels at the anode and a low current production in these areas, see pp. 186, could not be observed within the current density range of measurement (0-200 mA cm^{-2}).

In addition, the scale up from an active area of 30 cm^2 to 100 cm^2 resulted in severe performance losses, which could be related to anodic mass-transfer limitations [1].

2 Recommendations for Future Work

The challenges in realization of the DMFC are numerous and can roughly be classified in problems, which are related to the electrochemistry itself and in challenges that arise from the technical realization of the DMFC. Though all of these require very focused research it should be borne in mind that they all are interconnected at large. Thus, advances in the DMFC can be achieved on very different areas as was illustrated throughout this work. Consequently, future studies should be concerned with research on a broad basis, which may include the following topics:

2.1 Electrochemical Components

Solid polymer electrolytes

Surely, the water permeation mechanism of PSI-membranes deserves further attention. The issues that could be addressed are:

(iii) What is the limiting cause that restricts the water / methanol flux across the membrane?

(iv) How does the degree of grafting / cross-linking of a membrane affect the water permeation?

Presumably, the development and validation of *ex situ* measurements for the water and the methanol flux across a membrane would be of great help for precise characterization of the membrane's properties.

This work showed clearly that thick membranes are advantageous for use in the DMFC. Thus, even thicker membranes than FEP 75 membranes should be investigated in the DMFC. Because the preparation of thick FEP membranes could be difficult, it would be of interest to explore the potential to stack thin FEP based membranes as known from Nafion membranes [2] to achieve a thick solid polymer electrolyte. On the other hand, it may be of interest to explore the potential of PSI-membranes at low operating temperature. The latter would be required for most applications in the mobile / portables sector.

Electrodes designed for the DMFC

The effect of the electrode structure on the water flux and the methanol permeation across the membrane would be worth studying. The effect of the PTFE content in the backing, its porosity, and the amount of pore filler on the liquid / gas flux on the one hand and on the ohmic resistance on the other hand is surely an interesting research field of high potential. Eventually, the methanol crossover to the cathode can be diminished by the structure, porosity, and hydrophobicity of the anode electrode. In contrast, the cathode electrode may be designed to ease the flooding of the electrode or to prevent the permeation of excessive amounts of water.

2.2 Process Engineering

Operating conditions

Minimizing the methanol permeation across the membrane for a given polarization characteristic is one of the biggest tasks in realizing DMFC's. As shown in section 3 of *Chapter V* and also extensively discussed in *Chapter IV*, the methanol crossover not only affects the efficiency of a DMFC but, as shown in *Chapter V*, also leads to significant inhomogeneities of the current distribution. However, reducing the anodic methanol concentration and lowering the anodic flow rate have both the potential to improve the current distribution of a DMFC greatly. Therefore, the average stoichiometric supply of the aqueous methanol solution at a low methanol concentration is a necessity for operation of a DMFC system and would be surely worth to explore. First results were promising (*Chapter IV*) and indicated that a stoichiometric operation of the methanol flow can reduce the methanol crossover.

Flow-field patterns

Chapter V showed that special attention has to be paid to the design of the anodic flow pattern. Up to the present day, little is known about the influence of anodic flow patterns comprising multi- or interdigitated channels on the performance of DMFC's. It seems that a parallel flow field is considerable inferior to a single channel flow field. About the cause, however, one can currently only speculate. Experimental results (data were not shown) suggest that the lower performance of the parallel flow field is related to its lower pressure drop and thus the mass transport into the diffusion layer and

therefore to the catalytic sites is impaired [1]. Consequently, flow fields comprising interdigitated channels, which shall provide an even better mass transfer to the catalytic sites on the anode [3] may be the proper pattern for anodic flow fields of technical interest.

The choice of a flow pattern for the cathode side may be even more challenging than on the anode side for any cell of technical relevance. Because of the occurrence of water droplets in the cathodic flow field as illustrated in *Chapter V*, a flow field comprising a single-channel is surely the most desirable. Because of its inherent high-pressure drop, however, such a flow field is just not applicable in any technical realization. Furthermore, the experimental results of the current distribution measurements showed that a single-channel flow field results in highly inhomogeneous current distributions. However, how does an optimized cathodic flow-field pattern for the DMFC, which allows a homogeneous current distribution at low air stoichiometry, has to look like? In principle, multi-channel flow patterns, as used for H_2-fuel cells, provide a better distribution of the reactants and at the same time lower the pressure drop over the flow field considerably. Either would be highly desirable for any technical application. A blocking of the cathodic flow channels by liquid water could be anticipated or at least minimized by coating the channel walls with a hydrophobic layer and thus facilitate the water removal from the channels.

2.3 Diagnostic methods

On the basis of today's knowledge, some improvements can be made to the method of measuring the current distribution:

- A further decrease of the resistance inherent in each channel down to 2 mΩ is possible and increases the accuracy of measurement; decreasing the resistance of each circuit will further decrease the lateral currents from one segment to the other occurring within the backing and thus it will further increase the accuracy of measurement. The latter is even more important, if a "quasi-segmented" approach is used and would increase the accuracy of this approach considerably.

- Increasing the resolution, *i.e.*, the number of channels: Increasing the number of channels may be a tedious task for cells with small active area, e.g., 30 cm^2 and may be even counterproductive because then lateral currents from one segment to the other may not be ignored anymore. However, the nine channels currently available give only limited information for fuel cells of technical interest.

- Implementing a higher channel read-out (20 kHz per channel or higher): A higher channel read-out (because of the fast process) is required if one likes to tackle the CO poisoning in reformate-fuelled fuel cells. At the moment, the bottleneck is the data acquisition, which is too slow (60 Hz scan rate). In addition, the signals are scanned sequentially. Both will limit the significance of the experimental results.

Besides the combination of this method with the *in situ* visualization of the state of the flow field (see *Chapter V*, section 4, pp. 182), this approach of current distribution mapping opens up the exciting possibility to combine it with impedance spectroscopy. At present, impedance spectroscopy can only access integral cell values such as cell current or cell voltage, which limits its analysis to an average of the whole cell. However, the combination of impedance spectroscopy with this method of measuring the current distribution would allow to obtain *local* information by impedance spectroscopy. So far, preparatory work has been done and no contraindications for such a combination have been found [4].

The cell performance of the large-scale cell has to be improved so that these investigations can be performed at higher current densities. Unfortunately, nothing has been published on the essential scale up factors for anodic flow patterns of DMFC's so far. Therefore, a fundamental understanding of the mass transfer phenomena involved in the processes occurring in anodic flow fields has to be developed. The latter will hopefully allow to come up with either improved operating parameters or a better anodic flow pattern, which allows operating the large scale cell at a higher current density, e.g., at 500 mA cm^{-2}.

3 References

[1] D. Kramer, and A.B. Geiger, Paul Scherrer Institut, Villigen, Switzerland, unpublished results, 2002.

[2] B. Andreaus, "Die Polymer Elektrolyt Brennstoffzelle: Charakterisierung ausgewählter Phänomene durch Impedanzspektroskopie", EPFL, Dissertation, 2002.

[3] A.S. Aricò, P. Cretì, V. Baglio, E. Modica, and V. Antonucci, "Influence of flow field design on the performance of a direct methanol fuel cell", J. Pow. Sources **91** (2000) 202-209.

[4] B. Andreaus, and A.B. Geiger, Paul Scherrer Institut, Villigen, Switzerland, unpublished results, 2001.

Curriculum Vitae

Personal

Date of Birth:	May, 28, 1973
Place of Birth:	Munich, Germany
Marital Status:	Single
Nationality:	German

Education

1979 - 1983:	Elementary School, Munich, Germany
1983 - 1992:	High School, Munich, Germany
7/1992:	Abitur
11/93 - 12/98:	Student of Process Engineering, Faculty of Mechanical Engineering, Technische Universität München, Germany
5/98 - 12/98:	Diploma thesis with Prof. J.M. Prausnitz and J. Newman, Department of Chemical Engineering, UC Berkeley, USA and Prof. W. Peukert, Lehrstuhl für Feststoff- und Grenzflächenverfahrenstechnik, Technische Universität München, Germany
12/1998:	Diploma in Process Engineering
1999 - 2002:	PhD thesis with Prof. A. Wokaun, General Energy, Paul Scherrer Institut, Villigen, Switzerland